"DESIGN AND CHARACTERIZATION OF HALLOYSITE POLYMER DOPED NOVEL DRUG DELIVERY CONJUGATE"

Thesis submitted to

THE KLE ACADEMY OF HIGHER EDUCATION AND RESEARCH,BELAGAVI

(KLE DEEMED UNIVERSITY)

[Declared as Deemed-to-be-University u/s 3 of the UGC Act, 1956 vide Govt. of India Notification No.F.9-19/2000-U.3 (A)]
(Accredited 'A^{+}' Grade by NAAC 3rd cycle)
[Placed in Category 'A' by MoE (GoI)]

For the award of the degree of

Doctor of Philosophy

In the Faculty of Pharmacy

By

Ms. REVATI DHARAMPAL SAGARE

(Registration No: KLE/Ph.D./19-20/DO1219018)

Under the Guidance of

Dr. (Smt). FATIMA S DASANKOPPA M. PHARM, Ph.D.

Professor, Department of Pharmaceutics

KLE College of Pharmacy, Hubballi.

2024

UNDERTAKING

I, **Revati Dharampal Sagare,** hereby declare that the information and the data mentioned in my thesis entitled **"Design and Characterization of Halloysite Polymer Doped Novel Drug Delivery Conjugate"** belong to me and is original.

I am aware of the definition of plagiarism as detailed below:

- An act or instance of using or closely imitating the language and thoughts of another author without authorization and the representation of that author's work as one's own, as by not crediting the original author.
- A piece of writing or other work reflecting such unauthorized use or imitation.
- The deliberate or reckless representation of another's words, thoughts or ideas as one's own without attribution in connection with submission of academic work, whether graded or otherwise.

I hereby declare that the thesis prepared by me is original and does not involve plagiarism anywhere. In case at a later stage, it is found that I have indulged in plagiarism, then I am solely responsible for the same and the Institution is at liberty to take any disciplinary action against me including cancellation of the dissertation or any other penalties imposed by the University.

Place: Hubballi

Date:

Miss. Revati Dharampal. Sagare
Full time Ph.D. Research Scholar
Reg. No. DO1219018
KLE College of Pharmacy, Hubballi
KAHER, Belagavi-590010.

Ref. No. KAHER/AA/23-24/D-349

13th January 2024

Madam,

The soft copy of Ph.D. research thesis of **Ms. Revati D Sagare, KLE College of Pharmacy, Faculty of Pharmacy, Hubballi** has been submitted for anti-plagiarism check at the office of the undersigned through "Turn-it-in" package. The scan has been carried out and the scanned output reveals a match percentage of **4%** which is within the acceptable limit of 10%.

To obtain the comprehensive report of the plagiarism test, research scholar can send a mail to **diracademic@kledeemeduniversity.edu.in** along with the Registration Number, Name of the Scholar, Name of Guide/Co-guide and title of the thesis.

DIRECTOR ACADEMIC AFFAIRS Deemed-to-be University

Dr.(Mrs.) Roopa M. Bellad
Director, Academic Affairs

To,

Ms. Revati D Sagare
Full-Time Ph.D. Scholar,
2019-20 Batch, Faculty of Pharmacy,
KLE College of Pharmacy,
Hubballi.

Cc to :

1. The Principal, KLE College of Pharmacy, Hubballi
2. Dr. Fatima S. Dasankoppa, Professor of Pharmaceutics, KLE College of Pharmacy, Hubballi -Guide

KLE ACADEMY OF HIGHER EDUCATION AND RESEARCH,

(KLE DEEMED UNIVERSITY)

[Declared as Deemed-to-be-University u/s 3 of the UGC Act, 1956 vide Govt. of India Notification No.F.9-19/2000-U.3 (A)]

(Accredited 'A^{+}' Grade by NAAC 3rd cycle)

[Placed in Category 'A by MoE (GoI)]

BELAGAVI

COPYRIGHT DECLARATION

We hereby declare that **KLE ACADEMY OF HIGHER EDUCATION AND RESEARCH, BELAGAVI, KARNATAKA,** *shall have the rights to preserve, use and disseminate this thesis in print or electronic format for academic/research purpose*

Signature

Ms. Revati D. Sagare
Full time Ph.D. Research Scholar
Reg. No: DO1219018
KLE College of Pharmacy, Hubballi
KAHER, Belagavi-590010

Place: Hubballi

Date:

Signature

Dr. Fatima S. Dasankoppa
Professor,
Department of Pharmaceutics
KLE College of Pharmacy, Hubballi
KAHER, Belagavi-590010

Place: Hubballi

Date:

KLE ACADEMY OF HIGHER EDUCATION AND RESEARCH,

(KLE DEEMED UNIVERSITY)

[Declared as Deemed-to-be-University u/s 3 of the UGC Act, 1956 vide Govt. of India Notification No.F.9-19/2000-U.3 (A)]

(Accredited 'A^{+}' Grade by NAAC 3rd cycle)

[Placed in Category 'A' by MoE (GoI)]

BELAGAVI

DECLARATION

I hereby declare that the thesis entitled **"Design and Characterization of Halloysite Polymer Doped Novel Drug Delivery Conjugate"** *is a bonafide and original research carried out by me under the guidance of* ***Dr. (Smt.) Fatima S Dasankoppa,*** *Prof, Department of Pharmaceutics, KLE College of Pharmacy, Hubballi. The thesis or any part thereof has not formed the basis for the award of any degree/fellowship or similar title to any candidate of any University.*

Place: Hubballi

Date:

Miss. Revati Dharampal. Sagare
Full time Ph.D. Research Scholar
Reg. No: DO1219018
KLE College of Pharmacy, Hubballi
KAHER, Belagavi-590010

KLE ACADEMY OF HIGHER EDUCATION AND RESEARCH,

(KLE DEEMED UNIVERSITY)

[Declared as Deemed-to-be-University u/s 3 of the UGC Act, 1956 vide Govt. of India Notification No.F.9-19/2000-U.3 (A)]

(Accredited 'A^{+}' Grade by NAAC 3)

[Placed in Category 'A' by MoE (GoI)]

BELAGAVI

CERTIFICATE

This is to certify that the thesis entitled **"Design and Characterization of Halloysite Polymer Doped Novel Drug Delivery Conjugate"** *is a bonafide and genuine research carried out by* ***Ms. Revati Dharampal Sagare*** *under the guidance of* ***Dr. (Smt.) Fatima S Dasankoppa,*** *Prof, Department of Pharmaceutics, KLE College of Pharmacy, Hubballi.*

Place: Hubballi
Date:

Prof. (Dr.) M S Ganachari
Dean, Faculty of Pharmacy
KAHER Belagavi

KLE ACADEMY OF HIGHER EDUCATION AND RESEARCH,

(KLE DEEMED UNIVERSITY)

[Declared as Deemed-to-be-University u/s 3 of the UGC Act, 1956 vide Govt. of India Notification No.F.9-19/2000-U.3 (A)]

(Accredited 'A^{+}' Grade by NAAC 3)

[Placed in Category 'A' by MoE (GoI)]

BELAGAVI

KLE
EMPOWERING PROFESSIONALS

CERTIFICATE

This is to certify that the thesis entitled ***"Design and Characterization of Halloysite Polymer Doped Novel Drug Delivery Conjugate"*** *is a bonafide record of original research carried out by* ***Ms. Revati Dharampal Sagare*** *the award of the degree of* ***Doctor of Philosophy in Faculty of Pharmacy*** *under the guidance of* ***Dr. (Smt.) Fatima S Dasankoppa,*** *Prof, Department of Pharmaceutics, KLE College of Pharmacy, and Hubballi.*

Place: Hubballi

Date

Signature

Prof. (Dr). AHM Viswanath Swamy
Principal,
KLE College of Pharmacy, Hubballi.
KAHER Belagavi

KLE ACADEMY OF HIGHER EDUCATION AND RESEARCH,

(KLE DEEMED UNIVERSITY)

[Declared as Deemed-to-be-University u/s 3 of the UGC Act, 1956 vide Govt. of India Notification No.F.9-19/2000-U.3 (A)]

(Accredited 'A^{+}' Grade by NAAC 3)

[Placed in Category 'A' by MoE (GoI)]

BELAGAVI

CERTIFICATE

This is to certify that the thesis entitled ***"Design and Characterization of Halloysite Polymer Doped Novel Drug Delivery Conjugate"*** *is a bonafide record of original research carried out by* ***Ms. Revati Dharampal Sagare*** *the award of the degree of* ***Doctor of Philosophy in Faculty of Pharmacy*** *under my supervision and guidance.*

Place: Hubballi

Date

Dr. (Smt.) Fatima S Dasankoppa
Prof, Department of Pharmaceutics
KLE College of Pharmacy, Hubballi
KAHER Belagavi

ACKNOWLEDGMENT

*First of all, I bow before the sovereign Almighty **GODDESS MAYAKKA DEVI** and **SHREE SWAMI SAMARTH** for their blessings and showers on me.*

It is my immense pleasure and privilege to acknowledge the contributions of many individuals who have been inspirational and supportive throughout my work and endowed me with the most precious knowledge to see success in my endeavor. This thesis marks the end of my journey to the destination of Ph.D. in Pharmaceutics. This wonderful journey was not at all possible and imaginable without the help and support of my family, teachers, well-wishers, seniors, and juniors. I would like to express my gratitude towards all those who made this possible through their support and encouragement.

*It is indeed a great pleasure to express my deep sense of gratitude to my eminent, esteemed teacher and research guide **Dr. (Smt). Fatima S Dasankoppa**, Professor, Department of Pharmaceutics, KLE'S College of Pharmacy, Hubballi. I express my sincere thanks for her support since the beginning of my course. I express my deepest sense of indebtedness, heartfelt gratitude, and sincere thanks to my guide for being with me in all the way of Ph.D. journey. "Thank you so much mam"*

*I am thankful to the Principal **Dr. AHMV Swamy**, Principal KLE'S College of Pharmacy, Hubballi, for providing invigorative environment to purse this research work with great ease.*

*I extend my special thanks to our HOD, **Dr. S. P. Hiremath** for his elderly help and definitely valuable suggestion during my course.*

*I express my deep gratitude to **Dr. Hasanpasha N. Sholapur**, Assistant Professor, Department of Pharmacognosy for his scholastic guidance, patience, moral support, and inspiration, throughout my degree program.*

I would like to convey my sincere gratitude to ***Dr. S. K. Nimbal, HOD,*** *Department of Pharmacology,* ***Shri. S. B. Patil****, Assistant Professor and* ***Dr. L. A. Pattanshetti****, Assistant Professor for their timely help and valuable suggestions during the conductance of animal study design.*

I feel the inadequacy of words to express my heartfelt thanks to ***Dr. Basvanagowda H G,*** *for their untiring help and moral support throughout the pursuit of animal study.*

I take this opportunity to thank my Ph.D. colleague ***Ms. Lakshmi Swapna Sai****, for her friendly affection, constant encouragement, and moral support throughout my journey in the college.*

I would like to thank my beloved juniors Ms. Shreya Prabhu and Kamaladevi K. Mr. Mahesh, Shridhar, Sangameshwar, Sinchana, Navya, Shreya, Basavaraddi, Chetan, Sagar, Shivraj, Sarvesh, Siddu, Manas and Jyoti.

The completion of this dissertation is not only fulfilment of my dreams but also of my family who have taken lots of pain for me in the completion of my higher studies.

I would like to thank and express my deepest sense of indebtedness, heartiest gratitude to my beloved parents ***Mr. Dharampal Sagare*** *and* ***Mrs. Sandhya Sagare****, my dear brother* ***Dr. Rajat Sagare (Ph.D.),*** *for their love, sacrifice, patience and constant support during many up's and down's faced in the course of my completion of Ph.D. studies. It would have been really difficult to achieve this success without their encouragement and guidance. "Thank you mummy, papa and my brother"*

With immense gratitude and respect, I express my sincere thanks to my husband Mr. ***Shreyans Jodatti*** *and my father in-law and mother in-law for their constant support in completion of my study.*

Special thanks to ***Deshpande foundations****,* ***BVB College of Engineering and***

Technology and SDM Research Institute for Biomedical Sciences *for providing infrastructure to carry out my research work. Lastly, I would like to thank* ***Aarti Pharmaceuticals*** *for providing Ciprofloxacin Hydrochloride as a gift sample for my proposed research study.*

Mentioned are only a few, I sincerely express thanks to all those who have directly or indirectly been there with me on this wonderful journey.

"Dedication and passion, when combined with hard work, make a potent combination. That's the recipe for success"

Thank you one and all,

Revati Dharampal Sagare

TABLE OF CONTENTS

LIST OF ABBREVIATIONS

3DP	:	Three-dimensional printing
ANOVA	:	Analysis of Variance
CAD	:	Computer Aided Design
Cip HCl	:	Ciprofloxacin Hydrochloride
DHNTs	:	Doped Halloysite nanotubes
DSC	:	Differential Scanning Calorimetry
EDX	:	Energy Dispersive X-ray microanalysis
FDM	:	Fused Deposit Modelling
FTIR	:	Fourier Transform Infrared Spectroscopy
g	:	Gram
h	:	Hour
HNTs	:	Halloysite nanotubes
IAEC	:	Institutional Animal Ethics Committee
ICH	:	International Council for Harmonization
IPN	:	Interpenetrating Polymeric Network
µm	:	Micrometer
mg	:	Milligram
ml	:	Milliliters

MTT	:	(3-[4, 5-dimethylthiazol-2-yl]-2, 5 diphenyl tetrazolium bromide)
mV	:	Millivolts
nm	:	Nanometer
ODHNTs	:	Optimized doped halloysite nanotubes
PEO	:	Poly Ethylene Oxide
PVA	:	Poly Vinyl Alcohol
R^2	:	Coefficient of Regression
RH	:	Relative Humidity
RPM	:	Revolutions per minute
SD	:	Standard Deviation
SEM	:	Scanning Electron Microscopy Analysis
TEM	:	Transmission Electron Microscopy Analysis
TGA	:	Thermogravimetric analysis
XRD	:	X-Ray Diffraction Analysis
ZP	:	Zeta Potential Analysis
γ-MPS	:	γ-methacryloxypropyl trimethoxy silane
ºC	:	Degree Celsius
>	:	Greater than
<	:	Lesser than
p-value	:	Probability value

LIST OF TABLES

LIST OF FIGURES

ABSTRACT

Background: Despite of significant advancements in the arena of nanotechnology and novel drug delivery systems, nano-clays like halloysite nanotubes appears to be a potential boon for novel drug delivery system. However, these nanotubes do own some shortfalls. To overcome the drawbacks of halloysite nanotubes, doping of halloysite nanotubes serves as an ideal strategy to enhance the properties of halloysite nanotubes. Hence, the doped halloysite nanotubes functions as a nano-carrier for the design and development of antibacterial bio-polymeric wound dressings.

Objectives: The objective of the present research investigation is;

1. To design and characterize doped HNTs by homogenization technique, to enhance the desired properties of halloysite nanotubes.
2. To optimize the doped HNTs by the application of statistical tool JMP software.
3. To formulate and evaluate halloysite doped polymer conjugate into novel drug delivery system.

Methodology:

Strategy 1: Halloysite nanotubes was doped with γ-MPS using ultra turrax homogenizer. The doped HNTs were characterized for various analytical, thermal and morphological characterization studies. The doping of HNTs was optimized by 2^3 factorial custom design using a statistical JMP software. The concentration of γ-MPS, HNTs and Ethanol were selected as an independent variables. Whereas, diffraction angle (2θ) and zeta potential (mV) were considered as a dependent variables.

Strategy 2: The optimized DHNTs was used as a nano carrier to load Cip HCl by two different approaches intercalation and tubular entrapment assisted by homogenization, lyophilization and sonication technique. Furthermore, the Cip-HCl loaded doped

HNTs was incorporated for the fabrication of bio-polymeric sponges. The fabricated sponges were further subjected to various characterization studies: wetness integrity, swelling index, mechanical properties, porosity, morphological characterization, *in vitro* release study, bio-degradation studies, anti-microbial studies, *in vitro* cytotoxicity and *in vivo* wound healing activity.

Strategy 3: In the present research investigation Cip-HCl loaded doped HNTs PVA 3D scaffolds were designed and developed for the treatment of burn injuries. To begin with, the PVA pellets were coated with Cip HCl and Cip-HCl loaded doped HNTs and the coating efficiency was determined. Further, the PVA coated pellets were extruded using hot melt extrusion process to form filaments. The prepared filaments were further processed and designed for the fabrication of scaffolds by FDM technique using CAD software. The designed scaffolds were evaluated for physico-chemical studies, *in vitro* release, *in vitro* migration assay and stability studies.

Results:

Strategy 1: The results of various characterization studies for DHNTs revealed the successful doping of HNTs. The data obtained from zeta potential analysis presented a negative potential, signifying the presence of silica groups on the surface of nanotubes. The experimental findings derived from statistical analysis revealed that the selected independent variables were significant with respect to response variables. The overall desirability resulted to be D = 0.998, indicating the efficacy of custom design for measured response variables. The data obtained from SEM analysis indicated that, the extent of agglomeration of nanotubes in optimized DHNTs was significantly decreased as compared to pristine halloysite nanotubes. The % error for both the responses resulted to be less than 5 %, signifying the efficiency of custom design in optimizing the process parameters.

Strategy 2: The % encapsulation efficiency of Cip HCl by sonication method for 1:3 ratio was significantly increased to 98.70 % as compared to homogenization and lyophilization technique. The wetness integrity of sponge formulation indicated the formation of patch on instant gel within 60 s. The results of tensile measurements of sponges revealed that, SF2 sponge formulation presented an adequate tensile property 0.33 N/mm^2, with an elastic modulus and % break strain of 6.15 N / mm^2 and 48.4 %, identical to native skin structure. The BET analysis exhibited Type IV isotherm and confirmed the mesoporous nature of sponges. The SF1 and SF2 sponge formulations exhibited a pronounced porosity of 92.01 % and 84.25 % as compared to SF3 formulation i.e. 68.15 %. The *in vitro* release pattern of SF1 sponge formulation revealed an initial burst effect with a release of 82.49 % ± 0.01 at the end of 10 h. Further, SF2 formulation exhibited initial burst release followed by sustained release of 93.54 % ± 0.04 at the end of 24 h. Similarly, SF3 sponge revealed a complete sustained release pattern of 82.37 % ± 0.03 at 24 h, with no signs of burst release effect. The SF2 sponge was completely biodegraded within 60 min in wet soil conditions. While, in dry soil conditions the sponge was completely degraded within a span of 25 days. SF2 sponge showed an excellent anti-microbial activity and proved to have a significant potentials in antimicrobial dressing applications. The IC_{50} values for DHNTs and pure Cip HCl resulted to be 405.9 µg/ml and 52.16 µg/ml. The data obtained from cytotoxicity studies confirmed that DHNTs were bio-compatible and non-toxic in nature with a good cell viability. *In vivo* animal studies revealed a complete wound closure and epithelialization formation and thus, proved the wound healing potentials of SF2 sponge formulation. The stability studies performed for a period of 3 months revealed that the SF2 formulation was stable at the given storage conditions.

Strategy 3: The PVA pellets were coated with pure Cip HCl (PF1) and Cip HCl-DHNTs (PF2). The % coating efficiency of PF1 and PF2 resulted to be 60.23 % and 82.65 %. The coated pellets were extruded in the form of filaments and the filaments were further processed in the formation of 3D scaffolds (S1 and S2). The compatibility studies indicated that, the drug and excipients present in both the scaffolds were compatible with each other with no significant interactions. The tensile properties of both the scaffolds were identical to native skin structure with an ultimate tensile of 2.86 MPa for S1 and 4.17 MPa for S2. The overall porosity of S2 scaffold formulation was decreased to 60 % as compared to S1 formulation 82 %. The *in vitro* diffusion profile of S1 scaffold presented a complete release of 73.35 % ± 0.02 at 2 h, while S2 scaffold exhibited an initial burst effect followed by sustained release pattern of 85.54 ± 0.01 at 12 h. The *in vitro* migration assay of S2 scaffold on A549 cells revealed an excellent wound healing activity as compared to control (pure Cip HCl). The long-term stability studies revealed that both the scaffolds were stable at the given storage condition.

Conclusion: The present research study signifies the application of method optimization for doping of HNTs and then conjugated with polymers to design and develop the sponges and scaffolds, which in-turn proves to be an ideal approach for novel drug delivery system in pharmaceutical sciences.

Key words: Halloysite nanotubes; Doping; Ciprofloxacin hydrochloride; Sponges; Scaffolds; Lyophilization and 3D printing technique.

GRAPHICAL ABSTRACT 1

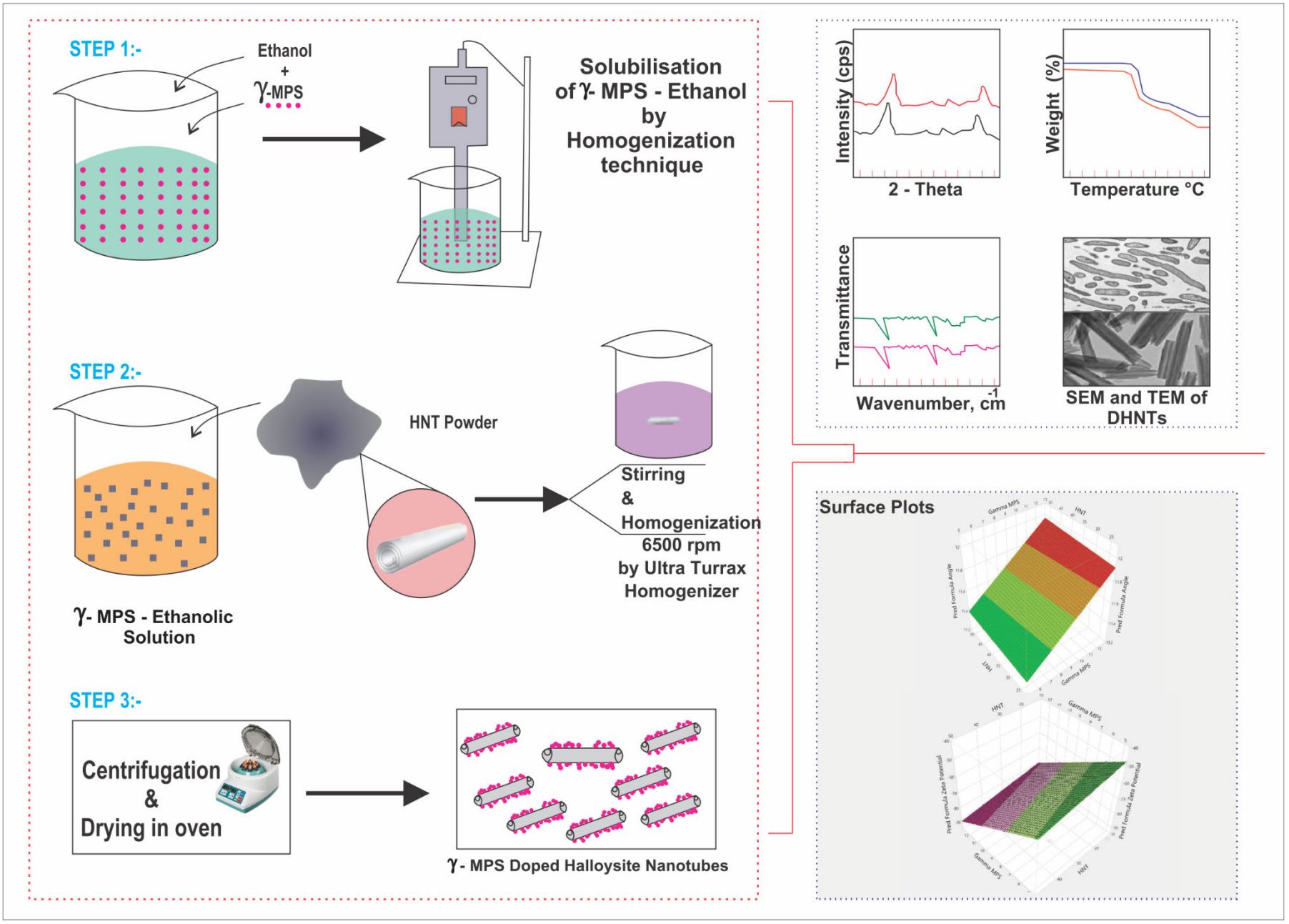

GRAPHICAL ABSTRACT 2

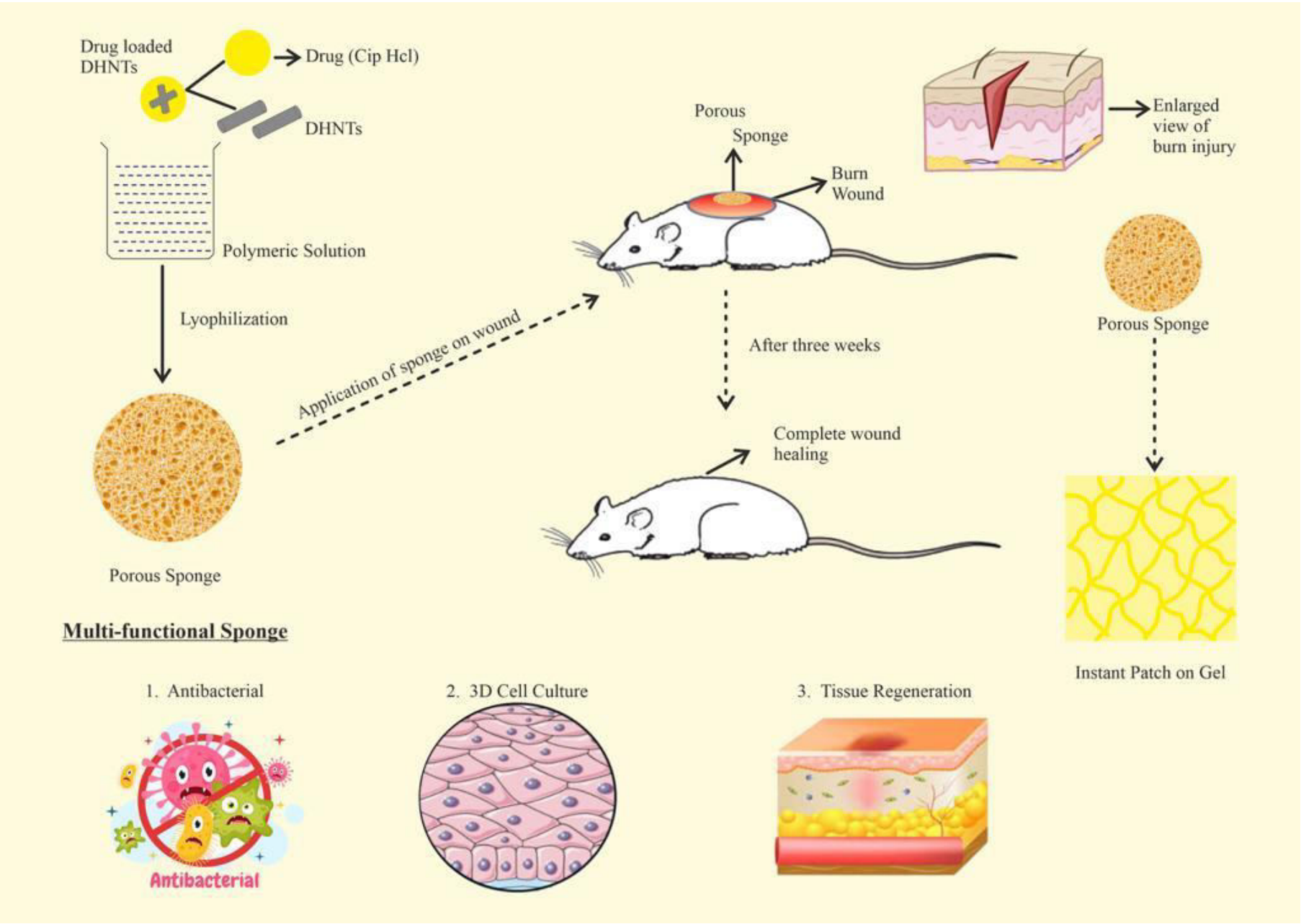

GRAPHICAL ABSTRACT 3

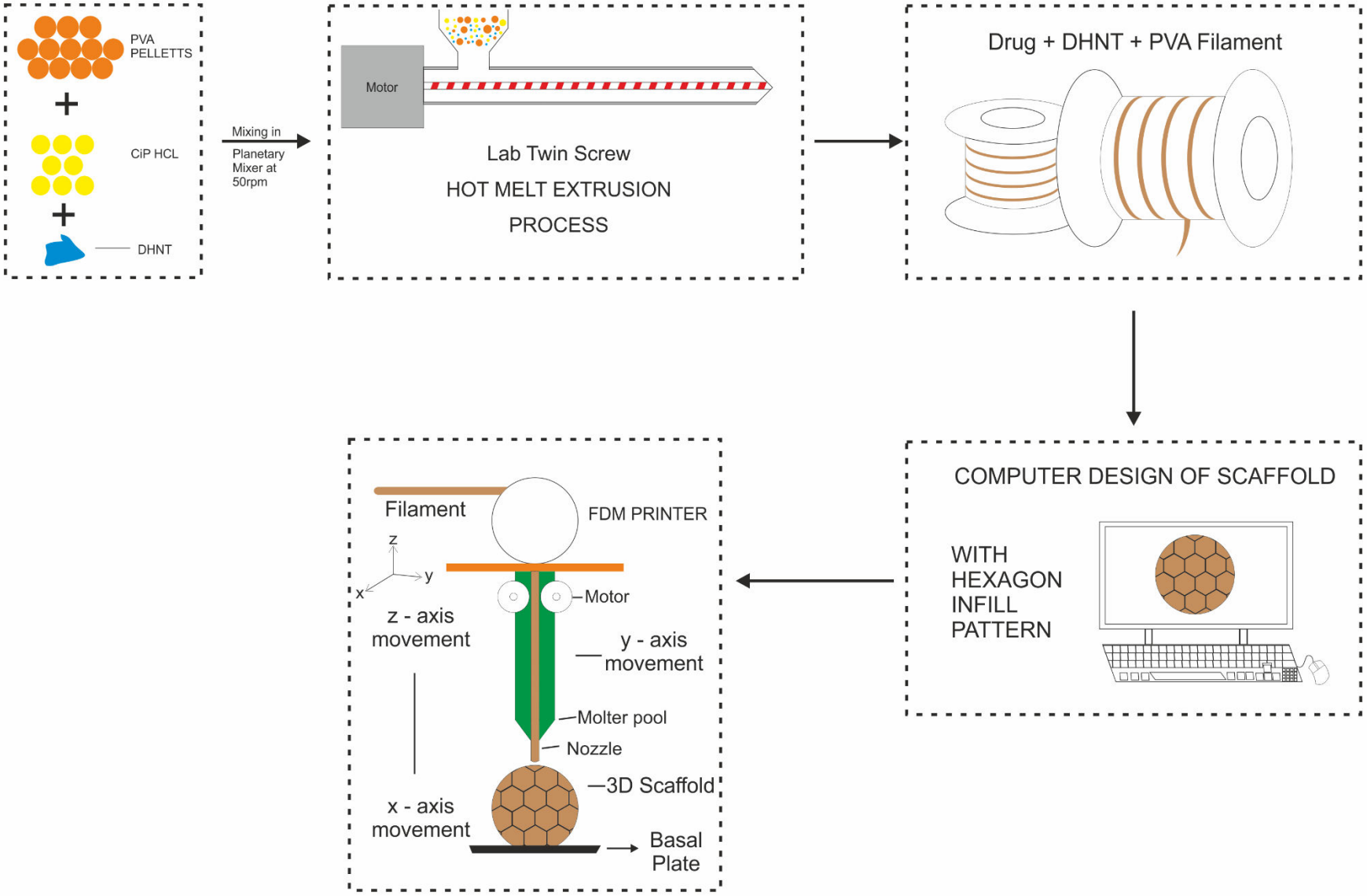

INTRODUCTION

This chapter outlines the concept of novel drug delivery systems, the significant class of clay minerals. It also presents the brief description of origin of Halloysite nanotubes, functionalization and its application as a nano container in the development of novel drug delivery system.

1.1. BACKGROUND

1.1.1. Novel Drug Delivery System

Over the last few decades, the term nanotechnology has been most extensively used in domains of science like bio-medical, pharmaceutical, engineering, electronics and physics. Nanotechnology is a multifaceted area, integrating the basic principles and experimental science of biophysics, molecular biology, and bio engineering [1]. In recent years, the advancements in the discipline of nanotechnology has offered an opportunity to research scientists, pharmaceutical and biomedical industries, enabling its application in the delivery of drugs and medical diagnosis [2]. Pharmaceutical nanotechnology encapsulates the incorporation of nanomaterials in pharmaceutical products as well as devices for drug delivery, diagnostics, imaging and biosensors [3].

A number of industries are making an effort to accelerate their development using a variety of approaches in order to meet the needs and expectations of the customers. The pharmaceutical industries functions on the principles of constant innovation and the implementation of advanced technology with the goal of addressing the global healthcare concerns and respond to healthcare emergencies [4]. The history of traditional drug delivery system dates back for almost five to six decades in the treatment a variety of diseases. However, the applications of traditional

drug delivery system have been outdated due to several reasons such as: poor bioavailability, frequent dosing and low therapeutic efficiency [5]. Therefore, to address the drawbacks associated with traditional drug delivery system, the process of drug delivery system must be optimized by adopting the concept of novel drug delivery system so as to ensure the enhancement of therapeutic efficiency of drugs [6].

Novel drug delivery system refers to "the new approach, formulations, technologies, and systems for transporting a pharmaceutical compound in the body as needed to safely achieve the desired therapeutic effects". These advanced drug delivery systems offers many potential benefits as compared to conventional drug delivery systems such as: increased bioavailability, target-specific activity, improved patient compliance and decreased potential for toxicity. Regardless of such significant benefits, the design and development of novel drug delivery system has posed a challenge for the researchers as a result of incorporation of expensive and toxic, non-biodegradable polymeric substances [7]. Thus, in order to refine these challenges, nanoclay based novel drug delivery system proves to be a boon for drug delivery system [8]. The incorporation of active drug molecule into the nano clay minerals with an appropriately designed therapeutic pathways leads to a promising novel drug delivery system [9].

1.1.2. Nano Clays

Clay minerals belong to the class of world's ancient materials, which has been widely used since from the long time for a variety of applications [10]. Clay minerals were preferentially utilized in prehistoric times to treat a variety of minor illnesses, such as infections, pains, aches, and food poisoning. Till date, clay minerals have traditionally been used as additives in the pharmaceutical sector. In addition to this,

these clay minerals can be efficiently employed as a diluent, nano carrier, taste masking agent and lubricant as an excipient in various pharmaceutical formulations [11].

The term clay refers to "a state of material comprising an organized layered silicate with a trace amounts of oxidized and organic materials [12]. The word "clay" springs from an ancient English word 'claeg' which means 'stiff or sticky to earth'. Clay minerals are basically the naturally occurring raw materials derived from sedimentary rocks with a dominant morphology of platy structures. Clay minerals are typically represented as "nano-clay" since they possess distinct nanoscale architecture. Nano-clay minerals belongs to a class of phyllosilicates ("phyllo" meaning sheet) with a layered structure, comprising two or more polymeric sheets of tetrahedral silica (SiO_2) along with a transitional octahedral alumina sheet (AlO_6) [13]. The tetrahedral and octahedral sheets functions as the cornerstone for clay layers. Therefore, these nano-clay minerals are classically categorized in accordance with the number and configuration of sheets in the layers of clay. Nano-clay minerals would likely to have one tetrahedral and one octahedral sheet (1:1) (e.g. Kaolinite and Halloysite), one octahedral sheet coupled with two sheets of tetrahedral groups (2:1) (e.g. Bentonite and Montmorillonite) and one octahedral sheet adjacent to another octahedral sheet fused between two sheets of tetrahedral groups (2:1:1) (e.g. Chlorite) [14].

The configuration of aluminosilicate groups topped on one another like a page of book or piles of leaves, with an intrinsic van der Waals gap between the layers, referred as an "Interlayer". In other words, the space within the layers, which can be easily accessible by water, polar organic liquids, or organic cations are collectively referred to as interlayer or galleries of clay mineral [15]. The spatial arrangements and

patterns of these tetrahedral and octahedral sheets influences a number of distinctive and identifiable characteristics of nano-clays. Therefore, in accordance with the mineralogical makeup, there are over 30 different varieties of nano-clays. The commonly found nano-clays are montmorillonite, kaolinite, laponite, halloysite, bentonite, hectorite, sepiolite, saponite, and vermiculite [16].

In general, nano-clay minerals exhibit a broad range of applications in pharmaceutical science, especially for the fabrication of novel drug delivery system, improved drug formulations and advanced therapeutic approaches. Subsequently, an extensive research and optimization necessitize to fully furnish the potentialities of nano-clay minerals in pharmaceutical industry [17].

1.1.3. Halloysite Clay Nanotubes – An Overview

Halloysite clay nanotubes (HNTs) are naturally occurring 1D aluminosilicate clay minerals, with an identical chemical composition to kaolinite. The name 'halloysite' was first coined by a mineralogist M. Berthier in 1826, in the tribute of Belgian geologist Omalius d'Halloy. These clay minerals are widely found to be deposited in soils, particularly within the moist tropical and subtropical areas and weathered igneous and non-igneous rocks present in USA, Brazil, Mexico, Australia, New Zealand and China [18]. HNTs are double layered aluminosilicate clay minerals with a chemical composition of $Al_2Si_2O_5$ (OH) $_4.2H_2O$, presenting a hollow nanotubular structure with their lengths ranging from 400 - 1000 nm, the inner and outer diameters of the nanotubes varying from 10 - 40 nm and 40 - 80 nm. HNTs are six membered rings 1:1 phyllosilicates, with one octahedral and one tetrahedral sheet. The octahedral sheet consists of aluminum or magnesium, which is coordinated six times with hydroxyl groups and oxygen from the tetrahedral sheet. Whereas, in

tetrahedral sheet, the silicon-oxygen tetrahedral are in association with adjacent tetrahedral by sharing three corners, while each tetrahedron's fourth corner is a component of neighboring octahedrons sheet. HNTs consists two types of hydroxyl groups, an inner hydroxyl groups and outer hydroxyl groups, present within the layers as well as on the surface of the nanotubes. The outer surface of HNTs are typically made up of siloxane (Si-O-Si) groups and the inner lumen of HNTs consists of a gibbsite-like array of aluminol (Al-OH) groups, with Al-OH and Si-OH groups present on the edges of nanotube [19].

HNTs are extensively characterized by the presence of porous nature, small particle size, an excellent surface area and increased surface to volume ratio. In addition to these characteristics, HNTs consists of positively charged inner surface (Al-OH) and negatively charged outer surface (Si-OH). The presence of these charges, enables HNTs to load a variety of therapeutic molecules on their surface or within the lumen of nanotubes [20]. However, these HNTs tend to develop a weak affinity with the guest molecules and results in insufficient loading capacity, which in-turn favors the fast release pattern of the drugs without achieving either controlled or sustained release behavior. The existence of weak affinity between HNTs and guest molecule is mainly due to the presence of weak Van der Waals forces [18]. Therefore, to overcome this limitation, it is necessary to customize the surface properties of HNTs by a process known as Functionalization.

Functionalization refers to “the process of modifying the surface nature of nanotubes by affixing various functional groups or molecules to further enhance their characteristics and customize them for specific application”. The word functionalization is colloquially referred to as doping or modification. The concept of

surface functionalization depends on the quantity of hydroxyl groups and their availability for bonding with other components [21]. Recently, a variety of methods are proposed to dope the surface of HNTs: acid etching method, organosilane coupling agent and surfactant modification. Among these techniques, organosilane coupling agent has emerged to be the most effective and reliable method for doping the surface of HNTs [20]. Doping of HNTs with organosilanes facilitates the expansion of basal spacing by enabling various organic and inorganic moieties to intercalate within the interface of HNTs.

Hence, doped HNTs are ideally considered to be the most potential nano-container for the delivery of drugs.

1.2 JUSTIFICATION FOR THE STUDY

Research Gap Identification I

The applications of various nano technological components like carbon nano-tubes, nano emulsions, nano fluids and nano capsules are been widely explored in the arena of health care and pharmaceutical sciences. Although being highly effective and demanding for large scale production, these nano-materials are not intended to be safe and acceptable for the humans as well as a natural environment due to their potential toxic effects. Therefore, in recent years there has been a rising concern over the applications of carbon nano-tubes. In consistence to these limitations, there are several other limitations which restrict the applications of carbon nano-tubes such as: these nano-materials are expensive, synthetic in origin, non-biodegradable and non-biocompatible in nature, has harmful effects and environmental hazardous in nature. Therefore, to alleviate these potential drawbacks, it is necessary to adopt the principles of one of the gifted technologies known as green nanotechnology [19]. Green nanotechnology is one of the advanced technologies that aims in the design and development of sustainable and environmental friendly nano-products. HNTs, nano powders and nano composites are currently being materialized as trendsetters in the field of green nanotechnology [22].

HNTs are naturally existing clay minerals having a unique tubular structure with a nanoscale dimension. These nano-materials are largely and easily available at low cost, biodegradable, biocompatible, with less harmful effects as well as environmentally safe. An alternative to these advantages, HNTs have some shortfalls like inadequate mechanical strength, lack of drug loading capacity, reduced drug polymer dispersion ability and inadequate chemical affinity with polymer [23].

In order to fill these gaps of HNTs, the interfacial juncture existing between the polymeric substrate and nanotubes must be engineered / tailored by a process known as Doping / Functionalization. The doping of HNTs results in significant enhancement in mechanical strength, increased drug loading capacity and enhances the dispersion ability of drug and polymer [19]. The increased drug loading capacity of HNTs, captivates a significant importance in the field of both pharmaceutical and biomedical sciences. Moreover, the increased drug loading capacity of HNTs intensifies the efficiency, safety and cost-effectiveness of novel drug delivery systems and make DHNTs as a potential nano-container or nano-carrier. Hence, there is a need to dope the surface of HNTs for achieving the desired properties of nanotubes [24].

The use of doped halloysite nano tube as a conjugate for novel drug delivery system is still an explored area of research for both bio-medical and pharmaceutical applications.

Thus, the present study assists in optimizing the surface properties of HNTs by doping process and suggests that these doped halloysite can be used as a conjugate as well as a nano container for the design of novel drug delivery system.

Research Gap Identification II

The latest advances in the field of tissue engineering have contributed towards the fabrication of biomaterial sponges [25]. Biomaterial sponges are preferentially utilized in transporting cells and/or biologically active substances, delivering a favorable microenvironment to support the cell proliferation and survival. Thus, it is essential to consider the biomaterial's potential to facilitate neo-tissue growth when designing sponges for regenerative medicine applications [26]. In consistence to this requirement, it is equally important to consider another set of pre-requisites which defines the ideal qualities of sponges for tissue engineering applications.

The following specifications necessitate while designing biomaterial sponges:

1. The collection of key factors that outlines the desirable characteristics of a sponge is: biocompatibility in nature, biodegradable and bioabsorbable [27].

In addition to these considerations, it is critically important to consider various design components and one of these components is the architecture of sponge.

With reference to architectural design, the major challenge associated with sponge is:

2. To have an adequate mechanical property, resembling to the native skin structure.
3. Sponges should be flexible enough in creating a complexed geometric design with sufficient porosity [25].

Thus, the fabrication of sponges with a tunable quality has consistently proved to be a quite challenging for every researcher. Therefore, in order to achieve a desirable quality of sponges, it is critically important to optimize an appropriate fabrication technique along with a proper selection of polymers.

A universal solution to design a customized sponge with desirable qualities is the application of freeze-drying technique. Freeze-drying technique also known as Lyophilization is a traditional simple technique used to fabricate sponge with enhanced porosity, mechanical strength and increased bio-absorption ability. Hence, lyophilization technique proves to be an approachable strategy for the development of sponges with tunable properties [28].

Research Gap Identification III

In the field of tissue engineering, a wide range of approaches are available for the restoration and regeneration of many anatomical deformities of functional tissues [29]. Traditionally, two-dimensional (2D) scaffold dressings are considered to be the first choice of treatment for injuries [30]. Since, these dressings fail to offer a desirable condition for the repairment of injury, a modernized dressing material with an advanced formulation have given a new avenue in the fields of pharmaceutical and tissue engineering. Thus, the drawbacks associated with conventional therapies has intensified the demand for fresh clinical approaches [31].

Another essential component to be considered when designing the scaffolds is to optimize the configuration of scaffolds. The most desirable choice for optimizing the configuration of scaffolds pops to be parametrically defined elemental analysis. The variables that constitutes the perfect configuration of scaffolds include: good resolution, proper architecture and geometry with an acceptable compressive strength and enhanced porosity. Therefore, to develop a scaffold with an adequate functionality, there is a need of an appropriate selection of technologically advanced manufacturing strategy [32].

The combination of CAD based software design with rapid prototyping / 3D printing technique offers a new paradigm shift in the fabrication of scaffolds with an advanced architectural design [29]. Hence, 3D printing technology sounds to be the most promising technology in designing the scaffolds with an advanced architecture for drug delivery system.

1.3 AIM, OBJECTIVES AND PLAN OF WORK

AIM:

To design, optimize and characterize halloysite doped polymer conjugate as novel drug delivery system.

RESEARCH OBJECTIVES:

- To design and characterize doped HNTs by homogenization technique to enhance the desired properties of halloysite nanotubes.
- To optimize the doped HNTs by the application of statistical tool JMP software.
- To formulate and evaluate halloysite doped polymer conjugate into novel drug delivery system.

PLAN OF WORK

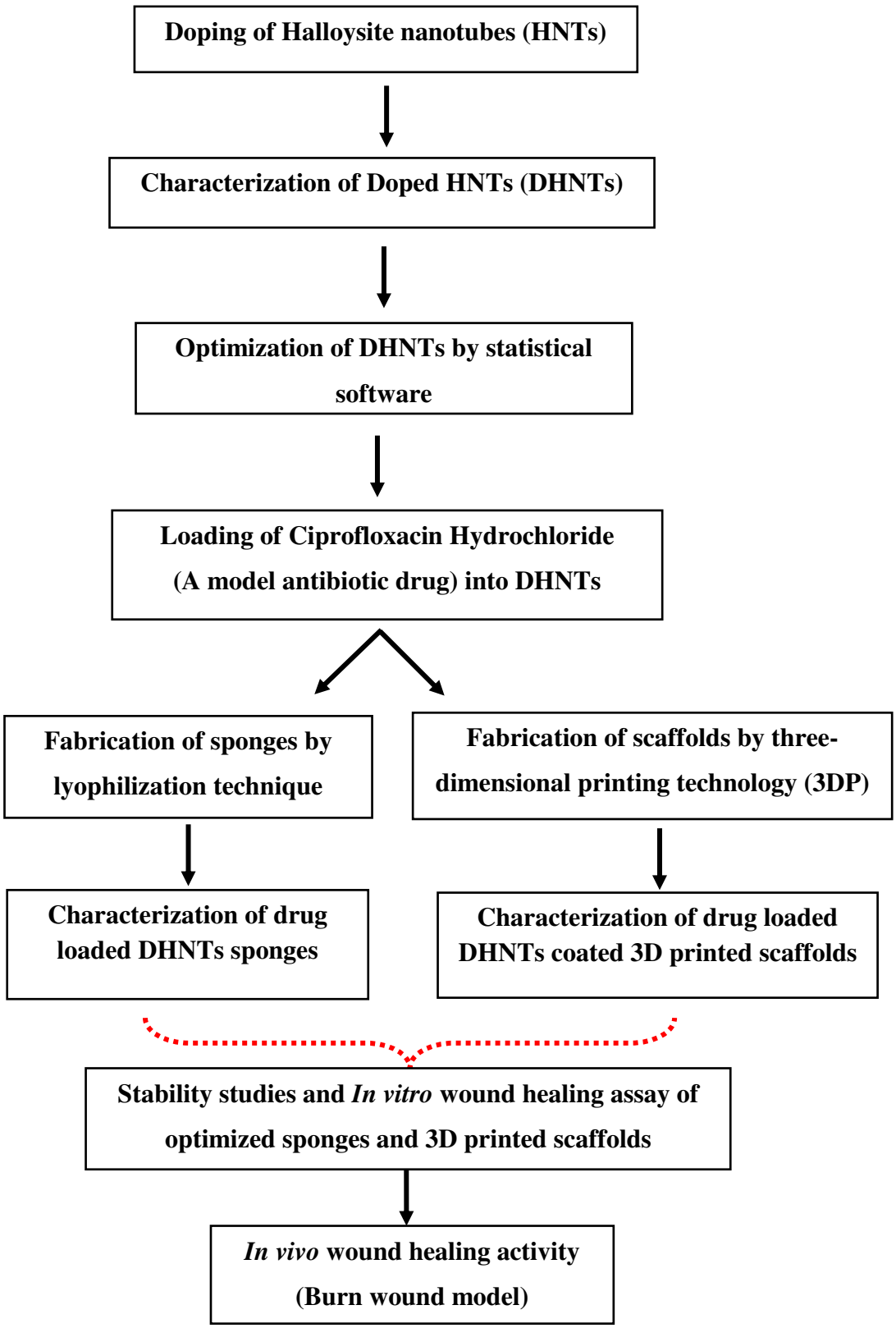
Doping of Halloysite nanotubes (HNTs)
Characterization of Doped HNTs (DHNTs)
Optimization of DHNTs by statistical software
Loading of Ciprofloxacin Hydrochloride (A model antibiotic drug) into DHNTs
Fabrication of sponges by lyophilization technique
Fabrication of scaffolds by three-dimensional printing technology (3DP)
Characterization of drug loaded DHNTs sponges
Characterization of drug loaded DHNTs coated 3D printed scaffolds
Stability studies and *In vitro* wound healing assay of optimized sponges and 3D printed scaffolds
In vivo wound healing activity (Burn wound model)

REVIEW OF LITERATURE

This chapter covers an overview of the literature survey in relation to structure and properties of HNTs. Doping of HNTs by using organosilane coupling agent, different techniques for loading of drug molecules and its applications with respect to wound healing activity are described. This chapter also includes a review on various strategies used for treatment of wound.

2.1. Halloysite Nanotubes (HNTs):

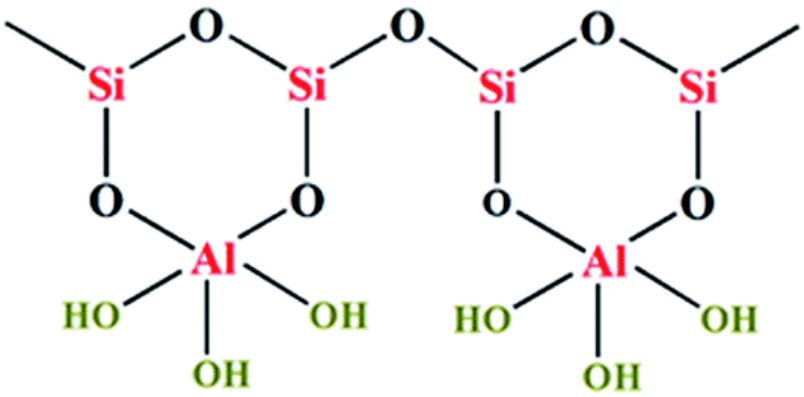

Chemical Formula: $Al_2 Si_2 O_5 (OH_4).2H_2O$

Molecular weight: 294.19

Functional category: Nano filler, mechanical reinforcement for plastics, nano-reactors, catalyst, nano-containers for loading of drugs, adsorbent for pollution remediation, nano-carrier.

HNTs are 1D nano-clay minerals derived from the deposits of natural clay minerals, which are widely distributed across the world in large quantities [33]. HNTs

belong to a family of alumino- silicates groups, by sharing a similar chemical property to that of kaolin except the presence of water molecules to form a monolayer. Therefore, in conjunction with the degree of hydration, HNTs can be broadly divided into two categories:

1. The presence of monolayer water molecules within the interlayer spaces of HNTs represents to the formation of state of hydration, which is commonly known as hydrated HNTs (basal spacing of 10 Å d_{001}).
2. Similarly, HNTs can be referred as dehydrated HNTs. Upon mild heating, the interlayer water molecules dissipate, which in-turn results in the reduction of interlayer basal spacing of HNTs (basal spacing of 7 Å d_{001}) [34].

HNTs are white to creamy white, odorless and tasteless fine amorphous powder with a unique tubular multi walled structure, high aspect ratio, natural availability, biocompatible, extensive functionality and porous in nature [35]. Due to its unique and novel properties as presented in Table 1, HNTs offer a wide range of applications in various fields. HNTs can be used as a cosmetic, as it functions as an exfoliant which helps in removal of cellular debris and maintains the structural integrity and fresh skin [36].

HNTs have emerged as an effective substitute in detecting and eliminating a variety of pesticides available in water and soil. Pandey et. al., [37] reported that HNTs are ideally recognized for their excellent catalytic and adsorptive properties, a prerequisite in prevention and management of environmental pollution. They can be utilized as a nanofiller in the packaging systems, preparation of polymeric nanocomposites, reinforcement material for the synthesis of various plastic and rubber composites. In consistence to these applications, HNTs have found to be a potential

nano-carrier, lubricants, additives, paints and sealants, pest repellant agents. The general structure of HNTs is depicted in Figure 1.

Table 1: Physical Properties of HNTs [38]

Physical Parameters	Values
Length	400 – 1000 nm
Outer diameter	40 – 80 nm
Inner diameter	10 – 40 nm
Aspect ratio (L/D)	10 – 50
Elastic modulus	140 GPa
Density	2.14 - 2.53 g/cm^3
Average pore size	80 - 100 Å
BET Surface area	22.1 - 81.6 m^2/g
Pore space	14 – 48.6 %
Lumen space	11 – 39 %
Specific gravity	2.53 g/cm^2
Cation exchange capability	0.1 - 0.7 mol/kg

2.1.1. Chemical Properties of Halloysite Nanotubes [39]

The outer surface of HNTs is negatively charged at the pH 6 – 7 (zeta potential -18 mV), possessing the similar properties as SiO_2 groups. Similarly, the inner lumen is positively charged resembling to Al_2O_3. The positively charged inner lumen of halloysite nanotubes facilitates in loading of negatively charged larger molecules. Similarly, the negatively charged outer surface of nanotubes supports in loading of positively charged guest molecules.

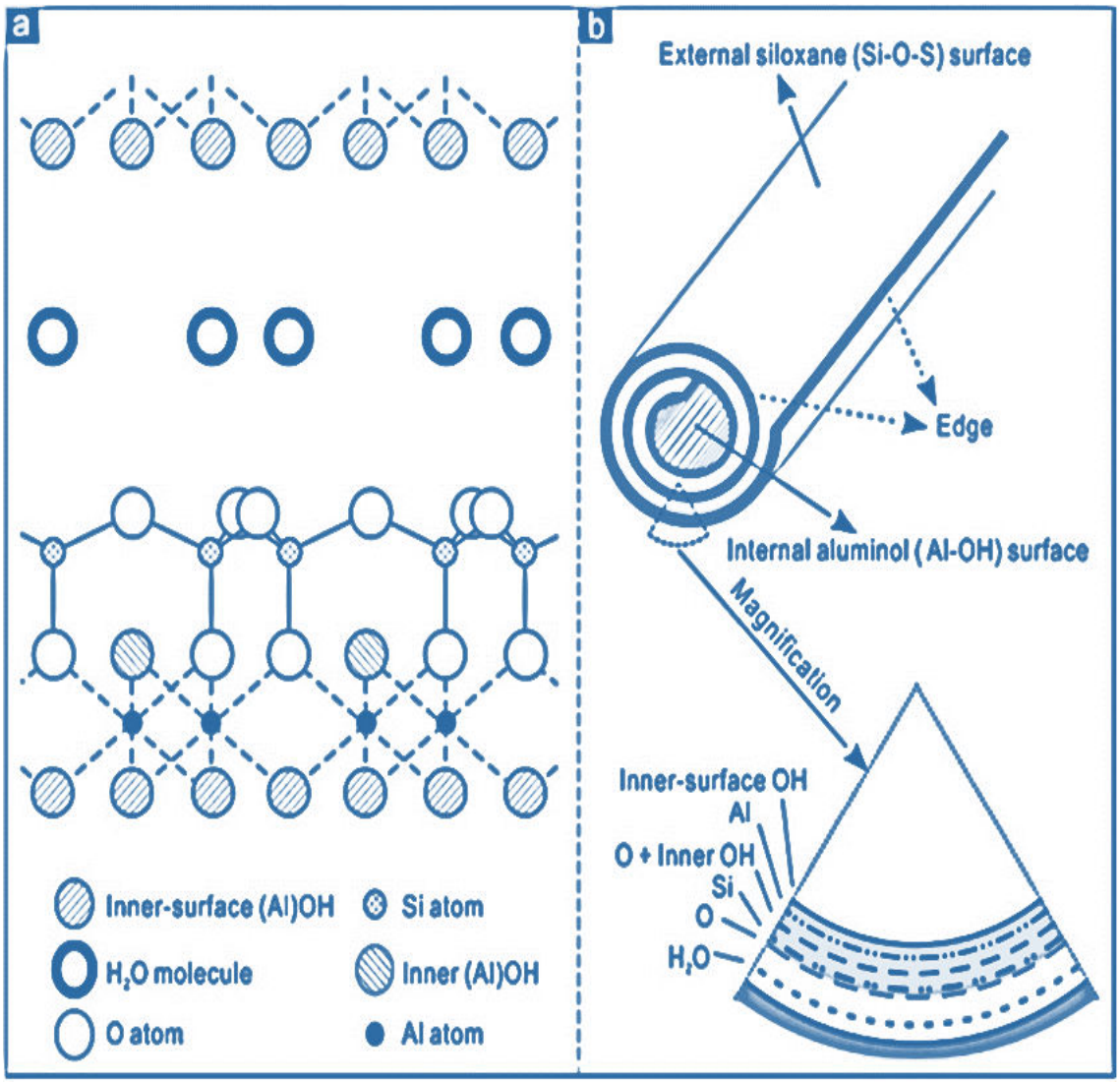

Figure 1: General Structure of Halloysite Nanotube

2.2. Surface Functionalization / Doping of HNTs

The functionality of HNTs as a nano-container is influenced by two essential key components: the very first component is the loading efficiency of HNTs or ability of HNTs to load the guest molecules and the second component is the existence of desirable affinity between guest molecules and HNTs [40]. Although HNTs have an ability to load a variety of guest molecules due to their unique surface chemistry and hollow nano-tubular structure. But achieving homogeneous drug molecule distribution within the HNT as well as achieving strong and stable interactions between HNTs and guest molecules is always a challenging for all the researchers [41]. This is due to the fact that, many studies have revealed that HNTs tend to develop weak interactions with drug molecules [42, 18]. Therefore, to enhance the desirable affinity and achieve uniform distribution of drug molecule within HNTs, it is necessary to functionalize the surface of HNTs by doping process. According to the literature survey, many studies have proposed the application of various silane coupling agent to dope the surface of HNTs and enhance the desirable properties of nanotubes.

2.2.1. Silane Coupling Agent

Silanes are basically a saturated silico-hydrogen compounds with a general formula $Si_n H_{2n+2}$ where (n = 1, 2, 3), composed of silicon and hydrogen atoms connected by single bonds. Silanes are the simplest, tiny silicon-based components with high degree of penetration into materials [43]. Due to their unique characteristic features, silanes have been extensively utilized in a variety of industrial applications as: crosslinking agents, adhesion promoter, coupling agents, dispersing agents, surface and polymer modifiers [44].

2.2.2 Chemistry of Silanes

"A silane is a molecule made up of one central silicon atom with four linkages". In other words, the term silane can be defined as a class of chemical compounds consisting monomeric silicon derivatives with four different functional groups attached to a central silicon atom. These functional groups may include non-reactive, organically reactive or in-organically reactive groups. A silane with at least one carbo-silicon bond structure (Si-CH_3) is referred as an organosilanes. The word silane is colloquially termed as, silane coupling agent, alkoxysilane or organofunctional silane [45].

Organofunctional silanes are "the substances with two distinct reactive groups bound to silicon atoms in such a way that they couple and interact with either organic resins or inorganic surface through covalent bonds". The primary structure of organo-silane is depicted in Figure 2

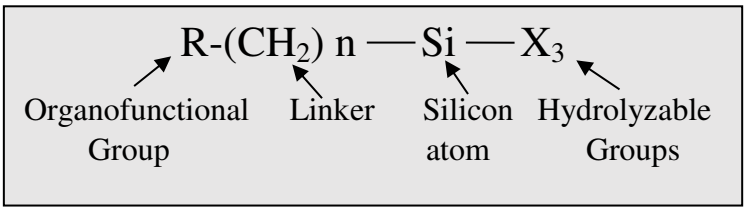

Figure 2: The Primary Structure of Organo-Silane [46]

Where, 'R' is a reactive non-hydrolyzable organic moiety, which means it may represent either an organo-functional, alkyl, aromatic, or a mixture of any of these groups. The presence of these groups contributes for the compatibility of organic moiety which is required for silanes to develop an interpenetrating polymeric

network (IPN). Similarly, the expression 'X' symbolizes the inclusion of alkoxy groups, predominantly the ethoxy or methoxy moieties, which reacts with a range of hydroxyl groups. These alkoxy groups are able to develop a bond with an inorganic moieties or nano-fillers to improve the dispersion ability as well as adhesion property. Subsequently, the methoxy groups reacts with hydroxy polymeric functional moieties [47].

2.2.3 Primary Reactions of Organo Functional Silane Coupling Agents

The reactions of silane coupling agents includes four phases:

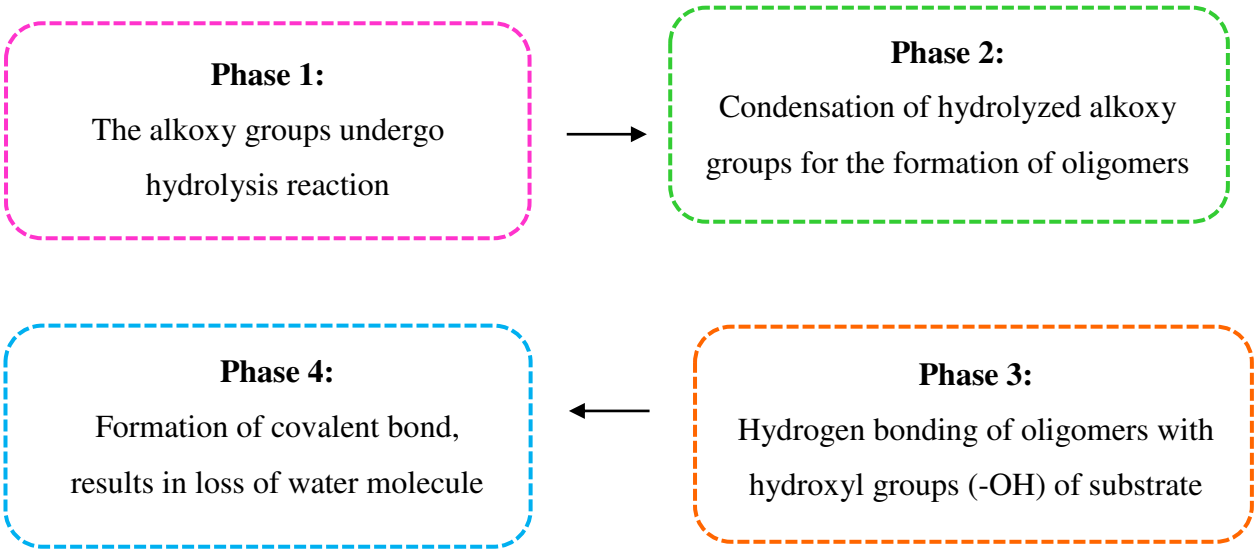

2.2.4. Role of Organo-functional Silanes in the Doping of HNTs

One of the most acceptable and widely used strategy to dope the surface of HNTs is grafting silanes. The silane moieties are grafted on the surface of HNTs by two step reactions:

Step 1: The hydrolyzable silanes comprised of silanol groups adsorbed onto HNTs (nano filler) via hydrogen bonding.

Step 2: Condensation of adsorbed silanol groups (Si – OH) with surface hydroxyl groups of HNTs by covalent interactions to form a siloxane bonds (Si - O - Si) [48]

Thus, the minimization of silanol groups, intensifies the surface properties of HNTs like:

1. Enhanced dispersion ability and reinforcement of HNTs within the polymeric matrix.
2. Improvisation in tensile properties of HNTs [49]
3. Ensures delayed release profile of various active ingredients
4. Enhanced drug loading capacity of HNTs [50]

The graphical representation of nanofiller surface treatment with silanes is depicted in Figure 3 [51]

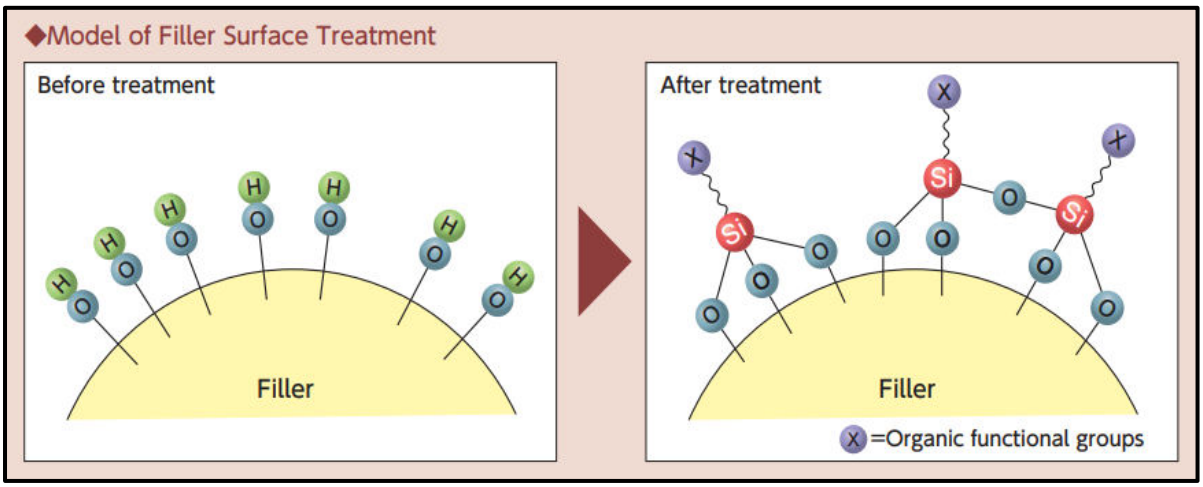

Figure 3: a). Filler Surface before Silane Treatment and b). Filler Surface after Silane Treatment

The commonly available silane coupling agents include: 3-aminopropyltriethoxysilane (APTES), γ-methacryloxypropyltrimethoxy silane (γ-MPS), Vinyltrimethoxysilane (VTMS), γ- Glycidoxypropyltrimethoxysilane (GPTS) and 3- Aminopropyltrimethoxysilane (APS) [52].

In the proposed research work, we have selected γ-methacryloxypropyltrimethoxy silane (γ-MPS) as a coupling agent to dope the surface of HNTs in order to optimize the surface properties of nanotubes.

2.3. γ-Methacryloxypropyltrimethoxysilane (γ-MPS)

Synonym: Silane A174, [3-(Methacryloyloxy) propyl] trimethoxysilane

Chemical name: 3-(Trimethoxysilyl) propyl methacrylate

Empirical formula: $C_{10}H_{20}O_5Si$

Molecular weight: 248.35 g/mol

Structure: [53]

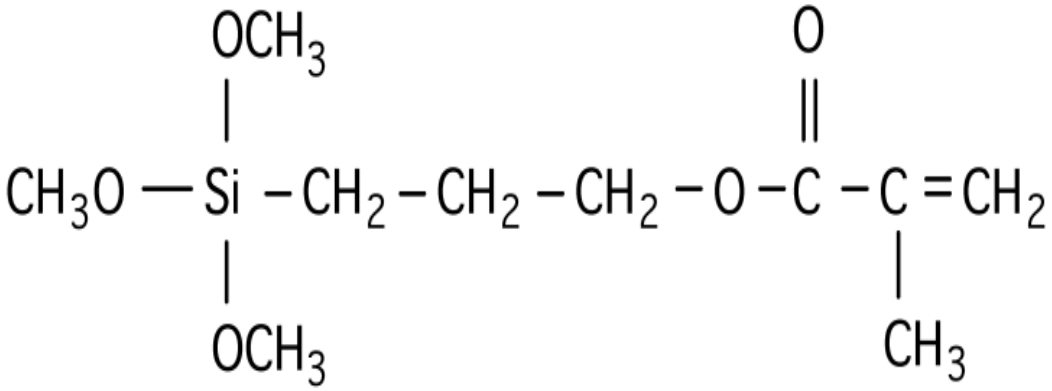

2.3.1. Physical Properties:

γ-MPS is freely soluble in organic solvents, relatively with simple hydrolysis and condensation results in the formation of polysiloxane. γ- MPS is a clear translucent liquid with a density of 1.045 ± 0.005 g/cm^3 and refractive index 1.43.

2.3.2. Applications:

γ- MPS is widely used as a coupling agent for the reinforcement of nanofillers and plastics, to improve the physical, electrical and mechanical properties of products. It is mainly used as an adhesive to enhance the bonding capabilities of both inorganic as well as organic substances such as siliceous fillers used in coatings, paints, glass fiber reinforced rubber and plastic [54].

How can a silane (γ- MPS) dope/modify the surface of HNTs?

1. The trimethoxy group's 3 (OCH_3) of **γ-** MPS undergo hydrolysis reaction to form 3(Si-OH) tri-silanols.
2. The tri-silanols associate with surface hydroxyl groups to form siloxane.
3. The minimization of tri-silanol groups enhances the surface properties of clay minerals [46].

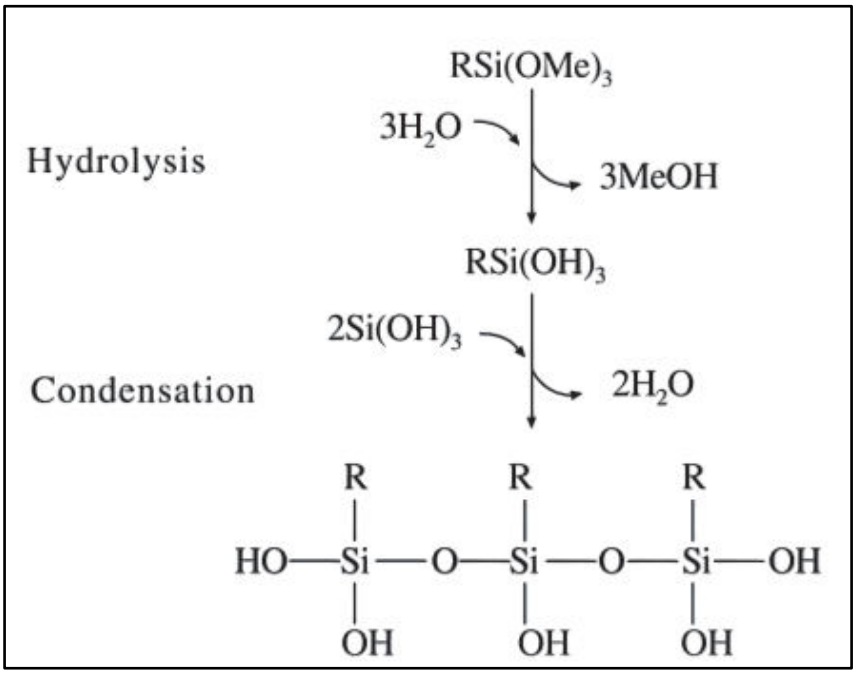

Tan et al., [55] functionalized the surface of HNTs using 3-aminopropyltriethoxysilane (APTES). Upon functionalization, the percentage loading efficiency of ibuprofen was increased as compared to unmodified HNTs. This was made possible, due to the formation of electrostatic interactions between the carboxyl groups of ibuprofen and aminopropyl groups of APTES silane coupling agent grafted on the surface of HNTs. Subsequently, the availability of amino groups delayed the *in vitro* release profile of ibuprofen. Whereas, unmodified HNTs presented an immediate release profile for ibuprofen.

Rawtani et al., [56] the APTES functionalized HNTs were utilized as a nano-carrier for the encapsulation of Cip HCl. The drug loaded functionalized HNTs exhibited the loading efficiency of 70% ± 1.7% and the successful loading of Cip HCl was confirmed by TEM, XRD, and FTIR analysis. The results of TEM analysis proved the existence of Cip HCl on the surface as well as within the lumen of functionalized HNTs. The drug loaded functionalized HNTs exhibited a controlled release drug profile at the end of 9 h with percentage drug release of 92.3%.

Padhi et al., [57] used γ-methacryloxypropyltrimethoxy silane (γ-MPS) as a silane to enhance the interfacial interactions and dispersion of HNTs in EVA polymeric matrix. The nanocomposites prepared by the incorporation of EVA-m HNTs resulted an increase in mechanical properties of nanocomposites. In addition, EVA-m HNTs nanocomposites showed an improved thermal stability as a result of high inter-tubular connectivity.

Buruga et al., [58] to enhance the interfacial interactions between polymer and HNTs, the nanotubes were modified using γ-MPS. These m-HNTs were further used for the preparation of PMMA nanocomposites by ultrasound assisted mini-emulsion

polymerization technique. The prepared nanocomposites consisting m-HNTs resulted in increased glass transition temperature as well as enhanced the mechanical strength of nanocomposites when compared with plain PMMA nanocomposites.

2.4. Various Techniques Used for Loading Drugs Into HNTs

The presence of large lumen diameter and nano porous structure of HNTs provide an active site and make HNTs as a potential nano-container to encapsulate a variety of anti-inflammatory, antibiotics, anti-cancer and anti-fungal drug moieties [59]. There are various methods to load the drug molecules into HNTs and the most important ones are being reviewed:

Adsorption, intercalation, and tubular entrapment are just a few of the several ways through which these guest molecules interact and bind with halloysite nanotubes [60]. The graphical design for loading of drugs into HNTs is depicted in Figure 4.

2.4.1. Adsorption: [61]

The presence of Si-OH and Al-OH functional groups on the surface and edges of HNTs facilitates in loading of drug by adsorption method via strong electrostatic interaction between the guest molecules and the negatively charged halloysite surface. HNTs have a positively charged surface at pH 3, further with an increase in pH, the HNTs acquire the negative charge on the surface. The presence of negative charge on the surface of HNTs counteract the ability of anionic molecules to have a strong attraction with HNTs.

2.4.2. Intercalation: [62]

HNTs are typically characterized by the presence of interlayer structures. The existence of interlayer structures, results in formation of interlayer spaces. Since HNTs are interlayer nano materials, they have an ability to intercalate a wide range of guest molecules between the interlayer spaces [19]. During this process, these guest molecules enter the interlayer space, resulting in the expansion of interlayers, due to the integration of water molecules in the inter-lamellar spaces. The expansion of these layers increases the d_{001} spacing between the layers. A class of drug molecules with anionic functional groups (e.g. aniline, amides, hydrazine, formamide, dimethyl sulfoxide and potassium acetate etc.) associate with alumina sheets and intercalate within the layers of HNTs [7]. Likewise, HNTs collaborate with silica and tetrahedral silicon sheets, so as to form the strong hydrogen bonds and dipole interactions. The process of intercalation is mainly related to the existence of interlayer water molecules. Therefore, the presence of water molecules within the layers of HNTs is required to achieve the intercalation process [62].

2.4.3. Tubular Entrapment: [63]

One of the most significant and widely accepted strategy for loading of drugs into HNTs is tubular entrapment method. It is also known as “Vacuum method”. This method was first introduced by Kelly et. al. in the year 2004 [64]. During this process, the air entrapped within the layers of nanotubes is substituted by saturated drug solution, followed by evaporation of solvent.

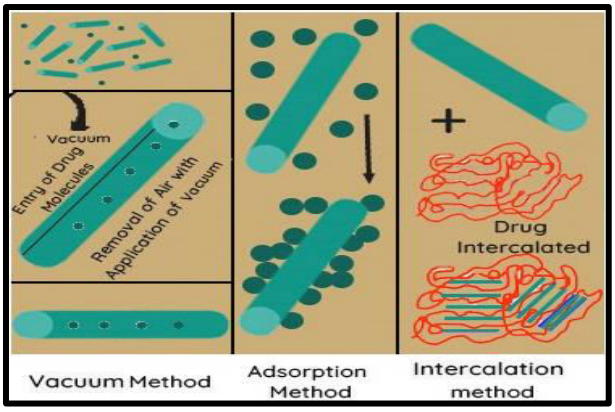

Figure 4: Drug Loading Techniques of HNTs

Mrinmoy et. al. (2020) [65] has selected a class of fluoroquinolone antibiotic model drug norfloxacin to study its antibacterial effect. Norfloxacin was loaded by tubular entrapment method within the lumen of HNTs. The drug loaded nanotubes were characterized for FTIR analysis, XRD analysis and morphological characterization. The data obtained from FTIR, XRD and morphological studies have confirmed the presence of norfloxacin within the lumen of HNTs. The norfloxacin loaded HNTs were further incorporated in the synthesis of nanocomposites. The prepared nanocomposites were flexible and capable of releasing the drug for an extended period of time. The data obtained from *in vitro* cytotoxicity study revealed that HNTs were biocompatible. Similarly, the results of antimicrobial study revealed that nanocomposites were found to be efficient against both gram-positive and gram-negative bacteria.

Pan et. al. (2017) [66] has developed vancomycin loaded HNTs as nano-carrier for sustained release system. The HNT: Van were loaded with different mass ratios by the application of principles of sonication and vacuum method. The 2:1 ratio of HNT: Van was considered as the optimized ratio with an increased loading efficiency (14.98 wt % Van) and an acceptable entrapment efficacy (8.83 %). HNT: Van presented an

effective prolonged release for a period of 33 days as compared to pure vancomycin. The antibacterial efficiency of HNT-Van was analyzed by performing Kirby-Bauer assay. The observations and findings obtained from Kirby-Bauer assay suggested that HNT-Van exhibited a prolonged release profile with an excellent antibacterial activity. Thus, it can be concluded that HNTs was considered as an efficient nano-carrier for the delivery of antibiotics in the treatment of bacterial infections.

2.5. Applications of Halloysite Nanotubes in Wound Healing

Wound is defined as the rupture of anatomic and cellular integrity of functional tissues on exposure to thermal, physical, chemical, immunological or microbiological injury to tissues. The term wound is derived from an old English word "wund" which means hurt, cut or damage. The phrase wound is commonly referred as injury, lesion or trauma [67]. Burns are typical injuries to the skin that pose significant challenges in reducing the scar formation and thereby, restoring the normal functions of skin. 'In response to a conservative assessment reports from World Health Organization (WHO) and National Association of Professionals involved in Burn Care in India (NABI), every year around 70 lakhs individuals in India suffer from burn injuries [68]. Traditionally, burn injuries are often categorized into three distinct types based upon intensity of skin injury and the portion of skin affected. The injury to the skin's epidermal surface represents as a superficial injury or first-degree burns. Subsequently, the injury to deeper dermal layers including sweat glands, hair follicles and blood vessels corresponds to partial-thickness wound or second-degree burns. Eventually, the rupture of deeper and subcutaneous fat tissues results in full-thickness injuries or third-degree burns. Although injuries might range from mild to severe, they have a significant impact on the nation's socioeconomic crises and

profoundly traumatize the individuals. Thus, providing a proper pharmaceutical treatment to improvise and revitalize the functions of the tissue is very essential and it has been presented as an issue of concern [20].

The process of wound healing consists of four different overlapping and interconnected phases: hemostasis, inflammation, proliferation and remodeling as depicted in Figure 5.

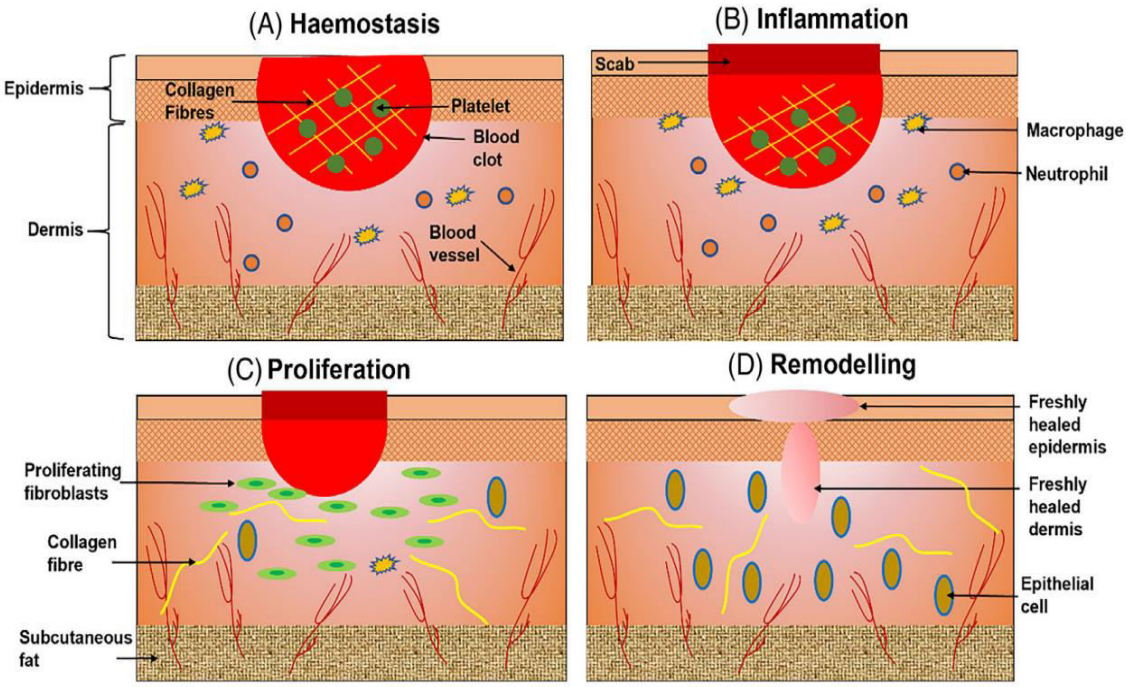

Figure 5. Diagrammatic Representation of Wound Healing. (A). Hemostasis, (B). Inflammation, (C). Proliferation and (D). Remodeling.

Wound healing is an intricate and multidimensional physiological process. Depending on the nature and extent of wound, a plenty of treatment modalities have been offered [69]. The various approaches for the treatment of burn injuries are depicted in Figure 6.

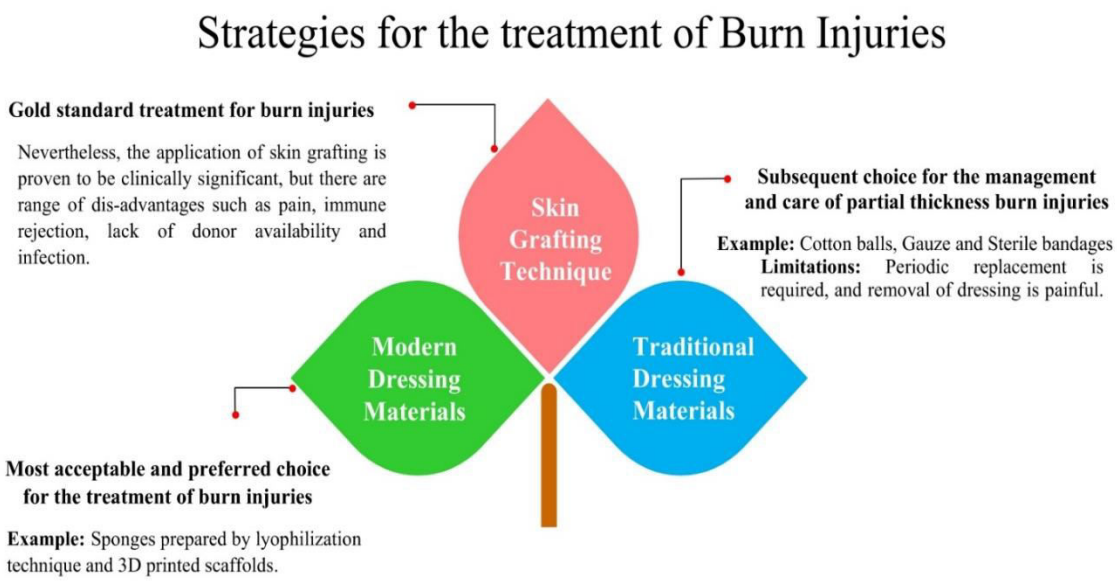

Figure 6: Strategies for the Treatment of Burn Injuries

From the last few decades the recent developments and advances in life sciences and health care system has propelled an excellent impact in pharmaceutical sciences and bio-medical engineering as an alternative to skin grafting technique and traditional dressings.

In light of this scenario, tissue engineering (TE) has become a potential topic to create a suitable templates and advancements to substitute an injured or dysfunctional organ as well as to facilitate the re-development of human tissues [70]. The tissue engineered biological substitutes are designed eventually by the incorporation of three basic components; active cells, signaling molecules and polymeric scaffolds [71]. The functions of three basic components of tissue engineering are shown in graphical presentation Figure 7.

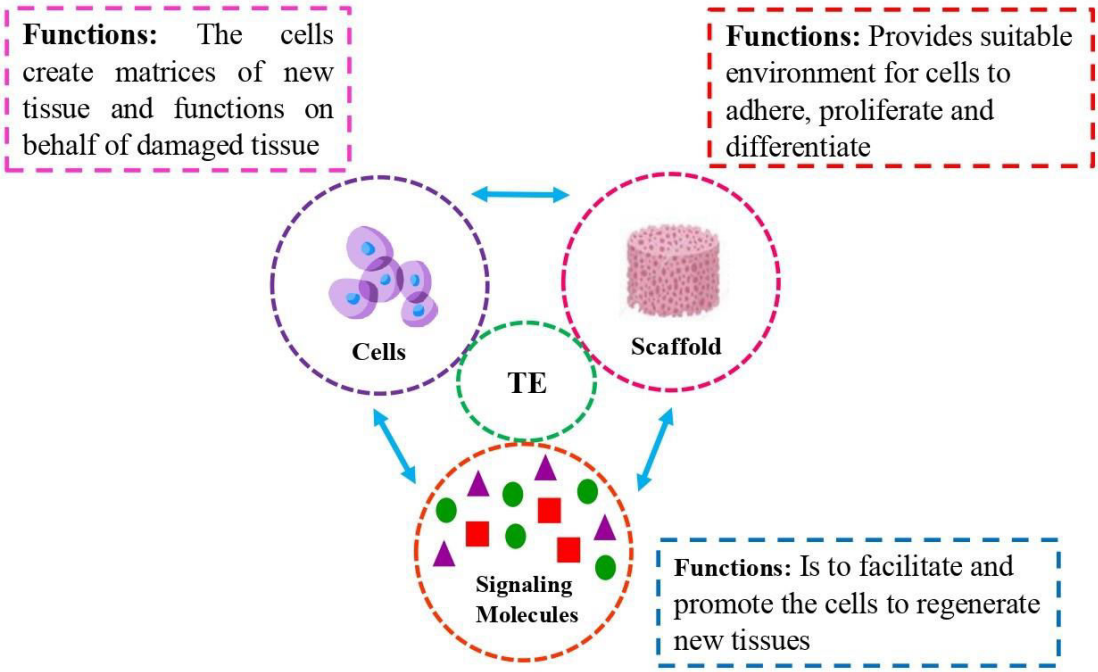

Figure 7: Functions of Basic Components of Tissue Engineering

2.6. Tissue Engineered Sponge / Scaffold

Tissue engineered sponge or scaffold is an artificially designed porous three-dimensional framework made up of bio-polymeric materials, which resembles to natural extracellular matrix (ECM) and offer a structural support for cellular attachment, migration, proliferation and tissue regeneration [72].

Over the past few years, a variety of advancing strategies have been devised for the design and development of sponges and scaffold. The commonly used techniques include: freeze drying / lyophilization, electro-spinning, gas foaming and 3D printing. However, lyophilization / freeze drying is widely accepted method for the development of sponges. The sponges prepared by freeze drying technique results in increased porosity with an interconnectivity structures, which facilitates in absorption of wound exudates and exchange of gases. Wen Y et al., fabricated

tetracycline hydrochloride loaded gelatin/sodium alginate sponges by freeze drying technique. The prepared sponges were reported to be highly porous in nature along with 3D network structure and an excellent water absorption ability [73]. Also, many research studies have concluded that the application of freeze-drying technique seems to be the most preferable choice for the preparation of sponges. Thus, in consistence to the applications of lyophilization technique, another potential strategy that perked an interest in the fabrication of scaffolds is three-dimensional printing technology.

2.7. 3D Printing Technique

Three-dimensional printing (3D printing), more commonly referred to as additive manufacturing (AM) or rapid prototyping [74], is an emerging and remarkable technology for creating complex geometries and an extensive range of products using 3D modelling data [75]. In 1980, 3D printing techniques paved the way for personalized drug delivery system with an inherent pliability to achieve an effective and safer drug therapy [76]. In recent years, the enrichment in 3D printing technology has enabled to achieve a refined control over shape, dimensions, spatial arrangements and porous interconnectivity within the scaffolds [77].

3D printing technique is the process of transformation of three-dimensional digital models (CAD designs) into a tangible object, by depositing a material layer in a sequential pattern [78]. Moreover, 3D printing method contributes in designing the scaffolds with precisely customized forms that simulate the dimensions of defected tissues. Thus, a combination of CAD designs with 3D printing technique enables to develop a customized biomaterial with a tunable property for tissue engineering and pharmaceutical applications [77].

One such technique that has been currently and widely explored in the domains of 3D printing is fused deposition modelling [79]. Fused deposition modelling (FDM), often designated as fused filament fabrication (FFF) is an extrusion based rapid prototyping technique, utilizes thermoplastic polymeric materials as a primary base material [80]. It is the process of sequential deposition of molten thermoplastics filaments extruded by means of an extremely high temperature nozzle to create a three-dimensional object. FDM technology has progressed as one of the most inventive prototyping technologies for the fabrication of scaffolds, implants and medical devices [81]. In terms of fabrication of scaffolds, FDM presents a couple of advantages such as reliable and effective methods of operation, excellent resilience, less expensive cost, minimal consumption of energy, relatively low temperatures and the ability to produce complex-shaped thermoplastic products. In accordance with the literature search, FDM technique proves to be the most promising approach in developing customized scaffolds with favorable outcomes [82].

Thus, the process automation in 3D printing technique and an excellent consistency developed by fused deposit modelling (FDM), constitutes in designing of potentially effective and safer pharmaceutical product [83].

2.8. Bacterial Infection in Burn Wounds

Individuals with an extensive burns are particularly susceptible to infection, resulting in impaired wound healing, notably more extensive hospitalization and increased mortality. Burn wounds symbolize a favorable habitat for the growth of micro-organisms and thus constitute a platform for bloodstream infections. The presence of infection triggers the formation of sepsis or hypovolemic shock, resulting in hypotension and lack of perfusion, which in-turn results in delayed healing of wound. Thus, the neutralization of infections in individuals with an extensive burn, impose a challenge to the researchers and physicians. Fortunately, there exist a number of strategies towards the minimization of bacterial infections in burn wounds [84].

In recent years, the development of antibacterial drug loaded dressing materials have paved a way in the treatment and management of burn wound infections [85]. This can be achieved by the inclusion of various antibacterial drug molecules, to fabricate lyophilized sponges or 3D printed scaffolds with tunable properties that aid in wound healing and regeneration of cells and tissues. Thus, by considering the significance of the above information, ciprofloxacin hydrochloride (Cip HCl), belonging to a family of fluoroquinolones was considered as a model antibacterial drug for the treatment of burn injuries [78].

MATERIALS AND METHODS

This chapter provides simple description of the chemicals and equipment that were consistently utilized in the current study; experimental design and protocols for doping of HNTs, loading of drug into doped HNTs. This chapter outlines the experimental approaches used in the development of drug loaded nano-filler based sponges and scaffolds. Additionally, the following section details the various physical and analytical strategies used to characterize doped HNTs, developed sponges and scaffolds.

MATERIALS

Table 2: List of Chemicals

S. No	Chemicals	Supplier	Uses
1.	Halloysite nanotubes	Sigma Aldrich, Mumbai, India	Nanofiller
2.	γ– methacryloxypropyltrimethoxysilane (γ-MPS)	Sigma Aldrich, Mumbai, India	Silane coupling agent
3.	Ciprofloxacin Hydrochloride IP	Aarti Drugs Ltd, Hyderabad, India	Active pharmaceutical ingredient
4.	Poly Ethylene Oxide WSR 308 (PEO/Polyox)	Dow Chemical Company, USA	Polymer
5.	Poly Vinyl Alcohol Pellets (M_W 26300 – 30000 Da)	Himedia Pvt Ltd. Mumbai, India	Polymer
6.	Potassium Dihydrogen Orthophosphate	Himedia Pvt Ltd. Mumbai, India	Buffering agent
7.	Disodium Hydrogen Phosphate	Himedia Pvt Ltd. Mumbai, India	Buffering agent
8.	Ethanol	Thermo Fischer Scientific Pvt Ltd. Mumbai, India	Solvent

Table 3: List of Equipment's and Instrument

Sr. No	Instrument name	Model	Make
1.	Electronic Balance	AA-2200	Anamed Instruments Mumbai
2.	Magnetic Stirrer	5MLH	REMI, Mumbai, India
3.	Ultra-Turrax Homogenizer	T-25 basic	IKA-WERKE Pvt Ltd. Mumbai, India
4.	Refrigerated Centrifuge	RC 4100 F	Eltek, Electro craft Pvt. Ltd. Mumbai, India
5.	Fourier Transform Infrared Spectrophotometer	IR Spirit	Shimadzu, Japan
6.	Differential Scanning Calorimeter	DSC – 60 Plus	Shimadzu, Japan
7.	X-Ray Diffractometer		Empyrean 3rd Gen, MalveranPANalytical, Netherlands
8.	Field Emission Scanning Electron Microscope	JSM-7610F Plus	Jeol, Japan
9.	Transmission Electron Microscope	JEM-1400HC	Jeol, Japan
10.	Zeta Meter 3.0+	ZM3-U-G	Somatco, USA
11.	Planetary Mixer	HD 410 AC	Rimek, Kalweka, Karnavati Engineering Ltd. Mumbai, India
12.	Parallel Twin Screw Lab Extruder	Aasabi/25/CO/225/30	AasabiMachinery Pvt. Ltd. Mumbai, India
13.	Fused Deposit Modelling (FDM) 3D Printer	ACCUCRAFTi250+	Flashforge Creator Pro Machine, USA
14.	Micro Universal Testing Machine	10ST	Tinius Olsen, UK
15.	Franz Diffusion Cell Apparatus	EDC-07	Electrolab Pvt Ltd. Mumbai, India
16.	UV –Visible Spectrophotometer	UV-1900	Shimadzu, Japan
17.	Incubator	NB203XL	N-Biotek, Korea
18.	Inverted Microscope	TS2	Nikon Eclipse USA
19.	Stability Chamber	TH 90S	Thermolab Mumbai, India

20.	Bath Sonicator		Chem Labs Bangalore, India
21.	Lyophilizer	FD-10-FT	Lab freeze, Hyderabad, India
22.	Hot Air Oven	T300	PSM Industries
23.	Surface Area Analyzer	Autosorb IQ-XR-XR	Anton Paar, Austria
24.	pH Meter	EQ - 610	Equip-Tronics
25.	Laminar Air Flow Bench		Klenzaides Bioclean

METHODS

3.1. STRATEGY 1:

DOPING OF HNTs USING SILANE COUPLING AGENT

3.1.1. Experimental Study Design

A two-level three-factorial (2^3) custom design was selected as an experimental study design using (JMP software ® Version 16, SAS Institute, Singapore) for the optimization of DHNTs. In this design, concentration of γ-MPS (X_1), HNT (X_2) and Ethanol (X_3) were considered to be an independent variable, which were coded with two different levels (low as -1 and high as +1). As the selected independent variables presented to be numerical with continuous data values, custom design was set to be the most preferential choice to analyze the effect of these independent factors on the selected response variables. The two selected response variables (Y_1 and Y_2) for the present experimental study design include:

1. Diffraction angle (2θ) from X-ray analysis (Y_1) and
2. Zeta potential (mV) represents as (Y_2) [20]

The selected independent and dependent variables along with their coded and actual values are listed in Table 4. Experimental design with coded and actual values for doping of HNTs are presented in Table 5.

Table 4: Two-Level Three-Factor Custom Design

Independent Variables	**Levels**	
	Low (-1)	**High (+1)**
X_1: Concentration of γ-MPS (ml)	6	12
X_2: Concentration of HNT (g)	25	50
X_3: Concentration of Ethanol (ml)	75	100
Dependent / Response Variables		
Y_1: Diffraction angle (2θ)		
Y_2: Zeta potential (mV)		

Table 5: Composition of an Experimental Design for Doping of HNTs

Runs	**Coded Values**			**Actual Values**		
	Conc of γ-MPS X_1	**Conc of HNTs X_2**	**Conc of Ethanol X_3**	**Conc of γ-MPS (ml) X_1**	**Conc of HNTs (g) X_2**	**Conc of Ethanol (ml) X_3**
F1	-1	-1	-1	6	25	75
F2	+1	-1	-1	12	25	75
F3	+1	-1	+1	12	25	100
F4	-1	-1	+1	6	25	100
F5	-1	+1	-1	6	50	75
F6	+1	+1	-1	12	50	75
F7	+1	+1	+1	12	50	100
F8	-1	+1	+1	6	50	100

3.1.2. Surface Doping of HNTs using γ-MPS by Homogenization technique

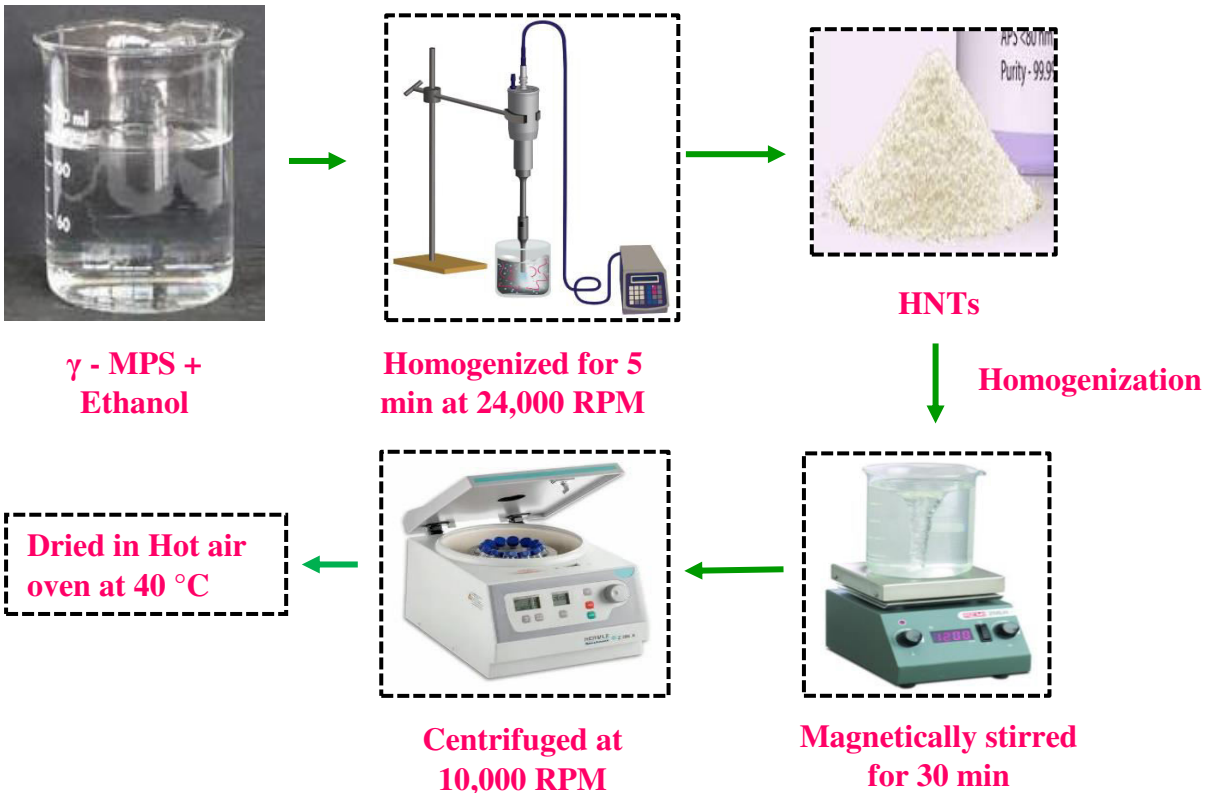

Figure 8: Schematic Presentation of Doping of HNTs using γ – MPS by Homogenization Technique

Experimental Protocol

The measured quantity of ethanol was poured into a 250 ml beaker, to which γ-MPS was added and homogenized by using ultra-turrax homogenizer T-25 basic at 24,000 RPM for 5 min. Subsequently, a weighed quantity of HNTs were added to an ethanolic / γ-MPS mixture as presented in Table 5, and then the suspension was magnetically stirred for 30 min [58]. The suspension was further homogenized at 24,000 RPM for 7 min and centrifuged using refrigerated centrifuge at 10,000 RPM for 20 min. The supernatant was discarded and the precipitate obtained (γ-MPS doped HNTs) was dried in a hot air oven at 40 ^{0}C for 24 h [20]. The schematic presentation of doping of HNTs is shown in Figure 8.

3.1.3. Characterization of Doped HNTs

The pristine HNTs and γ-MPS-DHNTs were characterized by Fourier transform infrared spectroscopy (FTIR) analysis by KBr pellet method using Nicolet 5700 FT-IR spectrometer (USA). The pellets were scanned from 4000 cm^{-1} to 400 cm^{-1} of spectral range with a resolution of 2.5 cm^{-1}. The thermal analysis of pristine and γ-MPS-DHNTs were investigated by thermo-gravimetry analysis (TGA). The thermal stability, weight loss of a material and compositional characteristics can be determined by TGA analysis using thermo-gravimetric analyzer (DTG 50 Shimadzu, Japan). The identification of structural properties and chemical composition of nanotubes, as well as the intercalation of γ-MPS within the layers of nanotubes were confirmed by X-ray diffraction analysis (XRD) by using Empyrean 3rd Generation Diffractometer. The intensity measurements and d-spacing values were obtained in the range of 2θ values of 2°- 80° along with the step time of 0.02°/s, by the application of Cu-Kα (λ = 1.504 Å) radiation with an electrical potential of 45 kV and a current rating of 40 mA. The morphological characterization of pristine and γ-MPS-DHNTs were investigated by scanning electron microscopy (SEM analysis) using Carl Zeiss Gemini 300 electron microscope. In consistence to SEM analysis, pristine HNTs and γ-MPS-DHNTs were also subjected to topographical characterization studies (TEM analysis) using JEM-1400HC, JEOL transmission electron microscope. The zeta potential analysis was performed to confirm the presence of surface charges and potential stability of nanotubes using 3.0+ ZM3-U-G Zeta- Meter (Somatco, USA).

3.1.4. Statistical Optimization of DHNTs

Optimization is characterized by the process of selection of best components from a pool of accessible alternatives [86]. The impact of independent variables on the responses were assessed by the inclusion of key concepts of desirability functions. The collective desirability values to achieve an optimized DHNTs are shown in Table 6.

Table 6: Desirability Values for Optimized DHNTs

Formulation Code	Variables		
	Concentration of γ-MPS	Concentration of HNT	Concentration of Ethanol
OF1	9 ml	37.5 g	87.5 ml

The prepared optimized DHNTs were characterized for FT-IR, TGA, X-RD and SEM analysis

3.2. STRATEGY 2:

FABRICATION OF CIPROFLOXACIN HYDROCHLORIDE LOADED DOPED HNTs SPONGES

3.2.1. Pre-formulation Study of Ciprofloxacin Hydrochloride

3.2.1.1. Determination of Melting Point [87]

The melting point analysis is considered to be the most essential technique for determining the purity of sample. The melting point analysis of ciprofloxacin hydrochloride (Cip HCl) was determined using Thiele tube by capillary method. According to the literature search, the melting point of Cip HCl ranges from 293.15 °C - 323.15 °C.

3.2.1.2. Determination of λ_{max} of Ciprofloxacin hydrochloride and Standard Calibration Curve

1. Preparation of Stock Solution:

A weighed quantity of Cip HCl (100 mg) was dissolved in 100 ml of 7.4 pH phosphate buffer in a volumetric flask to achieve a concentration of 1000 µg/ml (SS-I). Further, the dilution was made from the primary stock solution (SS-I) to obtain a final concentration of 100 µg/ml (SS-II). The wavelength of maximum absorption (λ max) of Cip HCl was determined by scanning a secondary stock solution (SS-II) in a wavelength range of 200 nm – 400 nm using UV-Visible Spectrophotometer (UV-1900, Shimadzu).

2. Calibration Curve of Ciprofloxacin Hydrochloride

From the secondary stock solution (SS-II), serial dilutions of different concentrations ranging from 2 µg/ml to 10 µg/ml were prepared using 7.4 pH phosphate buffer in a 10 ml volumetric flask. The calibration curve was obtained by measuring the absorbance of various dilutions at the observed λ max. A graph of concentration (µg/ml) on x-axis V/s absorbance on y-axis was plotted, linear equation was derived and R^2 value was recorded [88].

3. Fourier Transform Infrared Spectroscopy

The FTIR analysis of Cip HCl was performed using Shimadzu, IR Spirit spectrophotometer in attenuated total reflectance spectral mode. The spectrum of Cip HCl was recorded in the vibrational range of 4000 cm^{-1} – 500 cm^{-1} and the prominent functional groups present in the spectrum of Cip HCl was recorded and interpreted [89].

4. Differential Scanning Calorimetric Analysis

Differential scanning calorimetry (DSC) is an excellent tool of analysis to characterize the thermal characteristics of materials. DSC analysis was executed using

Shimadzu, DSC 60 Plus instrument. The sample was heated over the temperature ranging from 30°C-350°C with a constant heating pace of 10 °C/min and a nitrogen flow rate of 100 ml/min. The DSC thermogram of Cip HCl was recorded and analysed by Lab Solutions® software [90].

3.2.2. Drug Loading Protocols

The distinctive inner and outer surface chemistries, as well as the hollow nanotubular structure of HNTs, make them an ideal nano-reservoir and nano-containers for loading a wide variety of active compounds.

Example 1:

Intercalation of Cip HCl into γ-MPS doped HNTs by Homogenization technique

The anti-bacterial drug, Cip HCl was loaded into the hollow space of DHNTs by intercalation process using ultra-turrax homogenizer.

Cip HCl and DHNTs in the different ratios (1:1, 1:2, 1:3 and 1:4) were dispersed in 30 ml of 7.4 pH phosphate buffer. The suspension was intercalated by the application of homogenization technique using ultra-turrax homogenizer at 17500 rpm for 8 h. The intercalated suspension was centrifuged at 10,000 RPM for 20 min. The supernatant was decanted and the samples were dried in oven for 24 h at 40 ºC.

Example 2:

Tubular Entrapment of Cip HCl into γ-MPS doped HNTs by Lyophilization Technique

The Cip HCl was effectively encapsulated within the multilayer structure of DHNTs with the different ratios of (1:1, 1:2, 1:3 and 1:4). The suspension of Cip HCl/ DHNTs was prepared by dispersing the mixture of Cip HCl and DHNTs in 50 ml of 7.4 pH phosphate buffer. The prepared suspensions were freezed in the refrigerator at temperature of -20 ºC for 24 h and then lyophilized at -50 ºC for 6 h, by applying the

vacuum at the pressure of 0.01 Mbar. The lyophilized samples were centrifuged using refrigerated centrifuge at 10,000 RPM for 20 min. The supernatant was decanted and the solid component was separated and dried in an oven at 40 ºC for 24 h [91].

Example 3:

Intercalation of Cip HCl into γ-MPS doped HNTs by Sonication method

Cip HCl and fine powder of γ-MPS doped HNTs were blended in various ratios of (1:1, 1:2, 1:3 and 1:4). The samples were dissolved in a beaker containing 30 ml of 7.4 pH phosphate buffer and sonicated in bath sonicator at 20 Hz for 30 min, followed by centrifugation at 10,000 rpm for 20 min. The supernatant was decanted and the samples were dried in an oven at 40 ºC for 24 h.

3.2.2.1. Determination of Encapsulation Efficiency of Cip HCl Loaded Doped HNTs

A weighed quantity of Cip HCl loaded DHNTs (5 mg) was dissolved in 5 ml of 7.4 pH phosphate buffer. The samples were centrifuged for 10 min at 4000 RPM and the supernatant was collected, filtered through a Whatman filter paper (40 µ) [92]. The Cip HCl content in clear supernatant was analysed by measuring the absorbance at λmax 271 nm spectrophotometrically using Shimadzu UV-1900.

The Encapsulation efficiency (%) of Cip HCl in DHNTs was calculated by the following expression [93]

$$\textbf{\textit{Encapsulation efficiency}}\ (\%) = \left[1 - \frac{Drug\ in\ supernatant\ liquid}{Total\ drug\ added}\right] x\ 100$$

3.2.3. Fabrication of Bio-Polymeric Cip HCl Loaded γ-MPS doped HNTs Sponges by Lyophilization Technique

Table 7: Formulation of Cip HCl Loaded DHNTs Polymeric Sponges

Ingredients	Formulation Trials		
	SF1	SF2	SF3
Polyox WSR 308 (%)	2.5	5	7.5
Cip HCl loaded DHNTs (g) (1:3 ratio)	1.2	1.2	1.2
Aqueous solvent	qs	qs	qs

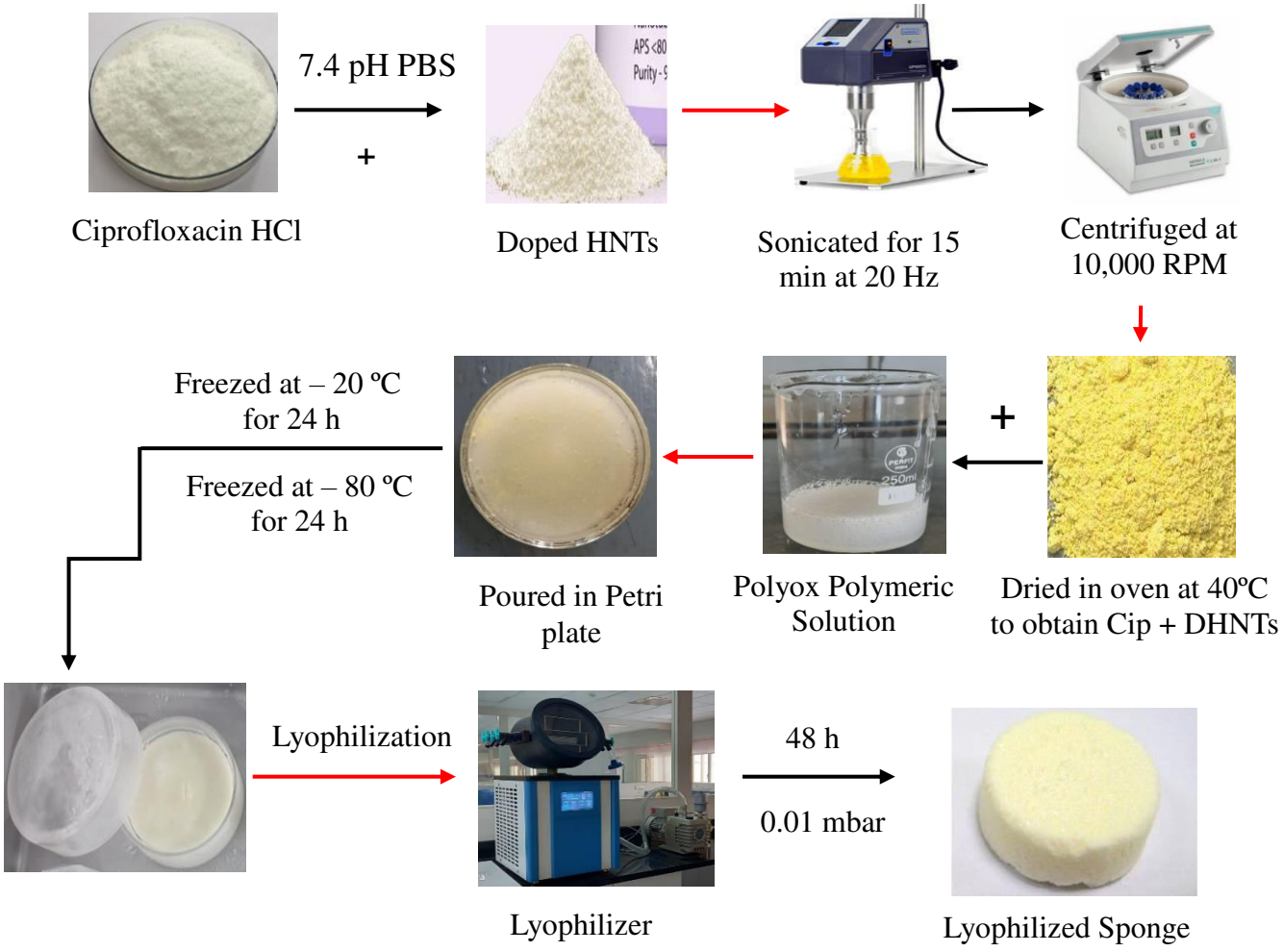

Figure 9. Schematic Representation of Preparation of Lyophilized Sponge

3.2.3.1. The steps involved in the fabrication of sponges includes:

Step 1: Preparation of Polymeric Solution:

Polyox WSR 308 in different concentrations as shown in Table 7 were dissolved and soaked in water overnight, until a clear and translucent polymeric solution was achieved.

Step 2: Preparation of Drug Loaded DHNTs based Polymeric Mixture:

To the polymeric solution of step 1, γ-MPS DHNTs equivalent to the drug substance (Cip HCl) in the ratio of 1:3 (selected from the data of drug loading efficiency), shown in Table 7 was dispersed in polymeric solution and homogenized for 5 min at a speed of 6200 RPM (assists in maintaining uniformity and prevents the formation of lumps) to obtain drug loaded nanomaterial based polymeric mixture.

Step 3: Preparation of Cip HCl loaded-γ-MPS Doped HNTs Polymeric Sponges:

Prepared drug loaded nanomaterial based polymeric solution was transferred to small petri plates and frozen at -20 ºC overnight, followed by freezing at -80 ºC in deep freezer for 24 h. Subsequently, the frozen samples were lyophilized at -50 ºC using Lab-freeze, FD-10-FT lyophilizer at 0.01mbar pressure for 48 h to obtain a porous sponge. The schematic representation of preparation of lyophilized sponges were depicted in Figure 9.

3.2.4. Characterization Studies

3.2.4.1. Chemical Compatibility studies

1. DSC Analysis

The thermal properties and chemical compatibility of the developed sponges from each batch of formulations were analysed by using DSC (Shimadzu DSC 60

Plus, Tokyo, Japan). A sample of 3 to 4 mg was weighed and hermetically sealed in an aluminum pan, analysed under nitrogen flow rate (100 ml/min) at a standard heating rate of 10 ºC/min over a temperature range of 30 ºC – 350 ºC [94].

2. FTIR Analysis

The presence of specific functional groups and the compatibility between drug and excipients in the developed sponges from each formulation was confirmed by using FTIR spectrophotometer (IR Spirit, Shimadzu) instrument. The samples were scanned and measured in the range between 4000-400 cm^{-1} and the FTIR spectra obtained were recorded and interpreted [89].

3.2.4.2. Diameter and Thickness of the Sponge

The diameter and thickness of sponges were measured by using Vernier Calliper. The data for thickness and diameter was recorded from three distinct spots of each sponge formulations and average value was calculated [95].

3.2.4.2.1. pH of Sponges

The pH of all the three formulated sponges were measured by using pH meter. The sample of each sponge (1 cm x 1cm) was dissolved in 20 ml of distilled water at room temperature and the pH was measured. The pH meter was calibrated using standardized pH solutions prepared from specified pH capsule.

3.2.4.3. Wetness Integrity

The wetness integrity of sponges was carried out according to the procedure described by Thirumalesh et al., [96] A test sample of three different sponge formulations, with a dimension of (1 x 1 cm) were placed in a conical flask containing 75 ml of phosphate buffer solution pH 7.4. The flask was gently shaked for 60 s without the formation of vertex and the physical integrity of the sample was visually observed.

3.2.4.4. Swelling Ratio

To determine the state of hydration of sponges, swelling assay was performed by immersion method. Previously dried Cip HCl loaded DHNTs polymeric sponges of each formulations were cut into a strip of (1.5 x 1.5 cm) dimensions and weighed [97]. After figuring out the initial weight (W_1) of these sponge strips, the strips were immersed in the release media (Phosphate buffer solution pH 7.4) at 37 ºC for 10 min. Subsequently after 10 min, the wet sponge strips were removed from the buffer and gently wiped using filter paper (excess buffer was removed) [98]. The swollen sponge strips were reweighed (W_2) and swelling ratio was calculated using following equation

$$Swelling\ Ratio\ (\%) = \frac{W2 - W1}{W1} x\ 100$$

[99] Where: W_2 is the weight of wet sponge after time t

W_1 is the weight of initial sponge at time 0

3.2.4.5. Mechanical Properties of Sponges

In compliance with the protocols of American Society for Testing and Materials (ASTM D882-12), Cip HCl loaded DHNTs sponges (SF1, SF2 and SF3 formulations) were cut into a rectangular strip with a specifications of 45 mm x 20 mm and a thickness of 2.5 mm. The materials flexural strength test was carried out with a load cell capacity of 500 N, using Micro Universal Testing Machine (Tinius Olsen 10 ST, UK) at a test speed of 1 mm/min and a grip separation of 50.0 mm. The ultimate tensile stress, elastic modulus and percent break strain were parameterized from stress-strain profile curves [100].

3.2.4.6. Porosity of Sponges

The pore size, pore volume and specific surface area of SF1, SF2 and SF3 sponge formulations were analysed using Surface Area Analyser (Autosorb IQ-XR-

XR, Anton Paar, Austria). The samples weighing approximately (0.016 g) were initially out gassed at 30 ºC for 1.5 h in a nitrogen atmosphere and the samples BET surface area were estimated using N2 adsorption kinetics at 77.35 K (6.58 x 10^{-5} Torr) [101].

3.2.4.7. Structural Analysis (SEM) and Energy Dispersive X-ray Microanalysis (EDX)

The topography and micro-structure of the sponges were characterized by field emission scanning electron microscope (FE-SEM- JEOL-7610F Plus, Tokyo, Japan). The sponges were sputter coated with a 5 nm thin lamination of Gold as conducting element for 60 s (ES 150R Quorum Q, USA), to analyse the micro-structure and topography of sponges at 100 X magnification with a low accelerated voltage of < 5kV [102]. In addition to SEM analysis, the existence and distribution of various elements in sponges were confirmed by Energy dispersive X-ray microanalysis, also known as EDX mapping or point analysis [103]

3.2.4.8. Drug Content Analysis

For the determination of drug content, each batch of sponge formulations were cut into small segments with a specific dimension of (1.5 cm x 1.5 cm), dissolved in phosphate buffer solution (7.4 pH) 50 ml and sonicated for 20 min. From the above solution, 1 ml was withdrawn and diluted up to 10 ml with phosphate buffer (7.4 pH). The resultant solution was filtered through What-man filter paper of 0.45 µ size and the absorbance of the sample was measured spectrophotometrically (Shimadzu, UV-1900 Spectrophotometer, Japan) at 271 nm. The tests were carried out in triplicates (n=3) for all the samples, the average values and standard deviation of drug content was calculated.

3.2.4.9. *In Vitro* Drug Diffusion Profile

The *in vitro* drug diffusion profile of Cip HCl loaded DHNTs sponges were performed using Franz diffusion cell apparatus (Electrolab EDC – 07, Mumbai, India). A dialysis membrane (molecular weight cut-off 12-14 kDa; LA401-1MT, Himedia with a pore size of 150 µ) was treated and thoroughly soaked overnight in 7.4 pH phosphate buffer as a releasing media, to ensure the complete hydration of the membrane. The receptor compartment was filled with 12.5 ml of 7.4 pH phosphate buffer solution and the hydrated dialysis membrane was mounted between the vertical diffusion cells, donor and receptor compartments. The temperature of the receptor compartment was pre-set at 32 ºC identical to the skin's temperature, as well as continuous stirring at a speed of 50 rpm was ensured to mimic the *in vivo* conditions. The prepared sponges of each formulations were cut into a specific dimensions of 1 cm x 1 cm and placed on the donor compartment. A 0.5 ml aliquot of diffusion fluid was withdrawn from the receptor compartment at the different time intervals (1, 2, 3, 4… and 24 h), after each withdrawal an equal volume of fresh phosphate buffer 7.4 pH was added to receptor compartment to ensure the restoration of sink conditions. The aliquots withdrawn were diluted suitably and analysed spectrophotometrically at 271 nm (Shimadzu, UV 1900 Spectrophotometer, Japan). A cumulative percent release of Cip HCl from the sponges were determined and a graph of percent drug release vs. time was plotted. The tests were carried out in triplicates (n=3) for all the samples and the average values as well as standard deviation of the drug release was analysed [104].

3.2.5. *In Vitro* Biodegradation Studies

A number of key variables that have contributed towards the selection of SF2 formulation as a best formulation includes safety, efficacy and stability of the

formulation. The SF2 formulation exhibited a remarkable ability to achieve an ideal qualities of sponge formulation. It consistently delivered the desired outcomes, making it the clear choice among the three formulations.

3.2.5.1. Biodegradation of SF2 Sponge Formulation

In accordance to the methodology presented by Deepthi et al., [105] with slight alterations, the biodegradation of SF2 sponge formulation was carried out by soil burial method. The detailed procedure for the biodegradation of SF2 sponge formulation is presented in flow chart as shown in Figure 10.

3.2.6. Antimicrobial Activity

The standard strains of microbial organisms used in the present research work were procured from KLE Society P C Jabin Science College, Hubballi, Karnataka. The microbial strain comprised of Gram-positive organism: *Staphylococcus aureus* (MTCC/737). While, the Gram-negative organism include: *Escherichia coli* (MTCC/261).

3.2.6.1. Sensitivity Test for Antibiotic

The antimicrobial efficiency of SF2 sponge formulation was evaluated by agar disc diffusion method, against two different types of microorganisms

1. Gram-negative organism (*E. coli*)
2. Gram-positive organism (*S. aureus*)

This procedure was carried out in Muller Hinton Agar medium (M-H Agar). A twenty-five (25 ml) of Muller Hinton Agar medium was poured into a sterilized petri-plates for the rapid growth of microorganisms. A single colony of *E. coli* and *S. aureus* were cultured in Muller Hinton Broth (M-H Broth) overnight at 35 °C on a rotary shaker with a frequency of 250 RPM. A dilution of an overnight culture was

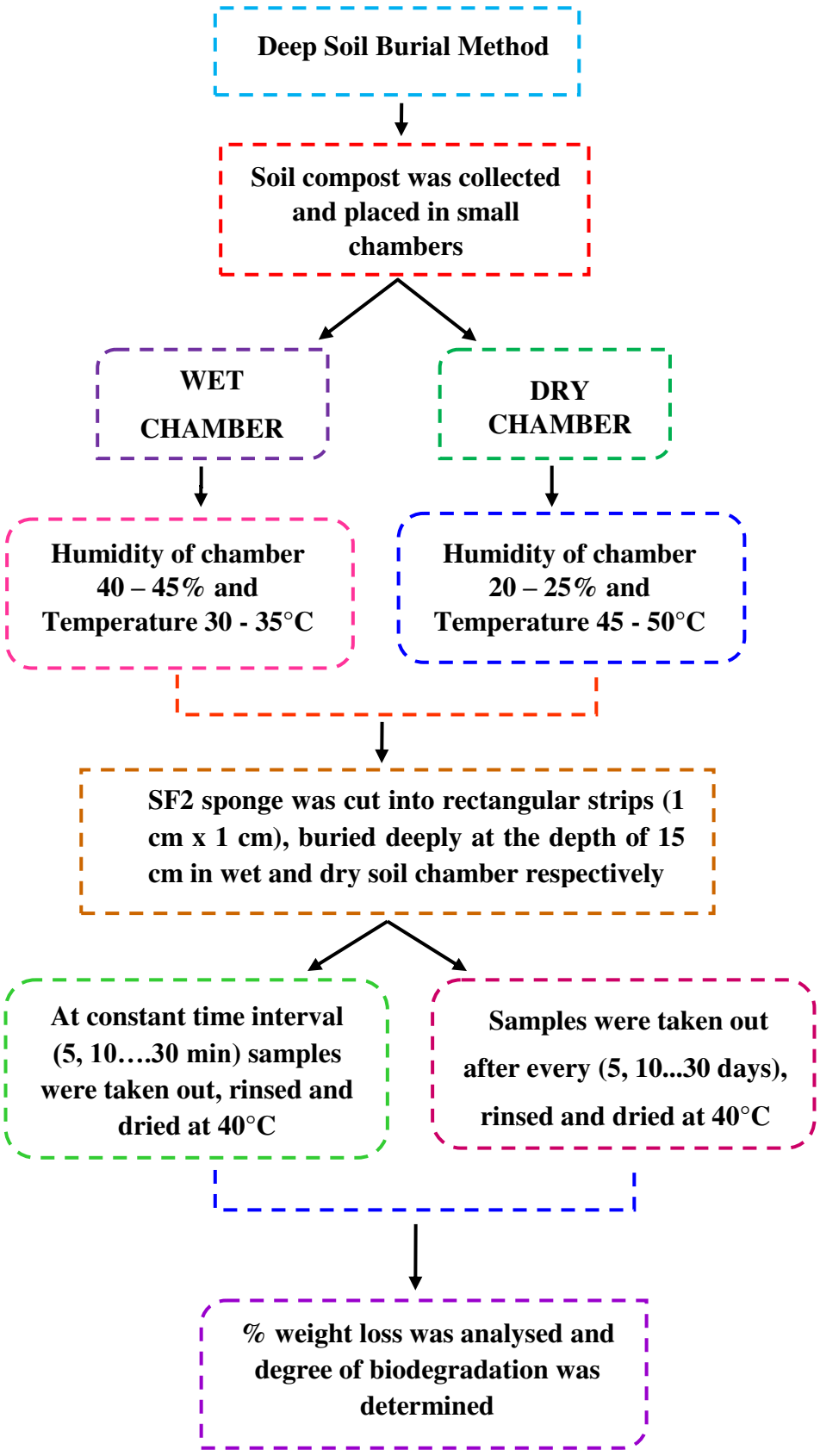

Figure 10: Flow chart presentation for the process of biodegradation of SF2 sponge

utilized to create an inoculum with a microbial concentration of 10^5 CFU/ml suspension, in accordance with the standards of 0.5 McFarland turbidity. Subsequently, a 100 µl of microbial suspensions were gently inoculated over the surface of M-H Agar and spread out in every direction using a sterilized L-shaped glass spreader. Furthermore, the sterilized paper discs of 6 mm in diameter were deposited on the M-H agar medium and infused with 8 µl of SF2 sponge formulation (concentration of 16 µg/ml). Likewise, Cip HCl Injection (16 µg/ml) functioned as a control. The M-H Agar plates with an infused antimicrobial disc were incubated at 37°C for 24 h, the zone of inhibition was measured and expressed in terms of millimetres [106].

3.2.7. Cell Culture Analysis [107]

Human alveolar carcinoma epithelial cells (A549) was procured from National Repository of Animal Cell Culture, National Centre for Cell Sciences (NCCS), Pune India. A549 cells were seeded in 96 F well culture plates (Tarson – 980040, 96 F well plates); Tarson, India. The cells were cultured in Rose-Well Park Memorial Institute Medium (RPMI 1640), followed by supplementation with 10% fetal calf serum (FCS) (Hyclone), 100 U/ml penicillin and 100 µg/ml streptomycin sulphate. The cell cultures were incubated before and throughout the experiment under a humidified atmosphere at 37 ºC with 5% CO_2 in incubator (Panasonic MCO-170AIC, Japan).

3.2.7.1. *In Vitro* Cytotoxicity Assay of Sponges [108]

A calorimetric cell viability MTT (3-(4, 5- dimethylthiazole - 2- yl) - 2, 5 diphenyl tetrazolium bromide) assay was performed to explore the cytotoxic effect of Cip HCl and SF2 sponge formulation. The A549 cells at a density of 10,000 cells/well were seeded in a 96 F well cell culture plates and incubated overnight under 5% CO_2

atmosphere at 37 ºC. Once the cells attain the complete stabilization, the non – attached cells were expelled out. In the course of experimentation, fresh medium containing cells with various concentrations of pure Cip HCl in suspension form at the concentrations of (20 – 500 µg/ml) was considered as positive control. Similarly, a suspension of SF2 sponges with the concentrations ranging from (20 – 500 µg/ml) was considered as a test sample and poured into each well.

Furthermore, the well plates were incubated for 12 h, 24 h and 48 h at 37 ºC to enable the cell growth. After the incubation process, 20 µl of MTT reagent (5 mg/ml) was added to each well plate and the plates were again incubated for 3h, the cultures were slightly shaken and the excess non-reacted dye containing media was aspirated and thereby the appearance of a purple formazan crystals were observed. Moreover, the coloured formazan crystals were solubilized with the addition of 1 ml dimethyl sulfoxide to the cells. The absorbance was measured at 590 nm using plate reader. In accordance with the findings of MTT tests absorbance values, the % of cellular viability in response to exposure to the different concentrations of sponge against control was computed and IC_{50} value was calculated.

3.2.7.2. *In Vitro* Wound Healing Migration Assay [109]

The characterization of wound repopulation activity of SF2 sponge formulation on A549 cells was assessed by performing a standard monolayer scratch assay test. In order to facilitate the cellular attachment and achieve more than 80 % of monolayer confluence, the cells at a density of 1 x 10^6 cells per well were seeded in each six well culture plates at 37 ºC for 36 h in a humidified atmosphere at 5% CO_2. The synchronized monolayer cells were delicately scratched along a straight line with a sterile 200 µl pipette tip. After scratching, each well plate was gently washed twice

with phosphate buffer, so as to remove any detached cells or cellular debris deposited on the cells and the well plates were replaced with fresh media. Subsequently, the cells were treated with 3 mg/ml of pure Cip HCl as a control and optimized SF2 sponge (3 mg/ml) as test sample, followed by incubation for 24 h under normal conditions.

Digital photographs were captured with an inverted microscope (Nikon Eclipse TS2, USA) at 4X magnification, immediately after giving a scratch to a cell monolayer t = 0 h. The plates were further incubated and images were captured at t = 24 h and t = 48 h. As a result of this, with the aid of computer programming software (Wound healing size tool, an ImageJ / Fiji ® Plugin), the captivated images from each sample were quantitatively analysed to determine the rate of cell migration (R_M), wound closure (%), wound area and wound width. The cell migration rate (R_M) and wound closure (%) was calculated from the following equations respectively:

$$R_M = \frac{Wi - Wf}{t}$$

Where,

W_i = Average of the initial wound width (µm)

W_f = Average of the final wound width (µm)

t = Time span of assay (h)

$$Wound\ Closure\ (\%) = \left(\frac{A_{t=0} - A_{t=\Delta t}}{A_{t=0}}\right) \times 100$$

Where,

$A_{t=0}$ = initial wound area (μm^2)

$A_{t=\Delta t}$= wound area after n hours of the initial scratch (μm^2) [110]

3.2.8. Sterilization of SF2 Sponge Formulation by Gamma Irradiation Method

The SF2 sponge was sterilized by exposing to γ-irradiation. The SF2 sponge was placed into a glass vial, labelled and sealed. The sample was radiated by exposing to γ-radiation, derived through a source of ^{60}Co at the dosage of 25 kGy [177]. The sterilization of sponge was carried out at M. M. Joshi Eye Institute Hubballi, Karnataka, India.

3.2.9. *In Vivo* Wound Healing Activity

The *in vivo* wound healing activity of SF2 formulation was performed on burn wound induced rat model, to evaluate the effectiveness of formulation in the treatment of burn wounds.

An *in-vivo* experimentation was conducted in compliance with the strict norms laid down by Committee for the Purpose of Control and Supervision of Experiments on Animals (CPCSEA), Government of India. The designed protocol was accepted by Institutional Animal Ethics Committee (IAEC) of KLE College of Pharmacy, Hubballi. The *in vivo* studies were performed on 18 male Wistar Albino rats (weighing 250 – 300 g).

All the animals were housed in an individual cage and the temperature was maintained at 25 ± 1 ºC with a 12 h light / dark cycles, provided with standard laboratory diet and water ad libitium throughout the experiment. The animals were acclimatized to the lab environment for one week prior to the start of the experiment [111].

3.2.9.1. Experimental design

The rats were segregated into three groups each group containing six animals (n = 6)

Group 1: Disease Control group (burn wound was inflicted to each animal, provided with no treatment)

Group 2: Standard group (infliction of burn wound to each animal, provided that the animals were treated with silver sulfadiazine marketed formulation)

Group 3: Test group (infliction of burn wound to each animal, provided that the animals were treated with sterilized SF2 sponge formulation)

3.2.9.2. Induction of Burn wound [112]

On the very day of activation of wound, the rats of each group were anaesthetized in combination with ketamine hydrochloride (50 mg/kg body weight) and xylazine (6 mg/kg body weight) intra-peritoneal. After anaesthetization, the hair on the dorsum of the rats was gently shaved using electric shaver and cleaned with 70 % alcohol. A deep partial thickness circular burn wound was inflicted by placing a pre-heated (at 100 ºC) a flat circular metallic disk with a diameter of 2 cm on the dorsum area of the rats for 10 seconds, the surrounding skin area was cleaned with 70 % alcohol.

3.2.9.3. Testing procedure

Normal Rat

The hair present on the dorsal part of the rats were shaved and the tissue was collected by using 5 mm punch biopsy needle. After the collection of tissue, the biopsy site was sutured with non-absorbable suture material (Polyamide 2-0), the rats were housed in cages individually under normal conditions [113].

Group 1: Disease Control Group

The animals in this group were induced with burn wound, but they were not subjected to any treatment protocol.

Group 2: Standard Group

The animals in this group were induced with burn wound and treated with standard drug in the form of cream (Marketed formulation: 1% w/w silver sulfadiazine cream). Silver sulfadiazine cream was gently applied as a thin layer on the wounded area for every 24 h in the initial week. Further the cream was applied after every two days until a complete wound closure was achieved.

Group 3: Test Group

The rats in this group were inflected with burn wound and treated with SF2 formulation. The sterilised spongy dressing was placed on the wound and it was ensured that the wound was completely covered with a dressing material with the aid of an adhesive tape, so as to firmly anchor the sponges in place. Subsequently, in the initial days of wound infliction, the spongy dressing material was changed on every alternative day, as the wound produced a considerable amount of exudates. Furthermore, while changing the sponges, the photographs were captivated and the wound area was measured using an Image J Software 1.53t (National Institute of Health, USA). The rats were then housed in cages individually under normal conditions.

3.2.10. Pharmacological evaluation

3.2.10.1. Wound Closure Analysis [114]

The gradual change in the wound area was analysed planimetrically. The edges of the raw wound were first traced on 1, 7, 14 and 21st day of post wounding on

a sheet of sterile transparent paper, without causing any damage to the wound area. The wound area was measured using a graph paper and its surface area was quantified using an Image J Software 1.53. The quantified surface area was used to calculate the percentage wound closure.

$$wound\ closure\ (\%)\ = \frac{Initial\ wound\ area - Specific\ day\ wound\ area}{Initial\ wound\ area}\ x\ 100$$

3.2.10.2. Epithelialization Period [115]

The time required to completely cover a denuded surface with an epithelium is known as the period of epithelialization. It is measured in terms of number of days required for the scar to fall off without leaving a raw wound behind.

3.2.10.3. Histopathology of Burn Skin Tissue [116]

On the 1st and 21st day of post wounding, all the rats from each group were anaesthetized intraperitoneally using ketamine hydrochloride (50 mg/ kg body weight) in combination with xylazine (6 mg/kg body weight) for the collection of burn skin tissue. After anaesthetization, the dorsal hair of the rat was shaved and the burn skin tissue was isolated using 5 mm punch biopsy needle, which includes the half portion of the tissue surrounding the burn area and another half portion of uninjured (healthy tissue) surrounding to the burn site.

Further, the biopsy site was sutured with non-absorbable suture material (Polyamide 2-0). The isolated tissue samples were initially rinsed in normal saline (to remove the blood stains), then fixed by immersion in 10 % v/v formalin solution for 24 h, sectioned and stained using Hematoxylin – Eosin (H & E) stain for the examination under microscopy. The slides were qualitatively analysed for the formation of

granulation tissue, epithelialization, new epidermal formation, fibroblasts and inflammation using light microscopy.

3.2.10.4. Statistical Analysis

All the data were expressed as mean ± S.D. and statistical analysis was performed using GraphPad Prism 8.0 (San Diego, CA, USA). Significance was assessed by using the two-way ANOVA followed by Tukey test. Values were considered statistically significant with *p* value is less than 0.05.

3.2.11. Short Term Stability Study [117]

Short term stability studies of best formulation (SF2 sponge formulation) was successfully carried out in compliance with ICH guidelines Q1A (R2). The samples were preserved in tightly sealed amber coloured bottles and stored at a room temperature 25 ± 2°C / 65 ± 5 % RH and an accelerated temperature 40ºC ± 2ºC / 75% RH ± 5% RH in a humidity chamber (Lab India) over a period of 3 months. The samples of SF2 sponge were analyzed for wetness integrity test, drug content analysis and *in vitro* diffusion studies.

3.3. STRATEGY 3:

FABRICATION OF CIPROFLOXACIN HYDROCHLORIDE LOADED DHNTs 3D PRINTED SCAFFOLDS

3.3.1. Preparation of Cip HCl coated PVA Filaments

According to the procedure outlined by Weisman et al., [118] with few slight changes PVA filaments with Cip HCl coating were prepared. The composition of Cip HCl loaded nano-filler coated PVA pellets are presented in Table 8. The detailed procedure for coating of PVA pellets is illustrated in Figure 11.

Table 8: Formulation Composition of Cip HCl Loaded DHNTs Coated PVA Pellets

S. No	Ingredients	Composition	
		PF1	**PF2**
1.	PVA Pellets (g)	1000	1000
2.	Pure Cip HCl (% w/w)	3	_____
3.	Cip HCl loaded DHNTs (% w/w)	_____	12
4.	Ethanol (ml)	20	20

The coating efficiency (%) pure Cip HCl and Cip HCl loaded DHNTs on PVA pellets were computed using the formula:

$$\boldsymbol{Coating\ Efficiency}\ (\%) = \frac{a-b}{c}\ x\ 100$$

Where,

a = Final pellet weight in coated form (g)

b = Pellets initial weight [uncoated pellets (g)]

c = Total coating material quantity

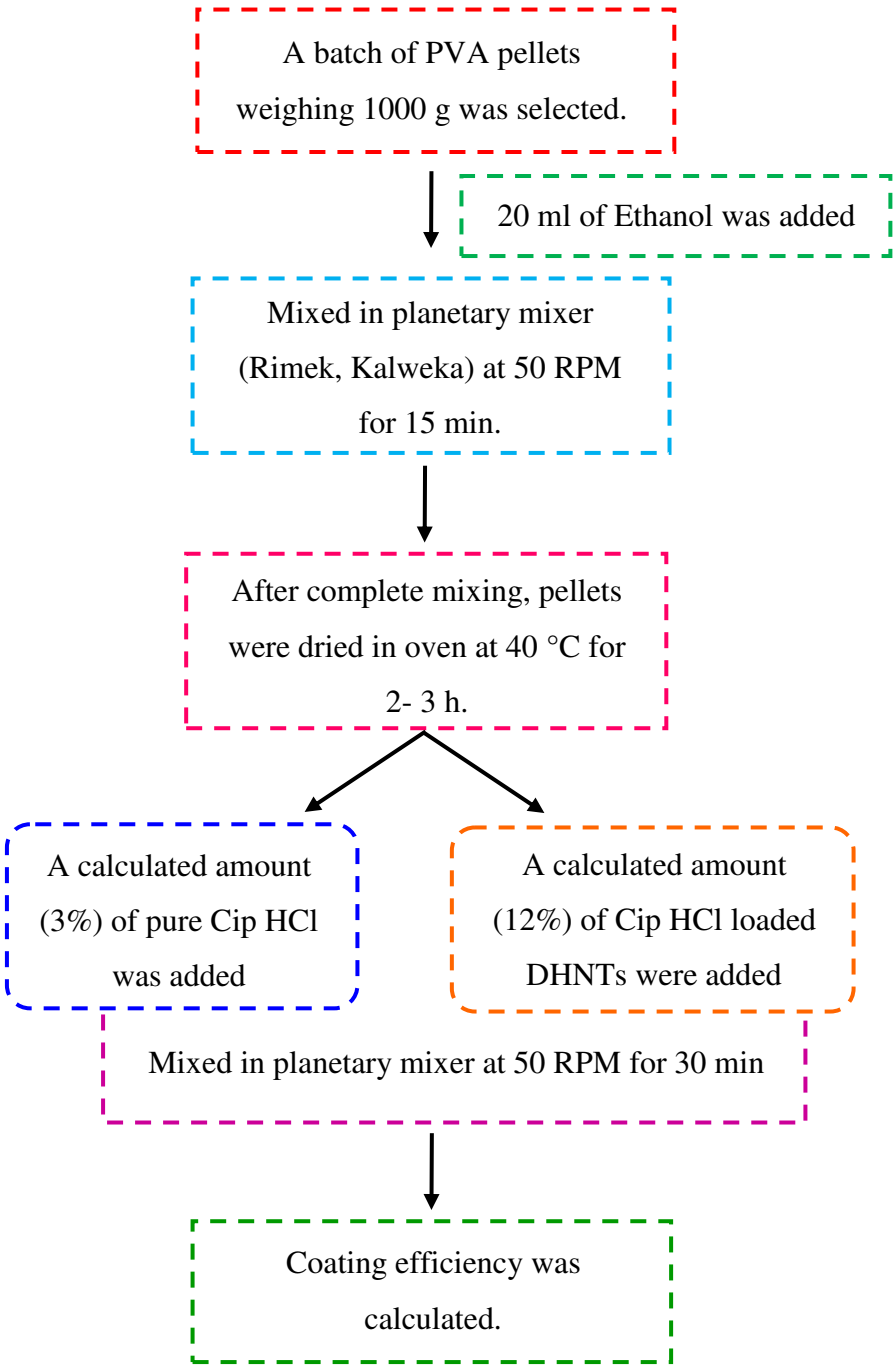

Figure 11: Diagrammatic Flow Chart Representation for Coating of PVA Pellets

3.3.2. Extrusion of PVA Filaments

A blend of formulation components was extruded by hot melt extrusion technique using Twin Screw Lab Extruder (Aasabi Machinery Pvt. Ltd., Mumbai). Pure Cip HCl and Cip HCl loaded DHNTs coated PVA pellets were fed into a feeder

from the hopper at the rate of 5g/ min. The molten pellets were fed into a horizontal barrel of a twin-screw extruder by means of a large rotating screw at speed of 50 RPM. The coated PVA pellets were extruded through a circular die at a temperature ranging from 180 – 200°C. The filaments were cooled, rolled, collected and finally stored in air tight container [119].

3.3.3. Design and Development of FDM based 3D Printed Scaffolds

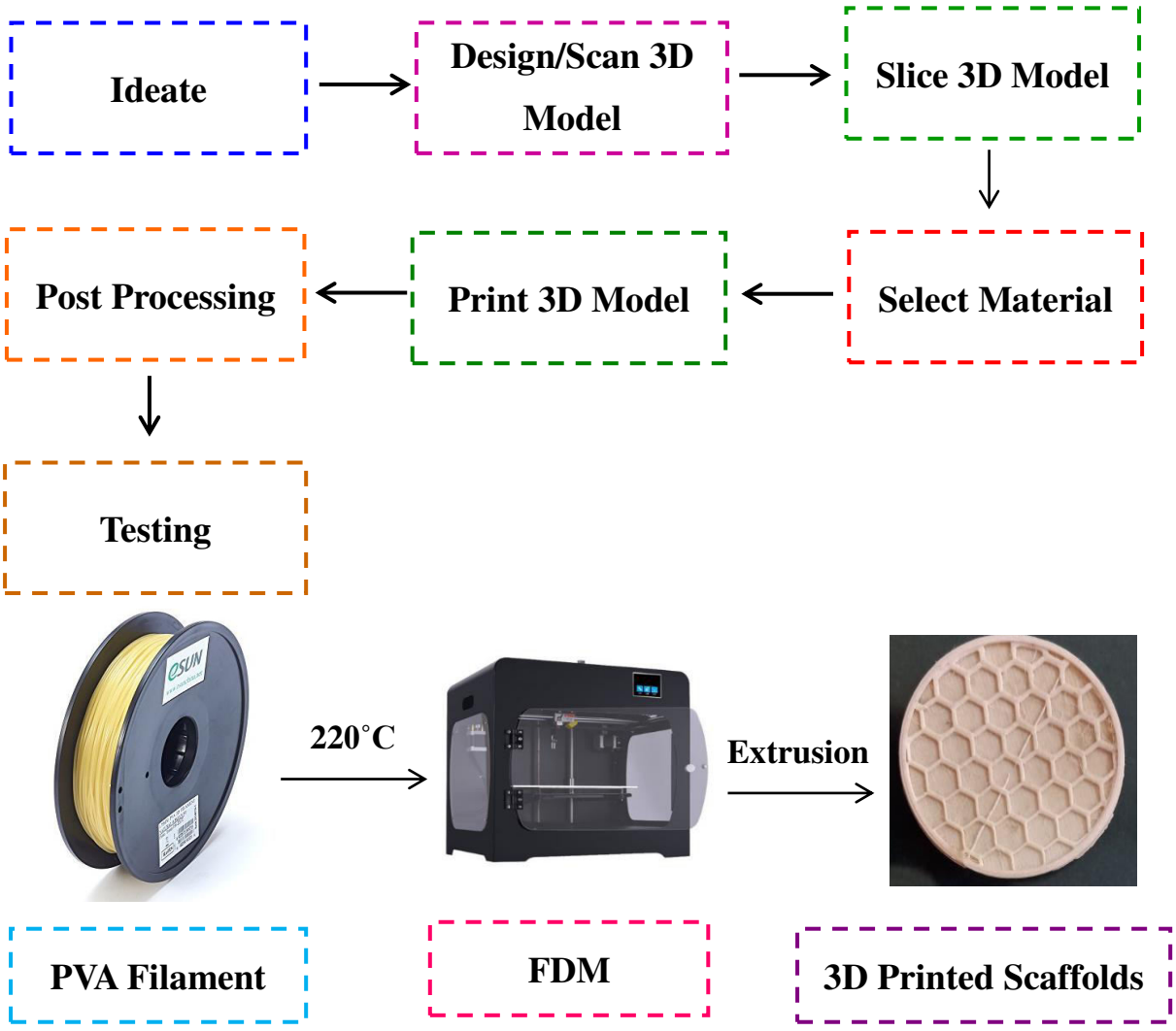

Figure 12. A Schematic illustration of 3D printing technology for the fabrication of scaffolds

3.3.3.1. Steps involved in the development of scaffolds by 3D printing technique

The key objectives of the proposed research work was to evaluate the potentiality of the filaments to print and develop a suitable design template using 3D printing technique.

Step 1: A design prototype for the fabrication of scaffolds was selected and created using computer - aided design model (CAD), integrated with computer modelling software program (Solid Works, Dassault Systems Solid Works Corporation, Waltham, MA, USA).

Step 2: Subsequently, the design template for scaffolds were created and expressed in terms of. stl pattern (as depicted in Figure 13).

Step 3: The. stl pattern was further customized to GCode system using a Flashforge Creator Pro Slicer.

Step 4: The customized data material was transferred to FDM 3D printer machine; the scaffolds were designed and printed with an infill ratio of 40% and a hexagonal infill pattern using a self-extruded PVA filaments [120]. The various parameters for the development of scaffolds are enlisted in Table 9. The overall schematic illustration of 3D printed scaffolds is depicted in Figure 12.

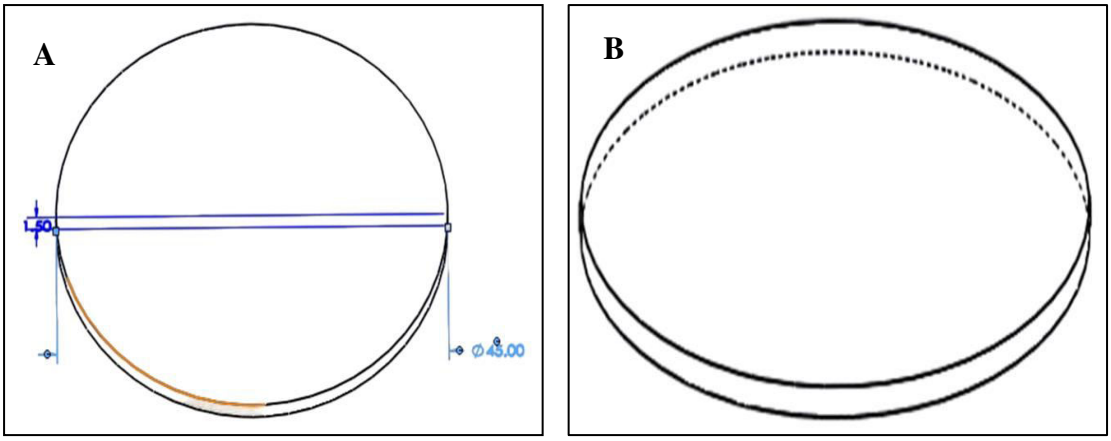

Figure 13. Computer Aided 3D Design of Scaffolds: [A]. Aerial View of Scaffold [B]. Peripheral View of Scaffold

Table 9: Parameters for 3D Printing of Scaffolds

S No	Parameters	Values
1.	Filaments	Cip HCl coated PVA filaments (PF1)
		Cip HCl loaded DHNTs coated PVA filaments (PF2)
2.	Extrusion temperature (°C)	220
3.	Build plate temperature (°C)	110
4.	Print speed (mm/sec)	60
5.	Travelling speed (mm/sec)	80
6.	Nozzle diameter (mm)	0.2
7.	Layer height (mm)	0.18
8.	Infill ratio (%)	40
9.	Infill pattern	Hexagon

3.3.4. Evaluation of Filaments and Scaffolds

3.3.4.1. Dimensional Analysis of Filaments and Scaffolds

The dimensional analysis includes the measurement of diameter and thickness of the scaffolds and filaments. A Vernier calliper was used to measure the thickness as well as the diameter of the filaments and 3D printed scaffolds. The data obtained was calculated and expressed in terms of mean values and standard deviation [95].

3.3.4.2. Compatibility Study of Drug and Excipients

1. FT-IR Spectroscopic Studies

The chemical composition and compatibility of drug and excipients in both the scaffolds (S1 and S2) were analysed by ATR-FTIR spectrophotometer (Shimadzu, Japan) in the frequency range of 4000-500 cm^{-1} with a resolution of 4 cm^{-1} at 32 scans. The spectra obtained was recorded and analysed using Lab Solution software® [89].

2. Differential Scanning Calorimetric Analysis

Differential scanning calorimetric analysis was performed to investigate the compatibility between drugs and excipients as well as to characterize the thermal properties of scaffolds. DSC analysis was actualized using (DSC 60 Plus, Shimadzu, Japan). A small amount of sample approximately 4 mg was precisely weighed, transferred to aluminium pan and hermetically sealed. Heating procedures were carried out at 10 °C/min from 30 °C to 350 °C, with the nitrogen gas purged at the flow rate of 100 ml/min. The DSC curves were recorded and interpreted by Lab Solutions® software [94].

3.3.4.3. Measurement of Mechanical Strength of Scaffolds / Tensile Strength Measurement of Scaffold

The mechanical strength of scaffolds (S1 and S2 formulations) were performed according to the specifications outlined by American Society for Testing and Materials (ASTM D882-12). The tensile strength measurements were determined using Micro Universal Testing Machine (Tinius Olsen 10 ST, UK) with the aid of a load cell having a capacity of 500 N at the rate of 1 mm per min. The scaffolds were sliced into a small piece (45 mm x 25 mm) and the mean values of elastic modulus, tensile strength and percentage break strain were recorded and measured [121].

3.3.4.4. Morphological Evaluation of Filaments and 3D Printed Scaffolds

The morphological characterization of each filaments (PF1 and PF2) and 3D scaffolds (S1 and S2) were analysed using JEOL JSM-7610F Plus, Scanning Electron Microscope. The scaffolds were consistently coated with a conducting element (Gold – Sputter) for 60 s using (150R ES Quorum Q). The samples were placed within the chamber and the images were acquired at the resolution of 100 X at an extremely low accelerated voltage (<5 kV) [78].

3.3.4.5. Determination of Drug Content

Drug content of each batch of scaffold formulation (S1 and S2) was analysed by UV-Visible spectrophotometric method. The scaffolds were cut to a particular dimension (1 cm x 1 cm), dissolved in a 100 ml of phosphate buffer (7.4 pH) and sonicated for 20 min. The solution was diluted up to 10 ml with phosphate buffer and filtered using 0.45 µ Whatman filter paper. The absorbance of the solution was measured at 271 nm using (UV-1900, Shimadzu, Japan) and % drug content of each scaffold formulation (S1 and S2) was determined.

3.3.4.6. *In Vitro* Diffusion Study

The *in vitro* drug release pattern of ciprofloxacin hydrochloride scaffolds (S1 and S2 formulation) was determined using diffusion cell apparatus (Electrolab 07-EDC, Mumbai) in phosphate buffer 7.4 pH, 12.5 ml buffer solution for 12 h. The formulated 3D scaffolds of each formulation in the dimension of (1 x 1 cm^2) were placed in the midst of the receptor and donor compartment. The bath temperature was maintained at 37 °C ± 2 °C and the solution was stirred on magnetic stirrer at 50 RPM. At pre-defined time intervals (1, 2, 3… 12 h), 1 ml of sample was withdrawn and then replaced with an equal volume of fresh media to maintain the sink conditions. The samples withdrawn were appropriately diluted and spectrophotometrically analysed at 271 λmax [104].

3.3.5. Cell Culture Experimentation

3.3.5.1. *In Vitro* Scratch Assay Test with A549 Cell Lines

The A549 Human alveolar carcinoma epithelial cells (A549) were seeded in 6-well culture plate with a density of 1 x 10^6. A confluent monolayer cell was scratched consistently using a micro pipette tip (200 µl) and the well plates were rinsed with phosphate buffered saline. A standard Cip HCl (1 mg/ml) was considered as a control. The 3D printed scaffold (S2- Cip HCl loaded DHNTs scaffold) at the concentration of 1 mg/ml used as a test sample and the well plates were incubated for 24 h. Subsequently, after the addition of standard drug and S2 formulation, the images of cellular gap closure were captured at 4 X magnification on TS2 Nikon Eclipse inverted microscope at the periodic time intervals of 0, 24 and 48 h and the cell migration rate were determined [109].

3.3.6. Stability Assessment of 3D Printed Scaffold [117]

The stability assessment of fabricated scaffolds (S1 and S2) was carried out as per the ICH guidelines of Q1A (R2). The samples were kept in a sealed amber coloured container, stored in a humidity chamber (Lab India) for 12 months (long term stability) at the temperature of 25 ºC ± 2 ºC / 60 % RH ± 5% RH. The samples of scaffolds were visually examined for the change in color and texture of the scaffolds. The samples were also analyzed for content uniformity and diffusion study with respect to the procedure defined in methodology chapter [117].

RESULTS

This chapter defines the outcomes and findings for the successful doping of halloysite nanotubes using silane coupling agents. Doping of HNTs was performed to enhance the surface properties of nanotubes. This section also describes the results and inferences derived from the characterization data of fabricated polymeric sponges by lyophilization technique and scaffolds by FDM technique. The findings and interpretation in this chapter are expressed in terms of texts, tables, figures and graphical representation.

4.1. STRATEGY 1:

DOPING OF HNTs USING SILANE COUPLING AGENT

4.1. Characterization of Doped HNTs

4.1.1. Characterization of Functional Groups of Pristine HNTs and Doped HNTs

The existence of functional groups in the spectra of DHNTs confirmed the successful doping of Pristine HNTs (PHNTs). The FT-IR spectra of PHNTs and DHNTs are depicted in Figure 14 - 17. The specific peaks wavelength and its relevance are presented in Table 10.

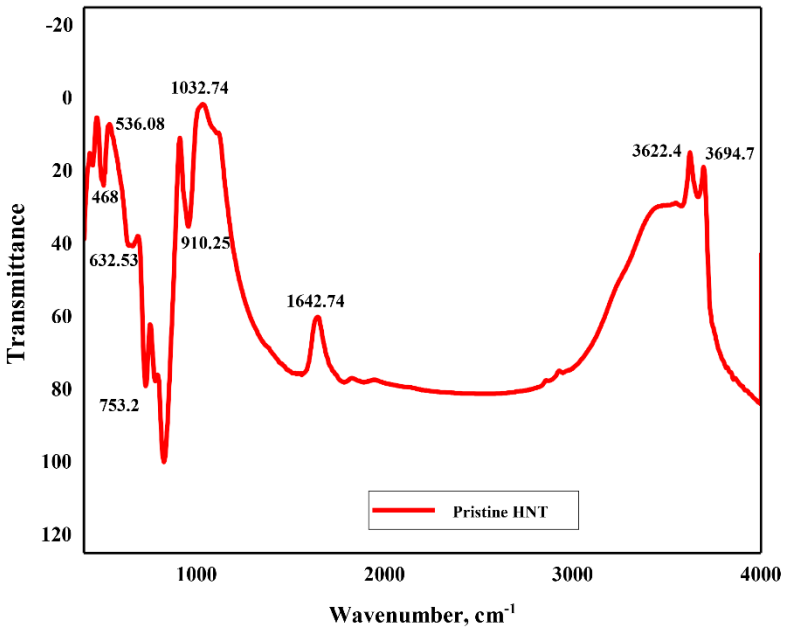

Figure 14: FT-IR Analysis of Pristine HNTs

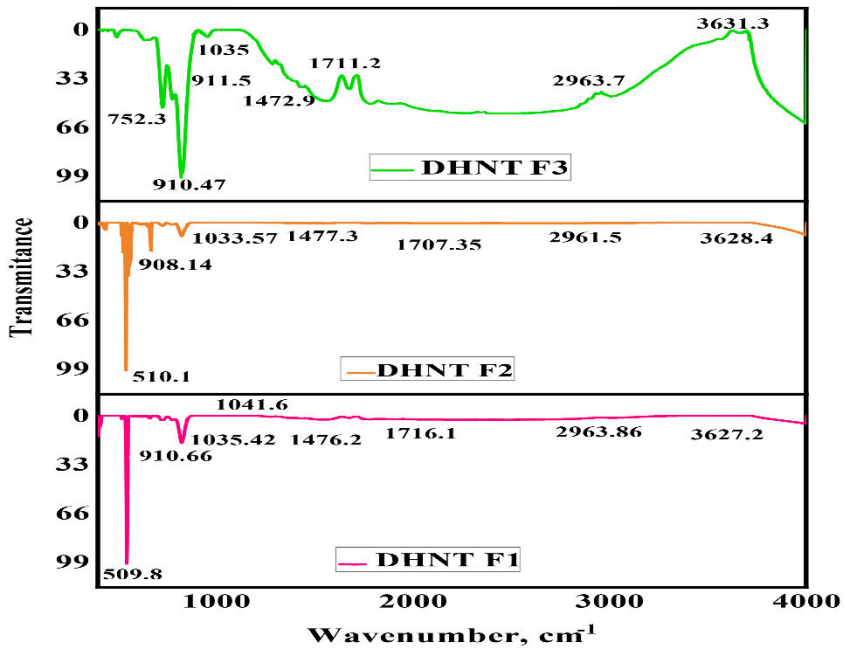

Figure 15: FT-IR Analysis of DHNT F1 - F3

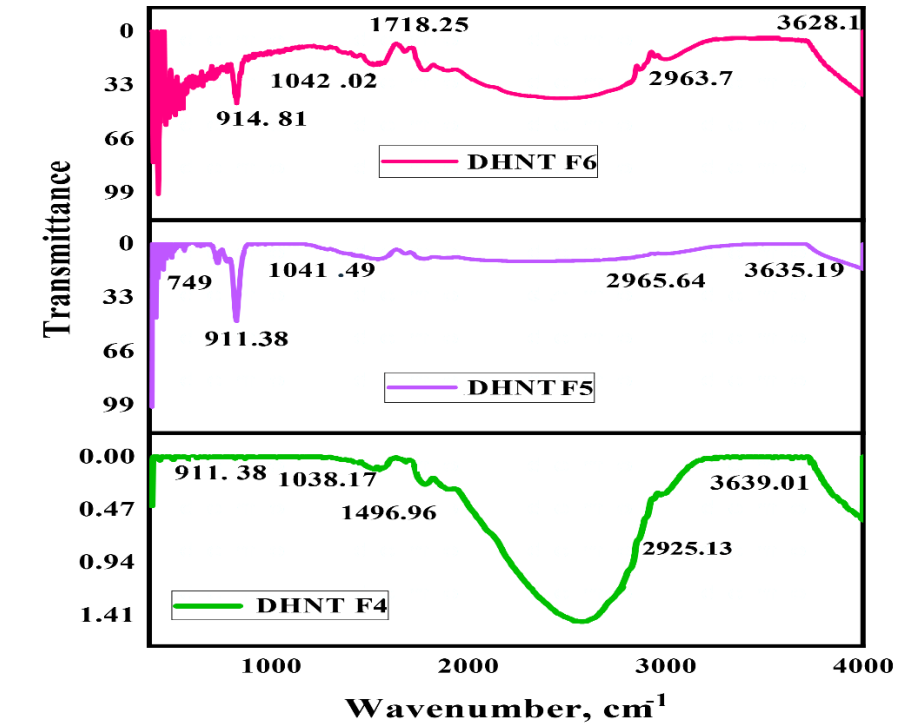

Figure 16: FT-IR Analysis of DHNT F4 - F6

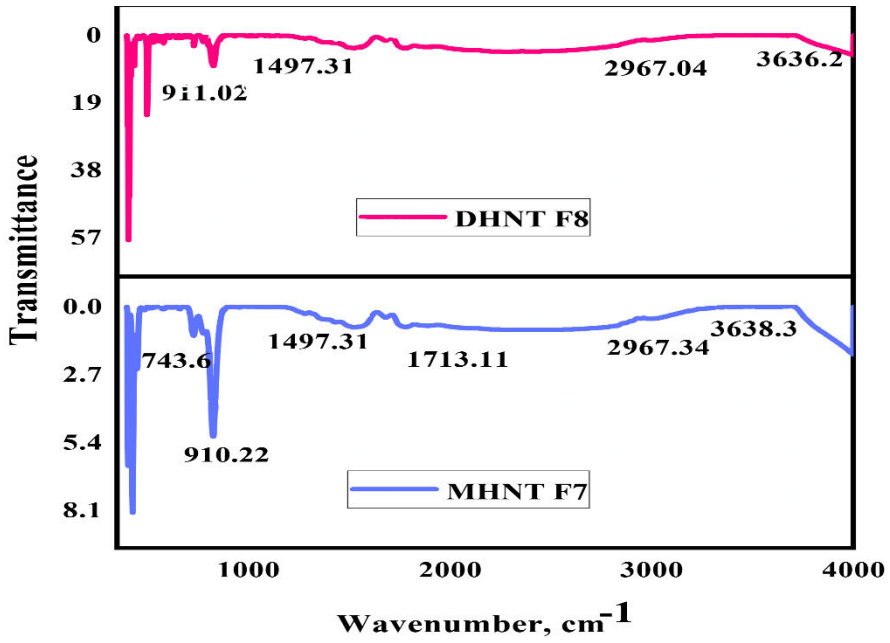

Figure 17: FT-IR Analysis of DHNT F7- F8

Table 10: FT-IR Frequency of HNTs and DHNTs

Sample	Frequency range (cm^{-1})	Peaks (cm^{-1})	Interpretation	Inference
DHNT F1	1700 – 1760 910 - 925 3600 - 3645	Absent 910.22 3638.3	C=O stretching vibration Deformation of inner hydroxyl groups (-OH) Stretching of inner hydroxyl groups (-OH)	Efficiency of HNTs modification was slightly decreased
DHNT F2 and F3	3600 - 3645	3631.3	Presence of inner hydroxyl groups	Doping efficiency of HNTs was enhanced
DHNT F4 and F8	1700 - 1760	1707.35 1726.14	C=O stretching vibration	HNTs were slightly doped
DHNT F5 and F6	910 – 925 1025-1055	911.38 and 914.81 1041.49 and 1042.02	Deformation of inner hydroxyl groups (-OH) Si-O stretching vibration	HNTs were doped
DHNT F7	910 - 925	910.22	RSi-O-Si and RSi-O-Al bonds	HNTs were successfully doped

4.1.2. Studies on Thermal Analysis of PHNT and DHNTs

4.1.2.1. TGA Analysis

Thermal stability of PHNT and γ-MPS DHNTs were determined by thermo-gravimetric analysis (TGA). The thermo-grams of PHNTs and DHNTs are illustrated in Figure 18 - 20. The data obtained from the thermo-grams of TGA analysis (as shown in Table 11) revealed the productive inclusion of γ-MPS on the surface as well as within the lumen of HNTs

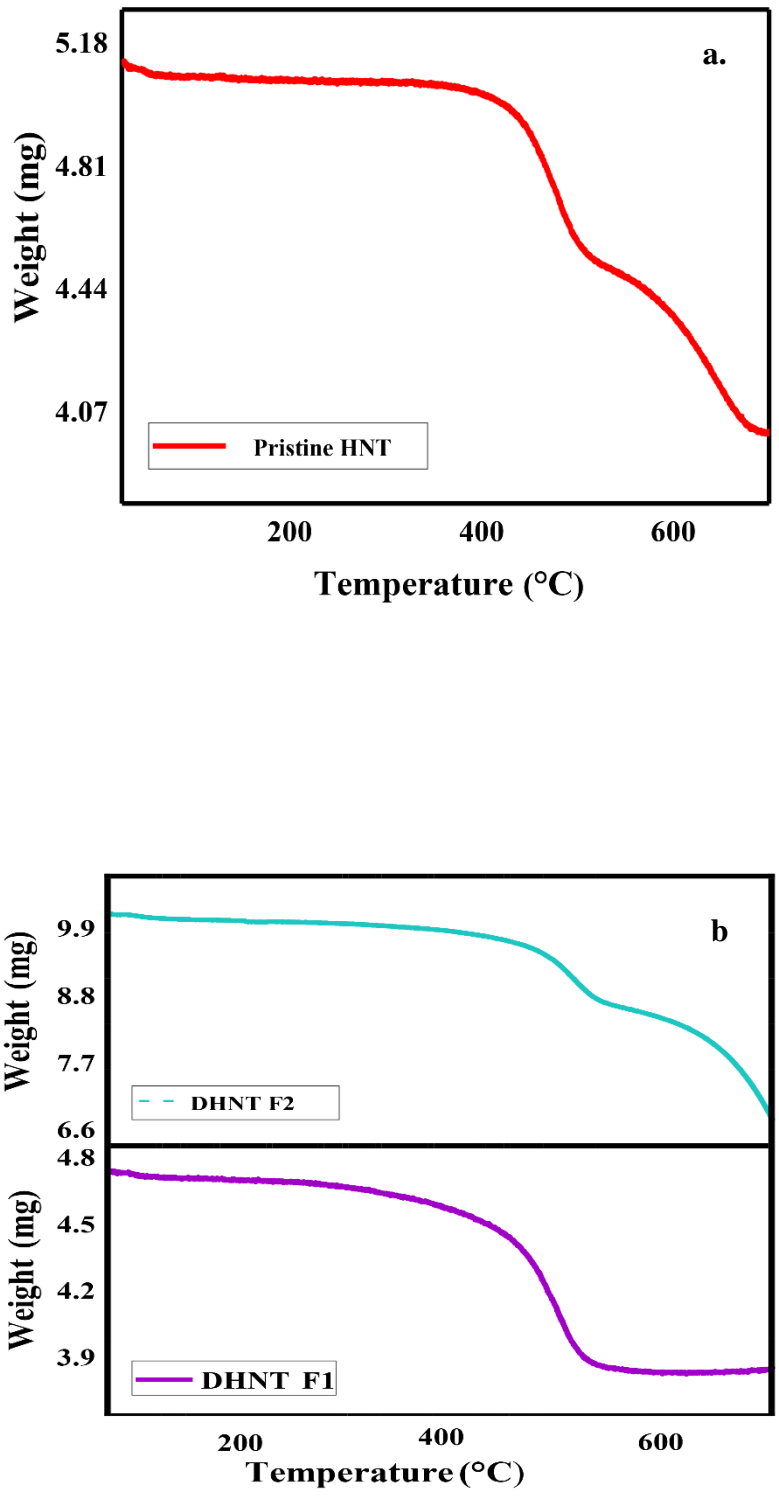

Figure 18: TGA Curves of a. Pristine HNT and b. DHNT F1-F2

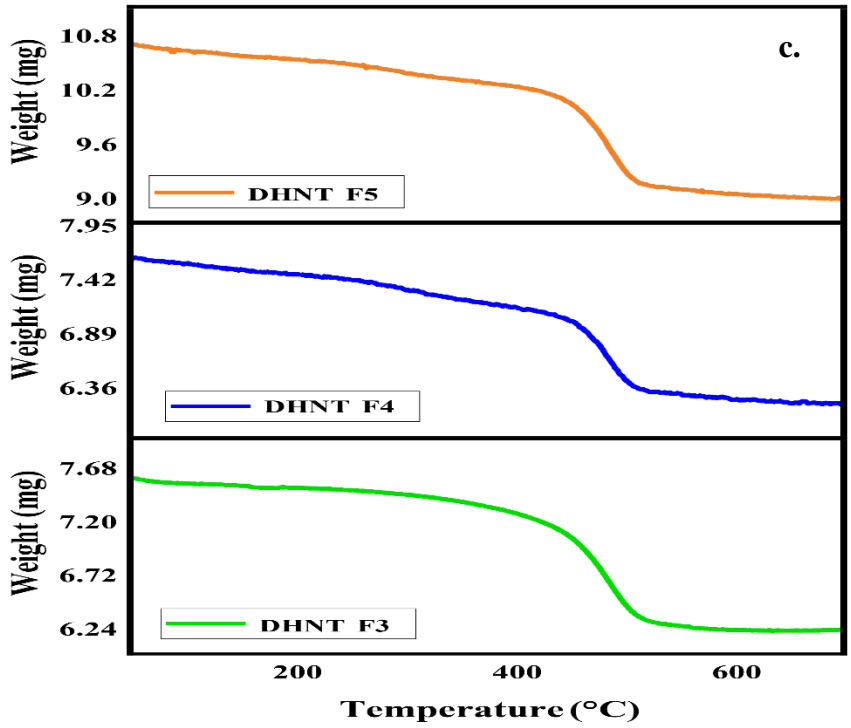

Figure 19: TGA Thermo-grams of DHNT F3 - F5

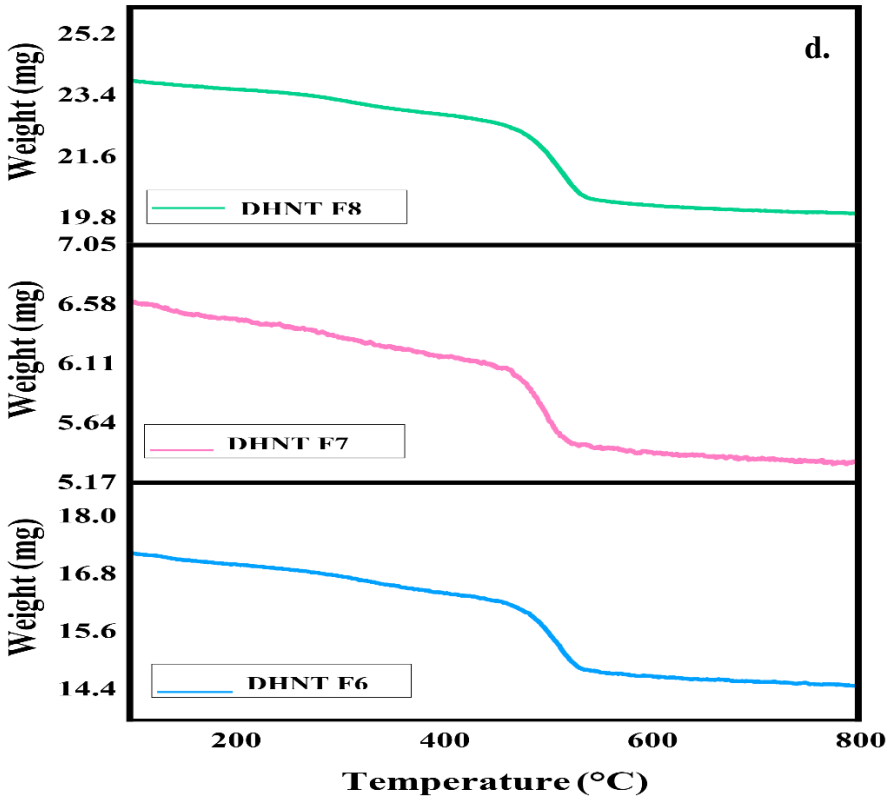

Figure 20: TGA Curves of DHNT F6 - F8

Table 11: Thermo-gravimetric Analysis data for Pristine and Doped HNTs

Sample	Mass loss (mg)			
	First Peak		Second Peak	
	Temp (ºC)	Justification	Temp (ºC)	Justification
PHNTs	50-100 ºC	Evaporation of water molecules deposited either on the internal or external surface of HNTs	360 - 550 ºC	Associated with de-hydroxylation of Al-OH and Si-OH groups of inner and outer surface of HNTs
	Up-to 350 ºC	Thermal stability was excellent without any mass loss	-------	-------
DHNT F1	45-90 ºC	Thermal decomposition of γ-MPS moieties, covalently attached to HNTs surface	400 - 590 ºC	Structural de-hydroxylation of Al-OH and Si-OH groups. Confirmed slight doping of HNTs
DHNT F2 and F3	50 - 210 ºC	Reduced mass of both the samples is attributed to doping with γ-MPS, that reduced the content of adsorbed water molecules	210 - 380 ºC	Fragmentation of hydrogen bonds present in HNTs, with a mass loss of 0.12% and 0.55%
DHNT F4	80 - 110 ºC	Dissipation of adsorbed water molecules	390 - 570 ºC	De-hydroxylation of Al-OH and Si-OH groups
DHNT F5 and F8	251 - 380 ºC	Thermal decomposition of γ-MPS silane functionalized on the surface of HNTs	385 - 595 ºC	De-hydroxylation of Al-OH and Si-OH groups. Increased mass loss was observed, due to interaction of methoxy groups of γ-MPS with -OH groups of HNTs
DHNT F6 and F7	467 - 550 ºC	Reduced mass loss was observed. Condensation of silanol groups resulted in siloxane groups formation	-----	-------

4.1.3. Structural Characterization of PHNTs and DHNTs

The structural identification of PHNTs and DHNTs were analyzed by X-ray diffraction analysis. The x-ray diffraction profiles of DHNTs displayed a remarkably rapid structural changes in PHNTs during the process of doping. The effect of functionalization/doping resulted in increased basal shifts, which in-turn enhanced the intensity of γ-MPS to intercalate within the layers of HNTs.

Thus, degree of intercalation and shifts in the basal spacing defined that PHNTs were effectively doped with γ-MPS. Diffraction profiles of PHNT and DHNTs are illustrated in Figure 21 - 22. The data values for d-spacing and diffraction angle of DHNTs are presented in Table 12.

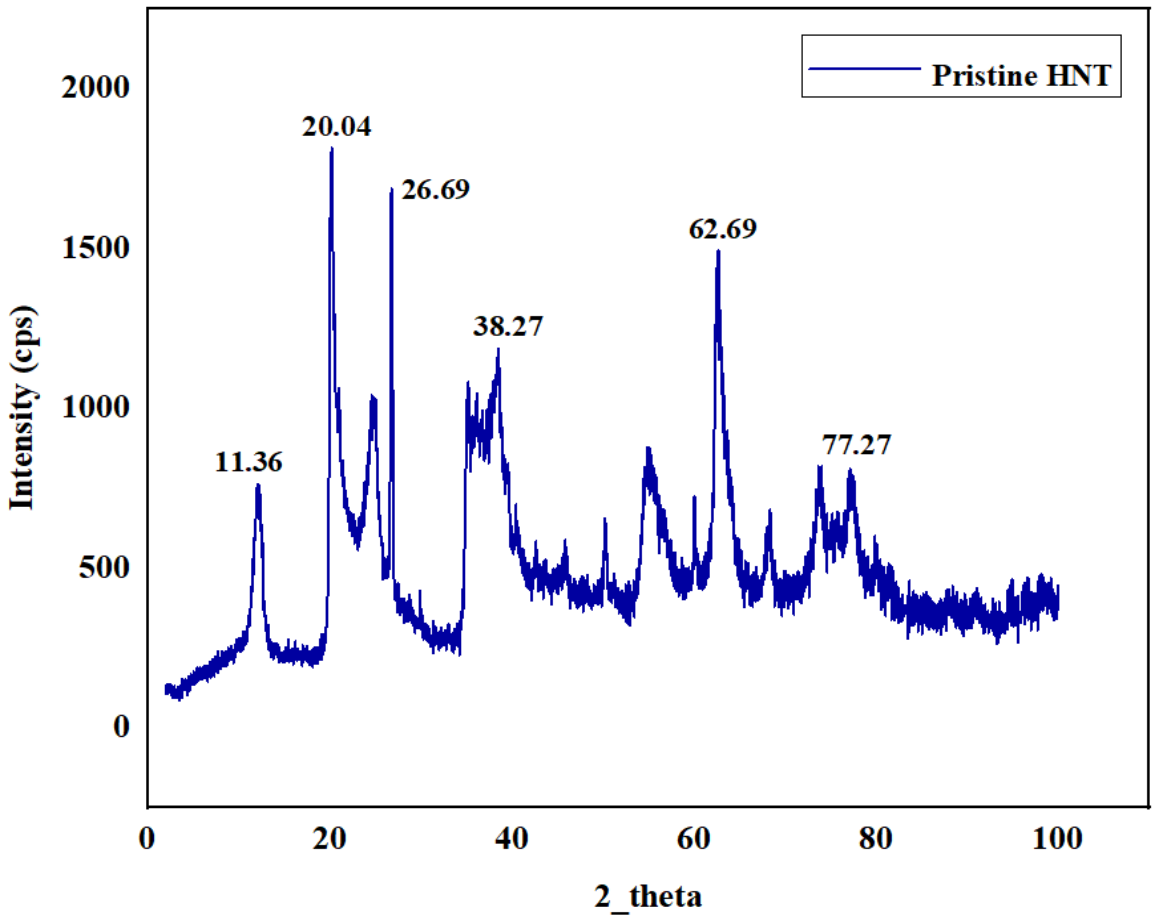

Figure 21: X-ray Diffraction Pattern of Pristine HNT

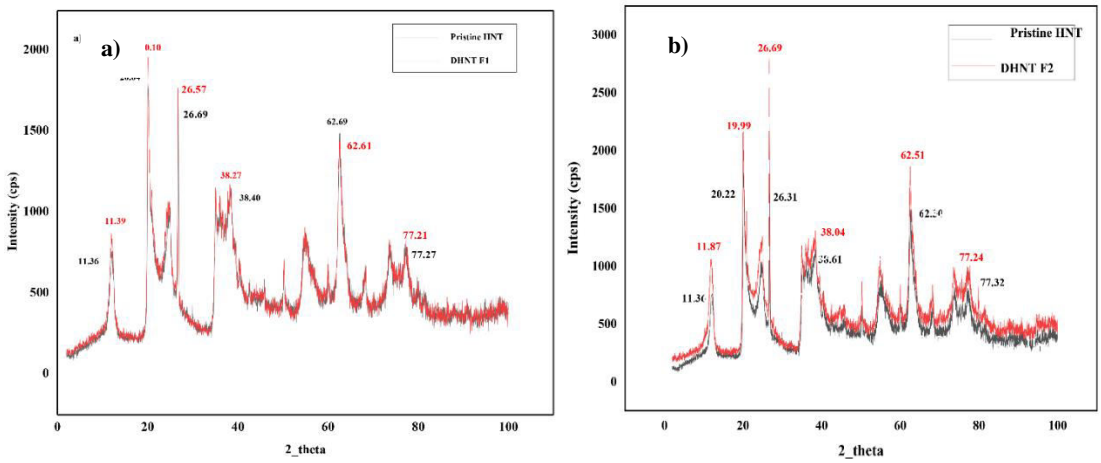
a)
Pristine IINT
DHNT F1
Intensity (cps)
2_theta
11.39
11.36
26.57
26.69
38.27
38.40
62.69
62.61
77.21
77.27
b)
Pristine IINT
DHNT F2
Intensity (cps)
2_theta
26.69
19.99
20.22
26.31
11.87
38.04
62.51
77.24
77.32

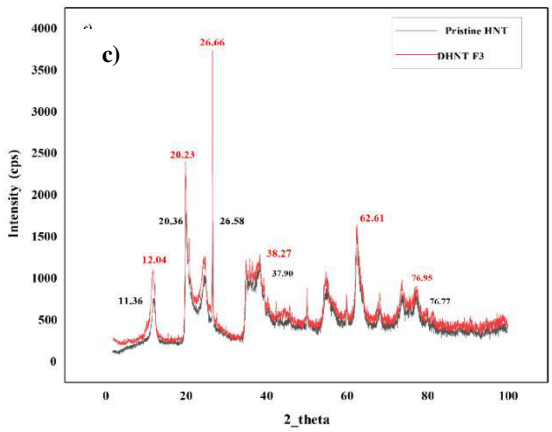
c)
Pristine HNT
DHNT F3
Intensity (cps)
2_theta
26.66
20.23
20.36
26.58
12.04
11.36
38.27
37.90
62.61
76.95
76.77

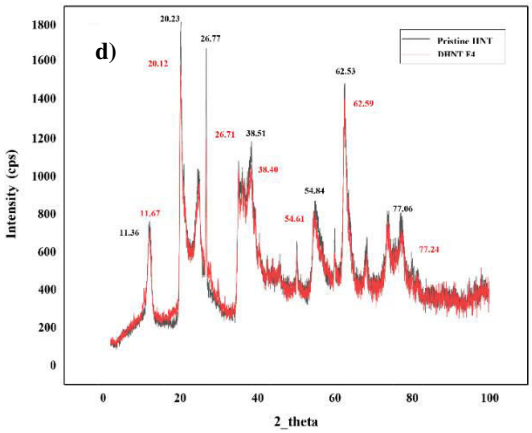
d)
Pristine HNT
DHNT F4
Intensity (cps)
2_theta
20.23
20.12
26.77
26.71
38.51
38.40
62.53
62.59
54.84
54.61
11.67
11.36
77.06
77.24

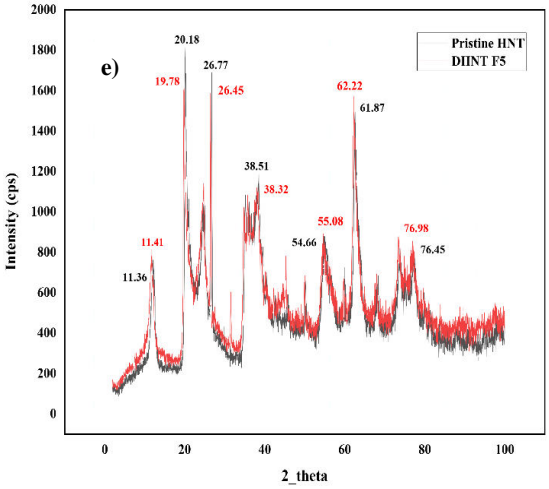
e)
Pristine HNT
DIINT F5
Intensity (cps)
2_theta
20.18
26.77
19.78
26.45
62.22
61.87
38.51
38.32
55.08
54.66
76.98
76.45
11.41
11.36

f)

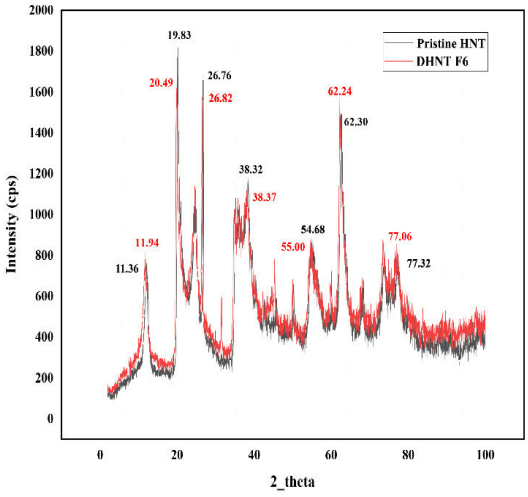
Pristine HNT
DHNT F6
Intensity (cps)
2_theta
19.83
20.49
26.76
26.82
62.24
62.30
38.32
38.37
54.68
55.00
77.06
77.32
11.94
11.36

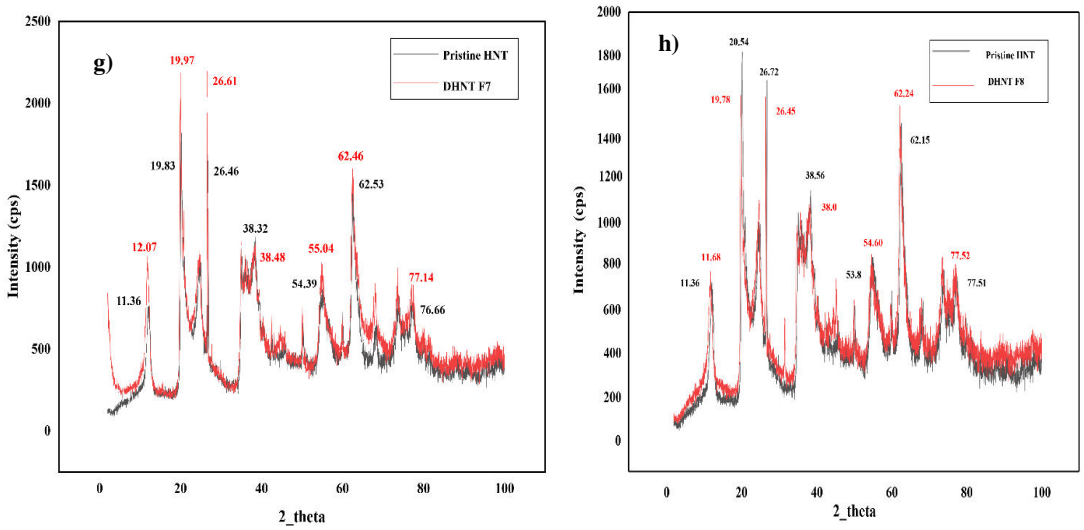

Figure 22: X-Ray Diffraction Profiles of (a-h) DHNT F1 – DHNT F8

Table 12: X-ray Diffraction Data Values of PHNTs and DHNTs

Sample	Diffraction angle (2θ)	d-spacing values (Å)	Characteristics of diffraction peaks
PHNTs	11.36°	7.47 Å	Sharp narrow peak
DHNT F1	11.39°	7.52 Å	Slightly broad peak
DHNT F2	11.87°	7.71 Å	Broad peak
DHNT F3	12.04°	7.75 Å	Broad peak
DHNT F4	11.67°	7.62 Å	Intensity of peak decreased
DHNT F5	11.41°	7.58 Å	Intensity and sharpness of peak reduced
DHNT F6	11.94°	7.73 Å	Broad peak
DHNT F7	12.07°	7.79 Å	Intense sharp broad peak
DHNT F8	11.68°	7.65 Å	Slightly broad peak

4.1.4. Topographical Characterization of PHNTs and DHNTs

The surface texture and topographical characterization of PHNTs and DHNTs were determined by TEM analysis. The TEM micrograph of PHNTs (Figure 23 - 24) presented multilayered hollow nano-tubular structure with the dimensions of (OD = 30 - 70 nm) and (ID = 10 - 30 nm). Similarly, upon doping with γ-MPS, the TEM micrographs of DHNTs revealed a relatively uniform surface morphologies along with the rough texture on the surface of DHNTs. The data observations of nanotubes derived from TEM analysis are tabulated in Table 13.

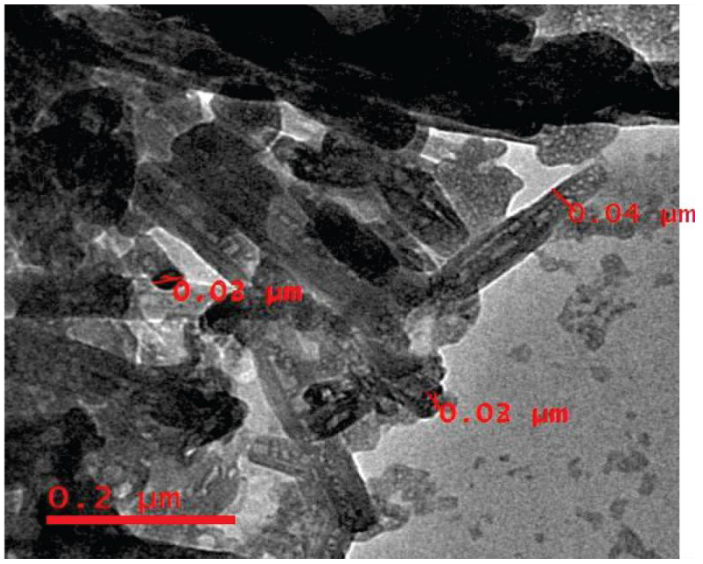

Figure 23: TEM Image of Pristine HNTs

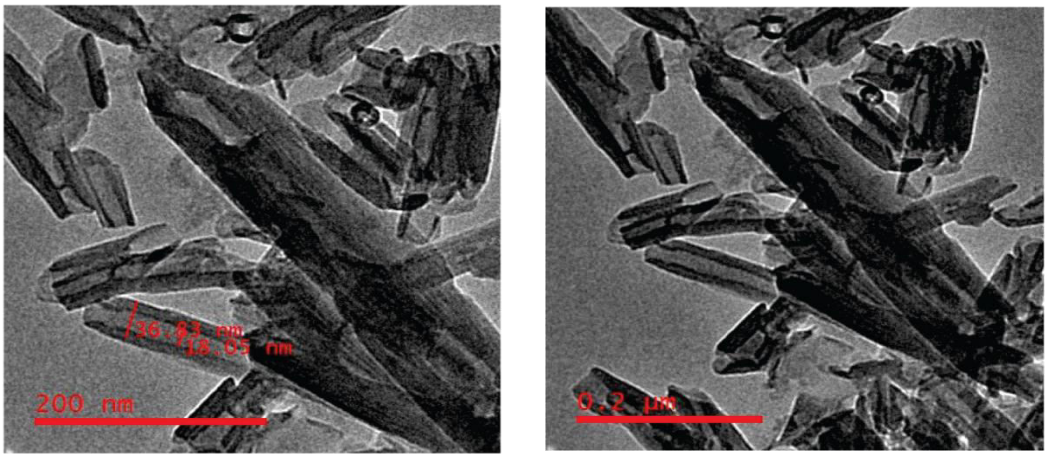

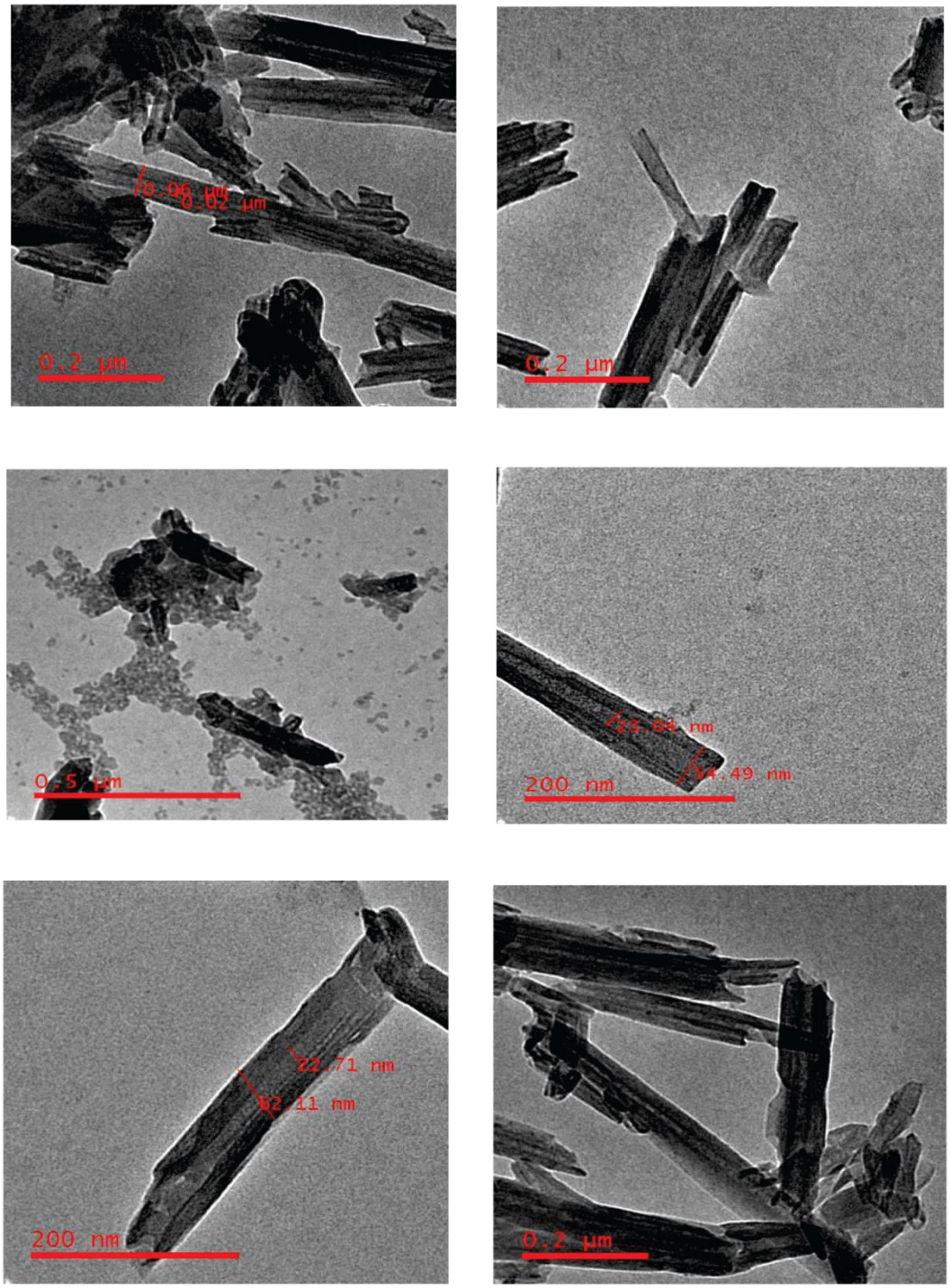

Figure 24: TEM Images of a). DHNT F1, b). DHNT F2, c). DHNT F3, d). DHNT F4, e). DHNT F5, f). DHNT F6, g). DHNT F7, h). DHNT F8

Table 13: Surface Topography and Dimensions of PHNTs and DHNTs

Sample	Dimensions of Nanotubes		Topography of nanotubes
	Inner diameter (nm)	Outer diameter (nm)	
PHNTs	10 - 30 nm	30 -70 nm	Hollow tubular multilayered structure, open ended lumen
DHNT F1	18.05 nm	36.83 nm	Surface texture was slightly rough in nature
DHNT F2	23.04 nm	54.49 nm	Surface topography was uniform with reduced entanglement of nanotubes
DHNT F3	21.47 nm	60.02 nm	Surface texture was highly rough with an irregular deposition of γ-MPS
DHNT F4	19.55 nm	48.15 nm	Smooth morphology with irregular diameter
DHNT F5	15.72 nm	41.29 nm	Aggregation of nanotubes
DHNT F6	23.04 nm	54.49 nm	Surface topography was extremely rough
DHNT F7	22. 71 nm	62.11 nm	Surface morphology was extensively uniform with high tubular integrity
DHNT F8	19.86 nm	45.23 nm	Smooth texture with uneven morphology

4.1.5. Characterization of Surface Charge Potential of PHNTs and DHNTs

The surface charge potential of HNTs and DHNTs were characterized by zeta potential (ζ) analysis. The zeta potential reveals the homogeneity and physical stability of PHNTs and DHNTs in water. At a neutral pH, the ζ-potential value for PHNTs was

found to be – 33.64 mV. Subsequently, the DHNTs presented an increased ζ-potential value of -58.15 to -95.7 mV, as depicted in Figure 25

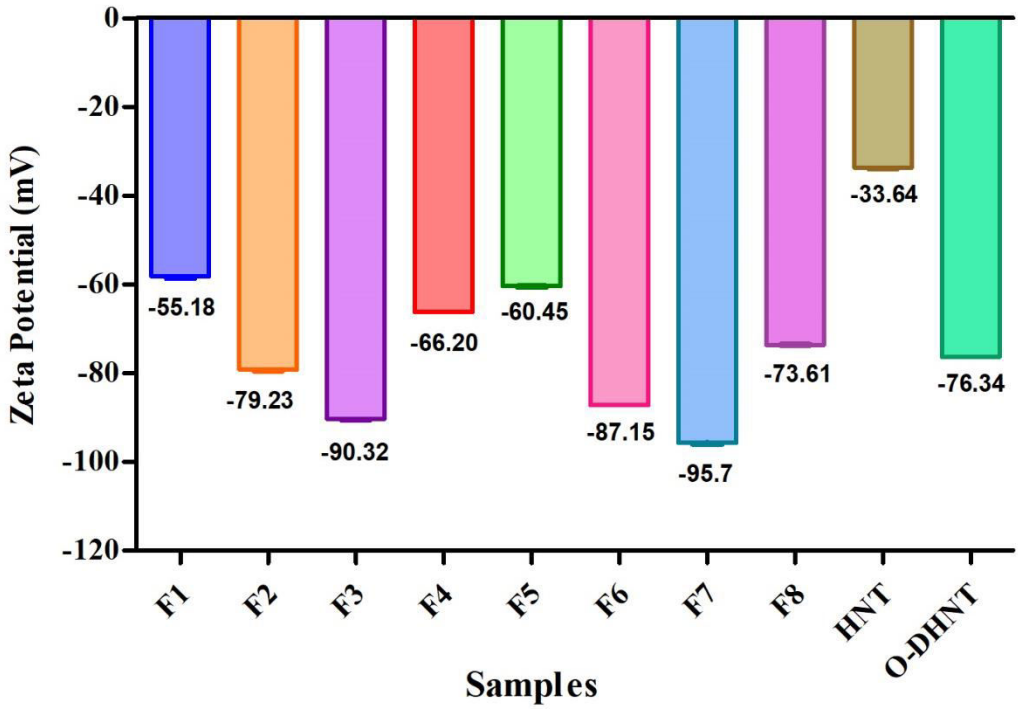

Figure 25: ζ-potential of HNTs, DHNTs and Optimized DHNTs

4.1.6. Design of Experiments

A 2^3 factorial custom design matrix was selected as a design template for an experimental research strategy, to analyze the significance of various independent factors on the selected response variables. The absolute framework of experimental study design with an actual response data values are presented in Table 14.

Table 14: Experimental Study Design for Doped HNTs

Variables				Actual responses	
Run	**Conc of γ-MPS**	**Conc of HNTs**	**Conc of Ethanol**	**Diffraction angle (2θ)**	**Zeta Potential (mV)**
	(X_1)	**(X_2)**	**(X_3)**	**(Y_1)**	**(Y_2)**
F1	6	25	75	11.39	-58.15
F2	12	25	75	11.87	-79.23
F3	12	25	100	12.04	-90.34
F4	6	25	100	11.67	-66.27
F5	6	50	75	11.41	-60.45
F6	12	50	75	11.94	-87.15
F7	12	50	100	12.07	-95.71
F8	6	50	100	11.68	-73.61

4.1.6.1. Statistical Assessment for Response Variables

An impressive method of data analysis that has been used to investigate the significance of variables associated with model is ANOVA. The ANOVA was analyzed for the electro-kinetic potential and the 2θ value of DHNTs, expressed in terms of two important key factors: *p*-value (Probability value) and F-ratio (Fisher's variance ratio). The higher the F-values and the lower *p*-values, the greater effectiveness of model. The results of ANOVA for both the response variables Y_1 and Y_2 are presented in Table 15

Table 15: ANOVA for Diffraction Angle (Y_1)

Source	Sum of Squares	DF	Mean Square	F-value	*p*-value	Model Significance
Model	0.4704	5	0.0941	114.65	0.0087	Significant
X_1	0.3737	1	0.3737	455.36	0.0022	Significant
X_2	0.0037	1	0.0037	4.45	0.1693	Non-Significant
X_3	0.0826	1	0.00826	100.68	0.0098	Significant
C. Total	0.4721	7				
R^2	R^2 (pred)	R^2 (adj)				
99.65 %	94.44 %	98.78 %				

4.1.6.2. Interpretation for Y_1

According to the findings of statistical data analysis as presented in Table 15, the F-value for response variable Y_1 was reported to be 114.65, which indicates that the selected design model was statistically significant ($p \leq 0.05$) for Y_1. In consistent to these findings, it was observed that the independent variables (X_1 and X_3) were found to be significant ($p \leq 0.05$) with respect to response variable Y_1. Likewise, the variable X_2 resulted to be non-significant for the response variable (Y_1) as the ($p > 0.05$).

Table 16: ANOVA for Zeta Potential (Y_2)

Source	Sum of Squares	DF	Mean Square	F-value	*p*-value	Model Significance
Model	1379.63	5	275.93	61.96	0.001	Significant
X_1	1103.80	1	1103.80	274.87	0.0001	Significant
X_2	66.30	1	66.30	14.89	0.0068	Significant
X_3	208.39	1	208.39	46.80	0.0207	Significant
C. Total	1388.54	7				
R^2	R^2 (pred)	R^2 (adj)				
99.36 %	95.74 %	97.76 %				

4.1.6.3. Interpretation for Y_2

In accordance with the results of statistical analysis as presented in Table 16, the proposed experimental design model proved to be statistically significant ($p \leq 0.05$), as evidenced by the F-value for response variable Y_2 being reported to be 61.96. In compliance with these observations, it was noted that all the three independent factors (X_1, X_2 and X_3) were significant ($p \leq 0.05$) in terms of the response variable Y_2.

4.1.6.4. Quadratic Models

The quadratic models were derived and expressed in terms of polynomial equations, to analyze the effect of independent factors on the response variables. The polynomial equations for the selected responses (Y_1 and Y_2) are shown in Table 17

Table 17: Polynomial Equations for Response Variables (Y_1 and Y_2)

Response	Polynomial Equation
Diffraction Angle (2θ) (Y_1)	$+9.525+0.156X_1 + 0.003X_2 + 0.0173X_3 - 0.0009X_1X_3 - 0.0001X_2X_3 - 0.0004X_1X_2$
Zeta Potential (mV) (Y_2)	$+0.6275 - 4.379X_1 - 0.0490X_2 – 0.3783X_3 + 0.0053X_1X_3 - 0.0020X_2X_3 - 0.0032X_1X_2$

The positive term in the generated polynomial equations signifies the synergistic effect whereas, the negative sign indicates the antagonistic effect of independent factors upon the response variables. The effect of each variable on the selected responses is emphasized in the form of surface and contour plots as depicted in Figure 26.

4.1.6.5. Surface Plots and Contour plots

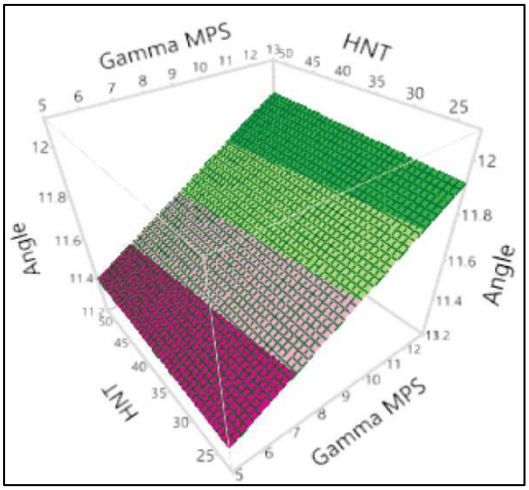

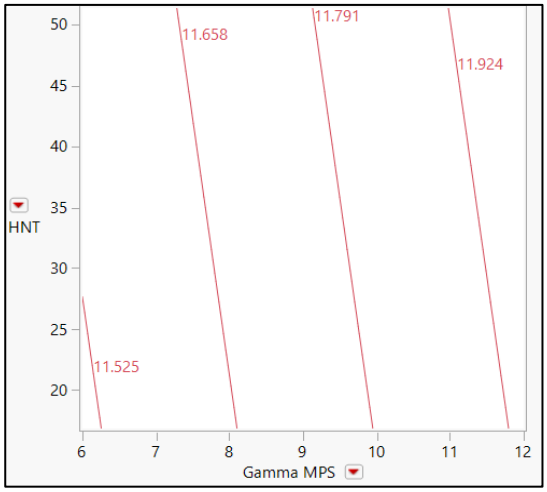

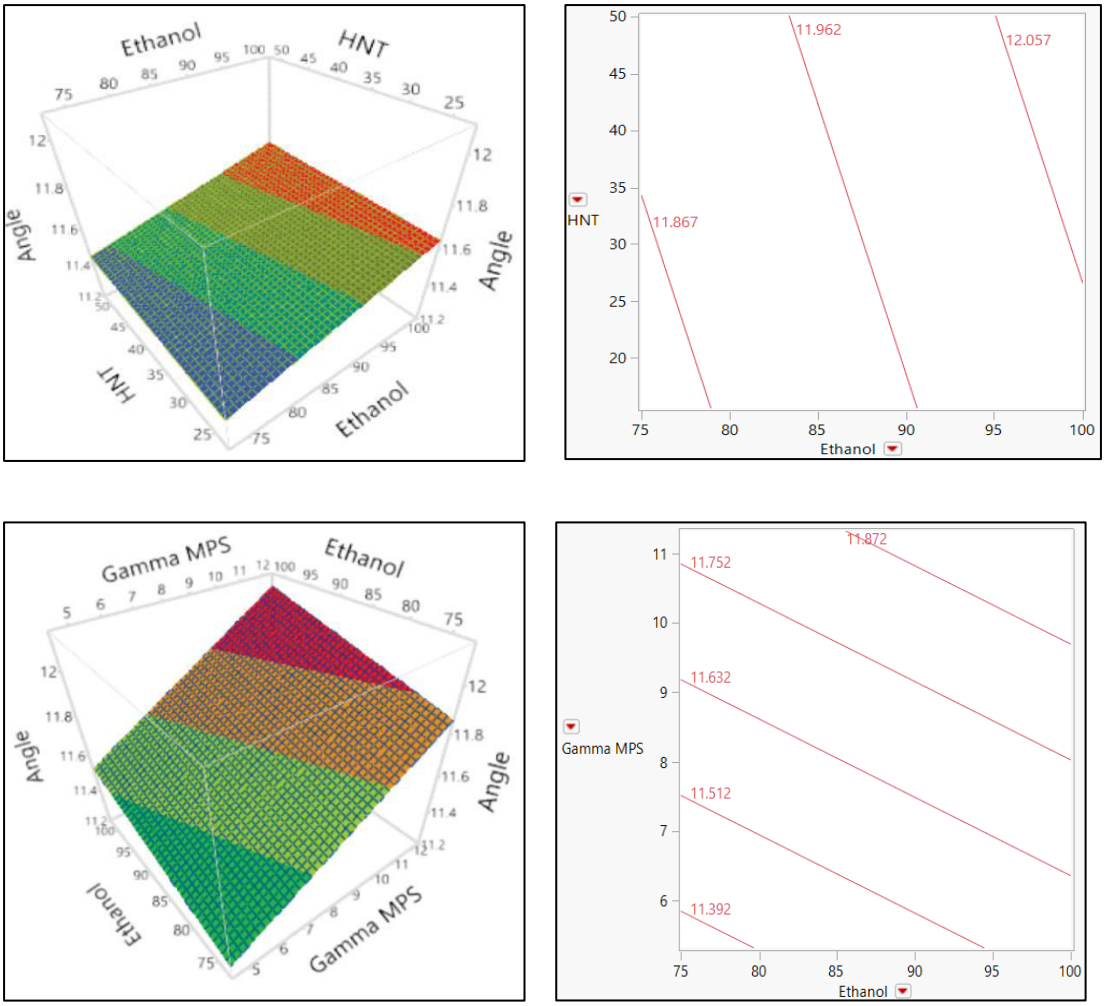

Figure 26: Surface and Contour Plots for the response - Diffraction Angle 2θ (Y_1)

4.1.6.6. Interpretation of Surface Plots for Y_1

The 3D surface plots for the response Y_1 - Diffraction Angle revealed that, the 2θ values of DHNTs obtained from (X-RD analysis) increased, with an increase in the concentration of γ-MPS (X_1). Similarly, in accordance to the 3D surface plots of the variables X_2 and X_3 with respect of Y_1, it was observed that an increased concentration of HNTs and Ethanol (X_2 and X_3) resulted in the increase of 2θ values of DHNTs. Thus, it can be concluded that all the three variables (X_1, X_2 and X_3) presented a significant impact on Y_1.

4.1.6.7. Surface Plots and Contour plots

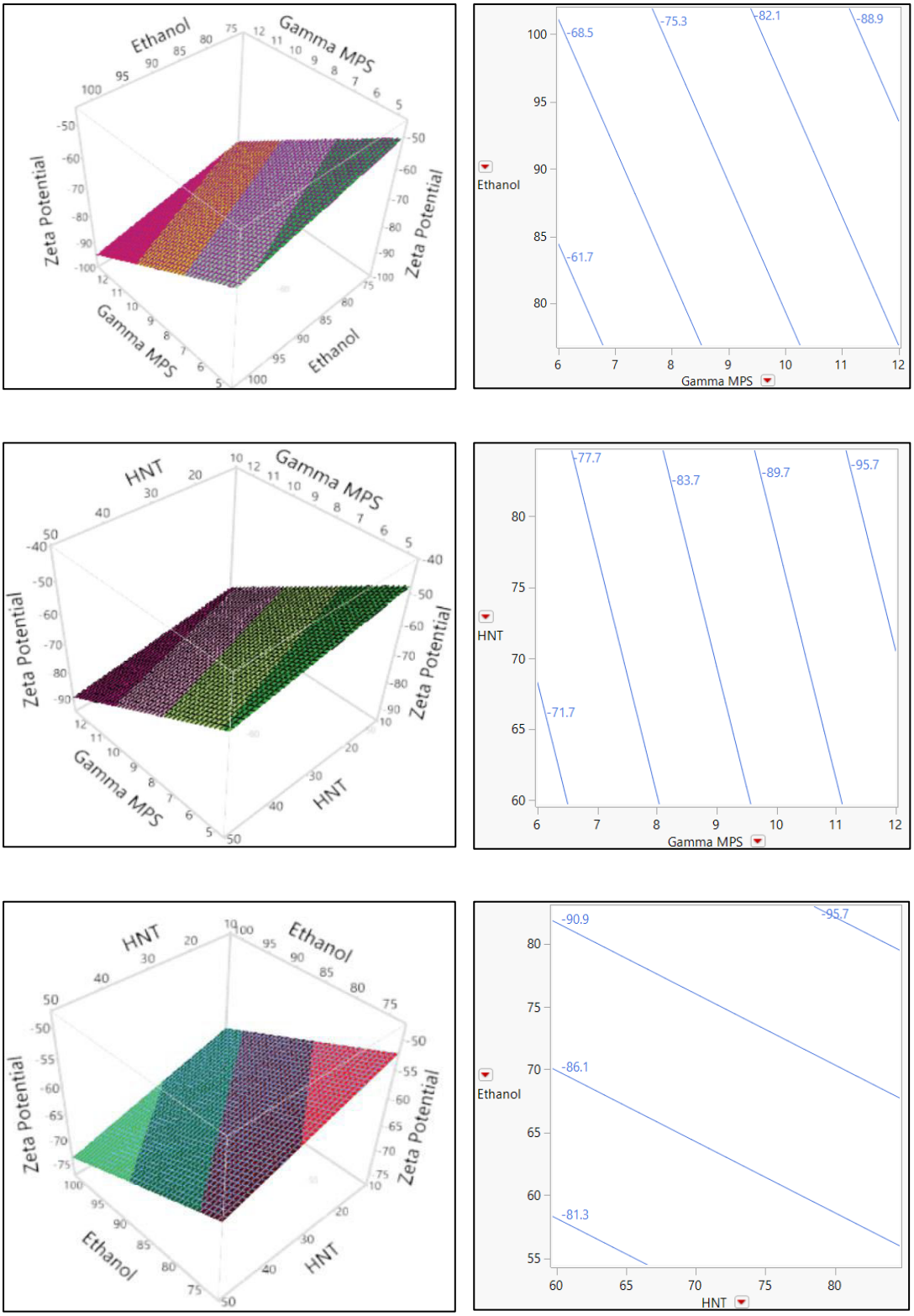

Figure 27: Surface and Contour Plots for the Response - Zeta Potential (Y_2)

4.1.6.8. Interpretation of Surface Plots for Y_2

The surface plots for the response Y_2 – Zeta Potential illustrated that, the zeta potential (mV) values of DHNTs decreased, with an increase in the concentration of all the three independent variables (X_1, X_2 and X_3). Thus, it could be potentially stated that, all the three variables exhibited a significant impact on response Y_2.

4.1.7. Statistical Optimization of DHNTs

The optimized formulation of DHNTs (ODHNTs) was designed and formulated in accordance with the obtained desirability values from the software.

4.1.8. Evaluation of ODHNTs for FTIR and X-RD Analysis

The formulated ODHNTs were evaluated for various characterization techniques and the data obtained for ODHNTs are shown in Table 18 - 19 and depicted in Figure 28 – 29.

Table 18: Evaluation of ODHNTs

Fourier Transform Infrared Spectroscopy				
Sample	**Frequency range (cm^{-1})**	**Peaks (cm^{-1})**	**Interpretation**	**Inference**
ODHNTs	700 - 745	734.2	Symmetric stretching of Si-O groups	ODHNTs were successfully doped
	910 - 925	910.19	Deformation of inner – OH groups	
	1025 - 1040	1033.46	Formation of Si-O-Si groups	
	1490 - 1495	1492.34	Scissoring of $–CH_2$ groups	
	2900 - 2930	2921.05	Symmetric stretching of CH_2 groups	
	1700 - 1720	1708.62	Stretching of C=O group	
	3600 - 3645	3631.09	-OH stretching of inner hydroxyl groups	
X-Ray Diffraction Analysis				
Sample	**Diffraction Angle (2θ)**	**d-spacing values (Å)**	**Characteristics of diffraction peak**	**Justification**
ODHNTs	12.02°	7.73 Å	Intense sharp broad peak	ODHNTs were successfully doped

Table 19: Thermal Characterization of ODHNTs

Thermo-gravimetric Analysis				
Sample	**First Peak**		**Second Peak**	
	Temperature (°C)	**Justification**	**Temperature (°C)**	**Justification**
ODHNTs	50 - 150°C	Evaporation of physically adsorbed water molecule	300 - 475 °C	Fragmentation of hydrogen bonds present in lumen of HNTs

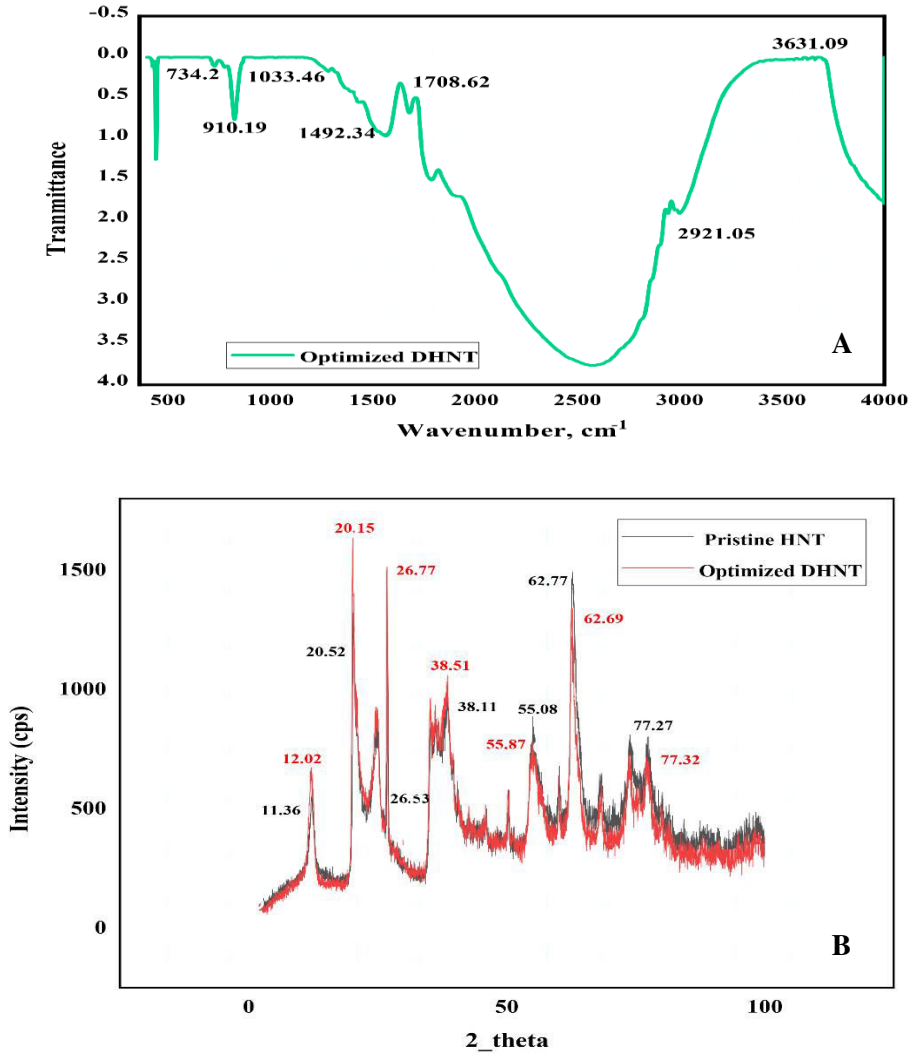

Figure 28: A. FTIR Spectrum of ODHNT and B. X-RD Pattern of ODHNT

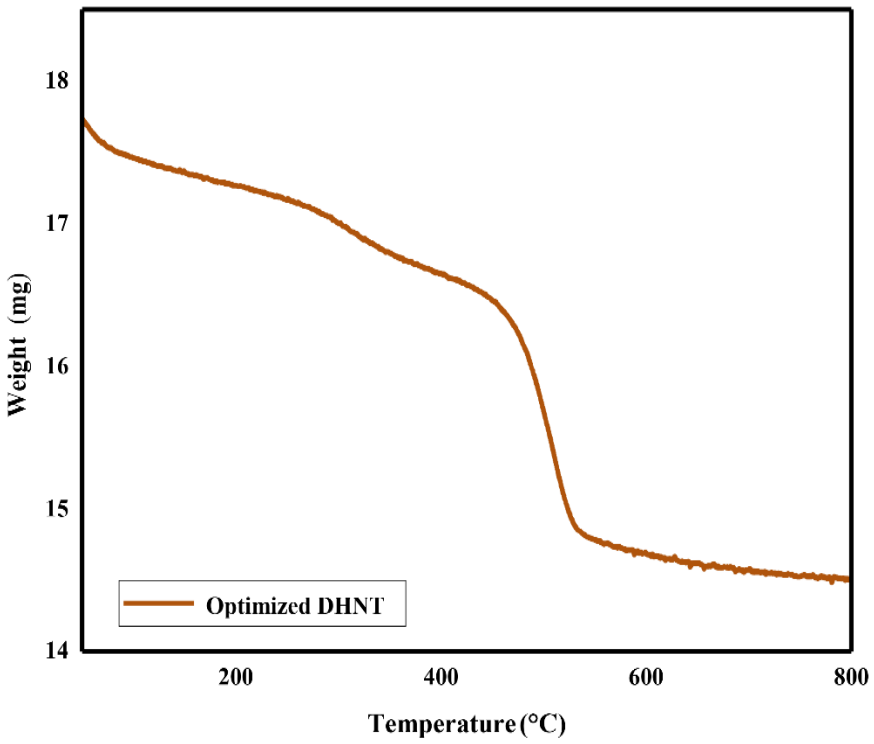

Figure 29: TGA Analysis of ODHNTs

4.1.8.1. SEM Analysis of ODHNTs

The morphological analysis of PHNTs and ODHNTs were characterized by Scanning Electron Microscopy (SEM). The SEM images of PHNTs and ODHNTs are depicted in Figure 30. The PHNTs lengths were relatively small with an irregular geometries. Furthermore, it was observed that these nanotubes were densely clumped together and they appeared as a cotton balls.

Subsequently, upon doping, the extent of nanotubes clumping was substantially decreased and these nanotubes were readily apparent with a promising dimensions.

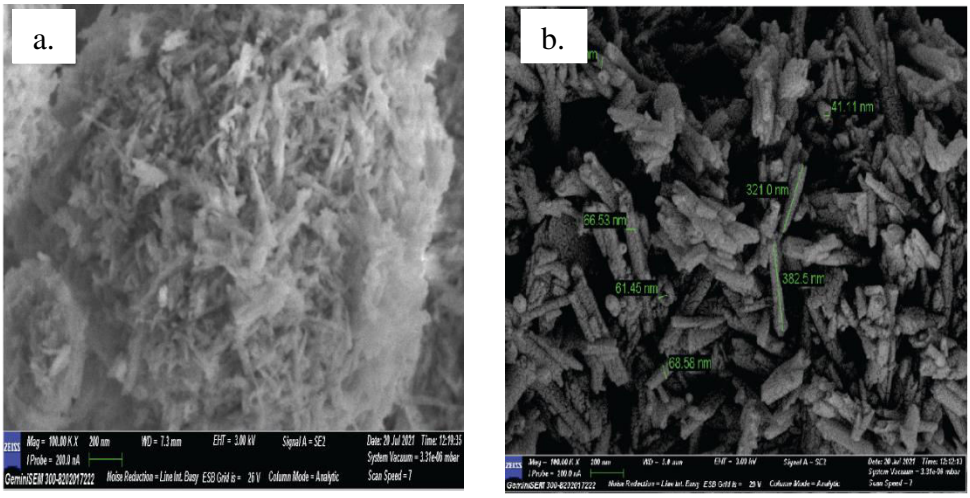

Figure 30: SEM Images of a. PHNTs and b. ODHNTs

4.1.8.2. Confirmatory Test

Confirmatory test was carried out to ensure the validity of predicted responses derived from the ideal configurations of indepenent factors (X_1 = 9 ml, X_2 = 37.5 g, X_3 = 87.5 ml). The ODHNTs were analysed for diffraction angle (Y_1) and zeta potential (Y_2) and the results of experimental findings were correlated with estimated outcomes as presented in Table 20. The percentage error (%) was determined for the each and every responses, to ensure the accuracy of designed experimental study.

The % error was calculated using the equation

$$\% \text{ Error} = \frac{(\text{Actual value} - \text{Predicted value})}{\text{Actual Value}} * 100$$

Table 20: Response Values of Predicted, Actutal and Percentage Error

Responses	Predicted values	Actual values	% Error
Diffraction angle (2θ)	11.75	12.02	2.24 %
Zeta potential (mV)	-76.34	-79.25	3.67 %

In accordance with the data presented in Table 20, it was evident that both the response variables, exhibited percent error (%) values lower than 5%. The total

desirability was determined to be D = 0.998 using the desirability curve as shown in Figure 31.

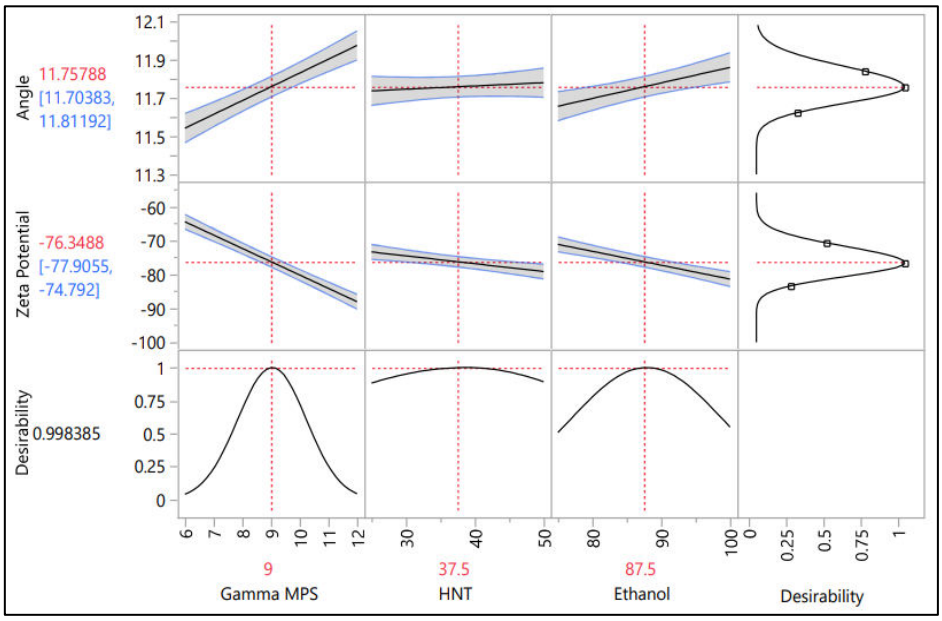

Figure 31: Desirability Curve for the Optimization of Process Parameters

4.2. STRATEGY 2:

FABRICATION OF CIPROFLOXACIN HYDROCHLORIDE LOADED DOPED HNTs SPONGES

4.2.1. Physico-Chemical Characterization of Pure Cip HCL

4.2.1.1. Melting Point of Cip HCl

The melting of Cip HCl was found to be 320 °C, which was within the specified range 293.15 °C - 323.15 °C as per IP.

4.2.1.2. Determination of λ max

The maximum absorption of Cip HCl was determined using UV spectrophotometer. The absorption spectra of Cip HCl revealed only one absorption peak at 271 nm as depicted in Figure 32, which represented the maximum absorption (λ max) of Cip HCl.

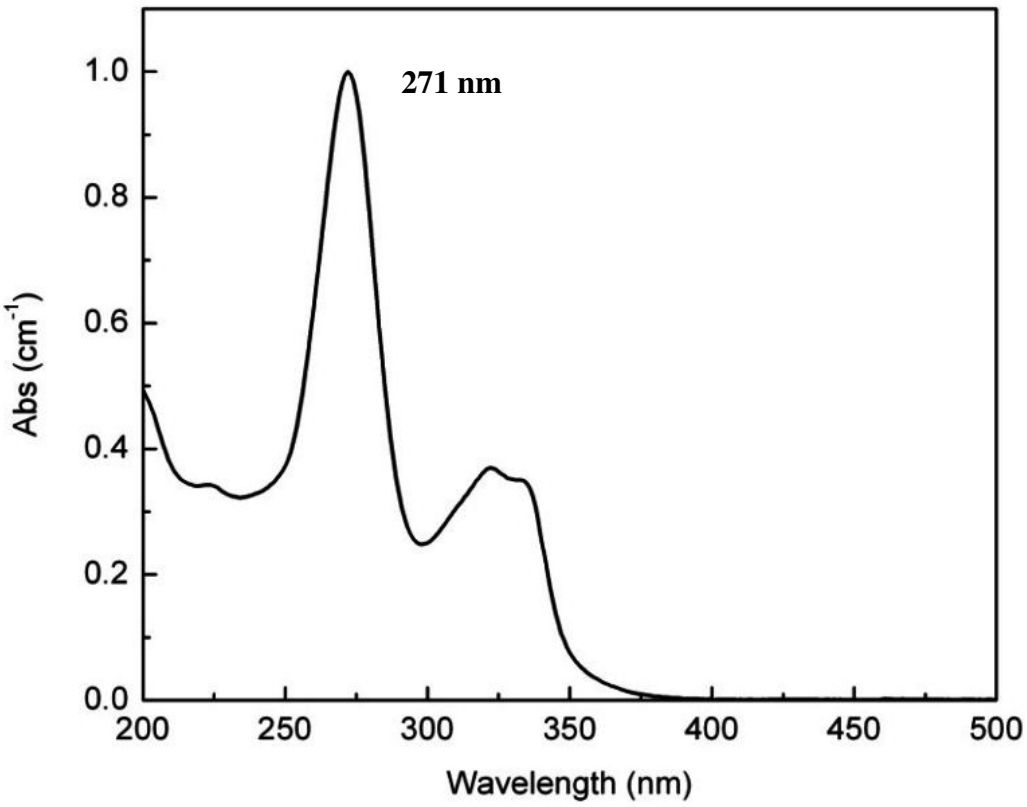

Figure 32: Absorption Maxima of Cip HCl

4.2.1.3. Calibration Curve of Cip HCl

Calibration curve of Cip HCl was carried out using UV absorption spectrophotometer. A linear regression curve was derived by plotting concentration (µg/ml) on x-axis and absorbance (nm) on y-axis as depicted in Figure 33. The linearity curve yielded a regression coefficient (R^2) = 0.994 over the range of 2 – 10 µg/ml at 271 nm. The various components and the data for calibration curve are presented in Table 21 - 22.

Table 21: Components of Calibration Curve

Components	UV Measurements
λ max	271 nm
Beer's Range	2 – 10 µg/ml
Regression Equation	y = 0.106x + 0.038
Regression Co-efficient (R^2)	R^2 = 0.994

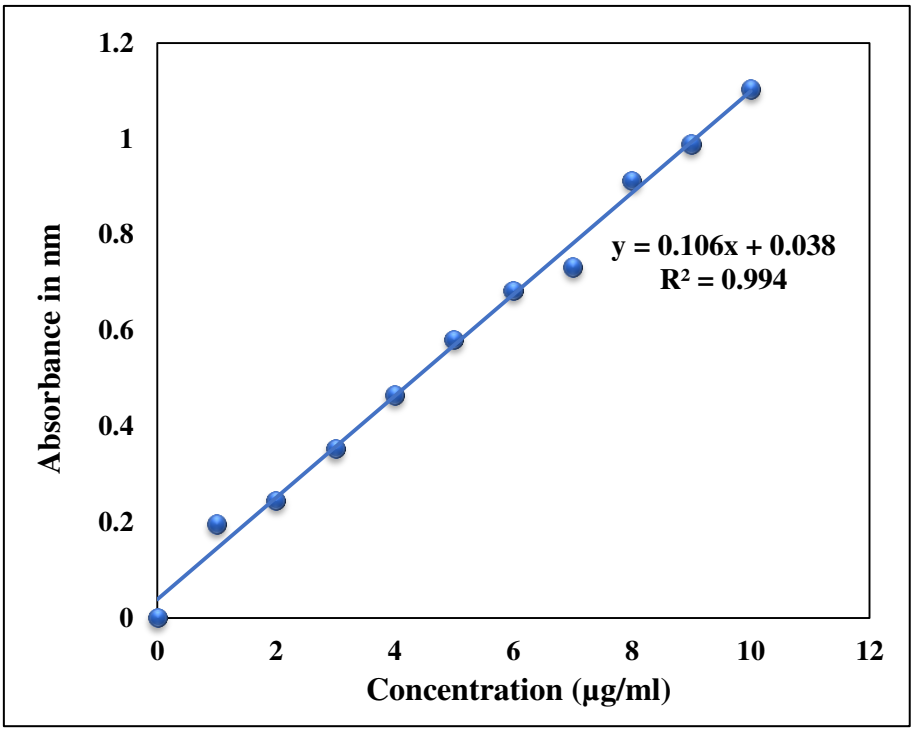

Figure 33: Calibration Curve of Cip HCl

Table 22. Data for Standard Calibration Curve of Ciprofloxacin Hydrochloride at 271 nm

Flask No	Volume of SS-II (ml)	Volume made upto	Concentration (µg/ml)	Absorbance at 271 nm Average ± SD n=3	Co-efficient of Variation
1	0.1	10 ml with 7.4 pH Phosphate Buffer	1	0.1952 ± 0.003055	0.209
2	0.2		2	0.2449 ± 0.004359	0.123
3	0.3		3	0.3528 ± 0.001858	0.582
4	0.4		4	0.4651 ± 0.003621	0.342
5	0.5		5	0.5809 ± 0.002947	0.256
6	0.6		6	0.6832 ± 0.003086	0.601
7	0.7		7	0.7318 ± 0.000924	0.401
8	0.8		8	0.9125 ± 0.000153	0.356
9	0.9		9	0.9886 ± 0.000252	0.306
10	1.0		10	1.1039 ± 0.001548	0.215

4.2.1.4. FT-IR Spectroscopic Analysis

The FT-IR spectrum of pure Cip HCl was recorded as illustrated in Figure 34. The characteristics functional groups were analyzed and interpreted in compliance with the structure of pure drug. The FT-IR spectrum revealed the presence of prominent peaks as shown in Table 23, which were exactly similar to the functional groups of Cip HCl as reported in the literature. Hence, it can be said the sample was Cip HCl, indicating the purity of sample.

Table 23: Characteristic Peaks in the FT-IR Spectrum of Pure Cip HCl

Functional groups	**Actual wave number (cm^{-1})**	**Observed wave number (cm^{-1})**
-OH Stretching	3500 - 3450	3524.49
N-H Stretching	3400 - 3300	3374.78
Aromatic CH Stretching	3000 - 2650	2683.01
C=O Stretching	1750 - 1700	1701.53
-OH Bending	1300 - 1250	1265.79
Quinolones	1650 - 1600	1607.24
C-F Stretching	1150 - 1000	1022.92

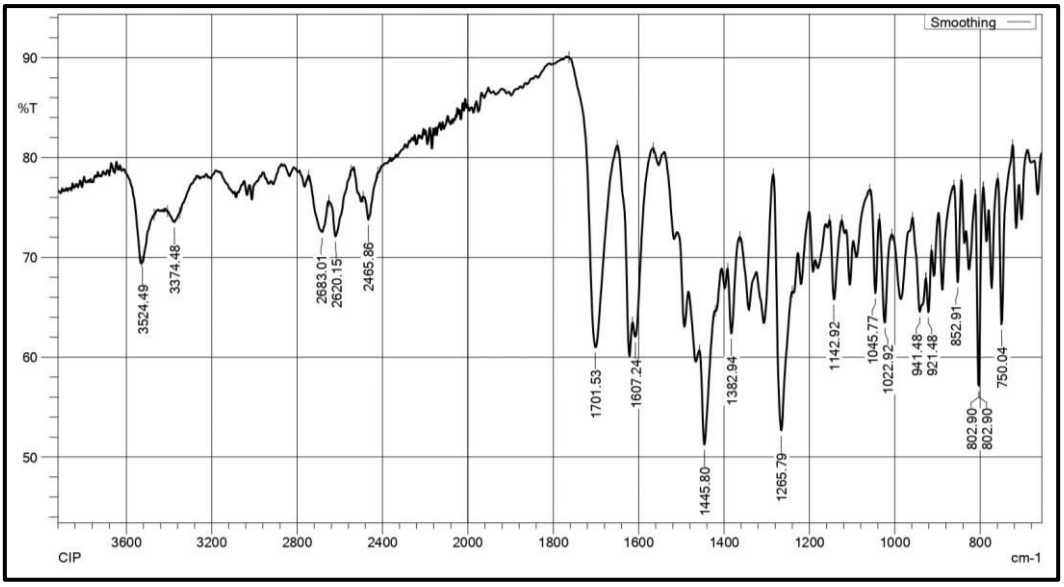

Figure 34: FT-IR Spectrum of Pure Cip HCl

4.2.1.5. DSC Analysis

The DSC curve of pure Cip HCl was within the standard range of IP (293.15 °C - 323.15 °C). The pure Cip HCl was characterized by a single, sharp endothermic peak at 321.82 °C, which was corresponded to the melting point of the pure Cip HCl. The DSC curve of pure Cip HCl was depicted in Figure 35.

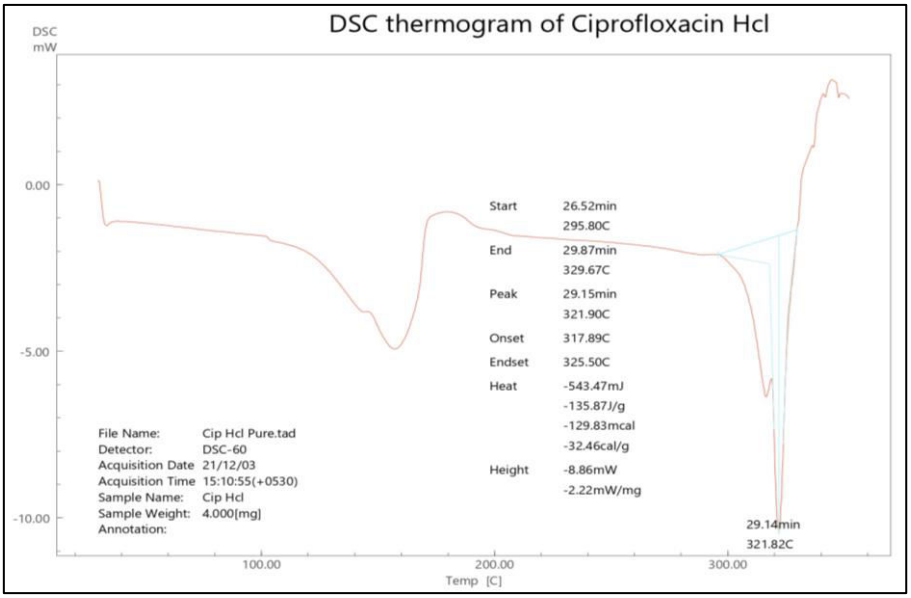

Figure 35: DSC Curve of Pure Cip HCl

4.2.2. Encapsulation of Cip HCl in DHNTs

The mesoporous tubular structure of HNTs with different inner and outer surface chemistry favors in encapsulating a wide variety of guest molecules (An antibiotic - Cip HCl). The most widely accepted strategy in encapsulating / loading an anti-bacterial drug Cip HCl into DHNTs includes: intercalation and vacuum / tubular entrapment assisted by homogenization, sonication and lyophilization technique. The results of encapsulation efficiency (%) for the ratios of 1:1, 1:2, 1:3 and 1:4 with respect to different loading techniques were presented in Table 24.

The data obtained from the Table 24 revealed that, the % encapsulation efficiency of Cip HCl by sonication method for 1:3 ratio was significantly increased to 98.70% as compared to homogenization and lyophilization technique in 7.4 pH phosphate buffer and confirmed the successful encapsulation of Cip HCl within the lumen of DHNTs.

Thus, in considerations with the findings of % encapsulation efficiency, 1:3 ratio was selected as an optimum ratio in the design of formulation table for the fabrication of lyophilized sponges.

Table 24: Encapsulation Efficiency of Cip HCl by Various Techniques

S. No	Sample	Ratio	Method	Encapsulation efficiency (%)
1	H1	1:1	Homogenization	29.76
2	H2	1:2	Homogenization	33.50
3	H3	1:3	Homogenization	35.15
4	H4	1:4	Homogenization	33.27
5	L1	1:1	Lyophilization	51.73
6	L2	1:2	Lyophilization	52.34
7	L3	1:3	Lyophilization	54.40
8	L4	1:4	Lyophilization	53.24
9	S1	1:1	Sonication	96.68
10	S2	1:2	Sonication	98.46
11	S3	1:3	Sonication	98.70
12	S4	1:4	Sonication	98.12

4.2.3. Fabrication of Lyophilized Sponges

The Cip HCl loaded DHNTs lyophilized sponges with different concentrations of polyox were prepared. The sponges of each batch formulations were white to off-white in color with a circular shape. The developed sponges were smooth and soft in appearance with an interconnected porous structure and fibrous in nature. The digital images of sponges were shown in Figure 36.

SF1 Sponge	SF2 Sponge	SF3 Sponge

Figure 36: Digital Photographs of Sponge Formulations

4.2.4. Evaluation of Sponges

4.2.4.1. Drug Excipient Compatibility Studies

1. DSC Studies

The DSC curves for each batch of sponge formulations were recorded and illustrated in Figure 37. The distinct sharp peak for Cip HCl was observed in the DSC thermograph of each batch of sponge formulation. The DSC curves of all the three sponge formulations revealed no significant change in the endothermic peak of Cip HCl, indicating the compatibility between drug and selected excipients. The interpretation of DSC thermo-grams were shown in Table 25.

Table 25: Interpretation of DSC Thermo-grams

S No	Sample	Melting Temperature (°C)	Characteristics of Peak	Significance
1	ODHNT	63.15 °C	Broad peak	Melting point of ODHNTs
2	SF1	59.89 °C	Slightly broad endothermic peak	Melting point of DHNTs
		64.39 °C	Slightly broad endothermic peak	Melting point of Polyox
		315.64 °C	Small sharp endothermic peak	Melting point of Cip HCl
3	SF2	57.00 °C	Slightly broad endothermic peak	Melting point of DHNTs
		62.43 °C	Small broad endothermic peak	Melting point of Polyox
		315.31 °C	Slightly sharp endothermic peak	Melting point of Cip HCl
4	SF3	57.59 °C	Slightly sharp endothermic peak	Melting point of DHNTs
		64.07 °C	Slightly sharp endothermic peak	Melting point of Polyox
		312.05 °C	Small sharp endothermic peak	Melting point of Cip HCl

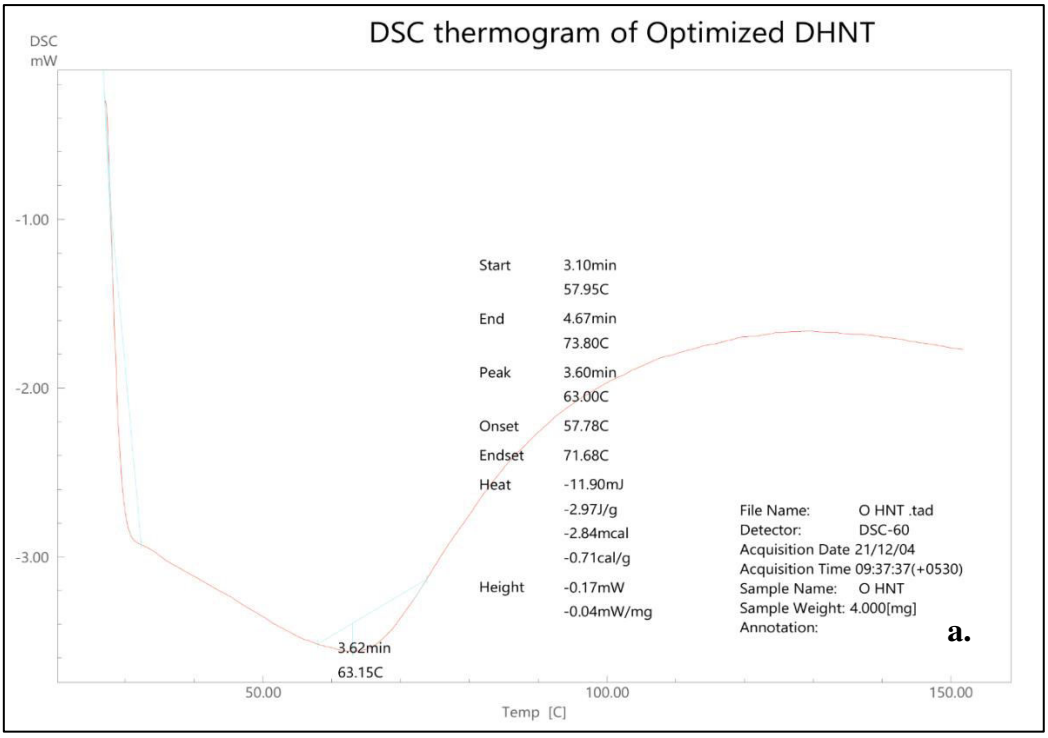
DSC thermogram of Optimized DHNT
DSC
mW
-1.00
-2.00
-3.00
Start 3.10min
57.95C
End 4.67min
73.80C
Peak 3.60min
63.00C
Onset 57.78C
Endset 71.68C
Heat -11.90mJ
-2.97J/g
-2.84mcal
-0.71cal/g
Height -0.17mW
-0.04mW/mg
File Name: O HNT .tad
Detector: DSC-60
Acquisition Date 21/12/04
Acquisition Time 09:37:37(+0530)
Sample Name: O HNT
Sample Weight: 4.000[mg]
Annotation:
3.62min
63.15C
50.00
100.00
150.00
Temp [C]
a.

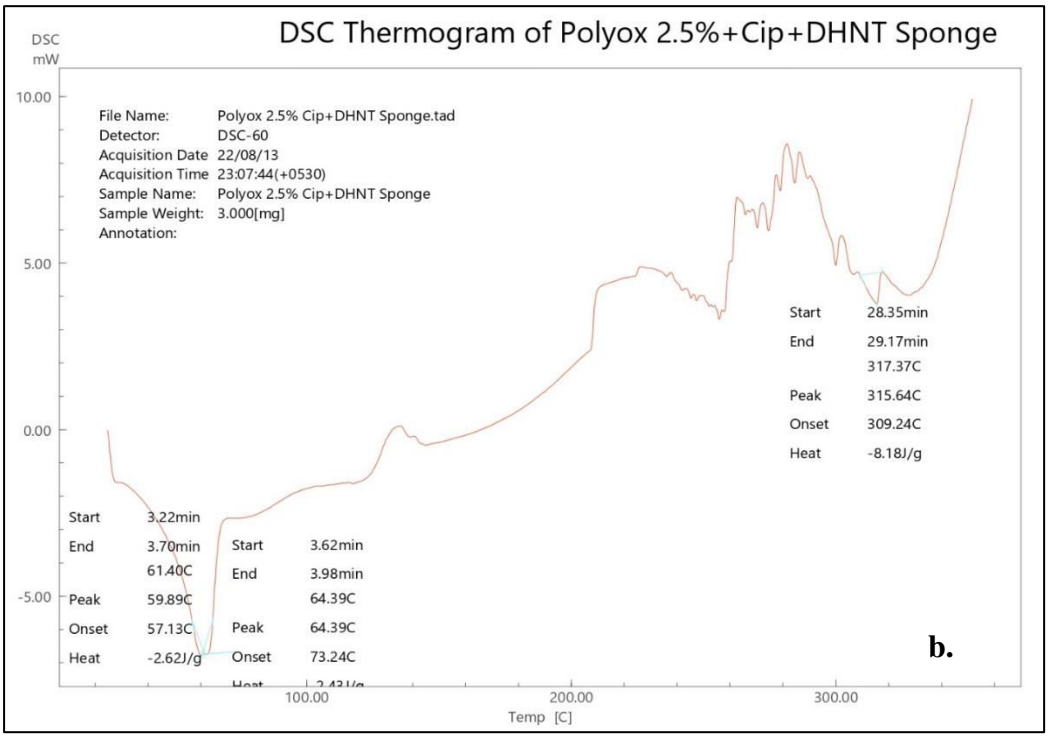
DSC Thermogram of Polyox 2.5%+Cip+DHNT Sponge
DSC
mW
10.00
5.00
0.00
-5.00
File Name: Polyox 2.5% Cip+DHNT Sponge.tad
Detector: DSC-60
Acquisition Date 22/08/13
Acquisition Time 23:07:44(+0530)
Sample Name: Polyox 2.5% Cip+DHNT Sponge
Sample Weight: 3.000[mg]
Annotation:
Start 28.35min
End 29.17min
317.37C
Peak 315.64C
Onset 309.24C
Heat -8.18J/g
Start 3.22min
End 3.70min
61.40C
Peak 59.89C
Onset 57.13C
Heat -2.62J/g
Start 3.62min
End 3.98min
64.39C
Peak 64.39C
Onset 73.24C
100.00
200.00
300.00
Temp [C]
b.

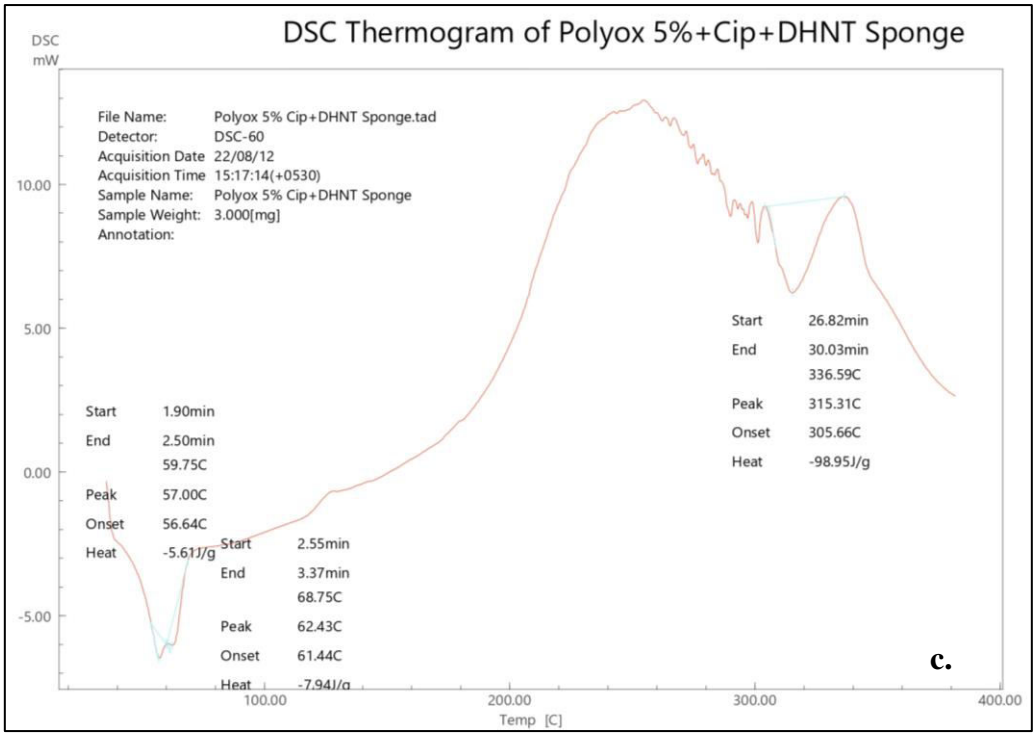

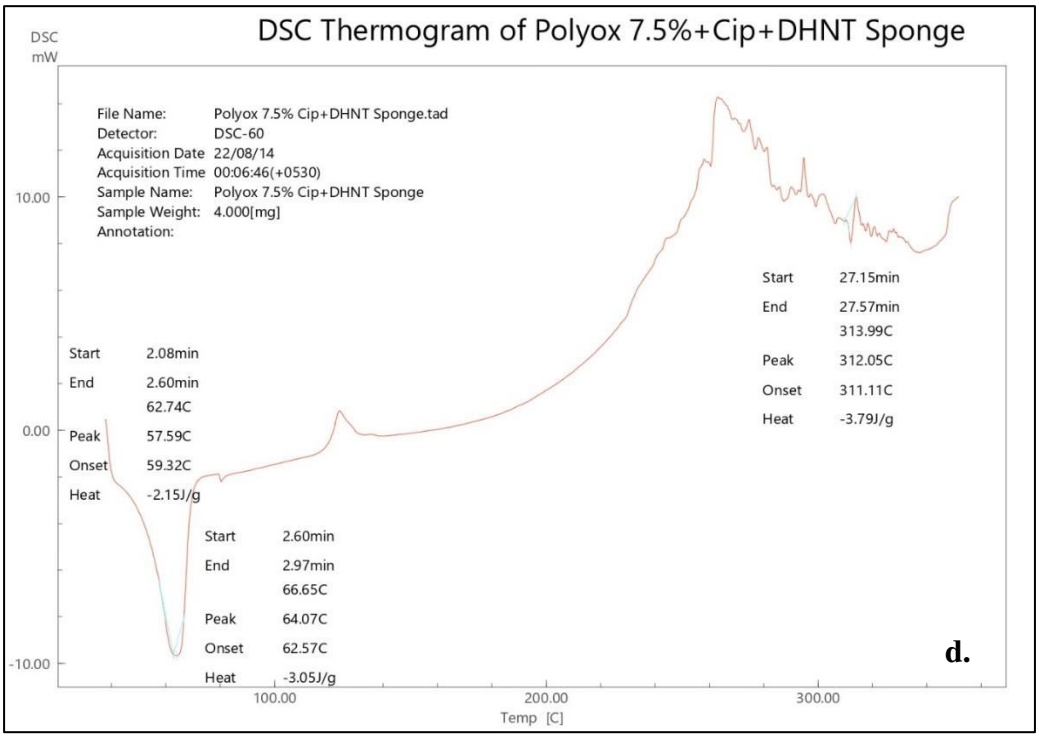

Figure 37: DSC Curves of a. ODHNT, b. SF1 Sponge, c. SF2 Sponge and d. SF3 Sponge Formulation

2. FT-IR Spectroscopic Studies

The FT-IR spectra of all the three sponge formulations were analyzed and recorded as illustrated in Figure 38 - 40. The IR spectra of each sponge formulation showed, the presence of all the characteristics peaks of Cip HCl. The peaks appeared revealed no change in the functional groups of Cip HCl in sponge formulations, signifying the compatibility of Cip HCl with the added excipients. Thus it can be concluded that, the selected excipients used in the preparation of sponges were compatible with Cip HCl.

The important characteristics peaks of drug in sponge formulations are enlisted in Table 26.

Table 26: FT-IR Spectral Data of Sponge Formulations

Functional groups	Frequencies (cm^{-1})			
	Pure Drug (Cip HCl)	Sponge formulations		
		SF1	SF2	SF3
-OH Stretching	3524.49	3528.27	3526.04	3527.14
N-H Stretching	3374.78	3375.02	3373.65	3375.28
Aromatic CH Stretching	2683.01	2684.07	2683.38	2684.51
C=O Stretching	1701.53	1705.07	1702.25	1705.18
-OH Bending	1265.79	1277.22	1278.64	1278.64
Quinolones	1607.24	1608.17	1608.3	1607.42
C-F Stretching	1022.92	1022.2	1022.57	1028.63

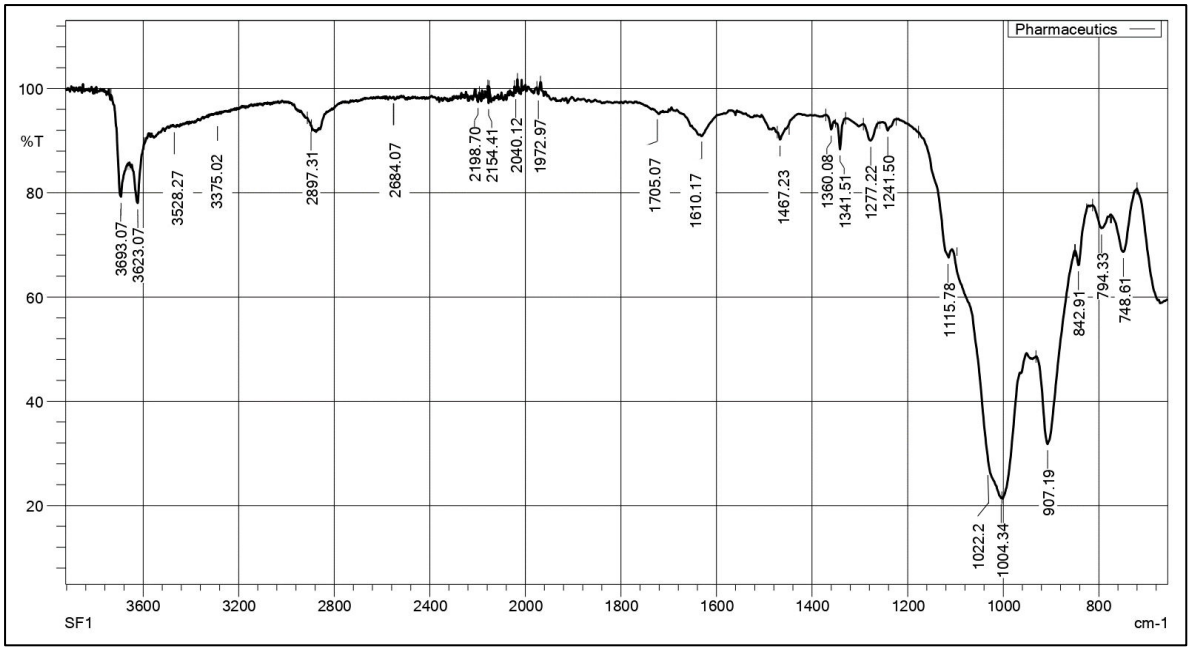

Figure 38: FTIR Spectrum of SF1

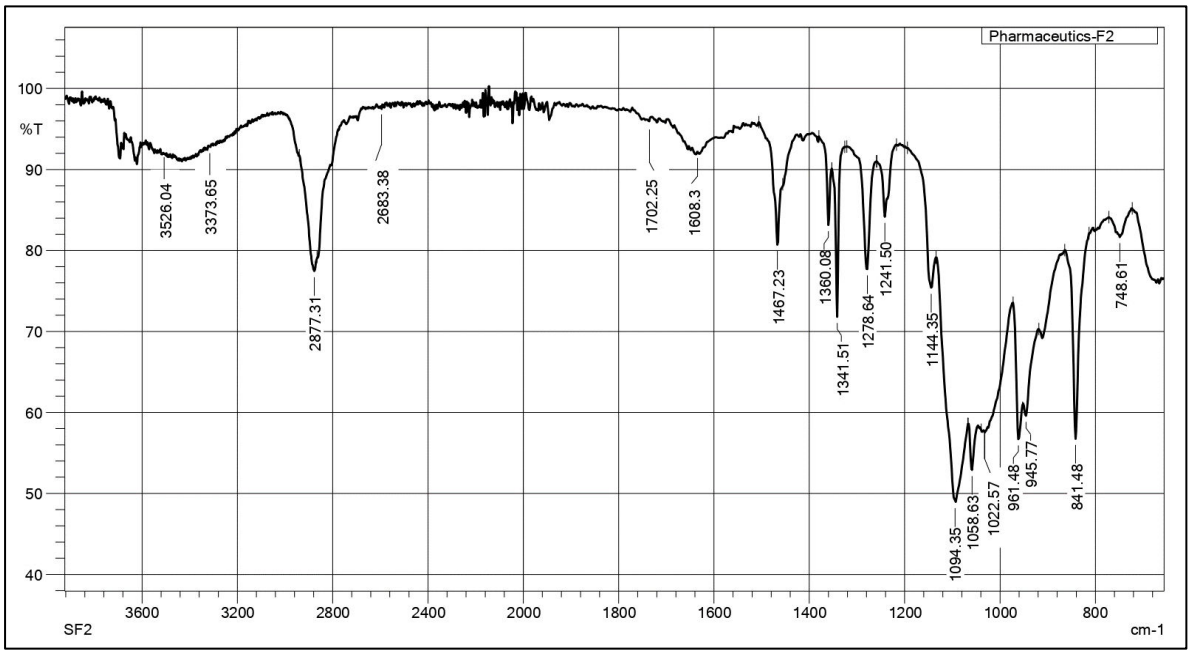

Figure 39: FTIR Spectrum of SF2

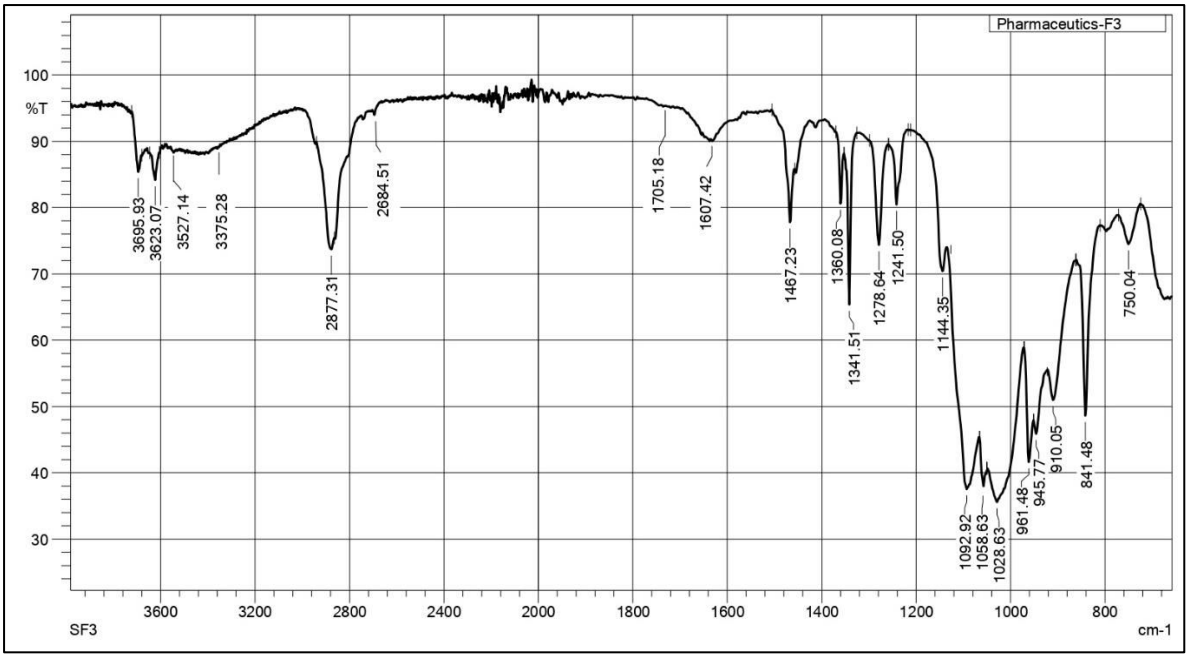

Figure 40: FTIR Spectrum of SF3

4.2.4.2. Diameter, Thickness and pH of Sponges

The diameter and thickness of each sponge formulations were measured and recorded as shown in Table 27. The diameter of sponges varied from 40.01 ± 0.02 mm to 42.05 ±0.03 mm, whereas, thickness of the sponges ranged between 2.2 ± 0.06 mm to 2.5 ± 0.01 mm. The pH of sponge formulations ranged from 6.8 ± 0.02 to 7.2 ± 0.03.

The results of thickness and diameter measurements confirmed the homogeneity and consistency of sponges, signifying the reproducibility of the method adopted in the preparation of sponges.

Table 27: Diameter, Thickness and pH Measurements of Sponges

Formulation	Diameter (mm)	Thickness (mm)	pH
SF1	40.01 ± 0.02	2.3 ± 0.03	6.8 ± 0.02
SF2	40.00 ± 0.01	2.2 ± 0.02	7.2 ± 0.03

SF3	42.05 ± 0.03	2.5 ± 0.01	6.9 ± 0.01

4.2.4.3. Wetness Integrity

The findings of wetness integrity analysis suggests the physical stability of sponges, when associated with or comes in contact with the discharge fluids or blood. The modifications in the structural framework of sponges like softness or gel formation or the structural deformation of polymers and the detachment or removal of sponge from the wound area implicates the simplicity of patient adherence.

The digital images captivated during wetness integrity test indicated the instant formation of patch on gel and thereby ensuring the easy removal of dressing material from the site of application. The images of wetness integrity test are depicted in Figure 41.

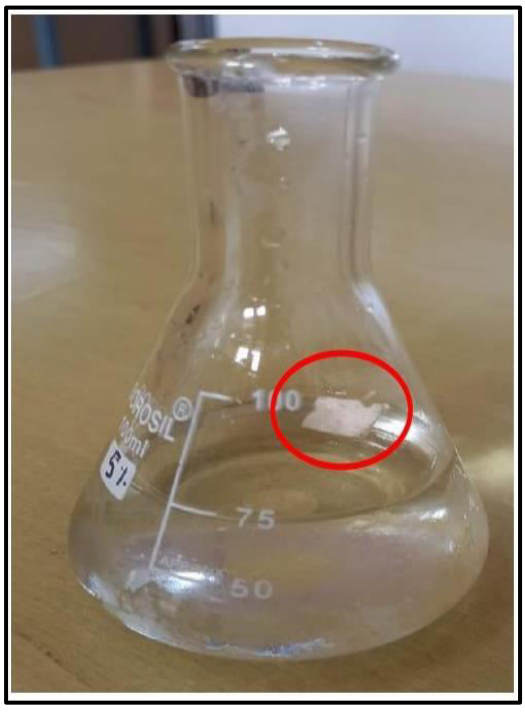

At 0 second

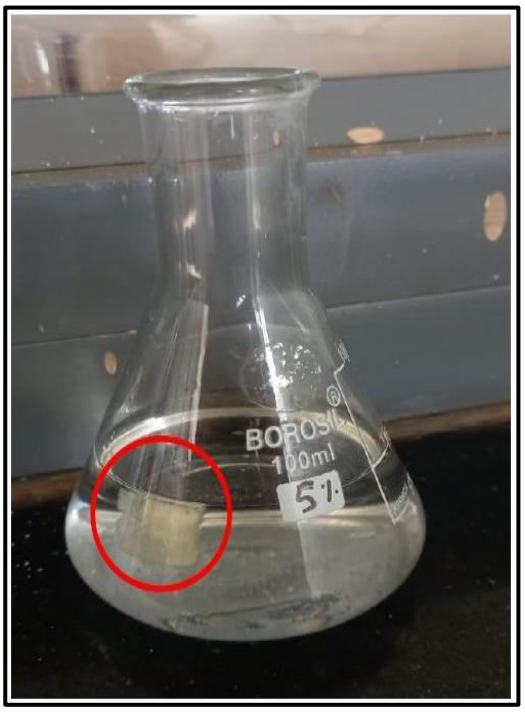

At 60 second

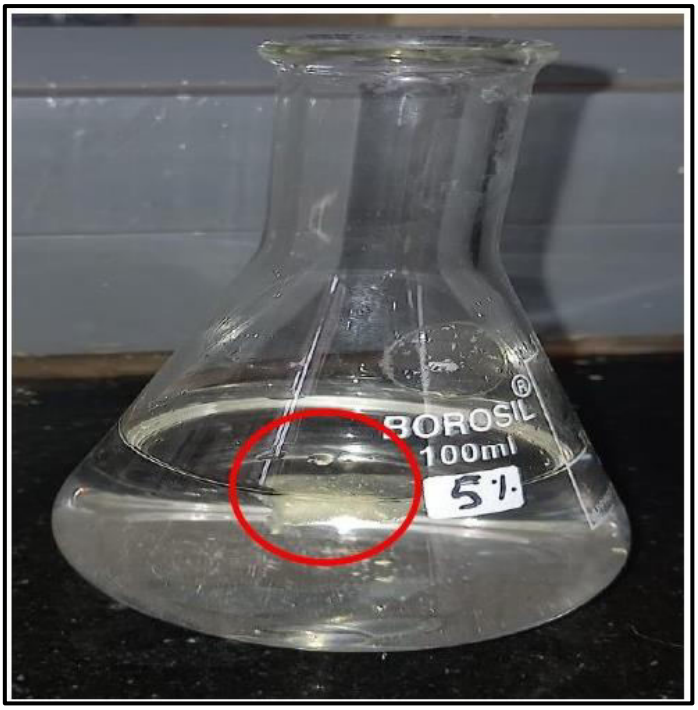

Figure 41: Wetness Integrity of Sponges

4.2.4.4. Swelling Index of Sponges

The tendency of spongy dressing material to absorb the fluid under normal physiological conditions is referred to swelling index. The swelling nature/ behaviour of the sponges played an important role in wound healing activity, as it helps in absorbing wound exudates by promoting the exchange of nutrients and medium for the cells during the progression of new tissue formation.

The swelling index of sponges comprised with three different concentrations of polyox polymer was depicted in Figure 42. The incorporation of 2.5 % of PEO in SF1 sponges presented a swelling index of 78.24 %. Similarly, with an increased concentration of PEO to 5 % and 7.5 % in SF2 and SF3 sponge formulations, the degree of swelling index was increased to 85.04 % and 93.78 %.

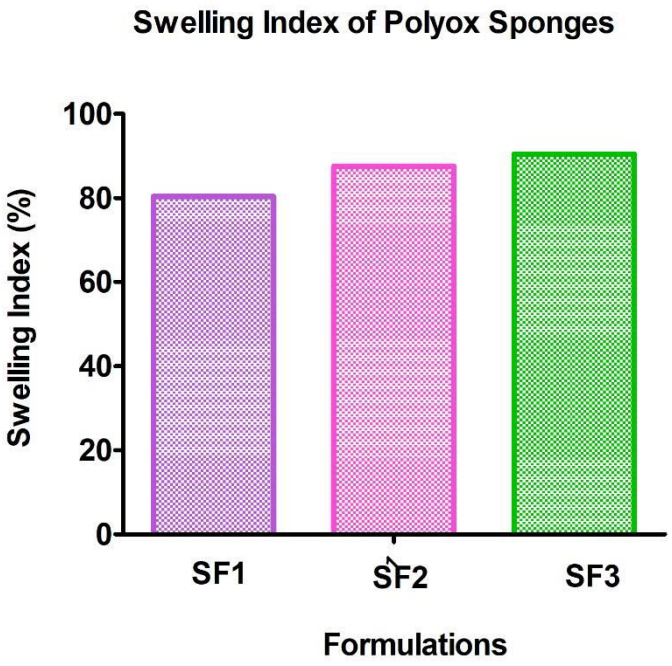

Figure 42: Swelling Index of Sponge Formulations

4.2.4.5. Compressive Properties of Sponges

Compressive properties also known as mechanical strength is defined as the structural stability and integrity of sponges. Compressive properties have played an important role in the design of tissue engineering sponges, as it is essential to determine the capability of sponges to withstand the load incurred during *in vitro* cultivation and regeneration of new tissues.

The results of ultimate tensile strength, elastic modulus and % break strain values of fabricated sponges with varied compositions of PEO were shown in Table 28.

The data obtained from the compressive strength analysis of sponges revealed that, the mechanical properties of SF2 sponges were identical to the native skin structure.

Hence, SF2 formulation was considered as an ideal formulation of tissue engineering applications. The graphical presentation of mechanical properties of sponges are depicted in Figure 43.

Table 28: Compressive Properties of Sponges

Formulation	Mechanical Properties		
	Ultimate Tensile Strength (N/mm^2)	**Elastic Modulus (N/mm^2)**	**Break Strain (%)**
SF1	0.19	30.3	5.09
SF2	0.33	6.15	48.4
SF3	0.18	3.52	66.0

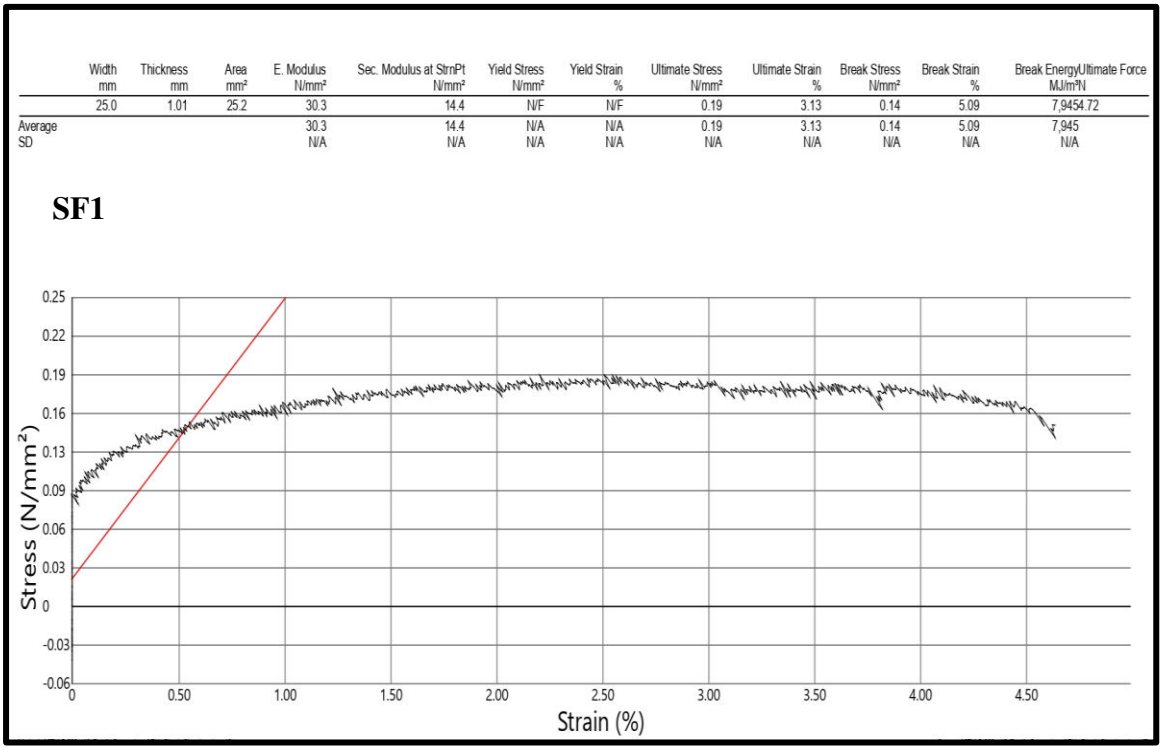

	Width mm	Thickness mm	Area mm²	E. Modulus N/mm²	Sec. Modulus at StrnPt N/mm²	Yield Stress N/mm²	Yield Strain %	Ultimate Stress N/mm²	Ultimate Strain %	Break Stress N/mm²	Break Strain %	Break EnergyUltimate Force MJ/m³N
	25.0	2.01	50.3	6.15	6.10	N/F	N/F	0.33	26.0	0.09	48.4	128,62916.7
Average				6.15	6.10	N/A	N/A	0.33	26.0	0.09	48.4	128,629
SD				N/A	N/A	N/A	N/A	N/A	N/A	N/A	N/A	N/A

SF2

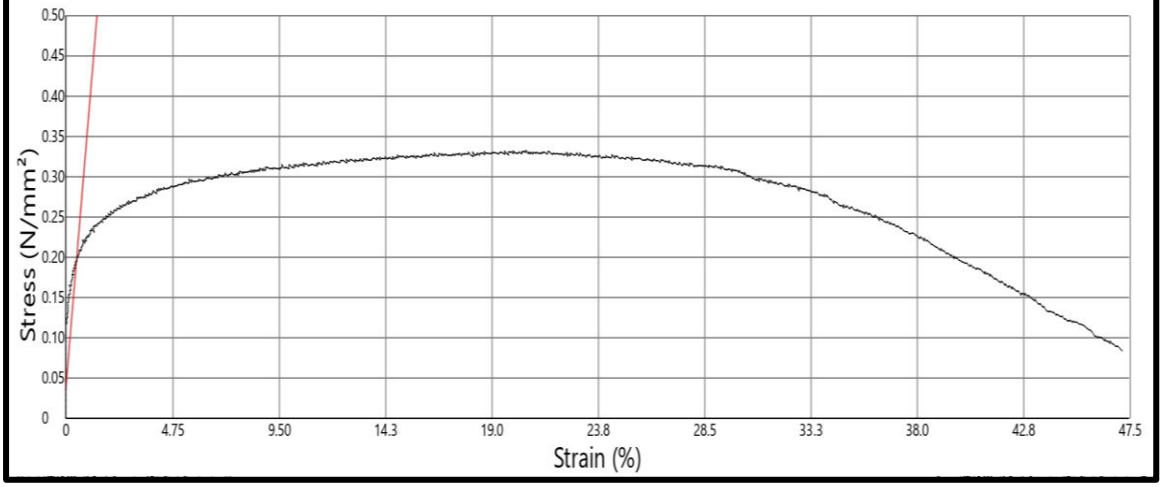

	Width mm	Thickness mm	Area mm²	E. Modulus N/mm²	Sec. Modulus at StrnPt N/mm²	Yield Stress N/mm²	Yield Strain %	Ultimate Stress N/mm²	Ultimate Strain %	Break Stress N/mm²	Break Strain %	Break EnergyUltimate Force MJ/m³N
	25.0	3.65	91.3	3.48	3.52	N/F	N/F	0.18	39.7	0.09	66.0	92,95116.1
Average				3.48	3.52	N/A	N/A	0.18	39.7	0.09	66.0	92,951
SD				N/A	N/A	N/A	N/A	N/A	N/A	N/A	N/A	N/A

SF3

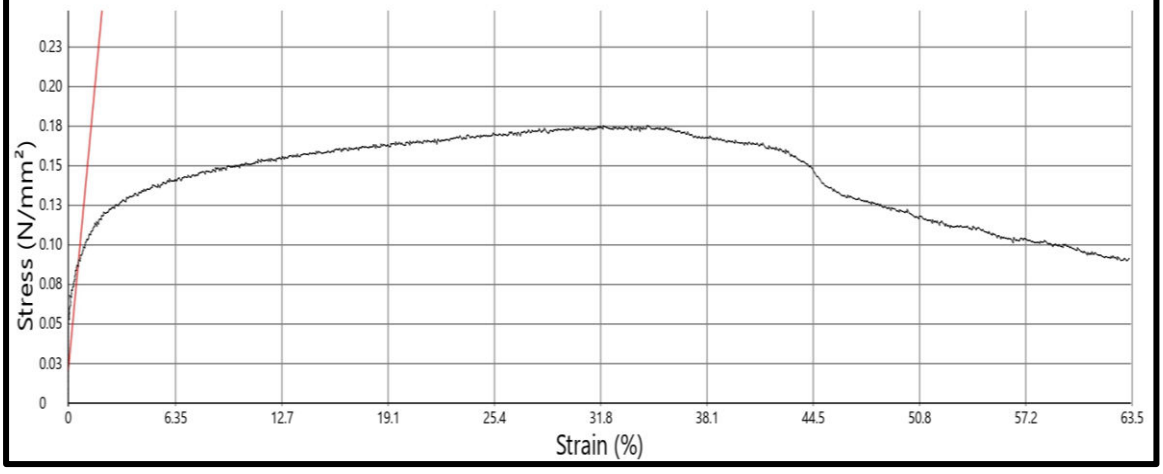

Figure 43: Compressive Properties of Sponge Formulations

4.2.4.6. Porosity of Sponges by BET Analysis

In an effort to develop an effective and functional sponge, the architecture and the structural framework of the sponge must be highly porous in nature with an appropriate interconnected network of pores. The interconnected pore matrix facilitates the transportation of vital nutrients and oxygen to the cells, promotes cellular attachments, growth and regeneration of new tissues and cells.

The data obtained from BET adsorption-desorption isotherms as depicted in Figure 44, confirmed that all the three sponge formulations exhibited Type IV isotherm with a distinct hysteresis loop of Type H3. The appearance of this particular type of isotherm represented a distinctive form of mesoporous materials with an average diameter of pore ranged between 2 – 50 nm. The experimental data derived from BET analysis were shown in Table 29.

Table 29: BET Values of Sponge Formulations

Formulation	Surface area (m^2/g)	Total pore volume (cc/g)	Average pore diameter (nm)	Isotherm
SF1	8.640	0.03449	14 - Mesoporous	Type IV
SF2	40.045	0.08449	8 - Mesoporous	Type IV
SF3	53.857	0.10761	5 - Mesoporous	Type IV

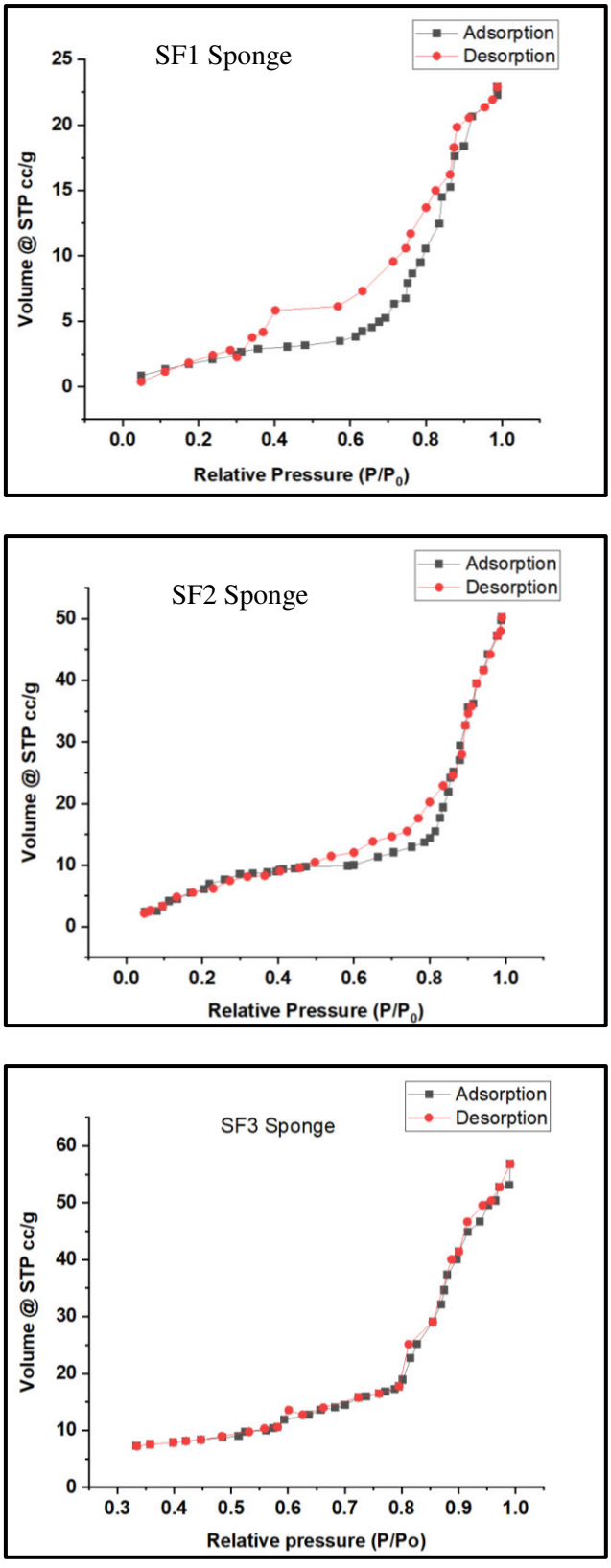

Figure 44: BET Isotherms of a. SF1, b. SF2 and c. SF3

4.2.4.7. Morphological Characterization with Elemental Analysis

The structural morphology of lyophilized Cip HCl – DHNTs polyox sponges (SF1, SF2 and SF3 formulations) were analyzed by SEM analysis. The SEM image of SF1 formulation as shown in Figure 45, exhibited an uneven oval shaped pores with an approximate pore size ranged between 30 – 50 µm and the porosity of SF1 sponge was observed to be 92.01 %. Similarly, the SF2 formulation presented an irregular shaped oval porous microstructure as depicted in Figure 46, having a pore size ranged between 25 – 40 µm, with a porosity of 84.25 %.

Whereas, SF3 formulation revealed that the pores were small with an uneven pore morphology. The pores were slightly interconnected with each other as illustrated in Figure 47, with a pore size varied between 15 – 20 µm. The porosity of SF3 sponge formulation resulted to be slightly significant with a porosity of 68.15 %. Thus, SEM micrographs of SF1 and SF2 formulations explicitly demonstrated that, these sponge formulations possessed a uniform and extensively interconnected pore arrangement with a pronounced porosity. In consistence to these findings, the EDX mapping and point analysis revealed the presence of Al and Si groups in all the three sponge formulations. The appearance of peaks for both Al and Si groups as shown in Figure 45 – 47, confirmed the existence of DHNTs in nanocomposites sponge formulations. Similarly, the increased peak intensities for C and O groups were mainly attributed to the presence polyox polymer. The elemental compositions of all the three sponge formulations are presented in Table 30 – 32.

a. b.

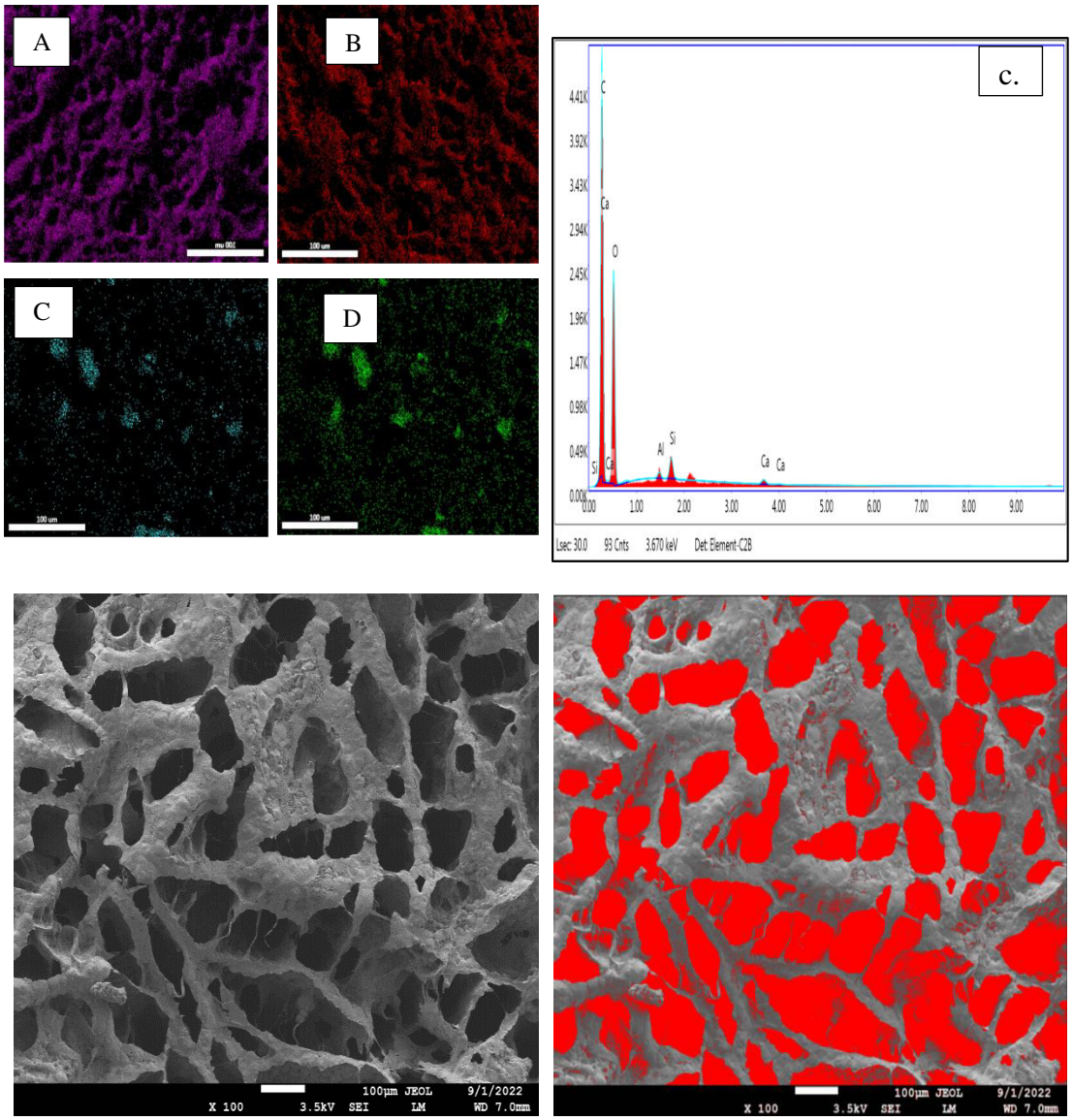
A
B
C
D
c.
C
Ca
O
Si
Al
Ca
Ca
Si
Ca
0.00 1.00 2.00 3.00 4.00 5.00 6.00 7.00 8.00 9.00
Lsec: 30.0 93 Cnts 3.670 keV Det: Element-C2B
100µm JEOL 9/1/2022
X 100 3.5kV SEI LM WD 7.0mm
100µm JEOL 9/1/2022
X 100 3.5kV SEI LM WD 7.0mm

Figure 45: SEM Image a. SF1 formulation b. Binary Thresholding image of SF1 formulation c. EDX point analysis and mapping of SF1 formulation (A. Carbon, B. Oxygen, C. Alumina, D. Silica groups)

Table 30: Elemental Composition of SF1 Sponge Formulation

Sample	Elemental composition (%)			
	Weight (%)			
SF1	C_K	O_K	Al_K	Si_K
	51.7	46.0	0.5	1.2
	Atomic (%)			
	59.3	39.6	0.2	0.6

a. b.

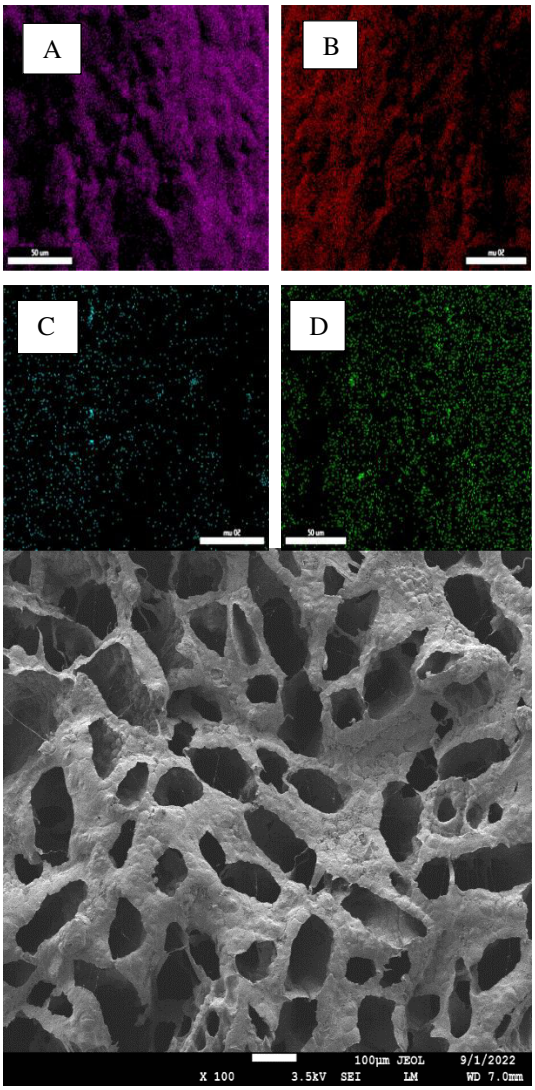
A
B
C
D
100µm JEOL 9/1/2022
X 100 3.5kV SEI LM WD 7.0mm

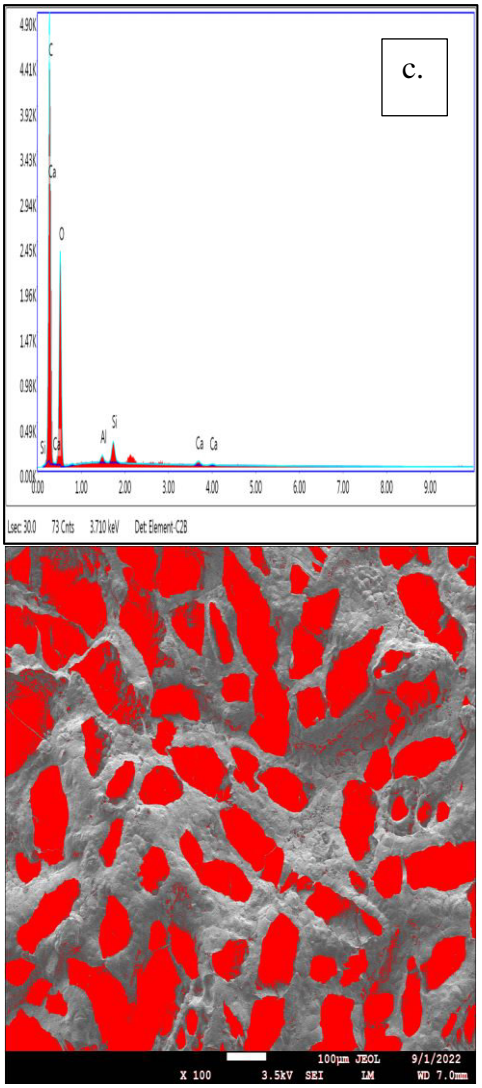
c.
C
Ca
O
Si
Al
Ca Ca
0.00 1.00 2.00 3.00 4.00 5.00 6.00 7.00 8.00 9.00
100µm JEOL 9/1/2022
X 100 3.5kV SEI LM WD 7.0mm

Figure 46: SEM Image a. SF2 formulation b. Binary Thresholding image of SF1 formulation c. EDX point analysis and mapping of SF2 formulation (A. Carbon, B. Oxygen, C. Alumina, D. Silica groups

Table 31: Elemental Composition of SF2 Sponge Formulation

Sample	Elemental composition (%)			
	Weight (%)			
SF2	C_K	O_K	Al_K	Si_K
	52.6	45.3	0.5	1.2
	Atomic (%)			
	60.2	38.8	0.2	0.6

a.

b.

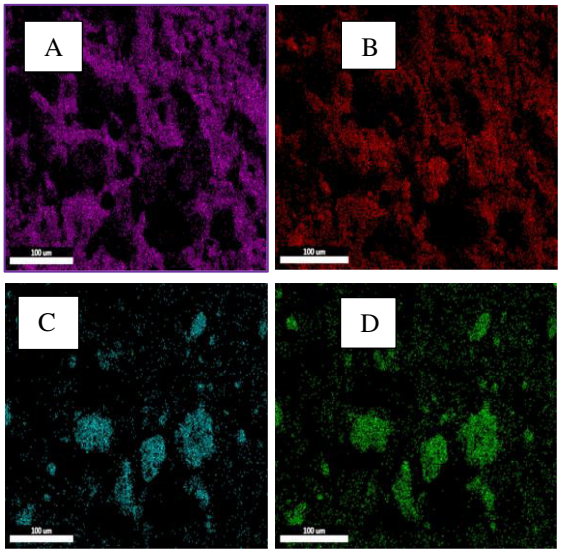
A
B
C
D

c.

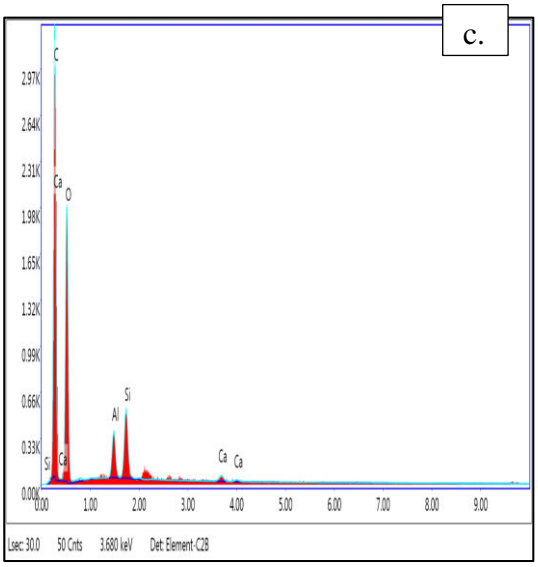
C
Ca
O
Si
Al
Ca
Ca
Si
Ca
0.00
1.00
2.00
3.00
4.00
5.00
6.00
7.00
8.00
9.00
Lsec: 30.0
50 Cnts
3.680 keV
Det: Element: C2B

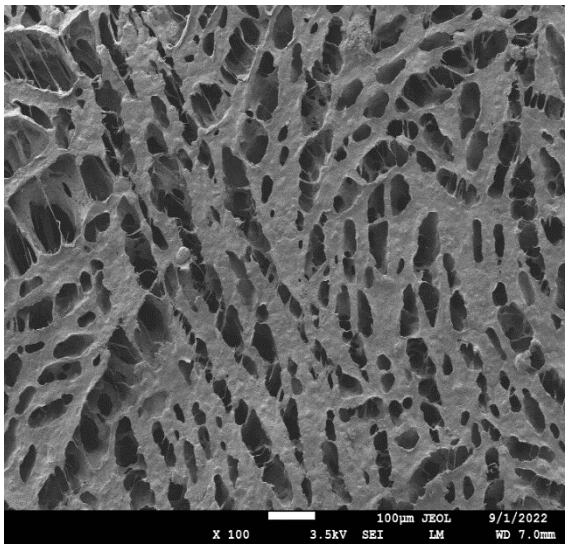
100µm JEOL 9/1/2022
X 100 3.5kV SEI LM WD 7.0mm

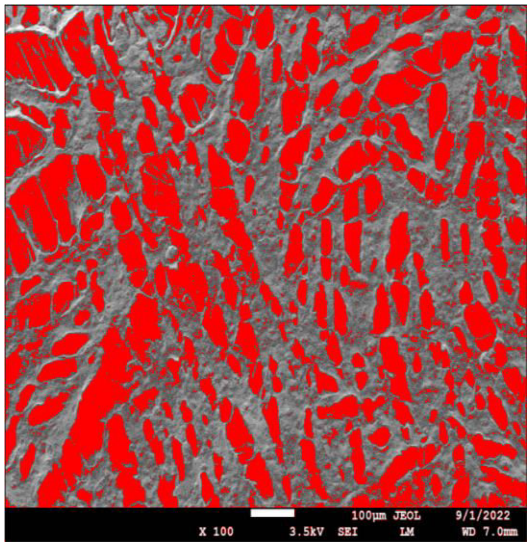
100µm JEOL 9/1/2022
X 100 3.5kV SEI LM WD 7.0mm

Figure 47: SEM Image a. SF3 formulation b. Binary Thresholding image of SF1 formulation c. EDX point analysis and mapping of SF3 formulation (A. Carbon, B. Oxygen, C. Alumina, D. Silica groups)

Table 32: Elemental Composition of SF3 Sponge Formulation

Sample	Elemental composition (%)			
	Weight (%)			
SF3	C_K	O_K	Al_K	Si_K
	52.6	45.3	0.5	1.2
	Atomic (%)			
	60.2	38.8	0.2	0.6

4.2.4.8. Drug Content

Drug content of Cip HCl in all the formulated sponges (SF1 to SF3) were in the range of 84.80 % ± 0.33 to 95.34 % ± 0.21. The drug content analysis was performed in triplicates and the mean as well as standard deviation values were calculated. The data obtained for drug content analysis was shown in Table 33.

Table 33: Drug Content Analysis of Sponge Formulation

Sponge Formulations	Drug Content (%)
SF1	87.47 ± 0.84
SF2	95.34 ± 0.21
SF3	84.80 ± 0.33

Data is expressed as mean ± SD (n = 3)

4.2.4.9. *In Vitro* Diffusion Profile of Sponge Formulations

The *in vitro* diffusion profile of Cip HCl – DHNTs polyox sponges were carried out in 7.4 pH phosphate buffer for a time period of 24 h, using Franz diffusion cell apparatus. The experimental data of diffusion studies were expressed in terms of mean ± SD (n = 3) as shown in Table 34 - 36. The graphical representation of diffusion profile of all the three sponge formulations were depicted in Figure 48.

The *in vitro* drug release pattern of SF1 sponge formulation presented an initial burst release effect with an extensive release rate of 82.49 % ± 0.01 at the end of 10 h. While, SF2 formulation revealed an initial burst effect followed by sustained release of 93.54 % ± 0.04 at the end of 24 h. Furthermore, SF3 formulation exhibited a sustained release pattern of 82.37 % ± 0.03 at 24 h without an initial burst release pattern.

Table 34: *In Vitro* Diffusion Profile of SF1 Sponge Formulation

Time (h)	Absorbance	Conc in mcg/ml	Conc in mg/10 ml	Conc in 12.5 ml	CLA	CDR	% CDR
0	0	0	0	0	0	0	0
1	0.098	0.56603	0.01132	0.14150	0	0.1415	7.521 ± 0.02
2	0.145	1.00943	0.02018	0.25235	0.0113	0.2636	14.02 ± 0.03
3	0.189	1.42452	0.02849	0.35613	0.0315	0.3876	20.61 ± 0.02
4	0.225	1.76415	0.03528	0.44103	0.0624	0.5010	26.65 ± 0.04
5	0.291	2.38679	0.04773	0.59669	0.0952	0.6919	36.80 ± 0.01
6	0.327	2.72641	0.05452	0.68160	0.1430	0.8246	43.86 ± 0.03

7	0.377	3.19811	0.06396	0.79952	0.1975	0.9970	53.03 ± 0.01
8	0.436	3.75471	0.0750	0.93867	0.2615	1.2001	63.83 ± 0.04
9	0.474	4.11320	0.08226	1.02830	0.3366	1.3649	72.60 ± 0.05
10	0.518	4.52830	0.09056	1.13207	0.4188	1.5509	82.49 ± 0.01

Data is expressed as Mean ± SD (n=3)

CLA: Cumulative Loss Added

CDR: Cumulative Drug Release

Table 35: *In Vitro* Diffusion Profile of SF2 Sponge Formulation

Time (h)	Absorbance	Conc in mcg/ml	Conc in mg/10 ml	Conc in 12.5 ml	CLA	CDR	% CDR
0	0	0	0	0	0	0	0
1	0.07	0.30188	0.00603	0.07547	0	0.0754	4.014 ± 0.05
2	0.092	0.50943	0.01018	0.12735	0.0060	0.1333	7.095 ± 0.12
3	0.13	0.86792	0.01735	0.21698	0.0162	0.2332	12.40 ± 0.31
4	0.15	1.05660	0.02113	0.26415	0.0335	0.2977	15.83 ± 0.02
5	0.211	1.63207	0.03264	0.40801	0.0547	0.4627	24.61 ± 0.04
6	0.26	2.09433	0.04188	0.52358	0.0873	0.6109	32.49 ± 0.11

7	0.318	2.64150	0.05283	0.66037	0.1292	0.7896	42.00 ± 0.01
8	0.375	3.17924	0.06358	0.79481	0.1820	0.9768	51.96 ± 0.03
9	0.417	3.57547	0.07150	0.89386	0.2456	1.1395	60.61 ± 0.04
10	0.459	3.97169	0.07943	0.99292	0.317	1.3100	69.68 ± 0.17
11	0.486	4.22641	0.08452	1.05660	0.3966	1.4532	77.29 ± 0.02
12	0.509	4.44339	0.08886	1.11084	0.4811	1.5919	84.67 ± 0.01
24	0.542	4.75471	0.0950	1.18867	0.57	1.7586	93.54 ± 0.04

Data is expressed as Mean ± SD (n=3)

Table 36: *In Vitro* Diffusion Profile of SF3 Sponge Formulation

Time (h)	**Absorbance**	**Conc in mcg/ml**	**Conc in mg/10 ml**	**Conc in 12.5 ml**	**CLA**	**CDR**	**% CDR**
0	0	0	0	0	0	0	0
1	0.04	0.01886	0.00037	0.00471	0	0.0047	0.250 ± 0.04
2	0.065	0.25471	0.0050	0.06367	0.0003	0.0640	3.407 ± 0.03
3	0.089	0.48113	0.00962	0.12028	0.0054	0.1257	6.689 ± 0.10
4	0.103	0.61320	0.01226	0.15330	0.0150	0.1683	8.957 ± 0.02
5	0.132	0.88679	0.01773	0.22169	0.0273	0.2490	13.24 ± 0.15

6	0.176	1.30188	0.02603	0.32547	0.0450	0.3705	19.71 ± 0.08
7	0.2	1.52830	0.03056	0.38207	0.0711	0.4532	24.10 ± 0.05
8	0.241	1.9150	0.03830	0.47877	0.1016	0.5804	30.87 ± 0.02
9	0.297	2.4433	0.04886	0.61084	0.14	0.7508	39.93 ± 0.21
10	0.355	2.99056	0.05981	0.74764	0.1888	0.9365	49.81 ± 0.15
11	0.41	3.50943	0.07018	0.87735	0.2486	1.1260	59.89 ± 0.09
12	0.468	4.05660	0.08113	1.01415	0.3188	1.3330	70.90 ± 0.07
24	0.525	4.59433	0.09188	1.14858	0.4	1.5485	82.37 ± 0.03

Data is expressed as Mean ± SD (n=3)

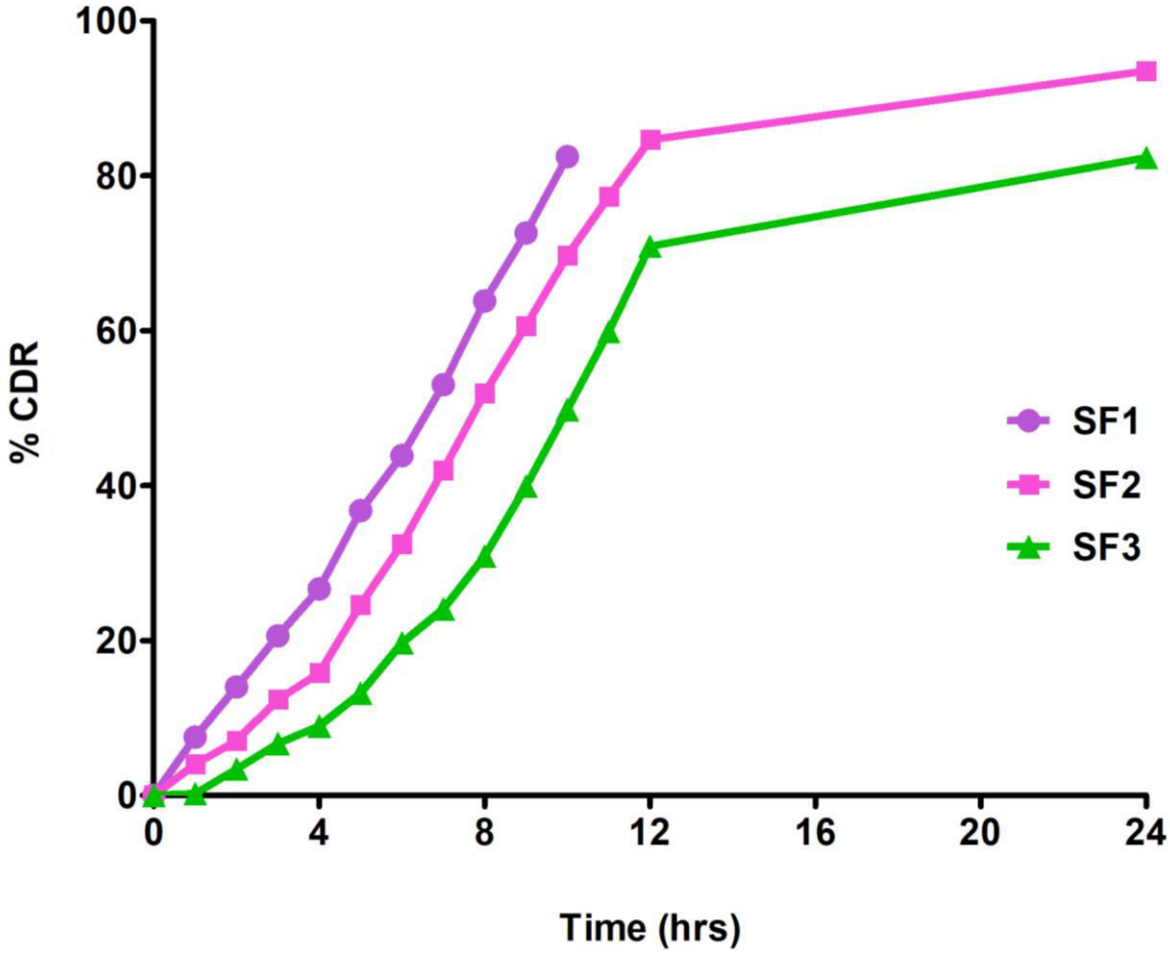

Figure 48: *In Vitro* Diffusion Profile of Sponge Formulations

Thus, in considerations with the data obtained from various experimental parameters, it could be concluded that SF2 formulation was selected as a best formulation for further experimental studies.

4.2.5. *In Vitro* Biodegradation studies

Another essential key component involved in designing scaffolds is their ability to undergo biodegradation. The biodegradation of sponges in an appropriate time frame results in an adequate remodeling and rejuvenation of cells and tissues.

Biodegradation of SF2 sponge was carried out in wet and dry conditions using deep soil burial method. In wet soil condition, the sponges were completely degraded

with 60 min whereas in dry soil condition, the time frame required for the complete degradation of sponge was 20 days. The graphical presentation of biodegradation of sponges in both wet and dry conditions were illustrated in Figure 49.

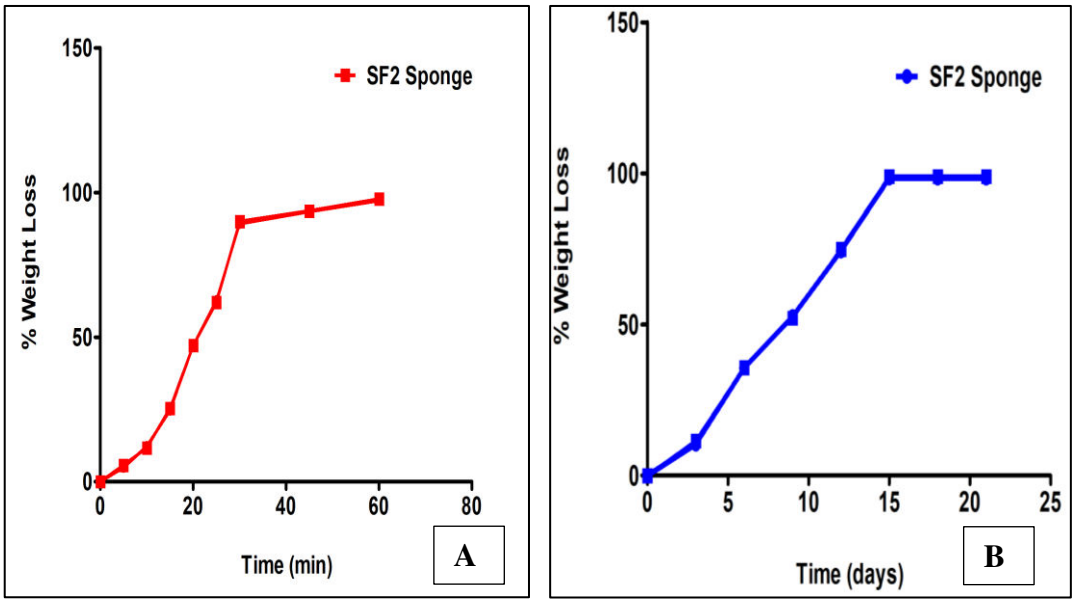

Figure 49: Biodegradation of SF2 Sponges in A. Wet Soil and B. Dry Soil

4.2.6. Antimicrobial Studies

The measurement of the diameter of inhibitory zone represents the degree of microbial susceptibility. The antimicrobial activities of pure Cip HCl and SF2 sponge formulation against *S. aureus* and *E. coli* were investigated using infused agar disc diffusion method.

As evidenced by the Figure 50, the inhibitory zone was increased for test sample (SF2 sponge formulation) against both the micro-organisms. While, the standard (pure Cip HCl) presented a minimum inhibitory zone for *S. aureus* and *E. coli*. The data obtained for antimicrobial studies are shown in Table 37.

Table 37: Data values for Zone of Inhibition Studies of SF2 Sponge Formulation

Organisms	Zone of Inhibition Diameter (mm)	
	Standard	**Test**
S. aureus	20.03 ± 0.05 mm	30.07 ± 0.02 mm
E. coli	25.04 ± 0.02 mm	32.01 ± 0.04 mm

Gram Positive

Staphylococcus aureus

Gram Negative

Escherichia coli

Figure 50: Zone of Inhibition of SF2 Sponge a). Gram Positive (*Staphylococcus aureus)* and b). Gram Negative (*Escherichia coli)*

4.2.7. Cell Culture Studies

4.2.7.1. Cytotoxicity Studies

Cell viability assay also known as MTT assay, is the most popular and widely established calorimetric assay to screen the reactance of the cells against the drug or any other chemical agent. The biosafety and biocompatibility of SF2 sponges were analysed by performing MTT assay on A549 cells and expressed in terms of % viability of cells or % proliferation.

The toxicity profile of doped halloysite nanotube (a primary component of SF2 sponge) was evaluated and compared with pure Cip HCl (control). The data obtained for the viability of A549 cells when treated with SF2 sponge and pure Cip

HCl at different concentrations for 24 h was depicted in Figure 51. The results of MTT assay for both test sample (SF2 sponge) and control (Cip HCl) were shown in Table 38.

Table 38: Data of % Viability of A549 Cells

Concentration (µg/ml)	**% Viability of cells**	
	Control	**Test**
20	58	93
40	51	92
60	49	92
80	56	81
100	42	64
150	43	63
200	34	60
250	33	60
300	32	60
400	30	56
500	27	46
	IC_{50}= 52.6 µg/ml	**IC_{50}= 405.9 µg/ml**

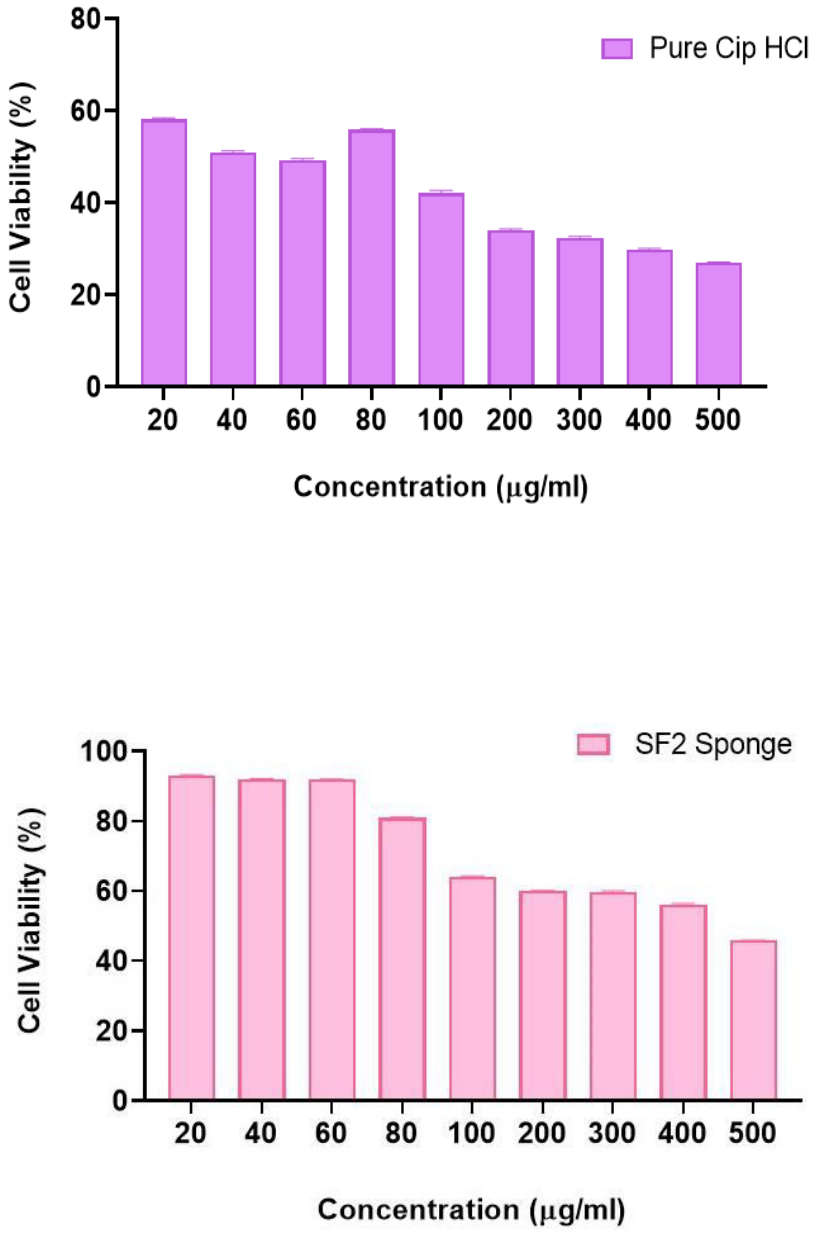

Figure 51: % Cell Viability of A549 Cells a. Control (Pure Cip HCl) and b. SF2 Sponge

4.2.7.2. *In Vitro* Wound Healing Assay

The essence of wound healing is collective cell migration and proliferation. During the process of wound healing, the cells proliferate and migrate at the edges of wound, leading to the formation of granulation tissue and re-epithelialization of wound surface. Therefore, it is very important to utilize the *in vitro* assay to determine the rate of proliferation and cell migration, that contributes towards faster and healthy healing of wounds.

In the present research study, to better understand the effect of SF2 sponge formulation comprising DHNT and pure Cip HCl on wound healing activity, an artificial *in vitro* cell line based (A549 cells) scratch assay test was performed. The ability of A549 cells to migrate for 0 h, 24 h and 48 h was studied and analysed, as depicted in Figure 52. Furthermore, the intensity and rate of cell migration at different time intervals was analysed by capturing an image and the data obtained was quantified.

A. CONTROL **B. TEST**

0 h

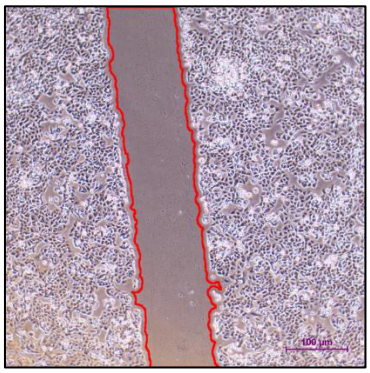

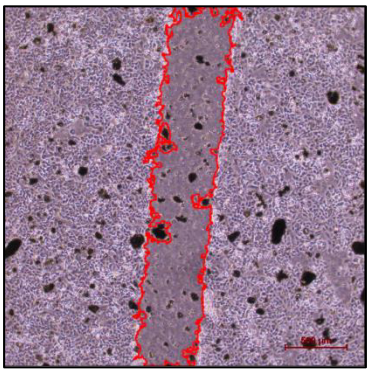

24 h

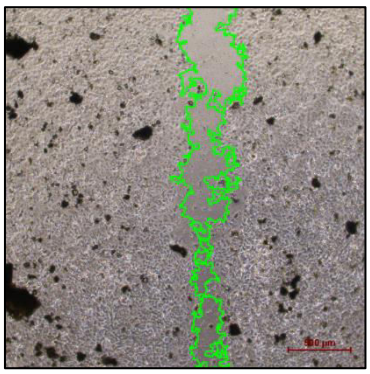

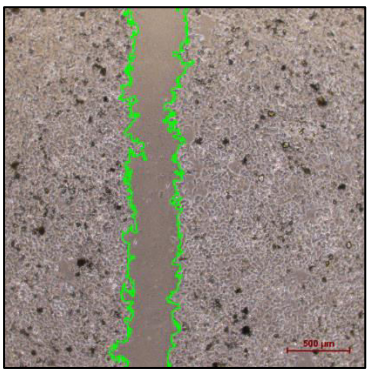

48 h

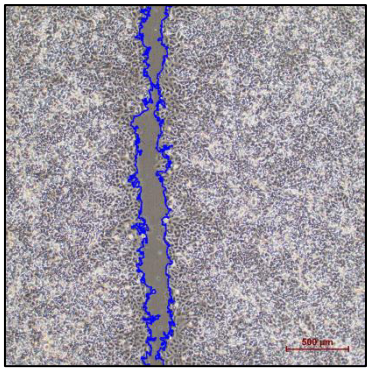

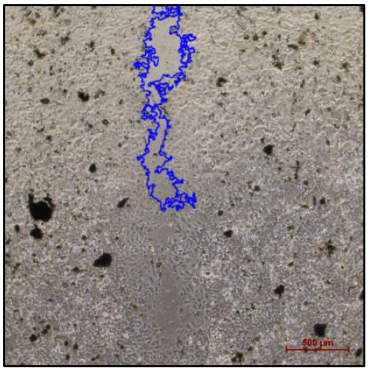

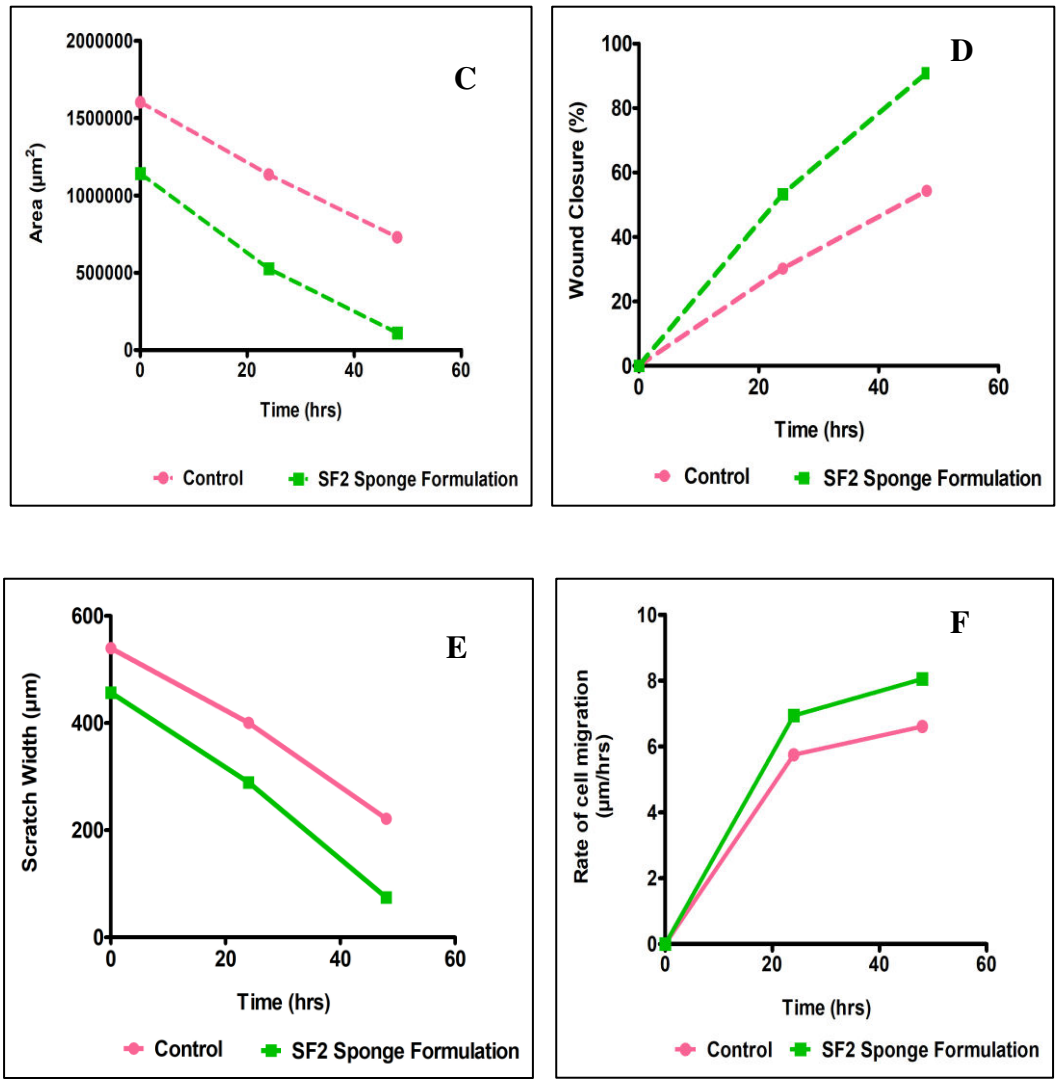

Figure 52: Microscopic and graphical illustration of monolayer wound healing migration assay of A549 cells treated with (A) Control, (B) Cip HCl loaded DHNTs polymeric sponges and for both the samples images were captured at 0 h, 24 h and 48 h, (C) Wound area in µm^2, (D) Percentage of wound closure area, (E) Wound width in µm and (F) Rate of cell migration in µm/h.

4.2.8. *In Vivo* Wound Healing Activity

In order to assess the wound healing efficiency of SF2 sponge formulation, the *in vivo* study was conducted in male Wister albino rats (weighing 250 – 300 g). The sponge was applied on the partial thickness burn wound spot on the dorsal area of the rats of Group III and the data obtained for % rate of wound closure was calculated and compared with the data of Group I Disease Control group (with no treatment) and Group II (animals treated with marketed silver sulfadiazine topical cream).

The photo galleries depicting the glimpse of wound reconstruction were captured at different time intervals 0^{th} day, 7^{th}, 14^{th} and 21^{st} day of post wounding and the surface area was measured and recorded, to assess the pace of wound healing and closure. The photographic images of wound reconstruction with respect to different time intervals were depicted in Figure 53.

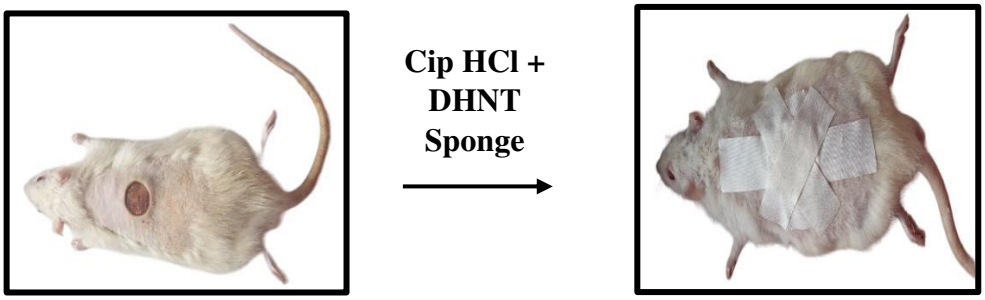

	GROUP I	GROUP II	GROUP III
Day 0			
Day 7			
Day 14			

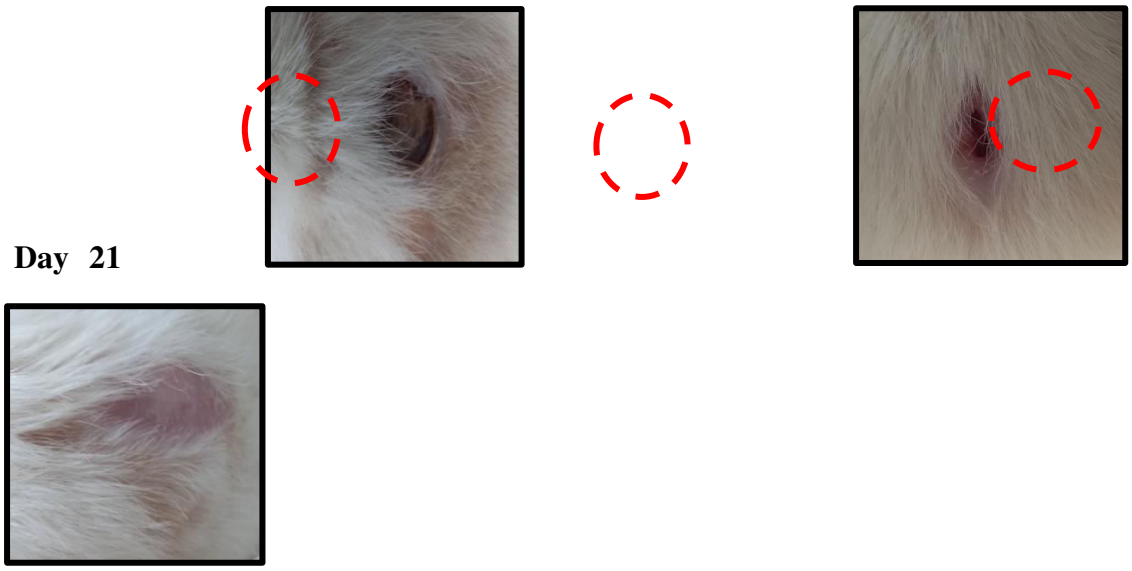

Figure 53: Photographic images representing wound healing potencies of Standard (Marketed formulation – Silver Sulfadiazine Cream Group II) and Test (SF2 sponge Group III) against Disease Control (open wounded Group I) at different time intervals 0, 7th, 14th and 21st day.

4.2.9. Pharmacological Evaluation of Wound Healing Activity

4.2.9.1. Studies on Percentage Wound Closure Activity

The wound closure (%) at different time intervals for Group I, II and III were illustrated in Figure 54. The data values obtained for % wound closure for Group I, II and III were represented in Table 39.

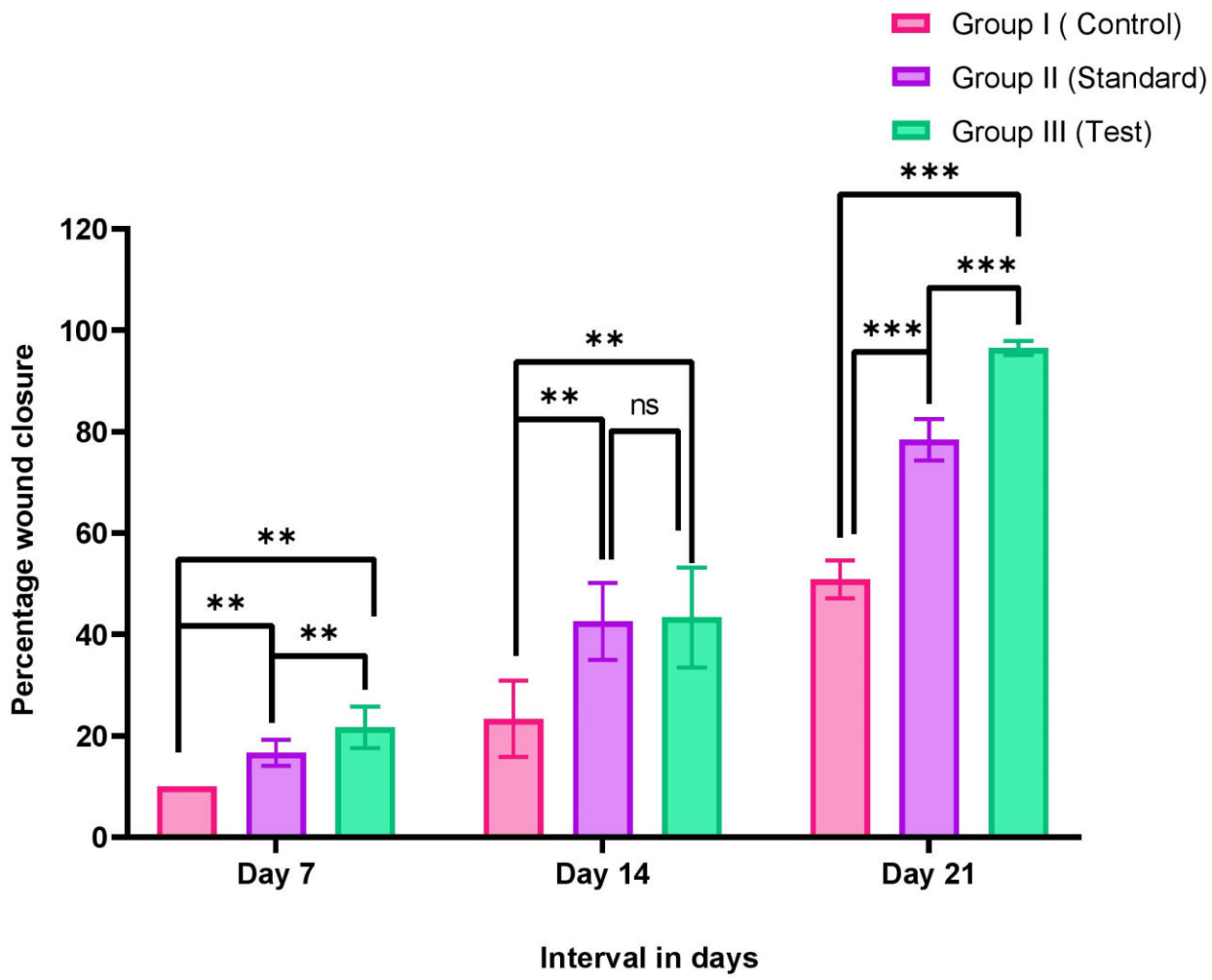

Figure 54: The percent wound closure at different intervals in days for GP I, GP II and GP III. Values are expressed as mean ± S.D. (*n* = 6 animals). Data were analyzed by Two-way ANOVA, followed by Tukey test ** $p \leq 0.01$, *** $p < 0.001$.

Table 39: Data Values for Percentage Wound Closure

Time in days	Wound Closure (%)		
	Group I	**Group II**	**Group III**
Day 7	10.00 ± 0.01	16.67 ± 1.05	21.66 ± 1.66
Day 14	23.33 ± 3.07	42.50 ± 3.09	43.33 ± 4.01
Day 21	50.83 ± 1.53	78.33 ± 1.66	98.66 ± 1.66

Values are expressed in terms of Mean ± SE

4.2.9.2. Epithelialization Period

The time required to completely cover a denuded surface with the formation of epithelium is known as the epithelialization period. It is expressed as the number of days needed for the eschar to come off without leaving a raw wound.

The average time for the formation of epithelialization was found to be significantly reduced in the group of animals treated with SF2 sponge formulation. The mean time for epithelialization for GP III resulted to be 12.30 ± 0.02 days. Furthermore, the epithelialization time for GP II animals (treated with marketed formulation) resulted to be slightly higher 15.67 ± 0.01 days as compared to GP III animals. Likewise, the time required to form an epithelium in GP I (open wounded animals) was very slow i.e. 20.25 ± 0.05 days. The graphical representation for epithelialization period of wound healing was illustrated in Figure 55.

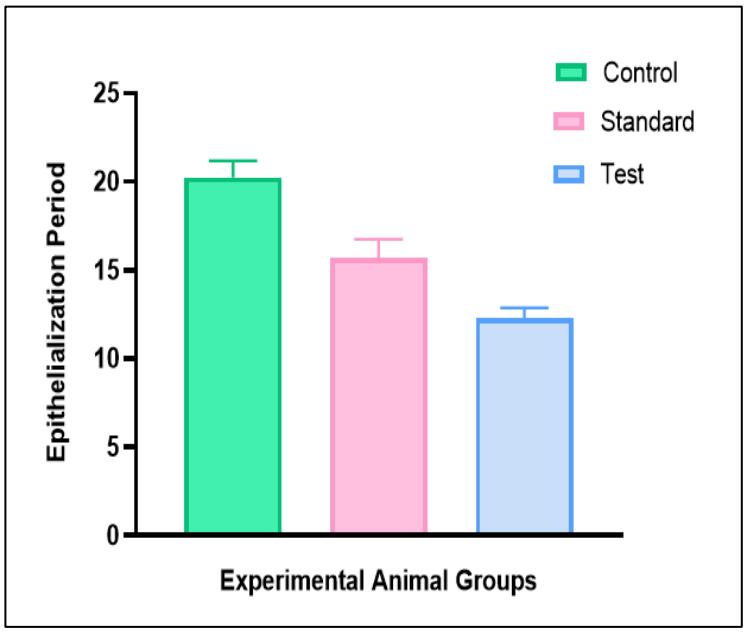

Data is expressed as Mean ± SE (n = 6)

Figure 55: Period of Epithelialization in Control, Standard and Test Groups

4.2.9.3. Histopathology of Burn Wounds

Histopathology has been always recognized as the standard of excellence in diagnosing and assessing the morphological changes, tracking the wound healing process during the course of treatment and better understanding the histopathology of non-healing wounds. The microscopic views of H and E stained histopathology sections for day 0 and day 21 of normal, disease control, standard and test group was illustrated in Figure 56.

The histopathology of normal healthy rat skin displayed an extensive well-defined structure with clear delineated epidermal and dermal layers. The epidermis was topped with a thin layer of stratum corneum, along with the multiple layers of squamous epithelial cells. As a result of this, a rich well organized collagen bundles, fibroblasts and hair follicles were observed to be present on the dermal region of the skin.

4.2.9.3.1. Histopathological Data for Day 0

The histopathological data for day 0, after the infliction of burn wounds in all the three groups of experimental rats revealed the presence of mono-nuclear inflammatory cells with a complete damage of epidermal and dermal layers of skin. A highly ulcerated area was observed with a damaged streaming of nucleus and collagen fibres. The fibroblasts were scattered (minimal fibrosis) along with the disappearance of hair follicles.

4.2.9.3.2. Histopathological Data for Day 21

Group I (Control)

As seen in the tissue slices of the 21st day of wounding, the control group manifested delayed wound healing activity as compared to other two groups of animals. The majority of tissue area was highly ulcerated with reasonable amounts of hair follicles, adnexa and collagen bundles.

Group II (Standard)

The histology of experimental rats treated with marketed formulation exhibited a fairly high intensity of epithelialization, followed by the formation of new epithelium. A very slight degree of necrosis along with the dense hair follicles and progression of granulation tissue was noticeable. The tissue was surrounded by mild inflammatory cell and fibrosis, indicating that animals treated with marketed silver sulfadiazine cream formulation demonstrated the better healing effect when compared with control group.

Group III (Test)

Subsequently, the histopathological analysis of burn wounds treated with sponge formulation (test – GP III) on day 21, confirmed the formation of complete re-epithelialization, signifying the remarkable wound healing activity. The histopathological sections of test formulation showed mild inflammatory cell infiltration along with the restoration of adnexa within the dermal layers of the skin, which is an indicatory for the healthy healing of wounds by fibrosis.

A. Normal Skin of Rat

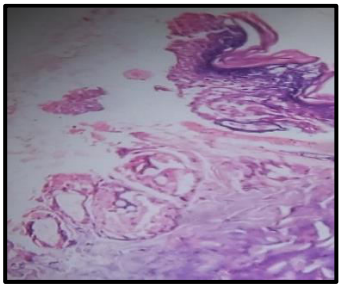

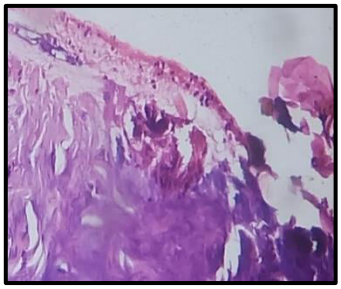

Day 0

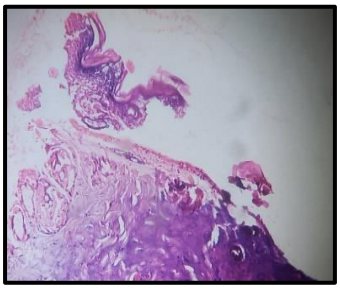

B. Group I **Group II** **Group III**

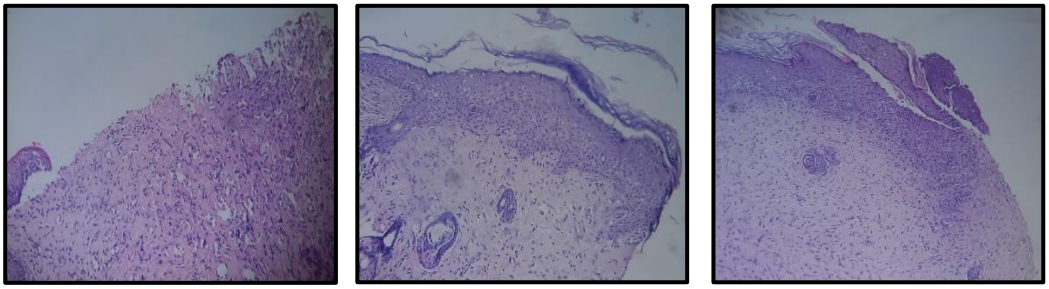

Day 21

C. Group I **Group II** **Group III**

Figure 56: Histopathology: (A). Normal rat skin, (B). at day 0 (Group I, Group II and Group III) and (C). At day 21 (Group I, Group II and Group III).

4.2.10. Stability Studies

Stability studies for SF2 sponge formulation was performed in accordance to ICH guidelines for three months at two different temperatures: Room temperature [25°C ± 2°C and RH 65 % ± 5 %] and accelerated temperature [40°C ± 2°C at RH 75 % ± 5 %].

At periodic time intervals, the sponges were analysed for Wetness integrity test, drug content and *in vitro* diffusion studies. The data obtained for stability studies were shown in Table 40.

Table 40: Stability Studies Data for SF2 Sponge Formulation

Evaluation Parameters	SF2 Sponge Formulation						
	Initial	1st month		2nd month		3rd month	
		25 ± 2°C/ 65 ± 5 % RH	40 ± 2°C/ 75 ± 5 % RH	25 ± 2°C/ 65 ± 5 % RH	40 ± 2°C/ 75 ± 5 % RH	25 ± 2°C/ 65 ± 5 % RH	40 ± 2°C/ 75 ± 5 % RH
Wetness Integrity	Instant hydrogel formation after 60 s	Instant hydrogel formation after 70 s	Instant hydrogel formation after 75 s	Instant hydrogel formation after 72 s	Instant hydrogel formation after 70 s	Instant hydrogel formation after 65 s	Instant hydrogel formation after 60 s
Drug Content	95.34 ± 0.21 %	91.12 ± 0.17 %	92.05 ± 0.04 %	92.78 ± 0.25 %	94.53 ± 0.3 %	95.14 ± 0.02 %	95.30 ± 0.15 %
% CDR at 24 h	93.54 ± 0.04 %	90.17 ± 0.11 %	89.01 ± 0.01 %	91.57 ± 0.05 %	92.32 ± 0.19 %	92.68 ± 0.25 %	93.08 ± 0.04 %

Data is expressed in terms of Mean ± SD (n = 3)

4.3. STRATEGY 3:

FABRICATION OF CIPROFLOXACIN HYDROCHLORIDE LOADED DHNTs 3D PRINTED SCAFFOLDS

4.3.1. Preparation of Cip HCl Coated PVA filaments

4.3.1.1. Efficiency of Pellet Coating

The efficiency of coating PVA pellets with Cip HCl (F1) resulted to be 60.23 %. Similarly, the coating effectiveness of Cip HCl-DHNTs pellets (F2) was found to be 82.65 %.

4.3.2. Extrusion of PVA Filaments

Pellets of PVA coated with Cip HCl and Cip HCl - DHNTs were extruded by hot melt extrusion technique in order to prepare the filaments. The pellets were free flowing, while not posing any impediment to the extruder. Subsequently, the designed filaments were multi-spectral with a consistent dimensional measurements. The digital images of designed filaments were shown in Figure 57.

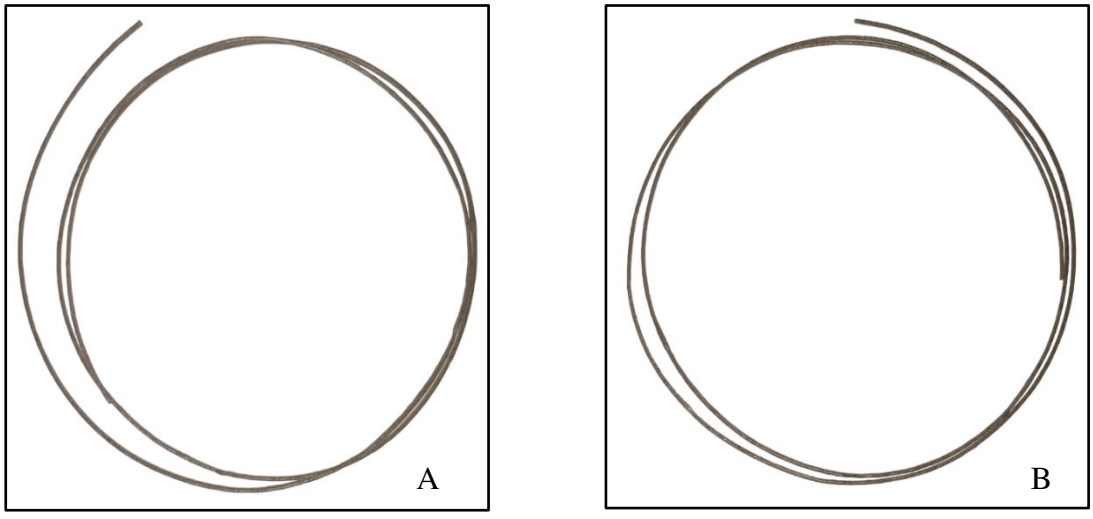

Figure 57: Digital Images of Filaments A. Cip HCl – PVA Filament (PF1) and B. Cip HCl-DHNT PVA Filament (PF2)

4.3.3. Fabrication of 3D Printed (3DP) Scaffolds

The 3DP scaffolds comprised with Cip – PVA and Cip –DHNTs PVA were fabricated using FDM technique. Cip - PVA scaffolds (S1) and Cip –DHNTs PVA (S2) presented a hexagonal shaped infill design. The scaffold S2 was encapsulated with an extremely soft and glossy surface layer on atop of the scaffold. These scaffolds S1 and S2 were featured with flawless and glossy texture towards the base and skirting of the scaffold. The digital photographs of developed scaffolds (S1 and S2) were illustrated in Figure 58.

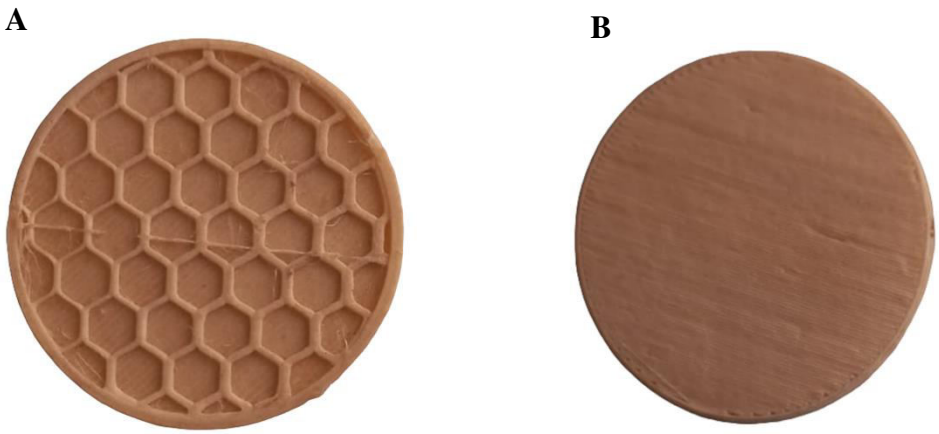

Figure 58: Digital Images of 3DP Scaffold A. Cip HCl – PVA (S1) and B. Cip HCl – DHNTs PVA (S2)

4.3.4. Studies on Evaluation Parameters of Filaments and Scaffolds

4.3.4.1. Dimensional Measurements of Filaments and Scaffolds

The diameter and thickness of filaments and scaffolds were measured and recorded. The results for dimensional measurements of filaments and scaffolds were shown in Table 41. The data obtained for dimensional measurements were expressed as mean ± SD (n = 3).

Table 41: Dimensional Measurements of Filaments and Scaffolds

Filaments	**Diameter (mm)**	
Cip HCl – PVA filament (PF1)	1.77 ± 0.02	
Cip HCl – DHNTs PVA filament (PF2)	2.15 ± 0.03	
Scaffolds	**Diameter (mm)**	**Thickness (mm)**
Cip HCl – PVA scaffold (S1)	45	1.3 ± 0.02
Cip HCl – DHNTs PVA scaffold (S2)	45	1.5 ± 0.01

Mean ± SD (n = 3)

4.3.4.2. Compatibility Study

1. Studies on FT-IR Analysis

FT-IR spectra of scaffolds (S1 and S2) confirmed the existence of functional compounds of pure Cip HCl and PVA polymer as illustrated in Figure 59. The IR spectra of S1 and S2 indicated no shift/change in absorption bands of functional groups of Cip HCl when mixed with other excipients of the formulations, signifying the compatibility between drug and added excipients. Thus it can be concluded that, the selected excipients used in the preparation of scaffolds were compatible with Cip HCl.

The appearance of prominent absorption bands for Cip HCl and other excipients were shown in Table 42.

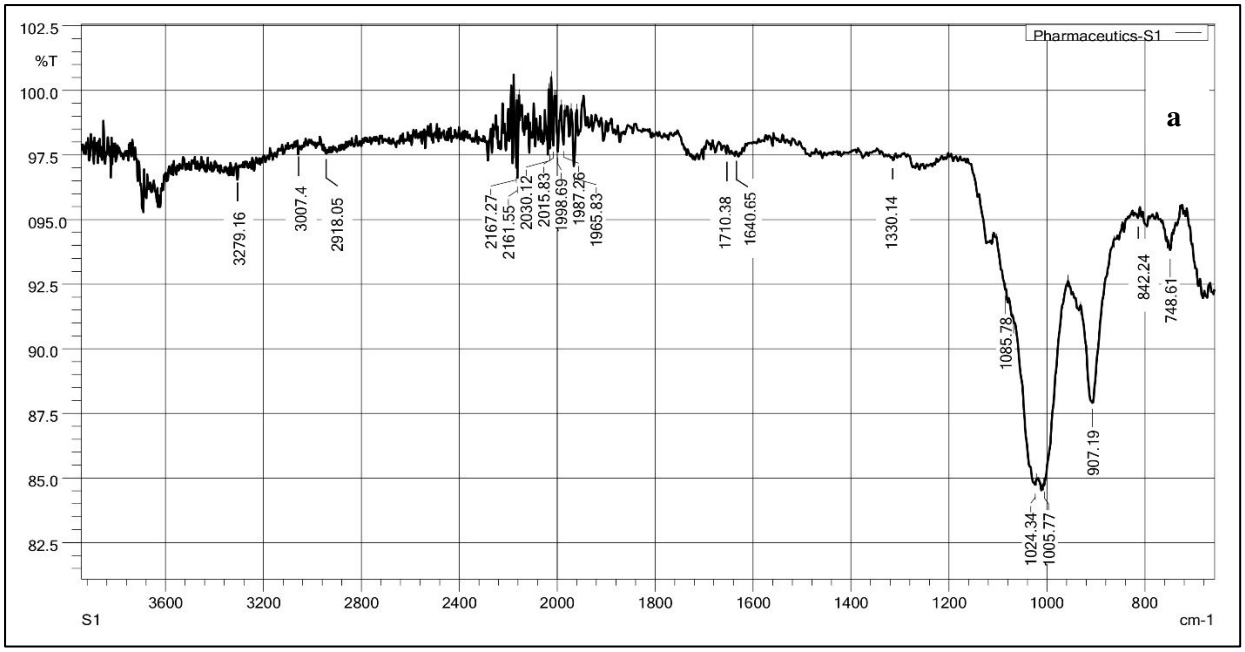

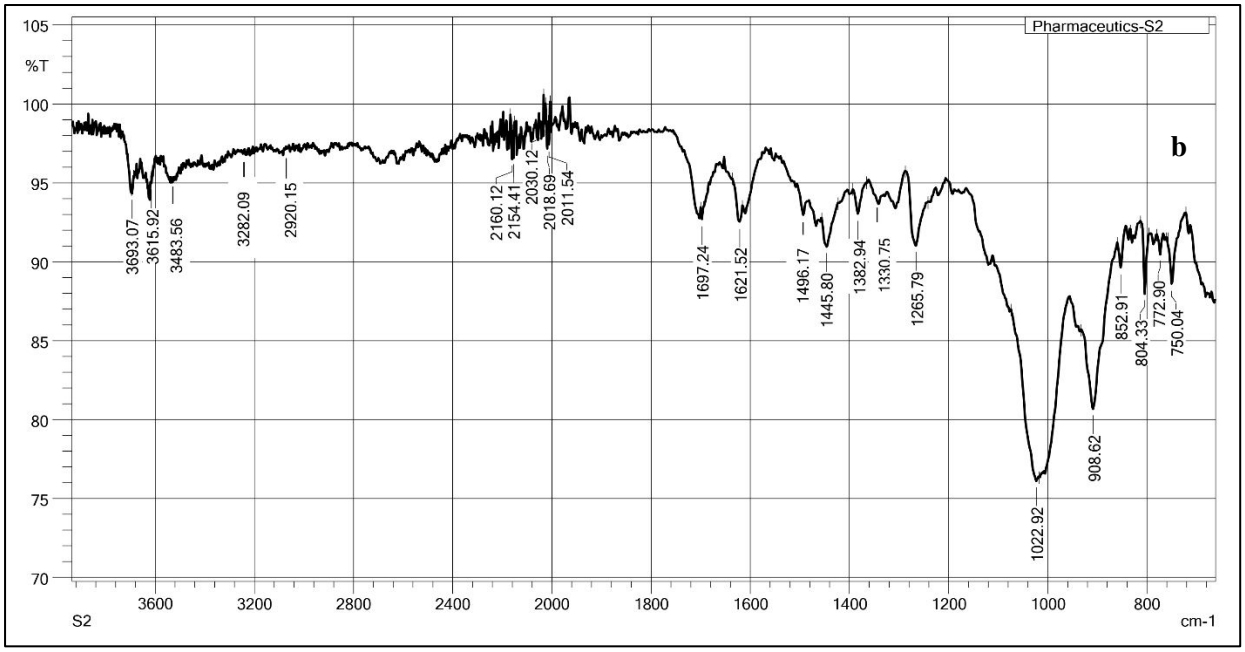

Figure 59: FT-IR Spectra of a. Scaffold 1 (S1) and b. Scaffold 2 (S2)

Table 42: FT-IR Frequencies of Scaffold Formulation

Functional groups	**Frequencies (cm^{-1})**		
	Literature Value	**Reported values**	
	Pure Drug (Cip HCl)	**S1**	**S2**
C=O Stretching	1750 - 1650	1710.38	1697.24
-OH Bending	1300 - 1250	1260.21	1265.79
Quinolones	1650 - 1600	1640.65	1621.52
C-F Stretching	1400 - 1000	1024.34	1022.17
Functional groups	**Pure PVA**	**S1**	**S2**
C-C stretching	890 - 800	842.24	852.91
OH stretching	3690 - 3100	3279.16	3282.09
C-H deformation	1350 - 1300	1330.14	1330.75
Functional groups	**DHNTs**	**S1**	**S2**
- CH_2 Scissoring	3000 - 1450	**------**	1496.17 and 2920.15
RSi-O-Si and RSi-O-Al	900 - 950	------	908.62

2. Thermal Analysis of Scaffolds

DSC curves for pure PVA polymer and scaffold formulations (S1 and S2) were shown in Figure 60. The DSC thermogram of pure PVA polymer revealed a sharp, slightly broad endothermic curve at 192.74 °C, which indicates the melting point (MP) of the polymer. The DSC thermogram of scaffold 1 (S1) exhibited a slightly broad endothermic curve at 305.66 °C, signifying to the melting point of pure Cip HCl. Another peak was observed in S1 scaffold at 162.15 °C, corresponds to the loss of water molecule.

Similarly, the S2 scaffold presented an extensively small peak at 61.95 °C, indicating the evaporation of adsorbed as well as interlayer water molecules. Another two peaks were observed at 192.31 °C and 310.51 °C. The presence of peak at 192.31 °C was associated with the MP of PVA polymer, while the appearance of broad peak at 310.51 °C was mainly attributed to the MP of Cip HCl.

Therefore, the results obtained from DSC analysis confirmed the compatibility of excipients and pure drug, no remarkable interaction was observed.

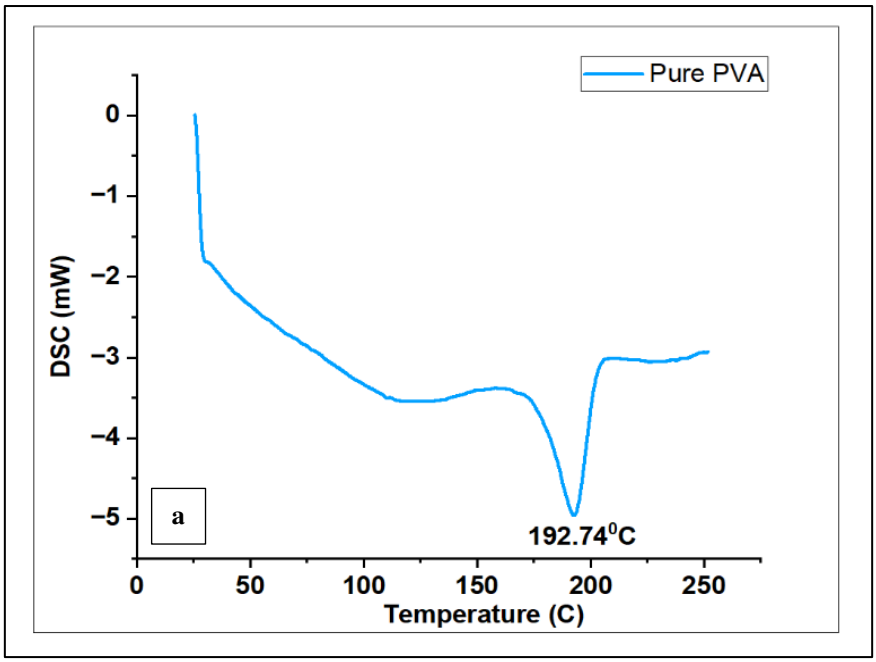

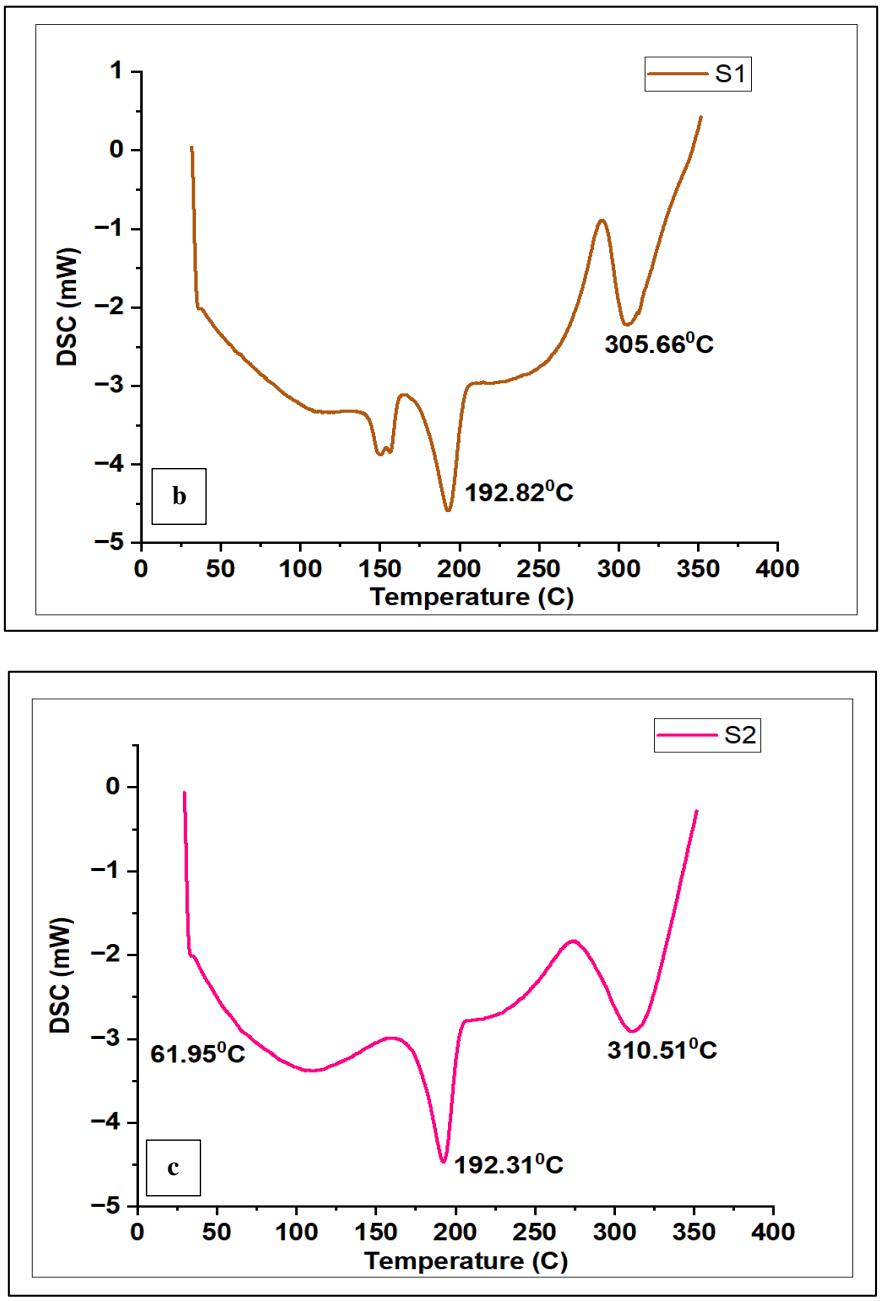

Figure 60: DSC Curves for a. Pure PVA polymer, b. Scaffold 1(S1) and c. Scaffold 2 (S2)

4.3.4.3. Mechanical Properties of Scaffolds

Mechanical property colloquially termed as tensile property of scaffolds were measured using universal testing machine. The mechanical properties of scaffolds revealed that, tensile strength and elastic modulus for S2 was considerably higher

with respect to scaffold 1 (S1) and it was statistically significant ($p \leq 0.05$). In contrast to these findings, it was observed that the % break strain for S2 was considerably decreased when compared with S1 scaffold ($p \leq 0.05$). The data derived from tensile strength measurements of scaffolds were tabulated in Table 43. The graphical presentation of tensile properties of scaffolds were illustrated in Figure 61.

Table 43: Tensile Properties of Scaffolds

Formulation	**Tensile Properties**		
	Ultimate Tensile Strength (MPa)	**Elastic Modulus (MPa)**	**Break Strain (%)**
S1	2.86 ± 0.01	160 ± 0.05	8.09 ± 0.2
S2	4.17 ± 0.02	533 ± 0.01	5.95 ± 0.1

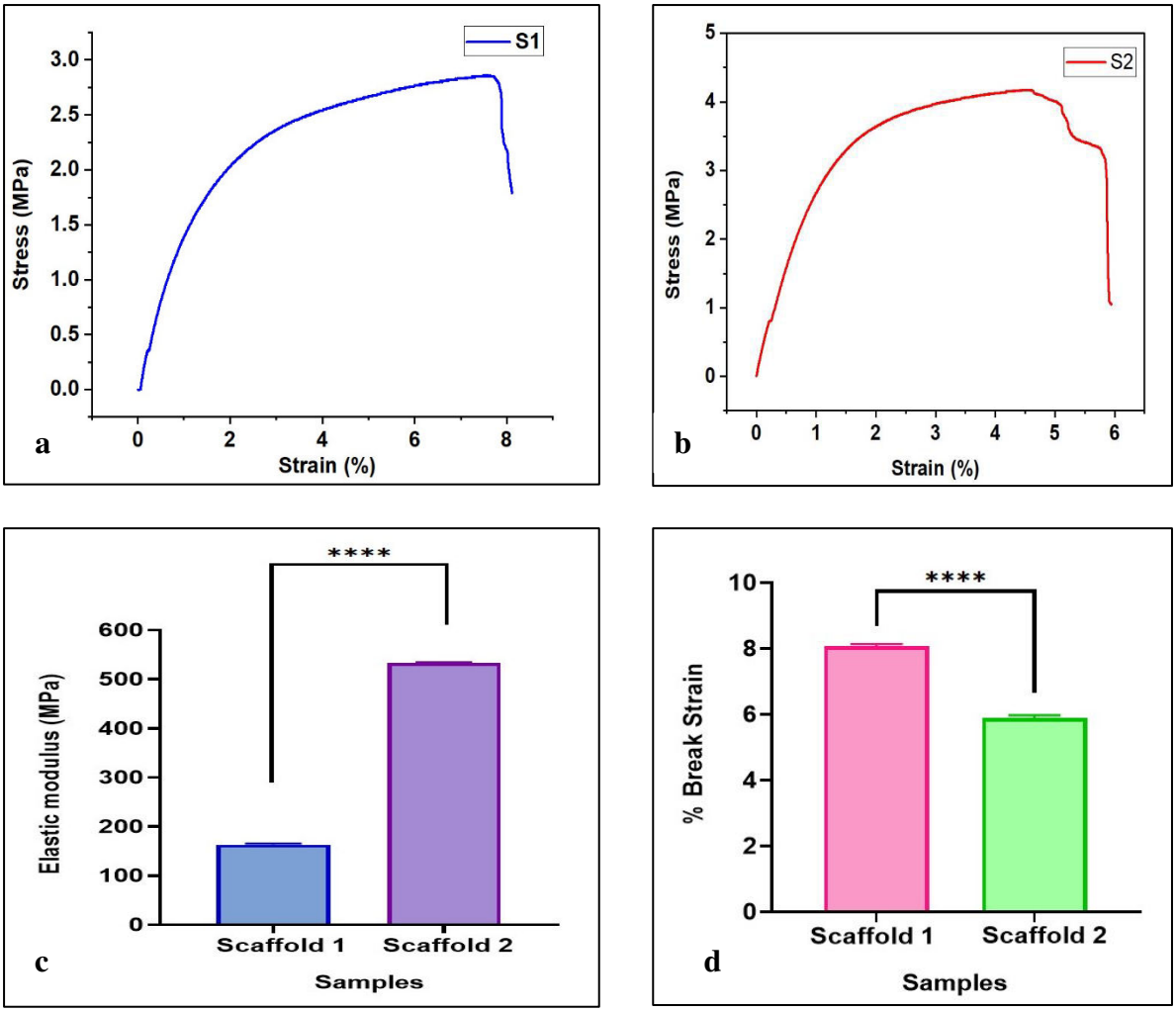

Figure 61: Mechanical Properties of Scaffolds: a. Tensile strength of S1, b. Tensile strength of S2, c. Elastic modulus of scaffolds and d. % Break strain of Scaffolds

4.3.4.4. Evaluation of Filament Morphology and 3D Printed Scaffolds

The filament (PF1) exhibited slight roughness, indicating an inclusion of PVA material coated with Cip HCl surrounding the filament. The emergence of tiny projections, symbolized by a pink arrow mark, on the filament's surface indicated the presence of Cip HCl. The surface of filament (PF2) was found to be extremely rough, with a dense and even layer of PVA material coated with Cip HCl loaded DHNTs. A red arrow mark denotes the extremely projected doped HNT lamination on the

interfacial region of the filament, and the filament's edge walls displayed an uneven, wrinkled pattern.

The PVA scaffolds coated with Cip HCl (S1) demonstrated an exemplary porous design, featuring an irregularly linked pore sizes and shapes. These scaffolds exhibited a thin walled, oval-shaped porous architecture with a little increased porosity. Although the scaffolds pore size spanned the range of 28 to 198 µm with an average pore diameter of 93.06 ± 52 µm and a porosity of 82%. Similarly, scaffold 2 (S2) revealed a granular porous elongated structure, a significant increase in the thickness of pore wall with an mean pore size of 50.82 ± 23 µm and a porosity of 60 %. The SEM micrographs of filaments and scaffolds in conjunction with the distribution curve for pore diameter was developed using Image J software were illustrated in Figure 62.

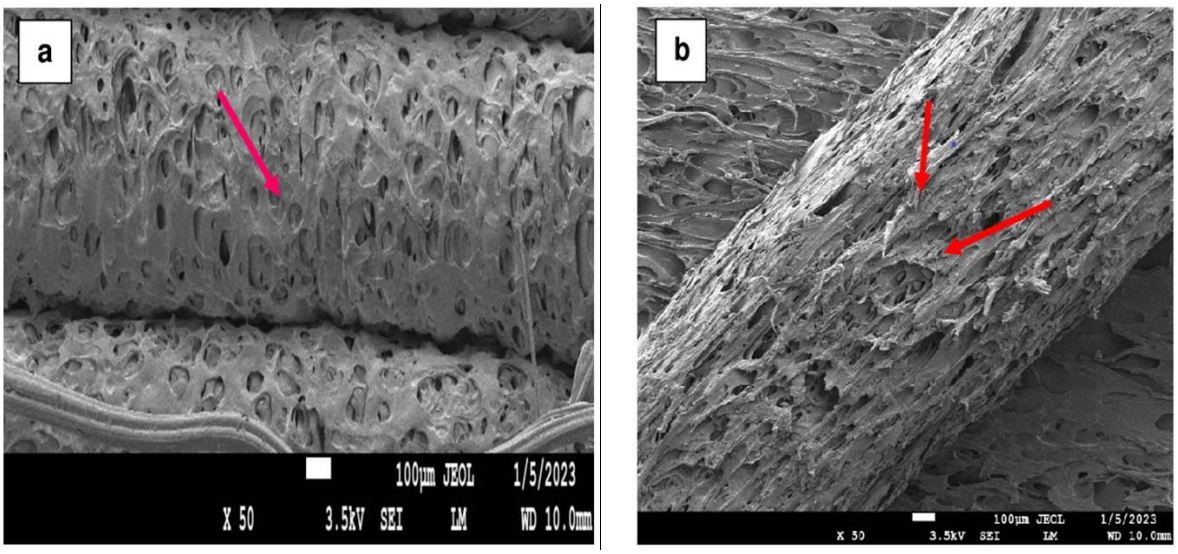

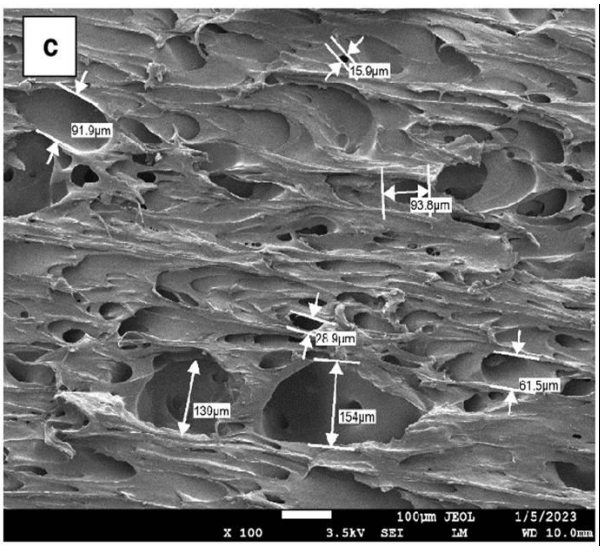

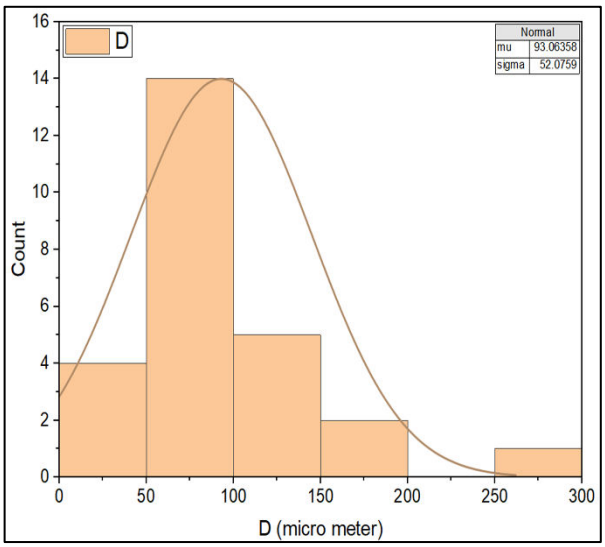

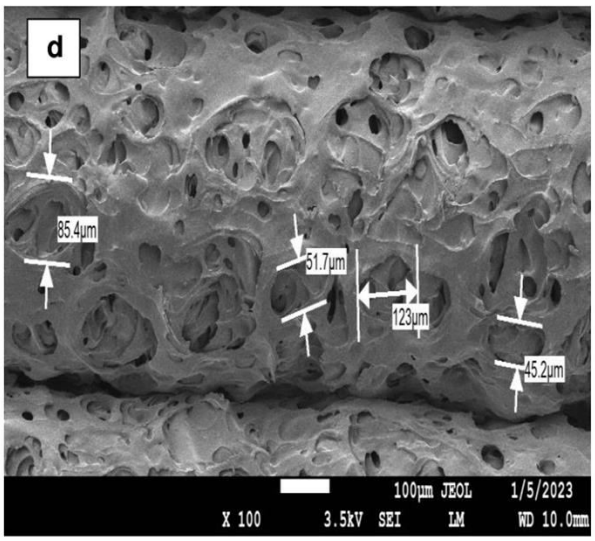

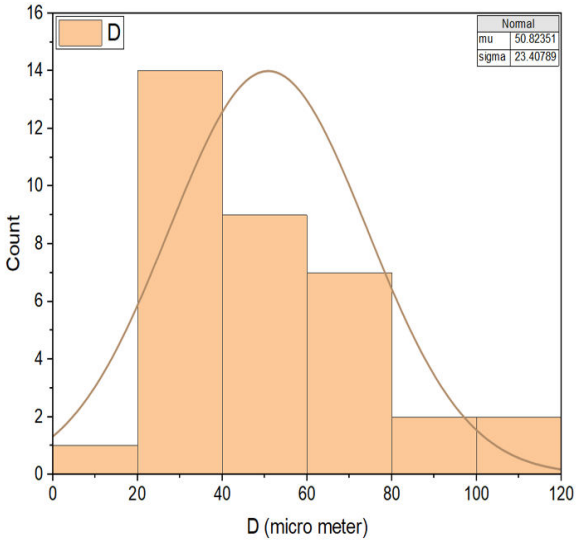

Figure 62: SEM Micrographs of with pore diameter distribution curve obtained by Image J software: a. Cip HCl coated PVA filament, b. Cip HCl loaded doped HNTs coated PVA filament, c. Scaffold 1 and d. Scaffold 2.

4.3.4.5. Determination of Drug Content

Drug content of Cip HCl in both the scaffolds (S1 and S2) resulted to be 81.13 ± 0.02 % and 88.24 ± 0.053 %, suggesting that both the scaffolds were satisfactory in terms of content of Cip HCl with little variation.

4.3.4.6. Studies on *In Vitro* Diffusion Pattern of Scaffolds

The *in vitro* diffusion pattern of scaffolds (S1 and S2) were performed and analyzed in 7.4 pH phosphate buffer using UV spectrophotometer. *In vitro* release profile of scaffold 1 (S1) showed a profound release sequence for Cip HCl of 73.35 ± 0.05 % at the end of 2 h. While, in contrast to these data findings, S2 scaffolds revealed an initial burst effect accompanied by delayed release of Cip HCl. Initially by 2^{nd} h of experimental investigations, there was a noticeable release of 42.84 ± 0.02 % as a result of burst impact of Cip HCl. Subsequently, the drug release rate was significantly sustained after the 2^{nd} h of analysis and reached around 80.92% ± 0.02 at 6^{th} h.

Likewise at the peak of 12^{th} h, the release profile of Cip HCl remained consistent around 85.54 ± 0.01 %. The results obtained from *in vitro* studies were expressed as mean ± SD (n = 3) as shown in Table 44 - 45. The graphical presentation of *in vitro* release pattern of scaffolds were illustrated in Figure 63.

Table 44: *In Vitro* Diffusion Profile of S1 Scaffold Formulation

Time (h)	Absorbance	Conc in mcg/ml	Conc in mg/10 ml	Conc in 12.5 ml	CLA	CDR	% CDR
0	0	0	0	0	0	0	0
0.25	0.105	0.6320	0.0063	0.0790	0	0.0790	8.371 ± 0.02
0.5	0.187	1.4056	0.0140	0.1757	0.0063	0.1820	19.30 ± 0.01
0.75	0.295	2.4245	0.0242	0.3030	0.0203	0.3234	34.29 ± 0.04
1	0.406	3.4716	0.0347	0.4339	0.0446	0.4785	50.75 ± 0.02
1.5	0.467	4.0471	0.0404	0.5058	0.0793	0.5852	62.06 ± 0.03
2	0.523	4.5754	0.0457	0.5719	0.1198	0.6917	73.35 ± 0.05

Data is expressed as Mean ± SD (n=3)

Table 45: *In Vitro* Diffusion Profile of S2 Scaffold Formulation

Time (h)	Absorbance	Conc in mcg/ml	Conc in mg/10 ml	Conc in 12.5 ml	CLA	CDR	% CDR
0	0	0	0	0	0	0	0
0.25	0.078	0.3773	0.0037	0.0471	0	0.0471	5.002 ± 0.05
0.5	0.134	0.9056	0.0090	0.1132	0.0037	0.1169	12.40 ± 0.01
1	0.169	1.2358	0.0123	0.1544	0.0128	0.1673	17.74 ± 0.05
1.5	0.21	1.6226	0.0162	0.2028	0.0251	0.2280	24.18 ± 0.03
2	0.257	2.0660	0.0206	0.2582	0.0414	0.2996	31.77 ± 0.04
3	0.328	2.7358	0.0273	0.3419	0.0620	0.4040	42.84 ± 0.02
4	0.404	3.4528	0.0345	0.4316	0.0894	0.5210	55.25 ± 0.02
5	0.491	4.2735	0.0427	0.5341	0.1239	0.6581	69.79 ± 0.04
6	0.541	4.7452	0.0474	0.5931	0.1666	0.7598	80.57 ± 0.02
8	0.54	4.7358	0.0473	0.5919	0.2145	0.8061	85.48 ± 0.03
10	0.5	4.3584	0.0435	0.5448	0.2615	0.8063	85.50 ± 0.01
12	0.465	4.0283	0.0402	0.5035	0.3031	0.8066	85.54 ± 0.01

Data is expressed as Mean ± SD (n=3)

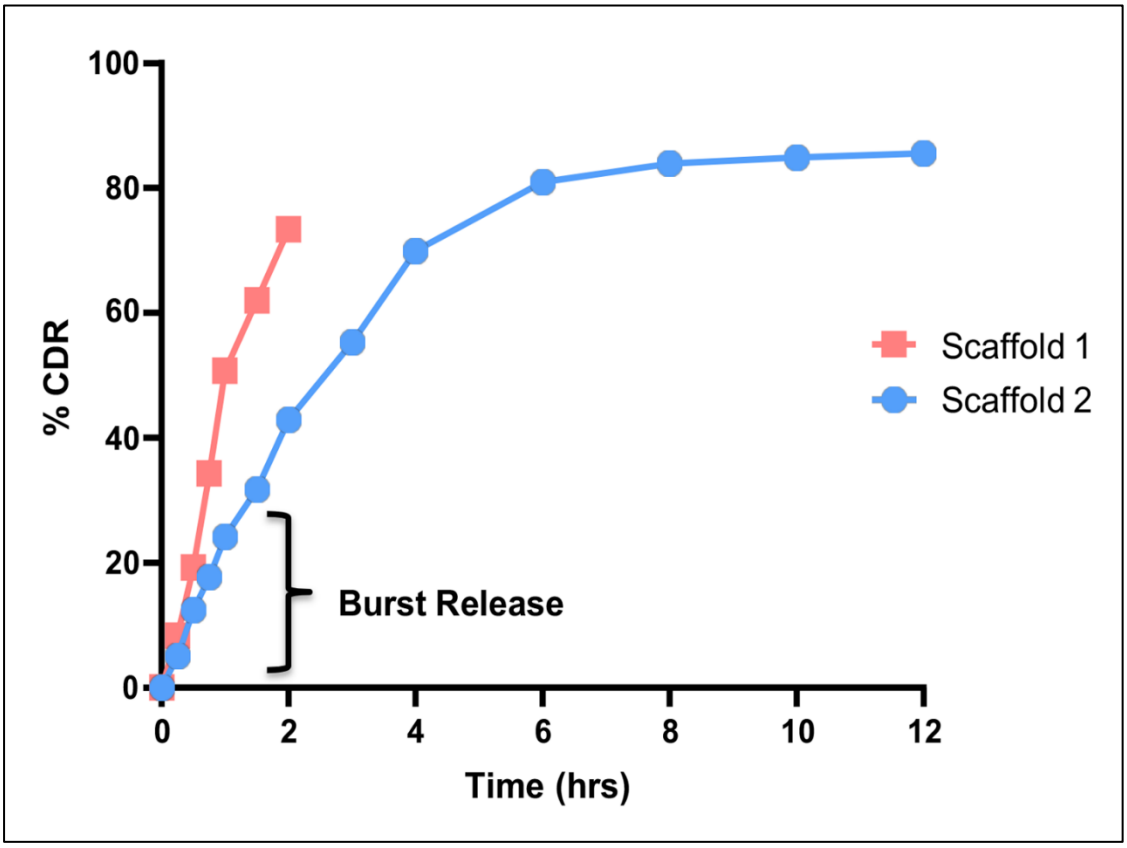

Figure 63: *In Vitro* Diffusion Profile of Scaffolds

4.3.5. Studies Cell Culture Experimentation

4.3.5.1. Test for *In Vitro* Wound Healing Activity of Scaffold S2 using A549 Cells

In the current investigation, the *in vitro* scratch assay was performed to analyze the impact of scaffold 2 (S2) in promoting the wound healing activity on A549 cells. In accordance with the findings of scratch assay test, it was observed that the cells exposed with test sample (S2 scaffold) at the concentration 1 mg/ml bridged the gap approximately with 63.30 % at 24 h and at 48 h the % wound closure resulted to be 80.16 %. Subsequently, the extent of wound's closure for A549 cells exposed

with control (pure Cip HCl 1 mg/ml) was decreased to 32 % at 24 h and 56.18 % at 48 h when compared with test sample.

Hence, it could be concluded that, the migration of cells was found to most intense in cells exposed with the test material. The digital photographs of A549 cell migration was captured and depicted in Figure 64.

A. CONTROL **B. TEST**

0 h

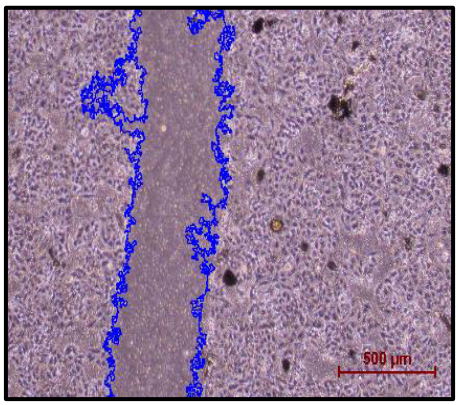

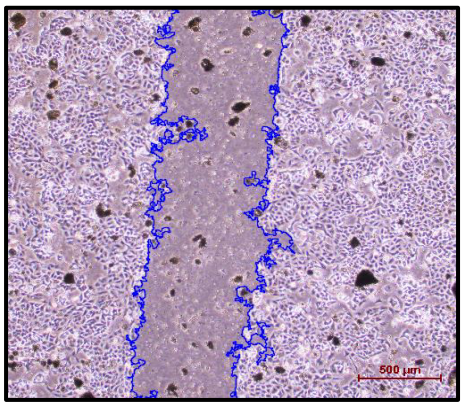

24 h

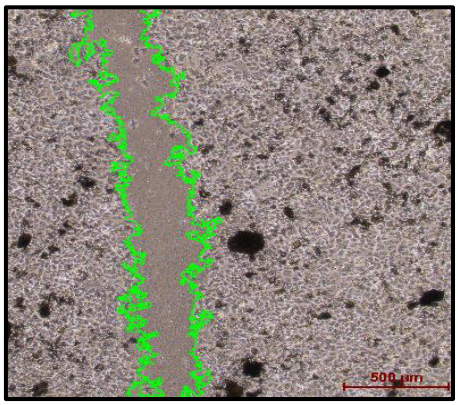

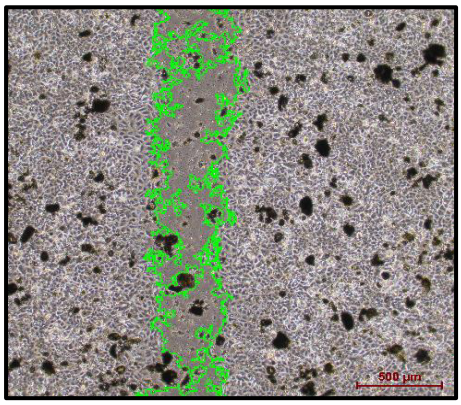

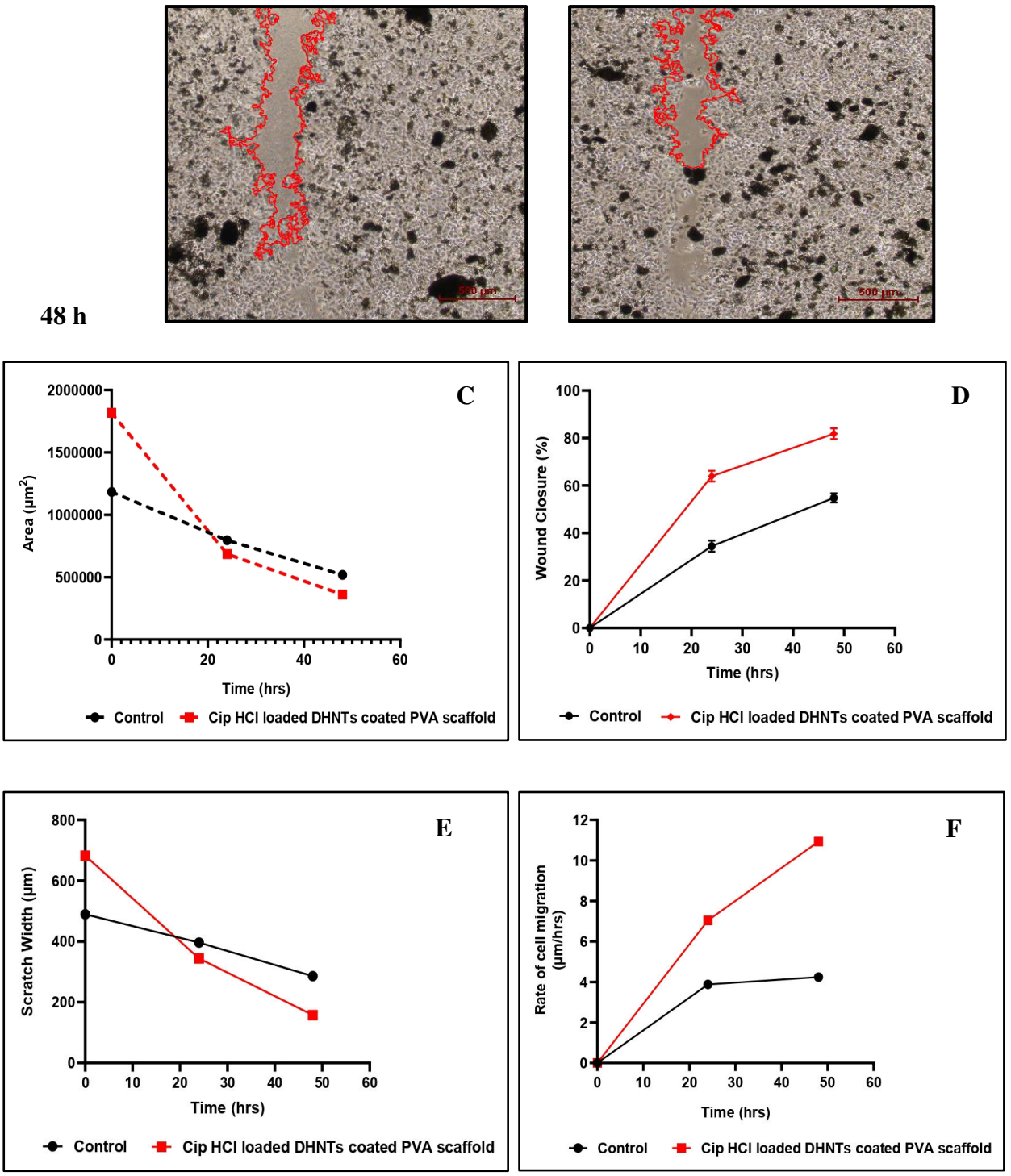

Figure 64: Microscopic and graphical illustration of monolayer wound healing scratch assay of A549 cells treated with (A) Control, (B) Cip HCl loaded DHNTs coated PVA scaffolds and for both the samples images were captured at 0 h, 24 h and 48 h, (C) Wound area in µm^2, (D) Percentage of wound closure area, (E) Wound width in µm and (F) Rate of cell migration in µm/h.

4.3.6. Studies on Stability Assessment of Scaffolds

Stability assessment of scaffolds were carried out in compliance with ICH guidelines at the room temperature of 25ºC ± 2ºC / 60 % RH ± 5% RH for 12 months. At regular intervals of time, the scaffolds were examined for color change, drug content and *in vitro* drug release. The results obtained for stability studies were tabulated in Table 46.

Table 46: Stability Studies of 3D Printed Scaffolds

Evaluation Parameters	S1 Scaffold Formulation			S2 Scaffold Formulation		
	Initial	6th month 25 ± 2°C / 65 ± 5 % RH	12th month 25 ± 2°C / 65 ± 5 % RH	Initial	6th month 25 ± 2°C / 65 ± 5 % RH	12th month 25 ± 2°C / 65 ± 5 % RH
Color change	No color change	No color change	No color change	No color change	No color change	No color change
Drug Content	81.13 ± 0.02 %	82.05 ± 0.02 %	82.42 ± 0.01 %	88.24 ± 0.05 %	89.31 ± 0.02 %	90.16 ± 0.01 %
% CDR at 2 h for S1 and 24 h for S2	73.35 ± 0.03 %	74.68 ± 0.05 %	75.27 ± 0.03 %	85.54 ± 0.01 %	84.12 ± 0.02 %	83.84 ± 0.02 %

Data is expressed as Mean ± SD (n=3)

DISCUSSION

This chapter highlights the importance of research findings and describes the justification to support the data analysis for γ -MPS doped HNTs. The current section also provides an explanation for data findings related to the fabrication and characterization of sponges as well as 3DP scaffolds.

5.1. STRATEGY 1:

DOPING OF HNTs USING SILANE COUPLING AGENT

5.1. Characterization of Doped HNTs

5.1.1. Characterization of Functional Groups of Pristine HNTs and Doped HNTs

The FT-IR spectrum of PHNTs highlighted the appearance of absorption bands at the frequency of 910.25 cm^{-1} and 1032.74 cm^{-1}, indicating the existence of Al-OH frequencies and Si-O compounds. In addition to these two peaks, another prominent absorption band appeared at the frequency of 3622.4 cm^{-1}, which confirmed the existence of inter-layer molecular structure of water. Thus, the presence of these prominent groups confirmed the purity of PHNTs [57].

Similarly, an alternative to these absorption bands, two fresh peaks were identified in the spectra of all the DHNTs. The 1st peak was ranged between 1472.9 cm^{-1} to 1497.31 cm^{-1}, and the appearance of this peak was mainly associated with -CH2 deformation. While, the 2nd peak was in the range of 2925.13 cm^{-1} to 2967.34 cm^{-1}, the existence of this peak was contributed to -CH2 stretching [58]. The FI-TR of DHNT F1 revealed that, the resultant effectiveness of doping of HNTs was marginally reduced due to the lack of free -OH groups and inability to form the hydrogen bonding

with γ-MPS. Whereas, the FT-IR spectra of all the other samples indicated that the γ-MPS was effectively and adequately doped on the outermost layer of HNTs [122].

5.1.2. Studies on Thermal Analysis of PHNTs and DHNTs

5.1.2.1. TGA analysis

The TGA thermogram of PHNTs demonstrated an excellent thermal stability, without experiencing any appreciable reduction in mass loss up-to the temperature of 350 ºC. Further, it was observed that there was slight decrease in primary and secondary mass loss (2.47 % and 3.55 %). The primary mass loss occurred at the temperature ranged from 50 to 100 ºC and secondary mass loss resulted to be in the range of 360 to 550 °C.

Subsequently, TGA thermogram of DHNT F1 presented an enhanced weight loss approximately 2 – 5 %, over the range of 45 - 90 °C when compared with PHNTs. Thus, the higher mass loss validated an insignificant HNTs doping with γ-MPS. While, the TGA curves for DHNT F2 and F3 showed a decreased mass loss at the temperature of 365-595 °C, attributed to Si-OH structural de-hydroxylation. Thus, the reduction in mass loss in both the samples (F2 and F3) proved the successful functionalization of HNTs [123].

The TGA curves for DHNT F4, F5 and F8 samples revealed that, there was a significant increase in loss of mass, which could be particularly attributed to the possible interactions between -OCH_3 functional groups of γ-MPS and HNTs comprised with -OH groups. Therefore, in accordance with the results derived from DHNT F4, F5 and F8 samples, it could be likely assumed that the interaction effect decreased the effectiveness of doping HNTs with -MPS [124].

Similarly, an alternative to the above-mentioned data findings, it was clearly observed that, the samples DHNT F6 and F7 exhibited decreased mass loss. The reduction in mass loss was associated with siloxane group formation on the HNTs surface, which in-turn facilitated towards an effective doping of HNTs using silane coupling agents [125].

5.1.3. Structural Characterization of PHNTs and DHNTs

The diffraction pattern of PHNTs showed an intense peak with a basal space of 7.47 Å, which confirmed the hydrated nature of HNTs. The diffraction peak of DHNT F1 sample revealed that there was a slight change in the interlayer spacing (7.52 Å), indicating that γ-MPS was slightly intercalated within the layers of nanotubes. Furthermore, it was observed that, sample DHNT F2 and F3 showed an enhanced doping efficiency of HNTs as compared to F1 sample.

Subsequently, in contrast to these findings it was noted that, the extent and magnitude of the peaks in DHNT F4, F5 and F8 sample was significantly reduced as compared with other doped samples. The reduction in the intensity of peaks were mainly associated with the formation of strong bonds of hydrogen within the interlayers, which in-turn contributed towards the immobilization of aluminol moieties present within the layers of HNTs [126].

In addition to these findings, the doped sample DHNT F6 and F7 exhibited a sharp and intense peak, with a higher basal value of ranged from 7.73 Å to 7.79 Å. The shift to higher basal values was achieved by the impact of an intense heat and acceleration developed during the application of homogenization technique, which in-turn provided an intense atmosphere within the nanoclay galleries for the occurrence of intercalation of γ-MPS [127].

Hence, the significant intercalation of γ-MPS within the layers of HNTs, provided the complete doping of HNTs.

5.1.4. Topographical Characterization of PHNTs and DHNTs

The surface topography of PHNTs and DHNTs were characterized by TEM analysis. PHNTs were typically identified as natural hollow elongated tube-shaped multilayer configuration with a wide open cavity. Meanwhile, upon doping with γ-MPS, it was observed that the surface of DHNT F1 was relatively rough in texture with an uneven appearance, signifying a thin layer of silane groups were laminated on the HNTs surface. From the TEM image of DHNT F2 it was evident that, HNTs were untangled, as a result of development of covalent interactions with silane groups on the HNTs surface and thereby, enhanced the dispersion ability of HNTs.

Similarly, the TEM image of DHNT F3 and F6 sample indicated that, the external dimensions of nanotubes were significantly enlarged with a relatively decreased internal dimensions of the nanotubes. Thus, the enlargement of external dimensions proved that the HNTs surface was significantly doped [128]. The morphology of DHNT F4 and F8 samples appeared to be smooth in texture with an asymmetrical dimensions and thin layered walls. The appearance of this type of morphology signified the inadequate tubular functionality of the nanotubes. The topography of F5 sample resulted to be highly aggregated in nature. This type of aggregation was attributed to the existence of weak van-der Waals forces, due to HNTs excessive energy at the surface and its nano-scale dimensions [58].

Eventually, the morphology of F7 sample was observed to be remarkably consistent in texture with an excellent tubular integrity. Such type of nature of nanotubes was mainly due to the surface Si-O-Si group formation, which in-turn enhanced the hydrophobicity of nanotubes [129].

5.1.5. Surface Charge Potential of PHNTs and DHNTs

Zeta potential (ζ) is considered to be one of the fundamental key factor for the measurement of homogeneity and degree of stability of PHNTs and DHNTs. The ζ - potential of PHNTs resulted to be negatively charged (− 33.64 mV). The appearance of negatively charged potential was mainly contributed to the existence of silica groups on the PHNTs surface. On the other hand, it was observed that the ζ - potential of DHNTs was significantly increased. The ζ - potential of F1 sample resulted to be − 58.15 mV, indicated the relatively stable nature of sample.

On the contrary, DHNT F2 and F6 samples exhibited a higher potential value of − 79.23 and − 87.15 mV, signifying the excellent homogeneity and stability of samples. While, F4, F5 and F8 sample revealed a ζ - potential value of − 66.2, − 60.45 and −73.61 mV. The reduced ζ – potential values of these samples were due to the lack of availability of surface -OH groups of HNTs. Subsequently, F3 and F7 samples displayed higher ζ - values – 90.3 mV and – 95.7 mV. The existence of increased negative ζ - values corresponded to high dispersibility and stability of the sample [130].

5.1.6. Experimental Study Design

A prominent tendency in the discipline of pharmaceutical research is to design a high-quality products, by maintaining the standards and thereby promoting an

optimal equilibrium between the experimental design's independent variables and the selected response variables.

In the current investigation, a 2^3 factorial custom design was chosen to design a conceptual model for the optimization of process variables. The concentration of γ-MPS (X_1), concentration of HNT (X_2) and concentration of ethanol (X_3) were considered to be a set of independent factors with respect to response variables i.e. diffraction angle (2θ) and zeta potential (mV). The data values collected from an experimental study design were statistically analyzed by ANOVA using JMP software 16.1 v.

The results obtained from the statistical analysis (ANOVA) of Y_1 response indicated that, both the variables X_1 and X_3 exhibited statistical significance ($p < 0.05$). Whereas, independent factor X_2 exhibited statistical non-significance ($p > 0.05$). The effect of an individual independent factor on the response variables were evaluated in assistance with polynomial equation and 3-D response surface graphs.

In terms of polynomial equation and 3-D surface graphs, it could be stated that, all the three independent variables presented a synergistic effect with respect to response factor (Y_1). The synergistic effect exhibited by variable X_1 was mainly associated with γ-MPS intercalation within the interlayers of HNTs, which in-turn increased the d-spacing values of DHNTs. Subsequently, variable X_2 demonstrated a positive effect for Y_1. Unlike the polynomial equation and 3-D plots, the data obtained from the statistical analysis indicated that variable X_2 revealed non-significant effect ($p > 0.05$) for Y_1. The in-significance effect of X_2 variable was due to the restriction of free mobility of silane molecules within HNTs layers and thereby, decreased d-spacing value [20]. Similarly, variable X_3 revealed a positive effect towards

variable Y_1, indicating the complete miscibility of γ-MPS in ethanolic solvent. The complete miscibility resulted in enhanced d-spacing values. The interaction effect of variables (X_1X_3, X_2X_3 and X_1X_2) presented a negative effect for Y_1 variable.

The experimental data derived from ANOVA analysis of Y_2 variable revealed that, all the three independent variables were statistical significant ($p < 0.05$). This prominent effect, was contributed to the development of Si-O-Si bonds, as a result of silanol moieties being wrapped on the HNT surface [131]. In terms of polynomial equation and 3-D surface graphs, it could be stated that, variable X_1, X_2 and X_3 exhibited negative effect on response variable Y_2. The interactions of two variables (X_1X_3) in the equation presented a synergistic effect. Whereas (X_2X_3 and X_1X_2) variables showed negative effect for variable Y_2.

5.1.7. Statistical Optimization of DHNTs

The essence of selecting an optimal component from a range of feasible possibilities is defined as optimization. It's the method of implementing a variety of extensive approaches to attain the optimal set of process and/or a final product attributes provided a particular set of variables.

The desirability functional values were derived from the software in order to design an optimized formulation of DHNTs (ODHNTs). The ODHNTs were formulated by considering the desirability values and subjected for various characterization parameters [132].

The FT-IR spectrum of ODHNTs revealed the existence of absorption band at the frequency of 1492.34 cm^{-1} signifying -CH_2 group stretching. While, the peak at 2921.05 cm^{-1} confirmed the -CH_2 symmetric stretching. Similarly, the presence of

other prominent functional groups confirmed the DHNTs optimization. The thermal analysis of ODHNTs indicated the reduced mass loss of 0.10 %, signifying the confirmation of DHNTs optimization. Furthermore, the successful optimization of DHNT was confirmed by an increased d-spacing value of 7.73 Å, indicating a uniform sheet of γ-MPS was intercalated within the successive layers of ODHNTs. Lastly, ODHNTs exhibited a ζ -potential of -79.25 mV, signifying the sample had presented an excellent homogeneity and stability [20].

SEM analysis of PHNTs and ODHNTs were carried out to study the morphological characteristics of nanotubes. The SEM image of PHNTs revealed that the hollow nanotubes were densely clustered. The cluster of nanotubes was mainly attributed to existence of forces of van der Waals. On the contrary, the ODHNTs revealed that the magnitude of nanotubes cluster was significantly reduced. The reduced nanotubes cluster was achieved as a result of impact of silane (γ-MPS) [58].

The desirability value (D = 0.998) confirmed the reliability of the custom design with respect to selected responses [133].

5.2. STRATEGY 2

FABRICATION OF CIPROFLOXACIN HYDROCHLORIDE LOADED DOPED HNTs SPONGES

5.2.1. Physico-Chemical Characterization of Pure Cip HCL

The physico-chemical characteristics of a drug are extremely important in the arena of pharmaceutical sciences and play a very important role in numerous aspects of drug discovery, development and formulation. It includes the characterization of physical as well as chemical characteristics, purity, composition and stability of drug substance.

The melting point of pure Cip HCl resulted to be 320 °C, which was within the designated range as per IP, signifying the purity of drug sample. The UV absorption spectra of pure Cip HCl showed a single, sharp absorption peak at 271 nm, indicating the maximum UV absorbance (λ max) of drug. The standard calibration curve of Cip HCl exhibited a linear curve in the Beer's range of 2-10 µg/ml at λ max 271 nm [134]. The plot of absorbance (y axis) vs. concentration (µg/ml) (x axis) described a linear regression equation (y = mx + c) as y = 0.106x + 0.038 with a regression co-efficient (R^2) = 0.994.

Thus, the data obtained for the determination of λ max and calibration curve revealed that, UV estimation method was simple, precise, accurate and specific. Hence, this method can be efficiently used to determine the content and purity of drug sample. The FT-IR spectrum of pure Cip HCl confirmed the existence of significant absorption peaks, indicating the purity of drug sample. From, the DSC thermogram of

pure Cip HCl it was observed that, the sample was characterized by a single, sharp endothermic peak at 321.82 ºC, corresponded to the melting point of the pure drug [135].

Hence, the above characterization studies confirmed the authenticity and purity of Cip HCl as per the certificate of analysis provided by Aarti Drugs Limited, Mumbai.

5.2.2. Encapsulation Efficiency of Cip HCl in DHNTs

The strategy of drug encapsulation within the interlayers of DHNTs was accomplished by various mechanisms such as intercalation and vacuum / tubular entrapment method, with the aid of homogenization, sonication and lyophilization technique. Similarly, there are various factors that do play a significant role in encapsulating a wide range of drugs into DHNTs. These factors include: method of loading, concentration of DHNTs and the application of different processing techniques.

1. Homogenization Assisted Intercalation of Cip HCl within the Lumen of DHNTs.

The encapsulation of Cip HCl into DHNTs was achieved by intercalation method assisted by homogenization technique using ultra turrax homogenizer. Initially, mass ratio of Cip HCl: DHNTs was set to a value of 1:1 ratio, for which % EE resulted to be 29.76 %. Subsequently, when the ratio of DHNTs was further increased to 1:2 ratio, the % EE was slightly increased to 33.50 % [21]. The increased encapsulation efficiency was mainly due to the existence of a strong electrostatic interactions between the carbonyl groups of γ-MPS silane doped on the surface of HNTs and amine groups of Cip HCl [136].

Furthermore, the mass ratio of DHNTs was increased to 1:3 ratio and the % EE was found to be considerably higher (35.15 %) as compared to 1:1 and 1:2 ratio. This was made possible by the influence of high speed and the temperature generated during the homogenization process, which further resulted in the collisions of particles and thereby increased the interlayer spacing of DHNTs [137].

Similarly, when the mass ratio of DHNTs was further increased to 1:4 ratio, the % EE was no longer increased i.e. (33.27 %). The very likely explanation for this type of data was correlated to the presence of DHNTs at higher concentrations. The DHNTs at higher concentrations tend to aggregate and leads to the formation of reduced interlayer space in the nanotubes and thereby, restricts the free movement of Cip HCl into DHNTs [138].

2. Lyophilization Assisted Tubular Entrapment of Cip HCl into DHNTs.

To begin with the investigation of encapsulation efficiency of drug by tubular entrapment method, the drug was pre-loaded into the cavity of DHNTs with a comparatively modest ratio 1:1 (Cip HCl: DHNTs). When the drug was encapsulated at 1:1 ratio, the % EE was found to be 51.73 %. In instance, as the mass ratio of DHNTs was relatively increased to 1:2 ratio, the % EE was observed to be increased to some extent 52.34 % as compared to 1:1 ratio. The increase in % EE was contributed to the existence strong affinity and electrostatic attraction between Cip HCl and aluminol groups present in the lumen of nanotubes; which indirectly favored the encapsulation of Cip HCl within the lumen of DHNTs [139].

In addition to these ratios, the encapsulation of Cip HCl into DHNTs was experimented at the higher ratio values of 1:3. As a result of this, it was notably observed that, there was an increased % EE i.e. 53.40 %. The increased % EE for 1: 3

ratio was related to the coexistence of application of the principles of tubular entrapment process assisted by lyophilization technique. The application of high-pressure vacuum facilitated in the removal of the air bubbles located within the cores and the lumen of nanotubes, thereby allowed the drug molecules to get entrapped within the lumen of DHNTs [63].

The drug was further encapsulated into DHNTs in the ratio of 1:4 (Cip HCl: DHNTs). When the ratio of DHNTs was increased, it was observed that there was a decreased % EE i.e. 53.24 %. The decrease in % EE was influenced by two significant reasons

1. The increased concentration of DHNTs resulted in the formation of weak hydrogen bonding between the clay layers, which in-turn inhibited the entrapment of drug within the nanotubes.
2. Another reason that has contributed towards a decreased % EE was, an increased concentration of DHNTs resulted in the formation of stacked clay layers and thereby reduced the interlayer lumen space and thus inhibited the encapsulation of drug molecules [140].

3. Sonication Assisted Intercalation of Cip HCl into DHNTs.

The Cip HCl was encapsulated into DHNTs through a sonication assisted intercalation treatment, by varying the concentration of DHNTs in the ratios of 1:1, 1:2, 1:3 and 1:4.

At the very first, when the mass ratio was set to a value of 1:1 ratio, the % EE resulted to be 96.68 %. Similarly at the very next, when the ratio was fixed to 1:2 ratio (Cip HCl: DHNTs), the % EE was reported to be 98.46 %. The higher % EE for 1:2 ratio was attributed to strong hydrogen bonding between Cip HCl and tetrahedral

silicon sheets as well as aluminol octahedral sheets present on the edges of DHNTs [140].

Subsequently, when the drug was encapsulated into DHNTs at the ratio of 1:3, the % EE was significantly increased to 98.7 %. The increased % EE was mainly governed or influenced by several reasons.

1. The application of high-speed ultrasonic waves propagated the collision of particles, resulted in the reduction of particle size, which in-turn increased the surface area of DHNTs and enhanced the % EE by facilitating the Cip HCl to intercalate within the layers, as well as on the surface of DHNTs [58].
2. The high frequency sound waves generated during sonication process enabled the disruption of weak bonds present on the surface of DHNTs, and thereby, offered an additional space for the intercalation of drug [141].

Furthermore, the Cip HCl was encapsulated into DHNTs at the ratio of 1:4. When the ratio was set to 1:4 (Cip HCl: DHNTs), the % EE was decreased to 98.12 %. The decreased % EE was due to saturation of DHNTs, which in-turn reduced loading efficiency [66]. Thus, the sequence of enhanced drug loading with respect to different loading techniques include: 1:3 > 1:2 > 1:4 > 1:1 with respect to sonication > lyophilization > homogenization technique.

5.2.3. Fabrication of Lyophilized Sponges

The polyox sponges were prepared by lyophilization technique. The sponges of each batch formulations were circular in shape with a smooth and soft texture. The fabricated sponges appeared to be white to off-white in color.

5.2.4. Characterization of Sponges

5.2.4.1. Drug Excipient Compatibility Studies

Drug excipient compatibility study is considered as an introductory phase in the design and development of pharmaceutical products. It covers the identification of potential interactions between drug and excipients and further specifies the appropriateness of the excipients utilized for the preparation of pharmaceutical products. The FT-IR spectra of each sponge formulation revealed the prominent absorption bands which were identified in the spectrum of drug, indicating no significant interaction between drug and excipients.

The DSC thermogram of each sponge formulation revealed no significant change in the endothermic peaks of Cip HCl and other excipients, indicating the compatibility between drug and selected excipients [135].

5.2.4.2. Physical Characterization of Sponges

The diameter and thickness of sponges confirmed the uniformity and efficiency of the sponges, denoting the level of accuracy of the technique used to prepare the sponges.

The wetness integrity test indicated the instant formation of patch on gel and thereby ensured the easy removal of dressing material from the site of application [96].

5.2.4.4. Swelling Index of Sponges

The swelling ability of sponge plays a very important role as it facilitates the uptake of wound exudates, exchange of nutrients and waste and support for regeneration of new tissue formation. The swelling index of SF1 formulation resulted

to 78.24 %, whereas both SF2 and SF3 sponges revealed an increased swelling index of 85.04 % and 93.78 %. As compared to the swelling index of SF2 and SF3, the degree of swelling index was decreased in SF1 sponge formulation. The decrease in swelling index was due to the decreased concentration of PEO and thereby produced a weak interaction between silicates and polymeric matrix [142]. As a result of this, it was observed that SF2 formulation produced an adequate level of swelling index and this type of behaviour was attributed to the hydrophillic nature of polyox. The rate of swelling index is proportional to the hydrophilicity of polymer as well as the concentration of PEO [143]. Subsequently, the SF3 formulation revelaed an increase in swelling index, which is mainly associated with an increased concentration of PEO in SF3 formulation. The increased intensity of hydrophilicity resulted in an excessive swelling index and thereby, affected the structural integerity as well as resilience of the sponges.

Therefore, the sponge with a moderate / adequate swelling index proved to be an ideal for wound healing activity [103].

5.2.5.5. Compressive Properties of Sponges

In order to generate a certain organized structure and functionality that is necessary for tissue engineering, a sponge needs to meet certain characteristics. Among these characteristics, mechanical qualities like ultimate tensile strength, young's modulus and % break strain are crucial prerequisites that endow the sponge with its structural integrity and longevity.

The ultimate tensile strength for SF1 sponge was decreased as compared to SF2 and SF3 sponges. The decrease in tensile strength value for SF 2 sponge formulation was due to the uneven distribution of DHNTs within the networks of

polymeric matrix [144]. On the contrary to the results of tensile strength, it was observed that the young's modulus was significantly increased by three – four folds as compared to SF2 and SF3 formulations. The significant increase in young's modulus was due to decreased concentration of PEO. The higher the young's modulus, resulted in stiffness of the material [145].

Similarly, it was observed that the ultimate tensile strength was increased with an increase in PEO concentration in SF2 sponge formulation. The increase in tensile strength was likely to be associated with uniform dispersion of DHNTs within the polymeric matrix [146]. Another reason for increased tensile strength was the stiffness of silicate layers with a high aspect ratio. These properties of nanotubes facilitated an acceptable interfacial bonding and a significant degree of contiguity between the nanotubes and a polymeric matrix. Thus, this pattern of conduct limited the free transit of polymeric chains and thereby, increased the tensile strength of sponges [144].

Furthermore, it was observed that, with an increase in the concentration of PEO, the young's modulus of the sponge was found to be within an acceptable of an ideal skin sponge for wound healing activity. This type of behavior was mainly due to the increased cross-linked connectivity within the polymeric matrix, which in-turn resulted in the development of dense matrix structure within the composite sponges [147]. As a result of this, the % break strain was found to be prominently increased, with an increase in PEO concentration and this could be attributed to the entanglement of DHNTs with the PEO polymeric chains, under the influence strong intermolecular forces such as hydrogen bonds and thereby making the sponges more extendable [145].

As compared to the tensile strength values of both SF1 and SF2 formulations, SF3 formulation revealed a slight decrease in ultimate tensile strength. While, the

elastic modulus of SF3 sponge was also decreased with an increased concentration of PEO. This form of behavior could be possible as a result of formation of weak interconnectivity in the polymeric matrix. In contrast to these findings it was observed that, the % break strain was significantly increased, with an increase in the PEO concentration. The addition of increased concentration of PEO improved the % break strain, because PEO acts like a form of plasticizer [148].

5.2.4.6. Porosity of Sponges by BET Analysis

The BET isotherms derived for all the three sponge formulations confirmed the existence of mesoporous in nature. The mesoporous nature of sponges was mainly associated with dehydrated state of DHNTs. The results of BET analysis for SF2 sponge formulation revealed an increase in surface area and total pore volume, with a decreased average pore diameter. This type of behavior indicated that the Cip HCl loaded DHNTs were occupied and filled within the pores of polymeric matrix [149]. In contrast to these findings, it was observed that the surface area and total pore volume of SF1 formulation was significantly decreased with an increased average pore diameter. The increased pore size was due to the addition of PEO, which in-turn strengthened the configuration of pores [150].

Similarly, from the data of SF3 formulation it was observed that, with further increase in the concentration of PEO, the pore size was significantly decreased. The decrease in overall pore size of SF3 sponge was attributed to the impact of PEO aggregation at the pores and thereby resulted in pore blockage [151].

Hence, the results of BET analysis confirmed the nano-porous nature of developed sponges.

5.2.4.7. Morphological Characterization with Elemental Analysis

The structural characteristics and appearance, as well as the porosity of the sponges were analyzed by SEM analysis. The SEM morphology of SF1 formulation revealed a pronounced pore structures with an increased porosity. The enhanced porosity in SF1 formulation was contributed to the addition of PEO, which increased pore size and thereby resulted in complete wetness of sponges [152]. Subsequently, in SF2 formulation it was observed that, the porosity of sponges were slightly decreased as compared to SF1 formulation. The slightly decreased porosity was due to further increased concentration of PEO, which in-turn increased the pore-wall thickness and reduced the overall porosity of sponges [108].

Furthermore, it was noted that, the SF3 sponge formulation showed a drastic decrease in porosity, with further increase in PEO concentration. The decreased porosity was attributed to an increased viscosity of polymeric solution [153].

The EDX mapping and point analysis confirmed the presence of DHNTs within the sponge formulations.

5.2.4.8. Drug Content and *In Vitro* Diffusion Profile of Sponges

The drug content analysis of sponge formulation showed the uniform dispersion of Cip HCl within the polymeric matrix of sponge formulation.

The *in vitro* diffusion profile of SF1 formulation showed an initial burst effect with a percentage release of 82.49 % ± 0.01 at the end of 10 h. The initial burst effect and complete release of drug within 10 h of time interval was mainly due to the low concentration of PEO. The lower the concentration of PEO, resulted in an enlarged pore size and thereby enhanced the porosity of sponges. The increased porosity

favored a complete pattern of release with an initial burst effect. Another reason for complete release pattern within a span of 10 h was associated with a decreased tensile strength property. Tensile strength and porosity are inversely proportional to each other, a decrease in tensile strength resulted in an increased porosity of sponges and thus, assisted for complete release profile.

While, SF2 formulation showed an initial burst release followed by sustained release of 93.54 % ± 0.04 at the end of 24 h. The early burst effect of Cip HCl was achieved as a result of the attachment of Cip HCl on the external surface of DHNTs [154]. Further, a sustained release pattern was evidenced with an increased concentration of PEO. The increased concentration of PEO in the sponge formulation enabled the emergence of a dense polymeric hydrogel film and then eventually reduced the erosion of the drug from the polymeric matrix, thereby retarded the release profile of SF2 sponge formulation [155].

Subsequently, it was evident from the release pattern of SF3 sponge formulation that, there was no sign of initial burst release in SF3 sponge. The release of Cip HCl in SF3 was completely a sustained release pattern with a release rate of 82.37 % ± 0.03 at 24 h. This type of release profile was mainly contributed towards an increased concentration of PEO polymer. At the higher concentration of PEO polymer, the viscosity of the polymeric solution around the sponge was increased and resulted in the development of layer of gel with an extended diffusion pathway. Hence, SF3 formulation witnessed a sustained release pattern with no burst release effect [156].

An initial burst effect of Cip HCl appeared to be more effective in suppressing the growth of bacteria prior to the proliferation at the location of wound infection [157].

Subsequently, along with a burst effect, it is equally important to achieve a sustained release effect. Thus, in consideration to this phenomena, it was evident that SF2 sponge formulation has met the necessary requirements and proved to an ideal and best formulation when compared to other formulations.

In consistent to all the characterization studies, it was evident that SF2 formulation revealed an acceptable swelling index, with an excellent mechanical properties, adequate porosity and appreciable drug release pattern as compared to other sponge formulations (SF1 and SF3). Thus, SF2 formulation was selected as a best formulation and subjected for further characterization studies.

5.2.5. *In Vitro* Biodegradation studies

Another key factor to be considered during the design and development of sponge is the biodegradability. The sponge should degenerate and degrade within an appropriate time frame after insertion so as to ensure optimal tissue remodeling [158].

The deep soil burial approach was successfully employed to biodegrade SF2 sponge in both wet and dry circumstances. In a wet soil conditions, the SF2 sponge exhibited a complete biodegradation within a span of 60 min. The complete and relatively faster degradation of sponge was attributed to the hydrophilicity and adequate porosity of sponges [159]. The increased porosity resulted in higher water impregnation and thereby, accelerated the degradation process [105].

While in dry soil conditions, rate of biodegradation of SF2 sponge was relatively slow. The delayed rate of biodegradation was associated with the pores of the dry soil which were practically and completely filled with the air molecules, which in-turn resulted in an extremely low soil moisture content. The presence of low

moisture content, thereby restricted the impregnation of water molecule and thus, delayed the complete degradation of sponge in dry conditions [160].

5.2.6. Antimicrobial Studies

The antimicrobial activity of SF2 sponge towards *S. aureus* (Gram positive) and *E. coli* (Gram negative) were studied by examining the inhibition of zone surrounding the samples after an incubation period of 24 h. The anti-microbial activity with respect to two selected strains of micro-organisms revealed that, the control sample showed a decreased area of inhibition as compared to test sample. The reduced area of inhibition signified that, control sample exhibited a slight anti-microbial activity.

While, an increased area of inhibition presented by test sample (SF2 sponge formulation) indicated an excellent anti-microbial activity towards two different strains of micro-organisms. The slight variations in anti-microbial effectiveness could be attributed to variations in susceptibility towards different strains of organisms.

Thus, SF2 sponge showed an excellent anti-microbial activity and proved to have a significant potentials in anti-microbial dressing applications [73].

5.2.7. Cell Culture Studies

5.2.7.1. Cytotoxicity Studies

In accordance to the results of MTT assay, SF2 sponge showed a significant increase in % viability of cells, with the decrease in the concentration of sponges. The % viability of cells resulted to be 93.13 ± 0.12%, 92.94 ± 0.16%, 92. 99 ± 0.05%, 81.89 ± 0.12% and 64.14 ± 0.16% at the concentrations of 20, 40, 60, 80 and 100

µg/ml [161]. This indicates that the DHNTs (present in SF2 sponge), at the concentration upto 100 µg/ml failed to substantially induce cytotoxicity to A549 cells after exposing for 24 h [107]. Furthermore, it was observed that by gradually increasing the concentration of sponges from 100 µg/ml to 500 µg/ml, the % viability of cells was significantly decreased in a dose dependent pattern. The IC_{50} values for DHNTs SF2 sponges in A549 cells was found to be 405.9 µg/ml.

Similarly, the results of MTT assay signified that, the cytotoxicity induced by pure Cip HCl at the low concentrations (20 – 80 µg/ml) was found to be negligible. As a result of this, with further increase in higher concentrations (100 – 500 µg/ml), the viability of cells substantially decreased by two folds as compared to DHNTs present in SF2 sponges for 24 h with the IC_{50} value of 52.16 µg/ml [162].

Thus, these observations proved that DHNTs were bio-compatible and non-toxic in nature with a good cell viability. The increase in % viability of cells facilitated the cell attachment, spreading and growth on sponges with good cyto-compatibility.

Lastly, these findings confirmed that the prepared SF2 sponges were biocompatible and have a potential application in tissue engineering [163].

5.2.7.2. *In Vitro* Wound Healing Assay

In vitro scratch assay is a simple and cost-effective technique to study the mechanism of cell migration in wound healing process. It involves a scratching of confluent cell monolayer, inducing an artificial wound and the closure of the wound through the migration of the cells. To better understand the effect of SF2 sponge

comprised with DHNT and pure Cip HCl on wound healing activity, an artificial *in vitro* cell based (A549 cells) scratch assay was performed.

The efficiency of wound closure was distinctly reduced to 30.19 % at 24 h and 54.31 % at 48 h (R^2 = 0.99) to the cells exposed with Cip HCl (pure drug) with respect to SF2 sponge (test sample). In contrast to the data of Cip HCl it was observed that, test sample (SF2 sponge) revealed the greatest extent of migration of cells and thereby, exhibited a more effective wound healing potentiality. The extent of an increased mobility of cells was contributed to the porous nature of the sponge. The highly porous nature of sponge enabled the cells to easily penetrate and propagate within a 3D framework of sponge.

Furthermore, the A549 cells treated with SF2 sponge contributed to a significant decrease in scratch wound width at 48 h of the experimental study. The decreased width of the scratch wound suggests that, the extent of the cellular population at the wound's margin was much higher as compared to control. The enhanced cellular population was primarily due to the inclusion of DHNTs within the polymeric matrix of sponge formulation. The DHNTs functions as a cell growth promoters and stimulates the complete wound’s closure and good healing.

Hence, the incorporation of DHNTs within the sponge formulation promoted a significant rise in wound gap closure and thus promoted higher rates of wound healing.

5.2.8. *In Vivo* Wound Healing Activity

To carry out the *in vivo* wound healing activity, a partial thickness burn wound was induced on the dorsal portion of Wister rats and pharmacologically evaluated for wound closure (%), epithelialization period and histopathology of burn skin tissue.

5.2.8.1. Studies on Percentage Wound Closure Activity

Day 0: Initially, on the day of wound infliction (Day 0), the % wound closure resulted to be 0 % in all the three groups of animals i.e. GP I (Disease control), GP II (Standard – marketed cream i.e. 1 % w/w Silver sulfadiazine cream) and GP III (Test sample – SF2 sponge formulation), with an average wound area of 20.00 ± 0.00 mm.

Day 7: Progressively on the day 7, the wound closure (%) for GP III animals revealed that, there was a gradual increase in wound closure of about 21.66 ± 1.66 %, with a decrease in an average wound area of 15.6 ± 0.03 mm. Whereas, the wound closure (%) for GP I and GP II animals resulted to be significantly decreased as compared to GP III animals i.e.10.00 ± 0.01 % and 16.67 ± 1.05 %, with an average wound area of 18.0 ± 0.02 mm and 16.6 ± 0.02 mm ($p < 0.05$).

Day 14: The % rate of wound healing was progressively increased to 43.33 ± 4.014 %, with a decrease in wound area of 11.3 ± 0.08 mm for the animals treated with sponge formulation (GP III animals). In accordance to the graphical representation of wound closure (%) as shown in Figure 54, it was observed that, there was no significant difference in wound closure (%) and wound area for GP II animals on the 14th day of post treatment, when compared with GP III animals ($p >$

0.05) and the % rate of wound closure for GP II animals was found to be 42.50 ± 3.09 % with an average wound area of 11.5 ± 0.06 mm.

Similarly, with respect to GP I animals it was observed that, there was a significant decrease in the wound closure (%) 23.33 ± 3.07 % ($p \leq 0.05$) as compared to GP II and GP III.

Day 21: The GP III animals revealed a complete recovery of wound, with % wound closure rate of 97.66 ± 1.66 % and an average area was significantly reduced to 1.1 ± 0.03 mm. After the complete recovery of wound, the newly formed regenerated skin was smooth with no scar formation and resembling to the structural functions of normal skin [164]. The significant increase in % wound closure in Group III animals ($p \leq 0.05$) was mainly associated with the presence of DHNTs into sponges. The presence of DHNTs and optimal concentration of polyox polymer (5 % w/w) in sponges influenced the formation of highly porous structures with an excellent mechanical strength, which in-turn enabled the exchange of fluids and gas and helped in absorbing an excess of wound exudates, resulting in the improvisation of cells adhesion on the sponge bed and thereby, promoted an acceleration for wound healing process [165].

Similarly, the % rate of wound closure on the 21st day of post wounding for both control group (GP I - open wounded) and standard group (GP II - marketed formulation) resulted to be 50.83 ± 1.53 % and 78.33 ± 1.66 %, with an average wound area of 9.8 ± 0.03 mm and 4.3 ± 0.03 mm. In comparison with the % rate of wound closure of GP I animals, the animals treated with marketed formulation (GP II) presented a better wound healing activity. This was made possible due to the application of a cream comprising silver sulfadiazine as an active ingredient in the

formulation, which helped in accelerating up the healing process by shielding the site from inflammation and bacterial infections [108].

5.2.8.2. Epithelialization Period

In accordance to the findings of epithelialization period as described in results section indicated that, a faster the period of epithelialization would result in quick tissue regeneration process. While, slower the period of epithelialization, more time required for the formation of epithelium. Therefore, the group of animals treated with SF2 sponge formulation (GP III) exhibited the pace of epithelialization, followed by the application of marketed formulation (GP II) and the control group (GP I).

5.2.8.3. Histopathology of Burn Wound

In consistence to the findings of histopathological studies of GP III animals treated with SF2 sponge formulation it was noted that, a quicker and healthy healing was observed, which was explicable by the existence of a well-formed granulation tissue with a dense hair follicles and neovascularization as compared to GP II (standard group) and GP I (control group) [166].

5.2.9. Stability Studies

Stability tests were performed to determine an ideal storage conditions for maintaining the physical and chemical integrity of sponge formulation. The data obtained from stability studies indicated that the SF2 formulation was completely stable after being exposed to various storage conditions for a period of three months. Absolutely no significant variations were observed in the data obtained for wetness integrity, drug content and *in vitro* drug release of SF2 sponge formulation.

5.3. STRATEGY 3:

FABRICATION OF CIPROFLOXACIN HYDROCHLORIDE LOADED DHNTs 3D PRINTED SCAFFOLDS

5.3.1. Preparation of Cip HCl coated PVA Filaments

5.3.1.1. Efficiency of Pellet Coating

The efficiency of pellet coating for F1and F2 pellets resulted to be 60.23 % and 82.65 %. The enhanced efficiency of pellet coating for F2 pellets was primarily related to the inclusion of DHNTs in the form of nanofiller material. Ideally, DHNTs are best identified for their unique surface properties and the existence of both aluminol and silanol groups. These functional groups serves as a templates / pathways for the amplification of covalent bonding of distinct conjugates, thus enhanced the efficiency of coating of pellets [167].

5.3.2. Extrusion of PVA Filaments and Fabrication of Scaffolds

The extruded Cip HCl (PF1) and Cip HCl - DHNTs (PF2) PVA filaments were reproducible with a uniform dimensional measurements. Sometimes, it turns out

that, at times when the diameter of filament is excessively small, the efficiency of the material coming from the nozzle of printer is decreased. Similarly, the fabrication of enormously large sized filaments greatly contributes to the lack of appropriate extrusion process. Hence, it is essentially important to design and fabricate a filament with an appropriate dimensional measurements.

Thus, the designed and self – extruded both the filaments were optimal and efficient for the fabrication of scaffolds.

Subsequently, the designed filaments (PF1 and PF2) were further processed in the fabrication of scaffolds. The fabricated 3D scaffolds (S1 and S2) exhibited a smooth and glossy textural morphology with a uniform dimensional measurements.

5.3.3. Studies on Characterization of Scaffolds

5.3.3.1. Compatibility Study

The IR spectra of S1 and S2 scaffolds revealed no significant change in frequency absorption bands of functional groups of Cip HCl when mixed with other excipients of the formulations and thus indicated the compatibility between drug and added excipients. Hence, it can be concluded that, the excipients used in the fabrication of scaffolds were compatible with Cip HCl.

The thermal analysis of both the scaffolds (S1 and S2) revealed no significant change in the endothermic peaks of Cip HCl and other excipients, indicating the compatibility between drug and selected excipients [135].

5.3.3.2. Mechanical Properties of Scaffolds

The ultimate tensile property of S2 scaffolds was increased significantly ($p \leq 0.05$) with reference to S1. The decrease in the tensile properties of S1 scaffold was primarily attributed to the inclusion of Cip HCl, which in-turn interrupted the uniformity of lattice frame work of polymeric matrix [168]. Subsequently, the enhanced tensile property of S2 scaffolds was due to the existence of silica moieties on the HNTs surface. The availability of silica functional groups resulted in the formation of stiff layer and thus facilitated an extensive level of interfacial adherence and interaction on the polymer matrix, thereby restricted the free movement of chains of polymeric structures [144].

Similarly, with respect to young's modulus, the S2 formulation presented an increased young's modulus as compared to S1. The significant increase in young's modulus was contributed to the inclusion of DHNTs as a nanofiller. The incorporation of DHNTs accelerated the intensity of stress transfer and enlarged the lattice structure of clay minerals, which would be desirable to improve the young's modulus of scaffolds. While, a significant decrease in young's modulus of S1 was due to a diminished interlaced network, which in-turn assisted in the development of a loose network in the scaffold [147].

In contrast to the tensile strength and young's modulus, the % break strain of S1 was significantly increased with respect to S2 scaffold. The increased % break strain resulted in the softness of the scaffold. Whereas, a decreased % break strain in S2 resulted in the rigidity of scaffold [169].

5.3.3.3. Evaluation of Filament Morphology and 3D Printed Scaffolds

The filament surface layer of (PF1) exhibited a slightly uneven texture. The appearance of an uneven texture on the surface of PF1 filament was contributed to the

deposition of Cip HCl – PVA component. Subsequently, it was evident that the filament (PF2) surface appeared to be extremely rough in texture, with a homogenous and dense layer of Cip HCl-DHNTs laminated PVA component. The appearance of such form of morphology suggested that Cip HCl-DHNTs laminated PVA component was perfectly wrapped around the filament.

Furthermore, the morphology of S1 scaffold presented an impressive porous architectural design, with an increased porosity upto 82 %. The presentation of an enhanced porosity was attributed to a homogenous distribution of Cip HCl within the PVA polymeric matrix of scaffold, in association with the establishment of strong intermolecular bonding between PVA polymeric matrix and Cip HCl [170].

Similarly, scaffold 2 (S2) exhibited a thick pore-wall with an increased intensity of roughness on the surface of scaffold. The overall porosity for S2 scaffold was comparatively decreased to 60 % with respect to S1 scaffold. A reduced porosity enabled the material to be more resilient with an increased tensile properties and young's modulus.

Hence, the average pore dimensions of scaffolds ranged between 50 and 250 μm turns out to be an ideal for the regeneration of damaged tissues.

5.3.3.4. Drug Content and *In Vitro* Diffusion Pattern of Scaffolds

The drug content analysis of scaffold formulation revealed the consistent dispersion of Cip HCl within the PVA polymeric matrix of scaffold formulation.

The *in vitro* diffusion profile of S1 scaffold formulation exhibited an entire release of Cip HCl upto 73.35 % ± 0.05 at 2 h. The complete pattern of diffusion profile of Cip HCl was due to porous structure of the scaffold. The scaffold's porous

structure contributed towards the emergence of an extremely loose and floppy core network, thus enabled releasing media to penetrate easily within a core network of the scaffolds, accompanied by a complete drug diffusion from the polymeric matrix of scaffold [171].

Whereas, the *in vitro* diffusion profile of S2 scaffold formulation revealed an initial burst release effect accompanied by delayed release profile of Cip HCl. It seems more likely that the initial burst release of Cip HCl (an antibiotic), would interrupt the growth of bacteria before it gets multiplied at the site of action [157]. Subsequently, after an initial burst release, a sustained release effect was achieved. The successful achievement of sustained release effect was possibly due to an extensive electrostatic interactions and hydrogen bond formation between Cip HCl and DHNTs.

Another possible reason for sustained release effect of Cip HCl was the extent of thickness of Cip HCl-DHNTs coated on the surface of PVA filament. The increase in thickness of coating resulted in longer drug transport pathway and thus, facilitated a sustained release effect of Cip HCl from the scaffold [154].

5.3.4. Studies on *In Vitro* Wound Healing Activity of Scaffold S2 using A549 Cells

An *in vitro* cell line based (A549 cells) migration assay test was carried out, to study the impact of S2 scaffolds (Cip HCl-DHNTs PVA scaffolds - test sample) on *in vitro* wound healing activity.

The extent of wound's closure presented by a test sample (S2 scaffold) resulted to be 63.30 % at the end of 24 h and 80.16 % for 48th h. Subsequently in contrast to test sample, the rate of wound's closure exhibited by a control sample

(pure Cip HCl) was relatively decreased to 32.00 % at the 24th h and 56.18 % for 48th h.

The more extensive rate of cell mobilization exhibited by test sample was predominantly attributed to the scaffolds porous structure. The highly porous nature of scaffold offered an effective penetration of cells and multiplication within the three-dimensional scaffold network and exhibited an identical environment that resembles to natively extracellular matrix. Furthermore, the scratch width of wound treated with test sample (S2 scaffold) was substantially decreased at the 48th h of experimental study. The decrease in scratch width signifies the extent of the cell populace around the edges was considerably higher as compared to control sample. An increased cell populace was contributed to the inclusion of DHNTs in scaffolds. The presence of DHNTs functions as a cell growth promoter and stimulates the complete wound's closure and good healing [172].

Hence, the inclusion of DHNTs within the scaffold formulation promoted a significant rise in wound gap closure and thus promoted higher rates of wound healing.

5.3.5. Studies on Stability Assessment of Scaffolds

Stability assessment of 3D printed S1 and S2 scaffolds were performed to determine an optimal storage conditions in order to ensure the physical and chemical stability of scaffold formulations. The data obtained from stability studies suggested that S1 and S2 scaffold were absolutely stable when subjected to a storage condition of 25 ± 2°C / 65 ± 5 % RH for a period of 12 months.

In accordance to the data collected from the stability studies it was evident that, no substantial variations were observed for surface texture, color, drug content and % drug release of both the scaffolds.

Hence, the developed scaffolds proved to be stable under the provided storage conditions.

SUMMARY

STRATEGY - I

Recently nanomaterials have emerged progressively important in technological innovations as a result of their improved performance and customized physical, chemical, and biological characteristics of nanomaterials. Nanomaterials are generally classified in accordance to their origin, size, structure, and morphology. Thus, in considerations to these characteristic features, nanoclays or layered silicates were constituted as a distinctive form of nanomaterials [173].

Among the various forms of clay minerals, organically mesoporous HNTs have materialized as a potential fascinating nanomaterials [174]. HNTs are natural, non-toxic, and biocompatible, with an adequate surface area and an effective adsorption at the surface. However, in contrast to these characteristics, HNTs revealed an inadequate affinity with guest molecules due to a deficient intermolecular attractions. Thus, in order to optimize the properties of HNTs, it is extremely desirable to dope the surface of HNTs [175].

Design optimization also termed as experimental design is the process of selection of an appropriate design variables for the development of a pharmaceutical product with a predetermined standard for excellence.

An experimental custom design with two levels and three factors (2^3) was chosen using a (JMP software ® Version 16, SAS Institute, Singapore) to optimize the properties of HNTs. A total of 8 experimental trials were generated, formulated and then evaluated to confirm the successful functionalization / doping of HNTs. The DHNTs were characterized for FT-IR, X-RD, TEM, TGA and zeta potential analysis.

The data obtained from these characterization techniques indicated that HNTs were efficiently doped. The zeta potential values with negative charges for HNTs and DHNTs confirmed the existence of silica groups on the outer surface of nanotubes.

The experimental data values derived from the study design for DHNTs were analyzed statistically using JMP software for the prediction of best-fitting model, as well as to determine the significance (*p* value) of selected response variables (Y_1 = diffraction angle 2θ and Y_2 = zeta potential mV) by performing ANOVA. The relationship between independent and dependent variables were defined by the polynomial equations and the effect of each selected independent variable with respect to response variables were graphically analyzed by the 3-D surface plots and contour graphs.

Further, the desirability values were generated for the optimization of DHNTs. The desirability values for independent variables include: X_1 = 9 ml, X_2 = 37.5 g and X_3 = 87.5 ml. By considering the desirability values, the optimized DHNTs (ODHNTs) was prepared and evaluated for various characterization studies. The PHNTs and ODHNTs were specially characterized for SEM analysis. The SEM analysis signified that, upon doping the extent of agglomeration of nanotubes in DHNTs was considerably decreased. In addition to these characterization studies, the % error and total desirability (D) for ODHNTs was determined. The % error of ODHNTs with respect to response variable Y_1 and Y_2 resulted to be less than 5 % and the total desirability was found to be D = 0.998.

STRATEGY - II

Globally, burn injury / wound accounts to be the fourth major cause of mortality. In India, every year, an approximately of about 1 to 1.5 lakhs of populous are hospitalized as a mark of burn injuries / as an infection. The occurrence of burn injuries leads to patient's poorer standard of living and thereby, resulting in a reduction of physical functionality. Thus, the treatment, care and management of burn wounds is considered to be a primary requirement in health care system [176].

One of the most essential and widely accepted tool in the management and care of burn wounds includes: a design of an appropriate and advanced dressing material. Thus, the present research work aims to develop an antibiotic drug (Cip HCl) loaded DHNTs bio-polymeric sponges for burn wound healing activity.

Pre-formulation study of Cip HCl was performed and characterized for melting point, λ max and standard calibration curve, FT-IR and DSC analysis.

In the proposed research study, Cip HCl was encapsulated within the lumen of DHNTs via intercalation and tubular entrapment method with the aid of homogenization, lyophilization and sonication by varying the ratios at 1:1, 1:2, 1:3 and 1:4. In consistence to the findings of % encapsulation efficiency it was evident that, Cip HCl was successfully encapsulated at the ratio of 1:3 by intercalation method assisted by sonication technique.

Thus, in considerations with the findings of % encapsulation efficiency, 1:3 ratio was selected as an optimum ratio in the design of formulation table for the fabrication of lyophilized sponges.

The lyophilized sponges were fabricated by the incorporation of Cip HCl loaded DHNTs with the varying the concentrations of polyox polymer. The fabricated sponges were further subjected to various characterization techniques like wetness integrity test, swelling index, mechanical strength, porosity and *in vitro* drug release studies.

The FT-IR and DSC analysis confirmed that, the selected drug and excipients for the fabrication of sponges were compatible with each other. The wetness integrity confirmed the formation of patch on instant gel and thus, ensured the easy removal of dressing material from the site of application. The swelling index of SF2 formulation presented an adequate swelling properties as compared to SF1 and SF3 formulation. The mechanical properties of SF2 formulation was within an acceptable range of an ideal skin condition.

The BET analysis revealed the mesoporous nature of sponges with a type IV isotherm and average diameter of pore ranging from 2 – 50 nm. The SF2 and SF3 sponge formulation presented an increased surface area and total pore volume, with a decreased average pore diameter. While, SF1 formulation exhibited an increased pore diameter as compared to SF2 and SF3 formulation.

The morphological characterization of sponge formulation presented a porosity of 92.01 % for SF1 formulation, 84.25 % for SF2 and a decreased porosity of 68.15 % for SF3 formulation. In addition to the porosity of sponge formulation, EDX analysis also confirmed the presence of DHNTs in each of the sponge formulation.

The *in vitro* diffusion profile of SF1 formulation presented an initial burst effect with a release of 82.49 % ± 0.01 at the time period of 10 h. While, SF2 formulation revealed an initial burst effect with a sustained release of 93.54 % ± 0.04 at 24 h. Subsequently, SF3 formulation revealed no initial burst release, with a sustained release of 82.37 % ± 0.03 at 24 h.

Thus, in consideration to all the characterization parameters, it was evident that SF2 proved to be an ideal and promising formulation as compared to other two formulations. Hence, SF2 formulation was further subjected for other characterization studies.

The SF2 formulation selected as a best formulation was further characterized for biodegradation study by deep soil burial method. In wet soil conditions, the SF2 sponge was completely degraded 98.0 % within a span of 60 min. While, in dry state conditions, the sponge was totally degraded upto 97.2 % at the time period of 21 days.

The SF2 sponge formulation was also characterized for its anti-microbial activity with respect to two different strains of micro-organisms such as *S. aureus* and *E. coli*. The results of cytotoxicity studies for SF2 sponge formulation comprised with DHNTs as nano-filler, confirmed the bio-compatibility as well as non-toxic nature of DHNTs. The *in vitro* wound healing assay of SF2 formulation facilitated a complete closure of wound gap of A549 cells and promoted higher rates of wound healing activity.

Similarly, in consistent to *in vitro* wound healing activity, the potentials of SF2 sponge formulation towards *in vivo* wound healing activity was studied by inducing a partial thickness burn wound model on the male wistar albino rats. The results of *in vivo* wound healing activity confirmed the potentialities of SF2 sponge

formulation towards complete wound closure and formation of epithelialization as compared to group of animals treated with marketed formulation and disease control group. Stability studies of SF2 formulation was performed for a period of three months at two distinct conditions: Room temperature [25^{o}C ± 2^{o}C and RH 65 % ± 5 %] and accelerated temperature [40^{o}C ± 2^{o}C at RH 75 % ± 5 %]. The data obtained from stability analysis revealed that, SF2 sponge formulation was stable at two distinct storage conditions.

STRATEGY - III

Since the initial days of wound care and management, conventional dressings were preferentially utilized as a primary or a secondary dressing material to protect the wound from various contaminations. Furthermore, the fibrous structures of these dressings facilitate in absorbing a wound exudate and thus, protect the wound from the occurrence of infections. However, these dressings are required to be freshly changed at a regular time interval, which in-turn affects the patient compliance.

Therefore, in considerations to the above limitations of conventional dressings, a new paradigm shift has taken place in the history of tissue engineering applications, includes the evolution of a modern or advanced dressing. The design and development of 3D scaffolds with the aid of 3D printing technology has proved to be an excellent strategy in the field of tissue engineering.

Thus, the present investigation aims to design and develop an advanced 3D printed dressing material for wound healing activity.

In the proposed research work, PVA pellets were coated with two different coating materials: pure Cip HCl and Cip HCl-DHNTs. Upon coating, the % coating

efficiency for both the pellets were analyzed and the maximum coating efficiency was presented by Cip HCl-DHNTs PVA pellets. Furthermore, these coated pellets were self-extruded using Lab twin screw extruder to develop filaments. The prepared filaments were further processed for the fabrication of scaffolds by 3D printing technique and the fabricated 3D scaffolds were characterized for compatibility studies, mechanical properties, morphological studies, drug release profile and *in vitro* wound healing activity.

The FT-IR and DSC analysis indicated that, the drug and ingredients incorporated in the fabrication of scaffolds were compatible with each other, with no sign of any interactions. The tensile properties of scaffolds was adequate and resembled to the native skin structure. The surface morphology of filaments revealed the perfect wrapping of pure Cip HCl and Cip HCl-DHNTs on the surface of PVA filaments. Furthermore, the morphology of both the scaffolds revealed the porosity of 82 % for S1 and 60 % for S2. The average pore dimensions of both the scaffolds ranged from 50 and 250 μm, which turns out to be an ideal for the regeneration of damaged tissues.

The *in vitro* diffusion profile of S1 scaffold revealed an overall pattern of release of 73.35% ± 0.05 within two hours of the time profile. While, S2 scaffolds presented an inaugural burst release pattern, followed by a sustained release profile of 85.54% ± 0. 01 at the 12^{th} h of experimental study design. The *in-vitro* migration assay of A549 cells was performed for S2 scaffolds. The scaffold 2 exhibited a complete closure of wound gap at the 48^{th} h, as compared to pure Cip HCl (control). The complete closure of wound gap was due to the inclusion of DHNTs in S2 scaffolds, which facilitated a significant rise in wound gap closure and thus, promoted

higher rates of wound healing. Lastly, the stability studies of both the scaffolds were carried out at the temperature of 25 ± 2°C / 65 ± 5 % RH for a period of 12 months and the findings derived from the stability studies confirmed that both the scaffolds were stable at a given storage conditions.

CONCLUSION

The present research study emphasized on doping of HNTs using a γ-MPS by homogenization method, with an ultimate objective of investigating the impact of silane coupling agent on the surface properties of doped nanotubes. The DHNTs were utilized for two distinct purposes: fabrication of sponge and 3D printed scaffolds as a dressing material for the treatment of burn wounds.

At the very first, the doping of HNTs were successfully optimized by using JMP a statistical software, with an experimental study of 2^3 factorial custom design. The application of optimization tool for the DHNTs facilitated in the generation of quadratic polynomial equations, contour as well as 3D plots, ANOVA and the desirability values. An optimal data values were derived to analyze desirability for the concentrations of γ -MPS = 9 ml, HNT = 37.5 g and Ethanol = 87.5 ml. The total desirability of D = 0.998 confirmed the efficacy of an experimental study design and the successful optimization of DHNTs. The analytical characterization of DHNTs confirmed the doping of HNTs.

The very next step was to study the encapsulation efficiency of Cip HCl into DHNTs by various strategies. The % encapsulation efficiency of Cip HCl into DHNTs at the ratio of 1:3 by sonication technique revealed an increased efficiency with respect to homogenization and lyophilization technique and hence, proved to be an ideal proportion to fabricate a bio-polymeric lyophilized sponges.

The Cip HCl loaded DHNTs sponges with different concentrations of polyox polymer were fabricated and evaluated for various characterization parameters. The wetness integrity test of sponge formulation facilitated in the formation of patch on

instant gel and enabled the easy removal of dressing material from the site of application. The tensile properties and porosity of SF2 sponges were identical to native skin structure with an optimum swelling property. Similarly, an *in vitro* release of SF2 formulation demonstrated a promising burst effect followed by a sustained release effect for the management and treatment of burn injury.

Furthermore, it was evident that the developed SF2 sponge was completely biodegradable and non-toxic in nature, with a potent anti-microbial activity. The *in vitro* (cell culture studies) and *in vivo* wound healing activity demonstrated an excellent therapeutic effect of SF2 sponge formulation in the management and treatment of burn injury / wound.

Lastly, in addition to the fabrication of sponge formulation, 3D printed scaffolds were also designed and developed using FDM technique. The developed 3D scaffolds presented a promising mechanical properties with an excellent porosity and *in vitro* release profile. The *in vitro* wound healing activity on A549 cells confirmed the therapeutic efficacy of scaffold formulation in the treatment of burn injuries.

LIMITATIONS AND FUTURE SCOPE OF THE STUDY

Limitations:

In the proposed research work, the achievement of an adequate tensile strength and porosity control was quite challenging and difficult. As a result, in accordance to the sources of literature, the tensile property of sponges decreases with an increase in porosity. Therefore, designing a sponge with an adequate tensile property and porosity was mainly a challenging factor.

Future scope:

To investigate the efficacy and potentiality of developed sponge dressings on human beings, clinical trials study should be prioritized and conducted on human volunteers. Detailed *in vivo* wound healing activity could be performed in order to investigate various changes in bio-chemical parameters associated with burn wounds.

BIBLIOGRAPHY

1. Rangasamy M. Nanotechnology: a review. J Appl Pharma Sci. 2011 Apr 14; 1(2): 8-16.
2. Chavan T, Muttil P, Kunda NK. Introduction to nanomedicine in drug delivery. AAPS Adv Pharma Sci. 2020 Mar 19; 3-26.
3. Maheshwari PV, Gupta VN. Advances in nanotechnology in health care. Int J Pharm Tech Res. 2012 Jul 11; 4(3): 1221-27.
4. Vora LK, Gholap AD, Jetha K, Thakur Singh RR, Solanki HK, Chavda VP. Artificial intelligence in pharmaceutical technology and drug delivery design. Pharmaceutics. 2023 Jul 10; 15 (1916): 1-46.
5. Bose P. Optimizing drug delivery using AI. 2022.
6. Liu M, Wei X, Zheng Z, Li Y, Li M, Lin J, Yang L. Recent advances in nano-drug delivery systems for the treatment of diabetic wound healing. Int J Nanomedicine. 2023 Dec 31; 18: 1537-60.
7. Hanif M, Jabbar F, Sharif S, Abbas G, Farooq A, Aziz M. Halloysite nanotubes as a new drug delivery system: a review. Clay Minerals. 2016 Jun 1; 51: 469-77.
8. Khatoon N, Chu MQ, Zhou CH. Nano-clay based drug delivery systems and their therapeutic potentials. J Mater Chem B. 2020 Jul 1; 8(33): 7335-51.
9. Cheng X, Xie Q, Sun Y. Advances in nanomaterial-based targeted drug delivery systems. Frontiers Bioeng Biotech. 2023 Apr 13; 11: 1177151.
10. Nomicisio C, Ruggeri M, Bianchi E, Vigani B, Valentino C, Aguzzi C, Viseras C, Rossi S, Sandri G. Natural and synthetic clay minerals in the

pharmaceutical and biomedical fields. Pharmaceutics. 2023 Apr 29; 15 (5): 1-35.

11. Massaro M, Cavallaro G, Colletti C, Lazzara G, Milioto S, Noto R, Riela S. Chemical modification of halloysite nanotubes for controlled loading and release. J Mater Chem B. 2018 Jan 25; 6 (21): 3415-33.
12. Rafiee R, Shahzadi R. Mechanical properties of nanoclay and nanoclay reinforced polymers: a review. Poly Comp. 2019 Feb 10; 40(20): 431-45.
13. Paras LP, Sanchez-Fernandez JA, Vidaltamayo R. Nano-clays for biomedical applications. Handbook of Eco materials. Springer International Publishing; 2018.1-19 p.
14. Bibi, Icenhower J, Niazi NK, Shahid M, Bashir S. Book Chapter. Clay minerals: structure, chemistry and significance in contaminated environments and geological CO_2 sequestration. Elsevier Publishers; 2016.1-25 p.
15. Nagaraju K, Prasad T.N.V.K.V, Munaswamy V. Ramu Reddy Y. Nanoclay and its importance. Current J Appl Sci Tech. 2021 May 14; 40(13): 71-81.
16. Williams L, Haydel SE. Evaluation of the medicinal use of clay minerals as antibacterial agents. Int Geo Rev. 2010 July 15; 52(7/8): 745-70.
17. Franco-Urquiza EA. Clay-based polymers nanocomposites: essential work of fracture. Polymers. 2021 Jun 15; 13(2399): 1-40.
18. Massaro M, Cavallaro G, Lazzara G, Riela S. Covalently modified nanoclays: synthesis, properties and applications. Clay Nanoparticles. 2020 Jan 1; 305-33.
19. Sagare RD, Dasankoppa FS, Sholapur HN, Buruga K. Halloysite nanotubes: design, characterization and applications: a review. Farmacia. 2021 Mar 1; 69 (2): 208-14.

20. Sagare RD, Dasankoppa FS, Sholapur HN. Design, optimization and characterization of γ – methacryloxypropyltrimethoxy silane doped halloysite clay nanotubes using ultra-turrax homogenizer. J Pharm Innov. 2022 Sep 9; 18: 719-34.

21. Tan D, Yuan P, Bergaya FA, Liu D, Wang L, Liu H, He H. Loading and *in vitro* release of ibuprofen in tubular halloysite. Appl Clay Sci. 2014 Jul 1; 96: 50-55.

22. Kamble R, Ghag M, Gaikwad S, Panda BK. Halloysite nanotubes and applications: a review. J Adv Sci Res. 2012 May 10; 3(2): 25-29.

23. Setter OP, Segal E. Halloysite nanotubes – the nano-bio interface. Nanoscale. 2020 Oct 20; 12: 23444-460.

24. Liu M, Jia Z, Jia D, Zhou C. Recent advance in research on halloysite nanotubes-polymer nanocomposites. Prog Polym Sci. 2014 Aug 1; 39(8): 1498-1525.

25. Ali Q, Malik S, Malik A, Hafeez MN, Salman S. Role of modern technologies in tissue engineering. Arch Neurosci. 2020 Jan 31; 7(1): 90394-404.

26. Naderi H, Matin MM, Bahrami AR. Review paper: critical issues in tissue engineering: biomaterials, cell sources, angiogenesis and drug delivery systems. J Biomater Appl. 2011 Nov 1; 26(4): 383-417.

27. O'Brien FJ. Biomaterials and scaffolds for tissue engineering. Mater Today. 2011 Mar 1; 14(3): 88-95.

28. Naumenko E, Guryanov ID, Yendluri R, Lvov YM, Fakhrulin RF. Clay nanotube-biopolymer composite scaffolds for tissue engineering. Nanoscale. 2016 Feb 28; 8(13): 7275-71.

29. Nikolova MP, Chavali MS. Recent advances in biomaterials for 3D scaffolds: a review. Bioact Mater. 2019 Dec 1; 4: 271-92.

30. Dhivya S, Padma VV, Santhini E. Wound dressings - a review. Biomedicine. 2015 Nov 28; 5(4): 24-28.

31. Unnikrishnan K, Thomas LV, Ram Kumar RM. Advancement of scaffold-based 3D cellular models in cancer tissue engineering: an update. Front Oncol. 2021 Oct 25; 11: 4468-479.

32. Bahraminasab M. Challenges on optimization of 3D-printed bone scaffolds. Bio Med Eng. 2020 Sep 3; 19(1): 1-33.

33. Pasbakhsh P, De Silva R, Vahedi V, Churchman GJ. Halloysite: prospects and challenges of their use as additives and carriers – a focused review. Clay Miner. 2016 Jun 1; 51(3): 479-87.

34. Abbasi S. Purification, size separation and ionic functionalization of halloysite nanotubes. 2018 (Doctoral dissertation).

35. Zhao X, Zhou C, Liu M. Self-assembled structure of halloysite nanotubes: towards the development of high-performance biomedical materials. J Mater Chem B. 2020 Jan 1; 8(5): 838-51.

36. Saif MJ, Asif HM. Escalating applications of halloysite nanotubes. J Chil Chem Soc. 2015 Jun 10; 60(2): 2949-53.

37. Pandey G, Tharmavaram M, Rawtani D. Functionalized halloysite nanotubes: an “ecofriendly” nano material in environmental industry. In Handbook of Functionalized Nanomaterials for Industrial Applications. 2020 Jan 1; 417-33.

38. Lvov Y, Abdullayev E. Functional polymer – clay nanotube composites with sustained release of chemical agents. Prog Poly Sci. 2013 Oct 1; 38 (10-11): 1690-1719.

39. Saif MJ, Asif HM, Naveed M. Properties and modification methods of halloysite nanotubes: a state-of-the-art review. J Chil Chem Soc. 2018 Dec 1; 63(3): 4109-25.

40. Pasbakhsh P, Churchman GJ, Keeling JL. Characterization of properties of various halloysites relevant to their use as nanotubes and microfiber fillers. Appl Clay Sci. 2013 Apr 1; 74: 47-57.

41. de Melo Barbosa R, Ferreira MA, Meirelles L.M.A, Zorato N, Raffin FN. Nanoclays in drug delivery systems. Clay Nanopart. 2020 Jan 1; 185-202.

42. Biddeci G, Spinelli G, Colomba P, Blasi FD. Nanomaterials: a review about halloysite nanotubes, properties, and applications in the biological field. Int J Mol Sci. 2022 Sep 29; 23(19): 11518-536.

43. Nihei T. Dental applications for silane coupling agents. J Oral Sci. 2016 Mar 21; 58(2): 151-55.

44. Aziz T, Ullah A, Fan H, Jamil MI, Khan FU, Ullah R, Iqbal M, Ali A, Ullah B. Recent progress in silane coupling agent with its emerging applications. J Polym Environ. 2021 Nov 1; 1-17.

45. Goyal S. Silanes: chemistry and applications. J Indian Prosthodont Soc. 2006 Jan 1; 6(1): 14-18.

46. Arkles B. "Gelest" Silane coupling agents: connecting across boundaries. 3rd edition. Morrisville, PA: 2014; 1-72 p.

47. Witucki G. A silane primer: chemistry and applications of alkoxy silanes. J Coat Technol. 1993 Oct 21; 65: 57-60.

48. Zhu D, Hu N, Schaefer DW. Water-based sol-gel coatings for military coating applications. Handbook of Waterborne Coatings. 2020 Jan 1; 1-27.

49. Yuan P, Southon PD, Liu Z, Green M.E.R, Hook JM, Antill SJ, Kepert CJ. Functionalization of halloysite clay nanotubes by grafting with γ-aminopropyltriethoxysilane. J Phys Chem C. 2008 Oct 9; 112 (40): 15742-751.

50. Yan Y, Chen Y, Leng F, Huang L, Wang Z, Tian W. Recent advances on surface modification of halloysite nanotubes for multifunctional applications. Appl Sci. 2017 Nov 24; 7(12): 1215-24.

51. "Shin – Etsu Silicone" silane coupling agents. Shin – Etsu Chemical Co., Ltd. Japan. 2017; 1-28.

52. Tham WL, Chow WS, Mohd Ishak ZA. The effect of 3-(trimethoxysilyl) propyl methacrylate on the mechanical, thermal and morphological properties of poly (methyl methacrylate) / hydroxyapatite composites. J Appl Poly Sci. 2010 Oct 5; 118(1): 218-28.

53. Obaid Abu A, Gokce A, Yarlagadda S, Advani SG. Enhancement of adhesion between copper and vinyl ester in glass fiber-vinyl ester composites. Compos Interfaces. 2007 Jan 1; 14(2): 99-116.

54. Zanchi CH, Ogliari FA, Silva RM, Lund RG, Machado HH, Prati C, Carreno N.L.V, Piva E. Effect of the silane concentration on the selected properties of an experimental microfilled composite resin. Appl Adhes Sci. 2015 Dec 22; 3(1): 1-9.

55. Tan D, Yuan P, Bergaya FA, Liu D, Wang L, Liu H, He H. Loading and *in vitro* release of ibuprofen in tubular halloysite. Appl Clay Sci. 2014 Jul 1; 96: 50-5.

56. Rawtani D, Pandey G, Tharmavaram M, Pathak P, Akkireddy S, Agrawal YK. Development of a novel "nanocarrier" system based on halloysite nanotubes to

overcome the complexation of ciprofloxacin with iron: an *in vitro* approach. Appl Clay Sci. 2017 Dec 15; 150: 293-302.

57. Padhi S, Acharya Raju PG, Nayak CN. Mechanical and morphological properties of modified halloysite nanotube filled ethylene vinyl acetate copolymer nanocomposites. J Polym Eng. 2018 Mar 28; 38(3) 271-79.

58. Buruga K, Kalathi JT. Fabrication of γ-MPS modified HNT-PMMA nanocomposites by ultrasound-assisted mini-emulsion polymerization. JOM. 2018 Apr 2; 70(7): 1307-12.

59. Fizir M, Dramou P, Zhang K, Sun C, Pham-Huy C, He H. Polymer grafted - magnetic halloysite nanotubes for controlled and sustained release of cationic drug. J Colloid Interface Sci. 2017 Nov 1; 505: 476 - 88.

60. Mobarki M, Karnik S, Li Y, Mills DK. Therapeutic applications of halloysite. Appl Sci. 2021 Dec 22; 12(1): 87-103.

61. Kiani G. High removal capacity of silver ions from aqueous solutions onto halloysite nanotubes. Appl Clay Sci. 2014 Mar 1; 90: 159-64.

62. Fakhruddin K, Hassan R, Aslam Khan MU, Allisha SN, Abd Razak SI, Zreaqat MH, Mohd Latip HF, Jamaludin MN, Hassan A. Halloysite nanotubes and Halloysite-based composites for biomedical applications. Arab J Chem. 2021 Sep 1; 14(9): 103294-314.

63. Krejcova K, Deasy PB, Rabiskova M. Diclofenac sodium entrapment and release from halloysite nanotubes. Ces Slov Farm. 2013 Feb 1; 62(1): 28-34.

64. Kelly HM, Deasy PB, Ziaka E, Claffey N. Formulation and preliminary in vivo dog studies of a novel drug delivery system for the treatment of periodontitis. Int J Pharm. 2004 Apr 15; 274(1-2): 167-83.

65. Barman M, Mahmood S, Augustine R, Hasan A, Thomas S, Ghosal K. Natural halloysite nanotubes/ chitosan-based bio-nanocomposite for delivering norfloxacin, an anti-microbial agent in sustained release manner. Int J Biol Macromol. 2020 Nov 1; 162: 1849-61.

66. Pan Q, Li N, Hong Y, Tang H, Zheng Z, Weng S, Zheng Y, Huang L. Halloysite clay nanotubes as effective nanocarriers for the adsorption and loading of vancomycin for sustained release. RSC Adv. 2017 Apr 18; 7(34): 21352-359.

67. Deng X, Gould M, Azam Ali A. A review of current advancements for wound healing: biomaterial applications and medical devices. J Biomed Mater Res Part B Appl Biomater J. 2022 May 17; 110(11): 2542-73.

68. Abazari M, Ghaffari A, Rashidzadeh H, Badeleh SM, Maleki Y. A systematic review on classification, identification, and healing process of burn wound healing. Int J Low Extrem Wounds. 2022 Jun 11; 21(1): 18-30.

69. Mirhaj M, Labbaf S, Tavakoli M, Seifalian AM. Emerging treatment strategies in wound care. Int Wound J. 2022 Mar 17; 19(7): 1934-54.

70. Granito RN, Custodio MR, Muniz Renno AC. Natural marine sponges for bone tissue engineering: the state of art and future perspectives. J Biomed Mater Res Part B: Appl Biomater. 2017 Aug 1; 105(6): 1717-27.

71. Kim IY, Seo SJ, Moon HS, Yoo MK, Park IY, Kim BC, Cho CS. Chitosan and its derivatives for tissue engineering applications. Biotechnol Adv. 2008 Jan 1; 26(1): 1-21.

72. Deb P, Deoghare AB, Borah A, Barua E, Lala SD. Scaffold development using biomaterials: a review. Mater Today Proc. 2018 Jan 1; 5(5): 12909-919.

73. Wen Y, Yu B, Zhu Z, Yang Z, Shao W. Synthesis of antibacterial gelatin/sodium alginate sponges and their antibacterial activity. Polym. 2020 Aug 26; 12(9): 1926-37.

74. Azad MA, Olawuni D, Kimbell G, Md. Badruddoza AZ, Md. Hossain S, Sultana T. Polymers for extrusion-based 3D printing of pharmaceuticals: a holistic materials-process perspective. Pharm. 2020 Feb 3; 12(2): 124-58.

75. Jain A, Bansal KK, Tiwari A, Rosling A, Rosenholm JM. Role of polymers in 3D printing technology for drug delivery-an overview. Curr Pharm Des. 2018 Nov 1; 24(42): 4979-90.

76. Mahmood A, Singhavi G, Manchanda P, Pandey MM, Dubey SK, Gupta G, Chellappan DK, Seyfoddin A, Dua K. Applications of 3D printing for the advancement of oral dosage forms. In advanced 3D-printed systems and nano-systems for drug delivery and tissue engineering. Woodhead Publishing Series, Elsevier; 2020. 39-57 p.

77. Viera Rey DF, St-Pierre JP. Fabrication techniques of tissue engineering scaffolds. Woodhead Publishing; 2019 Jan 1.109-25 p.

78. Sagare RD, Dasankoppa FS, Sholapur HN, Banapurmath NR, Umarfarooq MA. Doped halloysite nanotubes as a nano-container for the fabrication of ciprofloxacin hydrochloride loaded 3D printed scaffolds. J Drug Deliv Technol. 2023 Jun 7; 86: 104637-649.

79. Castro N, Goldstein P, Cooke MR. Synthesis and manufacture of photo cross-linkable poly (caprolactone)-based three-dimensional scaffolds for tissue engineering applications. Adv Biosci Biotechnol. 2011; 2: 167-73.

80. Mwema FM, Akinlabi ET. Basics of fused deposition modelling (FDM). Fused deposition modelling: strategies for quality enhancement. 2020 May 30; 1-15.

81. Prakash KS, Nancharaih T, Rao V.V.S. Additive manufacturing techniques in manufacturing-an overview. Mater Today Proc. 2018 Oct 30; 5(2): 3873-82.

82. Winarso R, Anggorro PW, Ismail R, Jamari J, Bayuseno AP. Application of fused deposition modelling (FDM) on bone scaffold manufacturing process: a review. Heliyon. 2022 Nov 22; 8: 11701-15.

83. Araujo M.R.P, Sa-Barreto LL, Gratieri T, Gelfuso GM, Cunha-Filho M. The digital pharmacies era: how 3D printing technology using fused deposition modelling can become a reality. Pharm. 2019 Mar 19; 11(3): 128-42.

84. Shiffman MA, Low M. Burns, infections and wound management. Springer. 2020.

85. Li L, Zhou Y, Li P, Xu Q, Li K, Hu H, Bing W, Zheng Z. Peptide hydrogel-based sponge patch for wound infection treatment. Front Bioeng Biotechnol. 2022 Dec 15; 10: 1066306-315.

86. Garg RK, Singhvi I. Optimization techniques: an overview for formulation development. Asian J Pharm Res. 2015 Sep 1; 5(3): 217-21.

87. Osonwa UE, Ugochukwu JI, Ajaegbu EE, Chukwu KI, Azevedo RB, Esimone CO. Enhancement of antibacterial activity of ciprofloxacin hydrochloride by complexations with sodium cholate. Bull Fac Pharm Cairo Univ. 2017 Dec 1; 55(2): 233-37.

88. Nijhu RS, Jhanker YM, Sutradhar KB. Development of an assay method for simultaneous determination of ciprofloxacin and naproxen by UV spectrophotometric method. S J Pharm Sci. 2011 Jun 1; 4(1): 84-90.

89. Bhongade B, Talath S, Dhaneshwar S. A validated method for the quantitation of ciprofloxacin hydrochloride using diffuse reflectance infrared fourier transform spectroscopy. Int J Spectrosc. 2014 Feb 5; 16: 1-7.

90. Okoye EI, Okolie TA. Development and in vitro characterization of ciprofloxacin loaded polymeric films for wound dressing. Int J Health Allied Sci. 2015 Oct 1; 4(4): 234-45.

91. Lisuzzo L, Cavallaro G, Pasbakhsh P, Milioto S, Lazzara G. Why does vacuum drive to the loading of halloysite nanotubes? The key role of water confinement. J Colloid Interface Sci. 2019 Jul 1; 547: 361-69.

92. Salatin S, Barar J, Barzegar – Jalali M, Adibkia K, Kiafar F, Jelvehgari M. An alternative approach for improved entrapment efficiency of hydrophilic drug substance in PLGA nanoparticles by interfacial polymer deposition following solvent displacement. Jundishapur J Nat Pharm Prod. 2018 Nov 30; 13(4): 1-10.

93. Aziz DE, Abdelbary AA, Elassasy AI. Implementing central composite design for developing transdermal diacerein-loaded niosomes: *Ex vivo* permeation and *In vivo* deposition. Curr Drug Deliv. 2018 Nov 1; 15(9): 1330-42.

94. Enrione J, Diaz-Calderon P, Caroline R, Oppenheimer W, Sanchez E, Fuentes MA, Brown DI, Herrera H, Acevedo A. Designing a gelatin/chitosan/hyaluronic acid biopolymer using a thermophysical approach for use in tissue engineering. 2013 Dec 1; 36: 1947-56.

95. Singh A, Bali A. Formulation and characterization of transdermal patches for controlled delivery of duloxetine hydrochloride. J Anal Sci Technol. 2016 Nov 28; 7 (25):1-13.

96. Chevala NT, Kumar L, Veetilvalappil V, Mathew AJ, Paonam B, Mohan G, Shastry S, Balasubramanian K, C. Mallikarjuna Rao. Nano-porous and nano thickness film-forming bioactive composition for bio-medical applications. Sci Rep. 2022 May 17; 12(1): 8198-217.

97. Salehi S, Bodohi S. New formulation and approach for mucoadhesive buccal film of rizatriptan benzoate. Prog Biomater. 2017 Nov 6; 6: 175-87.

98. Boateng JS, Pawar HV, Tetteh J. Polyox and carrageenan based composite film dressing containing anti-microbial and anti-inflammatory drugs for effective wound healing. Int J Pharm. 2013 Jan 30; 441(1-2): 181-91.

99. Obayemi JD, Jusu SM, Salifu AA, Ghahremani S, Tadesse M, Uzonwanne VO, Soboyijo WO. Degradable porous drug-loaded polymer scaffolds for localized cancer drug delivery and breast cell / tissue growth. Mater Sci Eng. 2020 Jul 1; 112: 110794-860.

100. Yuan TT, Jenkins PM, DiGeorge Foushee AM, Jockheck – Clark AR, Stahl JM. Electrospun chitosan / poly ethylene oxide nanofibrous scaffolds with potential anti-bacterial wound dressing applications. J Nanomater. 2016 Jan 1 ; 1-11.

101. Beiranvand M, Farhadi S, Md-Gholami A. Adsorptive removal of tetracycline and ciprofloxacin drugs from water by using a magnetic rod-like hydroxyapatite and MIL-101 (Fe) metal – organic framework nanocomposites. RSC Adv. 2022 Nov 25; 12(53): 34438-53.

102. Vazquez-Vazquez FC, Chanes-Cuevas OA, Masuoka D, Alatorre JA, Chavarria-Bolanos D, Vega-Baudrit JR, Serrano-Bello J, Alvarez-Perez MA. Biocompatibility of developing 3D- printed tubular scaffold coated with nanofibers for bone applications. J Nanomater. 2019 May 9; 1-14.

103. Same S, Kadkhoda J, Navidi G, Abedi F, Aghazadeh M, Milani M, Akbarzadeh A, Davaran S. The fabrication of halloysite nanotube based multicomponent hydrogel scaffolds for bone healing. J Appl Biomater Funct Mater. 2022 Jul 29; 1-15.

104. Alkilani AZ, Musleh B, Hamed R, Swellmeen L, Basheer HA. Preparation and characterization of patch loaded with clarithromycin nanovesicles for transdermal drug delivery. J Funct Biomater. 2023 Jan 19; 14(2): 57-78.

105. Gaurav A, Ashamol A, Deepthi MV, Sailaja R.R.N. Biodegradable nanocomposites of cellulose acetate phthalate and chitosan reinforced with functionalized nanoclay: mechanical, thermal and biodegradability studies. J Appl Polym Sci. 2011 Jul 20; 125(S1): E16-26.

106. Isa T, Bakar Zakaria ZA, Rukayadi Y, Md Hezmee MN, Jaji AZ, Imam MV, Hammadi NI, Mahmood SK. Antibacterial activity of ciprofloxacin – encapsulated cockle shells calcium carbonate (aragonite) nano particles and its biocompatibility in macrophage J774A.1. Int J Mol Sci. 2016 May 19; 17(5): 713-30.

107. Sawicka D, Zapor L, Puchta LC, Dzierzawska KM. The in vitro toxicity evaluation of halloysite nanotubes (HNTs) in human lung cells. Toxicol Res. 2021 Jul 10; 37(3): 301-10.

108. Tripathi S, Singh BN, Singh D, Gaurav kumar, Srivastava P. Optimization and evaluation of ciprofloxacin loaded collagen / chitosan scaffolds for skin tissue engineering. 3 Biotech. 2021 Mar 7; 11: 1-7.

109. Talekar YP, Apte KG, Paygude SV, Tondare PR, Parab PB. Studies on wound healing potential of polyherbal formulation using *in vitro* and *in vivo* assays. J Ayurveda Integr Med. 2017 Apr 1; 8(2): 73-81.

110. Saurez-Arnedo A, Figueroa FT, Clavijo C, Arbeleaz P, Cruz JC, Munoz-Camargo C. An image J plugin for the high throughput image analysis of *in vitro* scratch wound healing assay. Plos One. 2020 Jul 28; 15(7): 0232565-579.

111. Kulshrestha S, Chawla R, Alam Md T, Adhikari JS, Basu M. Efficacy and dermal toxicity analysis of Sildenafil citrate based topical hydrogel formulation against traumatic wounds. Biomed Pharmacother. 2019 Apr 1; 112: 108571-80.

112. Guo HF, Ali RM, Hamid RA, Zaini AA, Khaza ai H. A new model for studying deep partial-thickness burns in rats. Int J Burn Trauma. 2017 Oct 25; 7(6): 107-14.

113. Brubaker AL, Carter SR, Kovacs EJ. Experimental approaches to tissue injury and repair in advanced age. Methods Mol Biol. Springer; 2015. 35-51 p.

114. Avinash S, Gowda DV, Suresh J, Arvind Ram AS, Srivastava A, Osmani RA. Formulation and evaluation of topical gel using *Eupatorium glandulosum michx* for wound healing activity. Der Pharm Lett. 2016 Aug 31; 8(8): 255-66.

115. Yiblet TG, Tsegaw A, Ahmed N, Dagnew SB, Tadesse TY, Kifle ZD. Evaluation of wound healing activity of 80 % methanol root crude extract and solvent fractions of *Stephania abyssincia* (Dill & A. Rich) Walp. (Menispermaceae) in mice. J Exp Pharmacol. 2022 Jul 11; 14: 255-73.

116. Elzayat EM, Auda SH, Alanazi FK, Al-Agamy Md. Evaluation of wound healing activity of Henna, pomegranate and myrrh herbal ointment blend. Saudi Pharm J. 2018 Jul 1; 26(5): 733-38.

117. Stability testing of new drug substance and products Q1A (R2). ICH harmonized tripartite guideline. 2003.

118. Weisman JA, Jammalamadaka U, Tappa K, Mills DK. Doped halloysite nanotube for use in the 3D printing of medical devices. Bioeng. 2017 Dec 17; 4(4): 96-112.

119. Korte C, Quodbach J. Formulation development and process analysis of drug-loaded filaments manufactured via hot-melt extrusion for 3D-printing of medicines. Pharm Dev technol. 2018 Feb 9; 23(10): 117-27.

120. Castano GM, Jimenez MM, Linares V, Caraballo I. Assessment of the extrusion process and printability of suspension-type drug-loaded affinisol ™ filaments for 3D printing. Pharm. 2022 Apr 15; 14(4): 871-88.

121. Pangesty AI, Todo M. Improvement of mechanical strength of tissue engineering scaffold due to the temperature control of polymer blend solution. J Funct Biomater. 2021 Aug 14; 12(3): 47-59.

122. Deng S, Zhang J, Ye L. Halloysite-epoxy nanocomposites with improved particle dispersion through ball mill homogenization and chemical treatments. Compos Sci Technol. 2009 Nov 1; 69(14): 2497-505.

123. Zargarian SS, Haddadi-Asl, Hematpour H. Carboxylic acid functionalization of halloysite nanotubes for sustained release of diphenhydramine hydrochloride. J Nanopart Res. 2015 May 15; 218(17): 1-13.

124. Yiu H, Botting CH, Botting NP, Wright P. Size selective protein adsorption on thio-functionalized SBA-15 mesoporous molecular sieve. Phys Chem Chem Phys. 2001 Jul 3; 3(15): 2983-85.

125. Sederidou I, Karabela M. Effect of the amount of 3-methacycloxypropyltrimethoxy silane coupling agent on physical properties of dental resin nanocomposites. Dent Mater. 2009 Nov 1; 25(11):1315-24.

126. Albdiry MT, Yousuf BF, Ku H, Lau KT. A critical review on the manufacturing processes in relation to the properties of nanoclay / polymer composites. J Compos Mater. 2013 Apr 1; 47(9): 1093-115.

127. Schaak R, Holder C. Tutorial on powder x-ray diffraction for characterizing nanoscale materials. ACS Nano. 2019 Jul 23; 13: 7359-65.

128. Terzopoulou Z, Papageorgiou D, Papageorgiou G, Bikiaris D. Effect of surface functionalization of halloysite nanotubes on synthesis and thermal properties of poly (ε-caprolactone). J Mater Sci. 2018 Jan 16; 53(9): 6519-41.

129. Zhan W, Yi H, Song S, Zhao Y, Rao F. Hydrophobic agglomeration behaviors of clay minerals as affected by siloxane structure. Colloids Surf A. 2019 May 5; 568: 36-42.

130. Nguyen TC, Nguyen TD, Vu DT, Dinh DP, Nguyen AH, Li TN, Dao PH, Nguyen TL, Bach LG, Thai H. Modification of titanium dioxide nanoparticles with 3-(Trimethoxysilyl) propyl methacrylate silane coupling agent. J Chem. 2020 Oct 27; 1-10.

131. Erdogan RA, Ilker A, Cevdet K. Influences of aminosilanization of halloysite nanotubes on the mechanical properties of polyamide-6 nanocomposites. Polym Compos. 2014 July 1; 35(7):1350 - 61.

132. Bakhtiari A, Ghasemi FA, Naderi G, Nakhari MR. An approach to the optimization of mechanical properties of polypropylene / nitrate butadiene rubber / halloysite nanotubes / polypropylene - g- maleic anhydride nanocomposites using response surface methodology. Polym Compos. 2020 Jan 29; 41(6): 2330-43.

133. Tafere C, Yilma Z, Abrha S, Yehualaw A. Formulation, in vitro characterization and optimization of taste masked orally disintegrating co-trimoxazole tablet by direct compression. PLoS One. 2021 Mar 16;16(3):1–35.

134. Prasad AR, Ratna JV. Development and validation of a simple UV-spectrophotometric method for the determination of ciprofloxacin hydrochloride present in the taste masked drug resin complex. Int J Appl Pharm. 2018 May 7; 10(3): 37-41.

135. Ejele AE, Ukiwe LN, Enenebeaku CK, Ejele NU. Evaluation of drug quality (III): determination of ciprofloxacin hydrochloride concentration in pharmaceutical tablets. Niger J Chem Res. 2015 Dec 17; 20: 19-28.

136. Satish S, Tharmavaram M, Rawtani D. Halloysite nanotubes as a nature's boon for biomedical applications. Nanomed. 2019 Jul 12; 12(6): 1-16.

137. Dhankar P. Homogenization fundamentals. J Eng. 2014 May 1; 4(5): 1-8.

138. Murugesan S, Scheibel T. Copolymer / clay nanocomposites for biomedical applications. Adv Funct Mater. 2020 Feb 26; 30(17); 1908101-129.

139. Kushwaha Singh SK, Kushwaha N, Pandey P, Fatma B. Halloysite nanotubes for nanomedicine: prospects, challenges and applications. Bio Nano Sci. 2020 Oct 21; 11: 200-08.

140. Massaro M, Lazzara G, Milioto S, Noto R, Riela S. Covalently modified halloysite clay nanotubes: synthesis, properties, biological and medical applications. J Mater Chem B. 2017 Mar 9; 5(16): 2867-82.

141. Lokesh Kumar, Deshmukh RK, Hakim L, Gaikwad KK. Halloysite nanotubes as a functional material for active packaging applications: a review. Food Bioproc Tech. 2023 May 2; 1-14.

142. Tao L, Zhonglong L, Ming X, Zezheng Y, Zhiyuan L, Xiaojun Z, Jinwu W. *In vitro* and *in vivo* studies of a gelatin / carboxymethyl chitosan / laponite ® composite scaffold for bone tissue engineering. RCS Adv. 2017 Nov 24; 7(85): 54100-10.

143. Zarghami A, Irani Md, Mostafazadeh A, Golpour M, Heidarinasab A, Haririan I. Fabrication of PEO / chitosan / PCL / olive oil nanofibrous scaffolds for wound dressing applications. Fibers Polym. 2015 Jul 11; 16(6): 1201-12.

144. Ahmed W, Siraj S, Al-Marzouqui AH. Comprehensive characterization of polymeric composites reinforced with silica microparticles using leftover materials of fused filament fabrication 3D printing. Polym. 2021 Jul 23; 13(15): 2423-48.

145. Kuo CY, Hsu YR. Tissue engineered polyethylene oxide / chitosan scaffolds as potential substitutes for articular cartilage. J Biomed Mater Res Part A. 2009 Nov 3; 91(1): 277-87.

146. Wong LW, Sun Goh CB, Pasbakhsh P, Lee Tan JB. Natural hollow clay nanotubes and their applications as polymer nanocomposites in tissue engineering. J Sci Adv Mater Dev. 2022 Jun 1; 7: 100431- 444.

147. Barbon S, Contran M, Stocco E, Todras S, Macchi V, De Cara R, Porzionato A. Enhanced biochemical properties of polyvinyl alcohol-based hybrid scaffolds for cartilage tissue engineering. Proc. 2021 Apr 21; 9: 730-34.

148. Kim TR, Kim MS. Goh TS, Lee JS, Kim YH, Yoon SY, Lee CS. Evaluation of structural and mechanical properties of porous artificial bone scaffolds fabricated via advanced TBA-based freeze-gel casting technique. Appl Sci. 2019 May 13; 9(9): 1965-82.

149. Nyankson E, Abogye SO, Efavi JK, Tuffour BA, Paemkal L, Asimeng BO, Balapangu S, Arthur PK, Tiburu EK. Chitosan-coated halloysite nanotubes as vehicle for controlled drug delivery to MCF-7 cancer cells *in vitro*. Mater. 2021 May 26; 14(11): 2837-53.

150. Deka M, Kumar M. Ionic transport in P (VdF-HFP)-PEO based novel microporous polymer electrolytes. Bull Mater Sci. 2010 Feb 27; 32(6): 627-32.

151. Beiranvand M, Farhadi S, Md-Gholami A. Adsorptive removal of tetracycline and ciprofloxacin drugs from water by using a magnetic rod-like hydroxyapatite and ML-101(Fe) metal-organic framework nanocomposite. RCS Adv. 2022 Nov 30; 12(53): 34438-53.

152. Ezzati P, Ghasemi I, Karrabi M, Azizi H, Fortelny I. Morphology evolution of poly (L-lactic acid) (PLLA) poly (ε-caprolactone) (PCL) and polyethylene oxide (PEO) ternary blend and their effects on mechanical properties for bio scaffold applications. Polym Korea. 2014 Sep 5; 38(4): 449-56.

153. Guan J, Fujimoto KL, Sacks MS, Wagner WR. Preparation and characterization of highly porous biodegradable polyurethane scaffolds for soft tissue applications. Biomater. 2005 Jun 1; 26(18): 3961-71.

154. Bediako EG, Nyankson E, Arhin DD, Tuffour BA, Lukowiec D, Tomiczek B, Yaya A, Efavi JK. Modified halloysite nanoclay as a vehicle for sustained drug delivery. Heliyon. 2018 Jul 1; 4(7): 1-21.

155. Li H, Hardy RJ, Gu X. Effect of drug solubility on polymer hydration and drug dissolution from polyethylene oxide (PEO) matrix tablets. AAPS Pharm Sci Tech. 2009 Jun 10; 9(2): 437-43.

156. Shojaee A, Emami P, Mahmood A, Rowaiye Y, Dukulay A, Kaialy W, Cuming I, Nokhodchi A. An investigation on the effect of polyethylene oxide concentration and particle size in modulating theophylline release from tablet matrices. AAPS Pharm Sci Tech. 2015 Mar 15; 16(6): 1281-89.

157. Teno J, Figuerez MP, Lopez K.J.F, Prieto C, Lagaron JM. Development of multilayer ciprofloxacin hydrochloride electrospun patches for buccal drug delivery. J Funct Biomater. 2022 Sep 29; 13(4): 170-89.

158. Bitar KN, Zakhem E. Design strategies of biodegradable scaffolds for tissue regeneration. Biomed Eng Comput Biol. 2014 May 8; 6: 1-8.

159. Pradhan AK, Rana PK, Sahoo PK, Biodegradability and swelling capacity of kaolin-based chitosan-g-PHEMA nanocomposite hydrogel. Int J Biol Macromol. 2015 Mar 1; 74: 620-26.

160. Pepper IL, Brusseau ML. Physical-chemical characteristics of soils and the subsurface. Environmental and Pollution Science. 2019 Jan 1; 9-22.

161. Bhat MP, Suresh RK, Rudrappa M, Basavarajappa DS, Swamy PS, Almansour AI, Perumal K, Nayaka S. Bio-inspired silver nanoparticles from *Artocarpus lakoocha* fresh fruit extract and evaluation of their anti-bacterial and anti-cancer activity on human prostate cancer cell line. Appl Nanosci. 2023 Apr 1; 13(4): 3041-51.

162. Kloskowski T, Gurtowska N, Nowak M, Joachimiak R, Bajek A, Olkowska J, Drewa T. The influence of ciprofloxacin on viability of A549, HepG2, A375.S2, B16 and C6 cell lines *in vitro*. Acta Pol Pharm Drug Res. 2011 Nov 1; 68(6): 859-65.

163. Wali A, Gorain M, Inamdar S, Kundu G, Badiger M. *In vivo* wound healing performance of halloysite clay and gentamicin -incorporated cellulose ether-

PVA electrospun nanofiber mats. ACS Appl Bio Mater. 2019 Sep 28; 2(10): 4324-34.

164. Liu M, Shen Y, Ao P, Dai L, Liu Z, Zhou C. The improvement of haemostatic and wound healing property of chitosan by halloysite nanotubes. RCS Adv. 2014 Apr 30; 4(45): 23540-553.

165. Noor SM, Roslan R, Fong SC, Nayan N.H.M. A potential of halloysite nanotube as a delivery vehicle in wound treatment. Int J Res Rev. 2022 Jun 15; 9(6): 290-96.

166. Nejjari R, Benabbes M, Amrani M, BouatiaM, Toufik J. Phytochemical screening and wound healing activity of *Telephium imperati* (L) in rats. S Afr J Bot. 2019 Jul 1; 123: 147-51.

167. Taheri-Ledari R, Zhang W, Radmanesh M, Cathcart N, Maleki A, Kitaev V. Plasmonic photothermal release of docetaxel by gold nanoparticles incorporated onto halloysite nanotubes with conjugated 2D8-E3 antibodies for selective cancer therapy. J Nanobiotechnol. 2021 Aug 11; 19(1): 1-21.

168. Al-Mofty S, Karaly AH, Sarhan WA, Azzazy H.M.E. Multifunctional haemostatic PVA / chitosan sponges loaded with hydroxyapatite and ciprofloxacin. ACS Omega. 2022 Apr 11; 7(15): 13210-20.

169. Govindasamy K, Dahlan NA, Pushpamalar J, Lim GK, Chai SP, Pasbakhsh P. Electrospun chitosan / polyethylene oxide (PEO) / halloysite (HAL) membranes for bone regeneration applications. Appl Clay Sci. 2020 Jun 1; 190: 105601-645.

170. Abbas N, Qamar N, Hussain A, Latif S, Arshad MS, Ijaz QA. Fabrication of modified release custom-designed ciprofloxacin tablets via fused deposit modelling 3D printing. J 3D Print Med 4. 2020 Jun 1; 4(1): 17-27.

171. Kumar A, Bali V, Kumar M, Pathak K. Comparative evaluation of porous versus non-porous mucoadhesive films as buccal drug delivery system of glibenclamide. AAPS Pharm Sci Tech. 2013; 14(4) Aug 30: 1321-32.

172. Kevadiya BD, Rakkumar S, Bajaj HC, Chettiar SS, Gosai K, Brahmbhatt H, Bhatt AS, Balvaliya YK, Dave GS, Kothari RK. Biodegradable gelatin-ciprofloxacin-montmorillonite composite hydrogels for controlled drug release and wound dressing application. Colloids Surf B. 2014 Oct 1; 122: 175-83.

173. Jeevanandan J, Barhoum A, Chan YS, Dufresne A, Danquah MK. Review on nanoparticles and nanostructured materials: history, sources, toxicity and regulations. Beilstein J Nanotechnol. 2018 Apr 3; 9(1): 1050-74.

174. Prinz OS, Segal E. Halloysite nanotubes-the nano-bio interface. Nanoscale. 2020 Nov 25; 12(46): 23444-60.

175. Yang Y, Chen Y, Leng F, Huang L, Wang Z, Tian W. Recent advances on surface modification of halloysite nanotubes for multifunctional applications. Appl Sci. 2017 Nov 24; 7(12): 1215-24.

176. Lukomskyj AO, Rao N, Pye JS, Li H, Wang B, Li JJ. Stem cells-based tissue engineering for the treatment of burn wounds: a systematic review of preclinical studies. Stem Cell Rev Rep. 2022 Feb 12; 18(6):1926-55.

177. Fu PS, Wang JC, Lai PL, Liu SM, Chen YS, Chen WC, Hung CC. Effect of gamma radiation on the sterility assurance, antibacterial ability, and biocompatibility of impregnated hydrogel microsphere protein and drug release. Polym. 2021 Mar 21; 13(6): 938 – 56.

Animal Ethical Committee Approval Letter

CERTIFICATE

This is to certify that the project proposal no Ph.D./DO1219018/KLECoPH/22 entitled "Design and Characterization of Wound Healing Activity in Wistar Rats of Halloysite Polymer Doped Novel Drug Delivery Conjugate" submitted by Ms. Revati D Sagare has been approved/recommended by the IAEC of KLE College of Pharmacy, Hubballi - 580031 in its meeting held on 10/09/2022 and 18 Wistar albino rats have been sanctioned under this proposal for a duration of next 12 months.

Authorized by	Name	Signature	Date
Chairman	Dr. A H M V Swamy		10/09/2022
Member secretary	Mr. Santosh B Patil		10/09/2022
Main nominee of CPCSEA	Dr. Prabhakar Adake		10.09.22

Certificate of Analysis

RM190192

Aarti Drugs Limited
Manufacturers of : Bulk Drugs & Chemicals

QUALITY CONTROL
CERTIFICATE OF ANALYSIS

Page No. 1 of 1

PRODUCT NAME :- CIPROFLOXACIN HYDROCHLORIDE IP		BATCH PACKED QUANTITY :- 600 KG	
BATCH NO. :-	CP /19020184	A.R. NO.	:- N198/FP/19/0535
MFG. DATE :-	FEB - 2019	ANALYSIS DATE	:- 05/03/2019
EXP. DATE :-	JAN – 2024	CAS NO.	:- 15307–81-0

SR. NO.	TESTS	SPECIFICATION	RESULTS
1	Description	A pale yellow, crystalline powder.	A pale yellow, crystalline powder.
2	Solubility	Soluble in water; slightly soluble in acetic acid and in methanol; very slightly soluble in ethanol; practically insoluble in acetone, in acetonitrile, in ethyl acetate, in hexane and in dichloromethane.	Complies
3	Identification A [By IR]	The absorption maxima in the spectrum obtained with the substance under examination correspond in position and relative intensity to those in the spectrum obtained with the reference substance or working standard.	Complies
	Identification B [By TLC]	The principal band in the chromatogram obtained with the test solution corresponds to that in the chromatogram obtained with the reference solution.	Complies
	Identification C	A curdy white precipitate is formed.	Complies
4	pH	Between 3.0 to 4.5, determined in a 2.5% w/v solution in water.	3.84
5	Related Substances [BY HPLC]	Ciprofloxacin ethylenediamine analog : NMT 0.2% Any other Individual Impurity : NMT 0.2% Total Impurities : NMT 0.5%	0.17% 0.10% 0.35%
6	Fluoroquinolonic acid	Any secondary spot in the chromatogram obtained with the test solution corresponding to the spot of fluoroquinolonic acid is not more intense than the spot in the chromatogram obtained with the reference solution.	Complies
7	Heavy Metals	Not more than 20 ppm	Complies
8	Sulphates	Not more than 400 ppm	Complies
9	Sulphated ash	Not more than 0.1%	0.050%
10	Water	Between 4.7 to 6.7%	6.57%
11	Assay (On anhydrous basis)	Not less than 98.0% & Not more than 102.0%,	100.59%

Opinion :- The above material passes as per IP Specification.

Prepared By- Gauravi meher, QC Officer, Date - 05.03.2019
Checked By – Rupali bhagat, QC officer, Date - 05.03.2019
Approved By – Shivaji kedar, QC Head, Date - 5/3/2019

List of Publications

1. **Sagare RD, Dasankoppa FS, Sholapur HN, Banapurmath NR, Umarfarooq MA.** Doped halloysite nanotubes as a nano-container for the fabrication of ciprofloxacin hydrochloride loaded 3D printed scaffolds. **J Drug Deliv Technol**. 2023; 86: 104637-649. **Impact Factor: 5.062**
2. **Sagare RD, Dasankoppa FS, Sholapur HN.** Design, Optimization and Characterization of γ-Methacryloxypropyltrimethoxysilane-doped Halloysite Clay Nanotubes Using Ultra-turrax Homogenizer. **Journal of Pharmaceutical Innovation**. 2022, 18: 719 – 34. **Impact Factor: 2.538**
3. Sagare RD, Dasankoppa FS, Sholapur HN, Buruga K. Halloysite nanotubes: design, characterization and applications: a review. Farmacia. 2021; 69 (2): 208-14. **Impact Factor: 1.6**

List of Presentations

1. **Revati Dharampal Sagare, Fatima S Dasankoppa.** Halloysite nanotubes: Design, Characterization and Applications: A Review. International Conference on **"Recent Advances in Drug Discovery (QSAR Modelling, Molecular Docking, Molecular Simulation)** held at Dr. Rajendra Gode Institute of Pharmacy, Amravati on 15th and 16th December 2021.
2. **Revati Dharampal Sagare, Fatima S Dasankoppa.** Design, optimization and characterization of γ-methacryloxypropyltrimethoxysilane doped halloysite clay nanotubes using ultra turrax homogenizer. **For the award of "Dr. T.M.A. Pai Researcher Award"** in the **"International Conference on Biomaterial – Based Therapeutics, Engineering and Medicine".** Organized by Manipal Institute of Technology, MAHE on 17th - 20th December 2021.
3. **Revati Dharampal Sagare, Fatima S Dasankoppa.** Optimization and Characterization of Organo-Functionalized Natural Clay Nanotube with Selective Coupling Agent in the **"International Conference on Biomedical and Clinical Research.** Organized by Shri Dharmasthala Manjunatheshwar University, Dharwad, Karnataka on 21st to 22nd November 2022.

Journal of Drug Delivery Science and Technology 86 (2023) 104637

Contents lists available at ScienceDirect

Journal of Drug Delivery Science and Technology

journal homepage: www.elsevier.com/locate/jddst

Doped halloysite nanotubes as a nanocontainer for the fabrication of ciprofloxacin hydrochloride loaded 3D printed scaffolds

Revati Dharampal Sagare [a], Fatima Sanjeri Dasankoppa [a,*], Hasanpasha N. Sholapur [b], N.R. Banapurmath [c], M.A. Umarfarooq [c]

[a] Department of Pharmaceutics, KLE College of Pharmacy, Hubballi, Karnataka, India
[b] Department of Pharmacognosy, KLE College of Pharmacy, Hubballi, Karnataka, India
[c] Centre of Excellence in Material Science, School of Mechanical Engineering, K.L.E. Technological University, BVB Campus, Hubballi, Karnataka, India

ARTICLE INFO

Keywords:
Ciprofloxacin hydrochloride
Doped halloysite nanotubes
Poly vinyl alcohol
Filaments
3D printing
Scaffolds

ABSTRACT

Burn injuries are considered to be the most catastrophic form of skin injury, with a slight risk of mortality. This type of injury has a significant negative impact on both individuals and health care system. The hollow nanotubular structures of doped halloysite nanotubes (DHNTs) facilitate in loading a wide variety of active molecules and make a potential nanocarrier for the delivery of drugs. Coincidentally, the high mechanical strength, good biocompatibility, and hemostasis properties of DHNTs offer a new platform for the fabrication of scaffolds to promote faster wound healing activity. Ciprofloxacin hydrochloride (Cip HCl) was chosen as the model drug to control the bacterial proliferation at the site of injury. Therefore, the present study was aimed to design a customized drug loaded nano-polymeric scaffolds by three dimensional (3D) printing techniques for tissue engineered applications in pharmaceutical sciences. Cip HCl loaded DHNTs coated poly vinyl alcohol pellets were extruded for the preparation of filaments by the hot melt extrusion process, and the prepared filaments were further processed for the fabrication of 3D printed scaffolds by fused deposit modelling (FDM) technique. The pellets were free-flowing with a coating efficiency of 60.23 – 82.65%. Scaffold 1 (S1) presented an excellent porous structure, while scaffold 2 (S2) revealed a slight porous structure with the porosity of 60%. The average pore diameter for both scaffolds ranged from 50.82 ± 23 to 93.06 ± 52 μm. S1 expressed a conventional release pattern of 73.35% ± 0.02 within 2 h of the time profile, S2 evidenced an inaugural burst release of 42.84% ± 0.05 at 2 h, followed by a sustained release of 85.54% ± 0.17 up to 12 h. Thus the FDM technique proves to be an ideal approach for the design of drug nanofiller coated polymeric 3D scaffolds for personalized drug delivery systems in the arena of tissue engineering and pharmaceutical sciences.

1. Introduction

In accordance with the recent updates from World Health Organization (WHO), 'injury' ranks in top ten in contributing to premature deaths and disabilities [1]. The term "injury" is derived from a Latin word "in + jus" which means "not right", defined as physical damage to an individual inflicted by an intense flow of energy such as thermal, chemical, mechanical, electrical, and radial energy [2]. The most prevalent way to classify injuries is according to the presumptive detrimental impacts: categorized into intentional and accidental injuries. However, the large chunks of injuries fall under the category of accidental injuries of which, burn injuries serve as the root cause for skin and tissue damage [3].

Burn injury is considered as the one of the most difficult, complexed and incapacitated forms of trauma, serves as a primary cause in inducing physiological stress, disability and skin damage thereby, facilitating in the reduction of patients quality of life. Every year, it is estimated that over 3,00,000 individuals are injured or die as a result of various types of burns such as high voltage-electricity, heat, radiation or chemical exposure and thereby resulting in the formation of (Second-degree) partial or (Third-degree) full-thickness burns. These considerations potentially contribute to serious complications such as bacterial infections, hypovolemic shock, loss of body fluids, electrolyte imbalance, respiratory failure and tissue contraction [4]. Nevertheless, injuries could be minor or severe; they play a substantial role in the socio-economic crisis of the country as well as severely traumatize the

* Corresponding author. Department of Pharmaceutics, KLE College of Pharmacy, Hubballi, (A Constituent Unit of KAHER, Belagavi), 580031, Karnataka, India.
E-mail address: fsdasankop@gmail.com (F.S. Dasankoppa).

https://doi.org/10.1016/j.jddst.2023.104637
Received 16 March 2023; Received in revised form 30 May 2023; Accepted 4 June 2023
Available online 7 June 2023
1773-2247/

individuals. Thus, catering to a systemic way of pharmaceutical treatment and trying to optimize and rejuvenate the tissue functions in burn injuries has posed new challenges time to time to the health-care professionals, and it has always been framed as a matter of concern.

Autografts are often chosen as the benchmark for the treatment of full-thickness burn injuries [5]. According to the literature search, a number of studies postulate that the application of autografts for the restoration of damaged tissue may have a chance of failure. The failure is due to a lack of donor availability and impotent revascularization of the tissue grafts. Another important aspect to be considered when it comes to the failure of these grafts is the immunological rejection of autografts [6], whereas, partial-thickness burn injuries are often treated by using traditional wound dressings. These dressings include cohesive wraps, sterile bandages, impregnated gauze, plasters, cotton and non-adherent dressings. The traditional dressing materials are frequently used to protect the skin from contamination. But, there are some shortfalls such as -

1. Periodic replacement of dressing material is necessitated to prevent the maceration of viable tissues.
2. It is painful and causes discomfort while peeling the dressing material, when it turns into moist and adheres to the injury as a result of excessive drainage of wound exudates [7].
3. Insufficient mechanical strength, delays healing of wounds and injuries along with poor regeneration of tissue and skin appendages.
4. Restricted and uncomfortable for free body movement.
5. Specially used to clean the superficial injuries.
6. Poor oxygen permeability and a lack of biomimicry.

Thus, to overcome these challenges, there is a critical need to come up with unique and innovative strategies [8].

Fabrication of dressing material impregnated with antibiotics and targeted to release at the wound site in order to prevent bacterial infection offers an advantage over traditional dressing material. The essence of a drug delivery dressing on an infected injury is to absorb wound exudates, suppress the bacterial load and insulate the wound from bacterial infection. As a result, these ideal qualities of drug delivery dressings intensify the healing process and fosters the development of tissue engineered scaffolds as advanced solutions over traditional dressing materials [9].

Over the last few decades, tissue engineered scaffolds have proven to be the most attractive and incredibly effective in the treatment of burn injuries. Scaffolds are designed to offer optimal structural support and create a three-dimensional network to promote the transplantation of cells and to revitalize the damaged tissue [10]. Traditionally, a wide range of scaffolds have been designed and fabricated by adopting conventional techniques (solvent casting, freeze drying, gas foaming and electro-spinning). By taking into consideration, these techniques do own a few limitations such as high energy utilization, consume more time, pretty small with uneven pore configurations [11]. To overcome these limitations, many alternative approaches, such as three-dimensional (3D) printing technologies, have come out with an attractive offering for the preparation of prototypes.

3D printing also known as additive manufacturing or rapid prototyping is the process of depositing material layer in layers to fabricate three dimensional objects using a computer-aided design (CAD) model or scan. 3D printing technology enables us to devise a specifically tailored and complex biomaterial with desirable and tunable qualities for various clinical applications. The most favorable and acceptable form of prototyping technique, which is being constantly researched, is the fused deposit modelling for the design of scaffolds.

Fused deposit modelling (FDM) is colloquially termed as fused filament fabrication. It is a process that involves the deposition of layers onto the build platform by extruding the molten thermoplastic polymeric filaments through a high temperature nozzle. Filaments are tagged as a cornerstone for the successful application of 3D printing technology. Therefore, the fabrication of drug loaded and high caliber filaments with biodegradable and biocompatible characteristics has always been on the sets of priority for researchers in the development of customized scaffolds.

Poly vinyl alcohol (PVA) is a well-known thermoplastic polymer belonging to a class of synthetic materials. PVA is synthesized via suspension polymerization of vinyl acetate. It is non-toxic, water soluble, biocompatible and biodegradable in nature with excellent tensile properties. Due to its unique and versatile properties, PVA is a well-recognized supporting material in the domain of fused deposit modelling [12]. No doubt that PVA offers good mechanical strength but it is very important to maintain the structural integrity which is achievable by incorporating nanofillers, thereby allowing 3D printed objects to present incredible features like elasticity and potentiality.

Over the last few years, the utility of various organically-functionalized clay minerals has been widely explored in the fields of pharmaceuticals, nutraceuticals and biomedical sciences. Among them, halloysite clay nanotubes (HNTs) are a well-known class of phyllosilicate compounds mined from the natural clay deposits. They are hydrated alumino-silicates with an empirical formula $Al_2Si_2O_5(OH_4).2H_2O$ (similar to kaolin, separated by a layer of water molecules). HNTs are natural in origin, biocompatible, biodegradable, with a remarkable thermal stability and high aspect ratio (L/D 10 - 50). HNTs extensively characterized by a hollow tubular layered structure, typically composed of one sheet of tetrahedral (SiO_4) and another sheet of octahedral (AlO_3) in a stoichiometric ratio of 1:1. The lengths of the nanotubes range from 400 to 1000 nm, while the inner diameter varies from 10 to 40 nm and the outer diameter is in the range of 40 – 80 nm. The majority of Al–OH groups are situated within the lumen of HNTs, whereas, the outer surface of HNTs consists of siloxane Si–O–Si groups. The corner sheets of HNTs are primarily composed of Al–OH and Si–OH groups, which in turn make them hydrophilic in nature and offer gibbsite-like orientation [13]. The most defining quality of HNTs is the presence of selective charges on their surfaces; the outer surface is negatively charged while the inner surface is positively charged. Thus, the presence of selective charges provides multiple options for HNTs to resonate with a variety of biological and synthetic molecules and assist the drug substances to get entrapped either on the surface or in the lumen of HNTs. HNTs are used as a nanocarrier or nanofiller to increase the surface area, toughness, thermal stability, surface reactivity and mechanical strength; to achieve these properties HNTs are being subjected to dope with a variety of silane coupling agents. Examples: γ-methacryloxypropyltrimethoxy silane (γ-MPS), 3-Aminopropyltriethoxysilane (APTES), Vinyltrimethoxysilane (VTMS), 3-Mercaptopropyltrimethoxysilane (MPTMS) and Glycidoxypropyltrimethoxysilane (GPTMS). Sagare RD (2022) successfully demonstrated the doping of γ-MPS on the surface of HNTs by homogenization technique and reported the findings regarding an increase in basal spacing, negative zeta potential values and decrease in intensity of aggregation of nanotubes. These results facilitate in loading a wide range of biologically active molecules and make HNTs a potential nanocarrier for the delivery of drugs [14]. Thus, these unique and versatile properties of HNTs offer new possibilities for the design and development of various novel drug delivery systems such as scaffold drug delivery systems, hydrogel drug delivery systems, vesicles drug delivery system and microsphere drug delivery systems. Among these types of drug delivery systems, halloysite based hydrogel drug delivery systems have drawn a whole lot of interest as a wound dressing material. Recently, Sabbagh N (2017) has published an article on halloysite based hydrogel drug delivery systems. In reference to this article, halloysite based hydrogels with an excellent biocompatibility and biodegradability have the potential to mimic the natural extracellular matrix (ECM). In contrast, hydrogels present poor gel strength with an acceptable mechanical strength. As a result of this, these qualities of hydrogels slightly constrain their applications in the field of tissue engineering for the treatment of wound healing and bone regeneration activity [15]. Therefore, in comparison with halloysite

based hydrogels, tissue engineered halloysite based 3D printed scaffolds with tunable qualities (increased mechanical property) function as an ideal wound dressing material for the treatment of burn injuries.

When we talk about burn injuries, it is often associated with increased secretion of exudates, resulting in an increased microbial count. This is mainly due to the breakdown of growth factors and matrix metalloproteinase, which in turn impair cell growth and prolong the wound healing process. Thus, treatment of burn injuries always remains a challenging factor, especially to control and minimize the bacterial load [16]. This is made possible by incorporating a wide variety of active moieties, such as anti-inflammatory agents, steroids and antibiotics, to produce high resolution 3D printed scaffolds that facilitate and improve the wound healing process and regenerate the cells and tissues [17]. In general, Cip HCl, an antibiotic belonging to a well-known class of fluoroquinolone compounds is considered as the most preferable choice of drugs in the treatment of burn injuries.

Thus in the present study, it was aimed to fabricate biodegradable customized filaments by hot-melt extrusion process for the design and development of a bioactive 3D printed scaffold in combination with an antibiotic (Cip HCl) loaded with doped HNTs coated PVA filaments as a targeted drug delivery for tissue engineering applications.

2. Materials and methods

2.1. Materials

Poly Vinyl Alcohol (PVA) pellets was purchased from Himedia Laboratories Pvt. Ltd., M_W 26300 – 30000 Da, degree of hydrolysis 86.5 – 89%, Mumbai, India. HNTs in powder form was purchased from Sigma Aldrich (St. Louis, MO, USA). Ciprofloxacin Hydrochloride IP was obtained as a gift sample from Aarti Drugs Ltd (Mumbai, India). Ethanol used for coating PVA pellets was purchased from Thermo Fischer Scientific Rimek Pvt. Ltd. (Mumbai, India). All the other chemicals and reagents used in this study were of commercial grade and were used as received, without any purification.

2.2. Coating of PVA pellets for the preparation of filaments

2.2.1. Formulation 1

As per the method reported by Weisman and Tappa [18], with slight modifications, pure Cip HCl coated PVA filaments were prepared. Ethanol was chosen as a solvent to coat the surface of PVA pellets, as they exhibit thermal stability at an extrusion temperature of 180 – 200 °C. A batch of 1000 g of PVA pellets were taken, to which 20 ml of ethanol was added and mixed in a planetary mixer (Rimek, Kalweka Horizontal Main Drive-HD 410 AC attached with Agitator-AT, Karnavati Engineering Limited, Mumbai, India) at 50 rpm for 15 min, to ensure that the pellets were uniformly and completely coated. After complete mixing, all the pellets were placed in another container and then dried in an oven at 40 °C for 2–3 h. Once the pellets were completely dried, a calculated amount of pure Cip HCl (shown in Table 1) in powder form was added, followed by mixing in a planetary mixer at 50 rpm for 30 min. Then the drug coated PVA pellets were sieved and the fines were collected and weighed, to ascertain the amount of drug uncoated on to the pellets.

The coating efficiency (%) was calculated by using the formula:

Table 1
Composition of drug loaded nanofiller coated PVA pellets.

S. No	Materials	Composition	
		F1	F2
1.	PVA Pellets (g)	1000	1000
2.	Pure Cip HCl (% w/w)	3	–
3.	Cip HCl loaded doped HNTs (% w/w)	–	12
4.	Ethanol (ml)	20	20

$$\textit{Coating Efficiency}\ (\%) = \frac{a-b}{c} * 100 \quad (1)$$

Where,

a = Final weight of coated pellets in g
b = Initial weight of pellets (blank pellets in g).
c = Total amount of coating material.

2.2.2. Formulation 2

A batch of 1000 g of PVA pellets were taken, to which 20 ml of ethanol was added and mixed in a planetary mixer (Rimek, Kalweka Horizontal Main Drive-HD 410 AC attached with Agitator-AT, Karnavati Engineering Limited, Mumbai, India) at 50 rpm for 15 min, to assure that the pellets were uniformly and completely coated. After complete mixing, all the pellets were placed in another container and then dried in an oven at 40 °C for 2–3 h. Once the pellets were completely dried, a calculated amount of Cip HCl loaded doped HNTs (shown in Table 1) in powder form was added, followed by mixing in a planetary mixer at 50 rpm for 30 min. Then the Cip HCl loaded doped HNTs coated PVA pellets were sieved and the fines were collected and weighed, so as to ascertain the amount of drug loaded doped HNTs uncoated on to the pellets.

2.3. Hot melt extrusion (HME) of Pure Cip HCl coated PVA pellets and Cip HCl loaded

2.3.1. Doped HNTs PVA pellets

The composite mixtures were extruded using a Lab Twin Screw Extruder (Aasabi Machinery Pvt. Ltd. Mumbai). The drug-coated PVA pellets and drug-loaded nanofiller coated PVA pellets were gravimetrically fed from a hopper directly into a feeder at a feed rate of 5 g/min. The melted pellets were allowed to pass through a large spinning screw at the operating speed of 50 rpm, operating within a horizontal barrel of a twin-screw extruder. The pellets were extruded at an extrusion temperature of 180–200 °C through a 1.75 mm circular die. After the extrusion process, the filament was cooled by allowing it to pass through a water tank that rolled automatically and subsequently stored in an airtight containers [19].

2.4. Fabrication of 3D printed scaffolds by FDM technique

The primary objective of the study was to test the filaments printing potential and create an appropriate design using 3D printing software. Computer-aided design (CAD) software with the Solid Works computer software modelling programme (Dassault Systemes Solid Works Corporation, Waltham, MA, USA) was used to create a design model of the dosage form, such as scaffolds for 3D printing. Once the design model was created, it was exported to .stl format (stores information about conceptual 3D objects) (see Fig. 1). Then the .stl format was sliced to GCode (specific code containing exact instructions for the printer) using Flashforge Creator Pro Slicer. Table 2 presents the printer settings for the fabrication of scaffolds. Finally, the sliced documents were transferred to a fused deposition modelling 3D printer (Flashforge Creator Pro Machine, USA), and the scaffolds were printed layer by layer with a self-extruded drug coated PVA filament and drug-nanofiller coated PVA filament at a 40% infill ratio with a hexagonal infill pattern [20].

2.5. Characterization of filaments and 3D printed scaffolds

2.5.1. Diameter and thickness of the filaments and 3D printed scaffolds

The diameter and thickness of the filaments and 3D printed scaffolds were tested at three different locations using a vernier caliper. The average values and standard deviation were computed from the data.

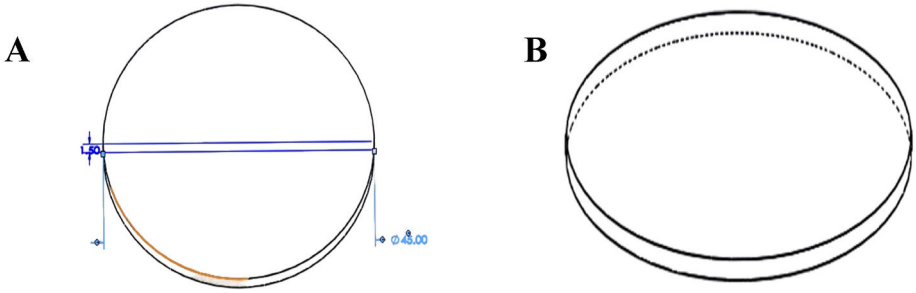

Fig. 1. Three-dimensional design of scaffold: (A) Top view of scaffold and (B) Side view of scaffold.

Table 2
3D printing specifications.

S No	Specifications	Values
1.	Filaments	Cip HCl coated PVA Cip HCl loaded doped HNTs coated PVA
2.	Extrusion temperature (° C)	220
3.	Build plate temperature (° C)	110
4.	Print speed (mm/sec)	60
5.	Travelling speed (mm/sec)	80
6.	Nozzle diameter (mm)	0.2
7.	Layer height (mm)	0.18
8.	Infill ratio (%)	40
9.	Infill pattern	Hexagon

2.5.2. Compatibility studies

2.5.2.1. Fourier-Transform Infrared Spectroscopy (FTIR analysis). The chemical structure and compatibility of the excipients present in the scaffolds were evaluated by FTIR analysis using (Shimadzu IR Spirit, Japan) integrated with an attenuated total reflection (ATR) diamond cell crystal accessory. All the spectra were measured in the spectral range of 4000-500 cm^{-1} with 32 scans at a resolution of 4 cm^{-1}. These recorded spectra were analyzed with Lab Solution software®. The data obtained were depicted by plotting the values of % transmittance vs. wave-number, cm^{-1}.

2.5.2.2. Differential scanning calorimeter (DSC). In order to evaluate the thermal behavior of the material and scaffolds as well as to validate the compatibility of drugs and excipients, differential scanning calorimeter (Shimadzu DSC 60 Plus, Tokyo, Japan) was actualized. A sample of weight 4–5 mg was accurately weighed, placed in an aluminum pan and crimped systematically. The samples were heated over a temperature range of 30–350 °C at a heating rate of 10 °C/min, the purge gas nitrogen was allowed to flow at the rate of 100 ml/min and the thermograms obtained were analyzed using the software Lab Solutions®.

2.5.3. Tensile properties of scaffolds

The tensile properties of the scaffolds were analyzed using a Micro Universal Testing Machine (Tinius Olsen 10ST, UK). According to the benchmark framed by American Standards for Testing Methods (ASTM D882-12), the scaffolds were cut into quadrangles with the dimensions of 45 mm × 25 mm and the tensile strength was measured by applying the load cell capacity of 500 N to scaffolds at a test speed of 1 mm/min. The tests were performed in triplicate (n = 3) for all the samples and the average values of Young's modulus, ultimate stress and % break strain was measured and recorded.

2.5.4. Morphological characterization of PVA filaments and scaffolds

The surface morphology and topography of PVA filaments and 3D printed scaffolds were characterized by a field emission scanning electron microscope (FESEM-Jeol JSM-7610F Plus, Tokyo, Japan). Since the scaffolds are non-conductive in nature, a thin layer of conducting element (Gold-Sputter) was uniformly wrapped using Quorum Q 150R ES for 60 s. After wrapping with gold, the samples were loaded inside the SEM chamber and vacuum was created. The images obtained were captured at 100 X magnification by applying a low accelerated voltage (<5 kV).

2.5.5. Drug content analysis

A specified area (1 cm × 1 cm) of scaffolds were cut and dissolved in 100 ml of phosphate buffer solution, pH 7.4, followed by sonication for 20 min. After sonication, the matrix was completely dissolved and the solution was filtered through What-man filter paper (0.45 μ) and appropriately diluted with phosphate buffer solution 7.4 pH to analyze % drug content spectrophotometrically (Shimadzu, UV-1900 Spectrophotometer, Japan) at 271 nm. The tests were performed in triplicate (n = 3) for all the samples and the average values as well as the standard deviation of drug content analysis were determined.

2.5.6. In - vitro drug release study

The drug release pattern of Cip HCl from the prepared 3D printed scaffold was carried out using the Franz diffusion cell apparatus (Electrolab EDC-07, Mumbai, India). A volume of 12.5 ml of phosphate buffer solution pH 7.4 was filled in a receptor compartment and the drug release studies were performed using a synthetic dialysis membrane 150 μ. The prepared 3D printed scaffolds were cut into pieces of 1 cm × 1 cm dimension and placed between the donor and receptor compartments. The whole set-up was systematically set and the solution in the receptor compartment was constantly and continuously stirred at 50 rpm using a magnetic bead and the temperature was maintained at 37 °C ± 2 °C. The aliquot samples (1 ml) were withdrawn at the appropriate time intervals (0, 0.5, 1, 2, 3, 4, 5, 6, 7 and 8 h) and replaced with the same amount of medium to maintain sink conditions. The aliquots withdrawn were diluted suitably and analyzed spectrophotometrically at 271 nm (Shimadzu, UV-1900 Spectrophotometer, Japan). A cumulative % release of Cip HCl from the scaffolds was determined and a graph of % drug release vs. time was constructed. The tests were carried out in triplicate (n = 3) for all the samples and the average values as well as the standard deviation of the drug content analysis were determined.

2.6. Cell culture study

2.6.1. Cell culture

A549 (Human lung adenocarcinoma epithelial cell line) was purchased from the National Repository of Animal Cell Culture, National Centre for Cell Sciences (NCCS), Pune, India. A549 cells were grown in 6 well cell culture plates (Tarson-980010, 6 well plates); Tarson, India. These cells were cultured in RPMI 1640 medium, supplemented with 10% fetal calf serum (FES) (HyClone), 100 U/ml penicillin and 100 μg/ml streptomycin sulfate and the cells were incubated under 5% CO_2 at 37 °C (N-Biotek NB203XL, Korea). The media was changed three times per week until the cells reached 80% confluency.

2.6.2. Monolayer wound healing migration assay

The potentiality of Cip HCl loaded DHNTs coated PVA scaffolds (S2) to heal the wound was analyzed by experimenting with an *in-vitro* migration assay on A549 cells using the standard scratch assay protocol. A density of 1×10^6 cells/cm^2 were seeded in 6 well plates and propagated for 36 h to accomplish the complete proliferation of cells, thereby resulting in the formation of 80% monolayer cell confluency for A549 cells. A linear scratch was given to monolayer cells by using a 200 μl pipette tip and then the cells were rinsed twice with phosphate buffered saline to remove the cellular debris deposited on the cells. The cells were then treated with 1 mg/ml of Cip HCl loaded DHNTs coated PVA scaffold as a test sample and 1 mg/ml of pure Cip HCl as a control and incubated for 24 h under standard culture conditions [21]. The rate of cell migration (R_M) and the width of cellular space were quantitatively analyzed and photographed using an inverted microscope (Nikon Eclipse TS2, USA) with a magnification of 4 X at the time intervals of (0, 24 and 48 h).

The rate of cell migration (R_M) and percent wound closure was computed by the following - equation (2) and equation (3) respectively:

$$R_M = \frac{Wi - Wf}{t} \tag{2}$$

Where,

W_i = Average of the initial wound width (μm).
W_f = Average of the final wound width (μm).
t = Time span of assay (h)

$$\textit{Wound Closure}\ (\%) = \left(\frac{A_{t=0} - A_{t=\Delta t}}{A_{t=0}}\right) \times 100 \tag{3}$$

Where,

$A_{t\,=\,0}$ = initial wound area (μm^2).
$A_{t\,=\,\Delta t}$ = wound area after n hours of the initial scratch (μm^2) [22].

2.7. Stability studies

The stability studies of the scaffolds (S1) and (S2) were performed at room temperature (25 °C ± 2 °C/ 60% RH ± 5%) for twelve months. Scaffolds were examined visually (surface texture and color change) and even tested for drug content and *in - vitro* drug release studies according to the procedure described in the methodology section.

2.8. Statistical data analysis of mechanical measurements of scaffolds

The data of mechanical measurements (tensile strength, elastic modulus and % break strain) of S1 and S2 were collected and analyzed using the statistical software GraphPad Prism 8.0 (San Diego, CA, USA). The data obtained was analyzed using two - tailed unpaired *t*-test with a level of $p \leq 0.05$ at the 95% confidence interval. The experimental data values were expressed in terms of mean ± standard error (SEM).

3. Results and discussion

3.1. Coating efficiency of PVA pellets

The coating efficiency of Cip HCl coated PVA pellets was found to be 60.23%, while the coating efficiency of Cip HCl loaded doped HNTs coated PVA pellets was 82.65%. The increased coating efficiency is mainly associated with the presence of HNTs as nanofiller. Doped HNTs are ideally recognized for their surface chemistry, which is characterized by the presence of both silanol and aluminol groups. These groups' function as channels for the propagation of covalent attachment of various conjugates and thereby facilitate the coating efficiency on the PVA pellets [23].

3.2. Preparation of drug loaded and drug-nanofiller coated PVA filaments

Cip HCl coated PVA filaments (F1) and Cip HCl loaded DHNTs coated PVA filaments (F2) were prepared according to the procedure described in the methodology section. There were no difficulties encountered while extruding the pellets for the preparation of filaments. The pellets were free-flowing, without causing any obstruction to the extruder and the prepared filaments were multispectral with a uniform diameter. The diameter of the filaments varied from 1.77 ± 0.02 to 2.15 ± 0.03 mm. Low standard values of the diameter measurements ensured uniformity of the filaments, which further indicated the reproducibility of the procedure followed for the preparation of the filaments.

It is revealed that the productivity of the material from the printer nozzle is down regulated when the filament diameter is too small, while in contrast the lack of extrusion is extensively triggered by the preparation of filaments of large diameter. Thus, it is very important to consider that any values that fall outside the range cannot be used as a customized material for 3D printing [24].

The 3D printed scaffolds containing Cip HCl coated PVA scaffold (S1) and Cip HCl loaded doped HNTs coated PVA scaffold (S2) are illustrated in (Fig. 2). S1 and S2 scaffolds exhibited a hexagonal infill pattern. The S2 scaffold was covered with a layer on top of the scaffold with a soft and polished surface. Both scaffolds have a smooth finish at the base as well as on the lateral side of the scaffold. The diameter of both scaffolds was reported to be 45 mm and the thickness of the scaffolds varied from 1.3 mm to 1.5 mm. Low standard values for the diameter and thickness measurements ensured uniformity of the scaffolds, which further indicated the reproducibility of the procedure followed for the preparation of scaffolds.

3.3. Compatibility studies

3.3.1. FTIR analysis

FTIR analysis confirmed the presence of functional groups of drug and polymer and their interaction with the prepared scaffolds.

FTIR spectra for S1 and S2 are depicted in (Fig. 3). In the FTIR spectra of S1, the data for the drug (Cip HCl) and polymer (PVA) are as follows: An absorption band at 3007.4 cm^{-1} is mainly attributed to the presence of alkenes and aromatic C–H stretching. The appearance of another peak at 1710.38 cm^{-1} confirms the presence of carbonyl (C═O) stretching vibration, while the peak at 1640.65 cm^{-1} signifies the presence of quinolones. In addition to this, the emergence of another peak at 1024.34 cm^{-1} belongs to the C–F group [25]. Similarly, the characteristic peak of PVA appeared at 842.24 cm^{-1} which is associated with C–C stretching. A peak exists at 1085.78 cm^{-1} which describes the C–O stretching of PVA. The Appearance of a small absorption peak at the frequency of 1330.14 cm^{-1} confirms the C–H deformation of PVA polymer.

Whereas, in the FTIR spectra of S2, an absorption peak exists at 3282.09 cm^{-1} confirms the presence of OH stretching of PVA. Two new peaks were observed at the frequencies of 2920.15 cm^{-1} and 1496.17 cm^{-1}, which are attributed to the deformation (scissoring) of the CH_2 group of doped HNTs. The characteristic peak appeared at 1697.24 cm^{-1} signifying the carbonyl (C═O) stretching of PVA. The signals at a wavenumber of 1621.52 cm^{-1} are associated with the quinolones (functional groups present in Cip HCl). A sharp peak was observed at 1445.80 cm^{-1} which describes the C–O stretching of Cip HCl. A peak at 1330.75 cm^{-1} signifies the deformation of the CH group of PVA. The presence of the frequency peak at 1265.79 cm^{-1} is attributed to the bending vibration of the OH group of Cip HCl and the existence of a broad peak at 1022.92 cm^{-1} signifies the presence of the C–F group (a vital functional group of Cip HCl). A sharp intensified peak was observed at the frequency of 908.62 cm^{-1} indicates the possibility of RSi-O-Si and RSi-O-Al bonds between RSi-OCH_3 and RSi-OH of γ-MPS with Al–OH groups present at the edges of HNTs and Si–OH of HNTs [14]. Thus, these findings authenticate the presence of functional groups of both

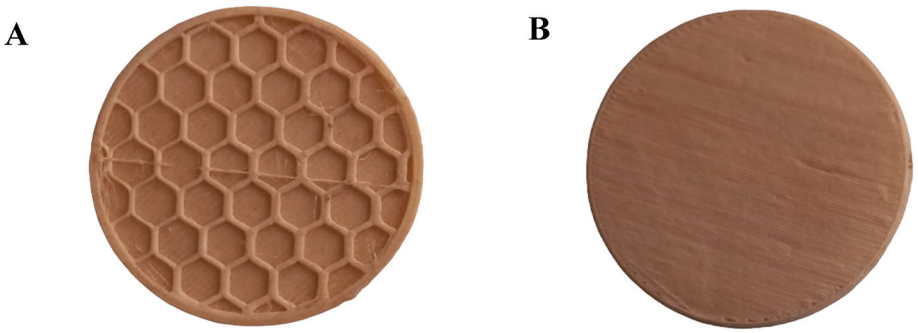

Fig. 2. (A) Cip HCl coated PVA 3D printed Scaffold 1 (S1); (B) Cip HCl loaded doped HNTs coated PVA 3D printed Scaffold 2 (S2).

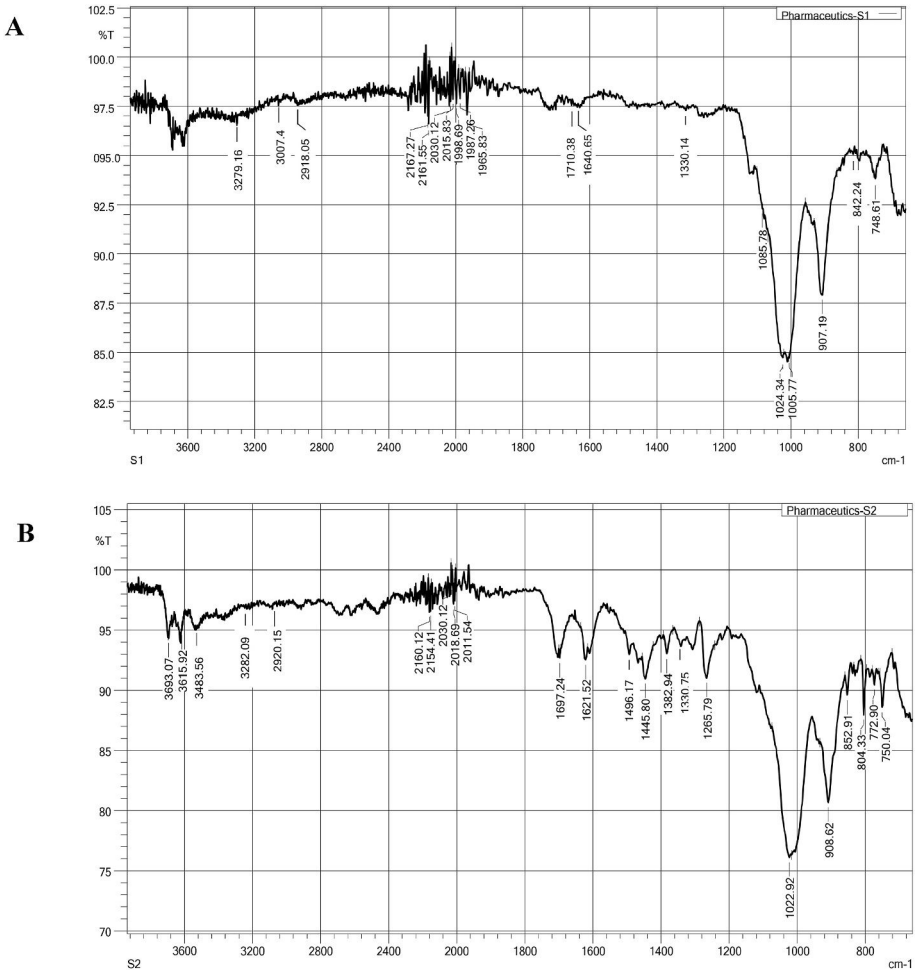

Fig. 3. FTIR spectra of (A) Scaffold 1 and (B) Scaffold 2.

drug and polymer in S1 and drug, nanofiller and polymer in S2, confirming that there is no evidence of drug-polymer and drug-nanofillers and polymer interactions, proving that these added excipients are compatible with each other in the prepared scaffolds.

3.3.2. DSC analysis

The DSC thermograms for pure drug, polymer and the formulations scaffold 1(S1) and scaffold 2 (S2) are depicted in (Fig. 4). The DSC thermogram of pure Cip HCl was characterized by the presence of two endothermic peaks. The first peak was observed at 160 °C, which corresponds to the evaporation or loss of adsorbed water molecules, while another single, sharp endothermic peak appeared at 321.82 °C, which corresponds to the melting point of the pure drug. The obtained thermogram was within the standard range of IP monograph (293.15–323.15 °C) and confirmed the authenticity and the purity of Cip HCl. Similarly, PVA polymer showed a single, slightly broad endothermic peak at 192.74 °C corresponding to their melting point, in association with an enthalpy of −27.29J/g and a degree of crystallinity of −19.68%, signifying the loss of crystalline nature of the polymer. While, the DSC curve of S1 revealed an endothermic peak at 305.63 °C corresponding to the melting point of pure Cip HCl. In comparison to the thermogram of pure drug, the intensity of the peak in S1 was slightly decreased and this could be attributed to the complete dispersion of Cip HCl into the polymeric matrix, thereby resulting in the formation of a new solid phase. Furthermore, it was observed that, there was no much difference in the peak intensity as well as the shape of PVA polymeric

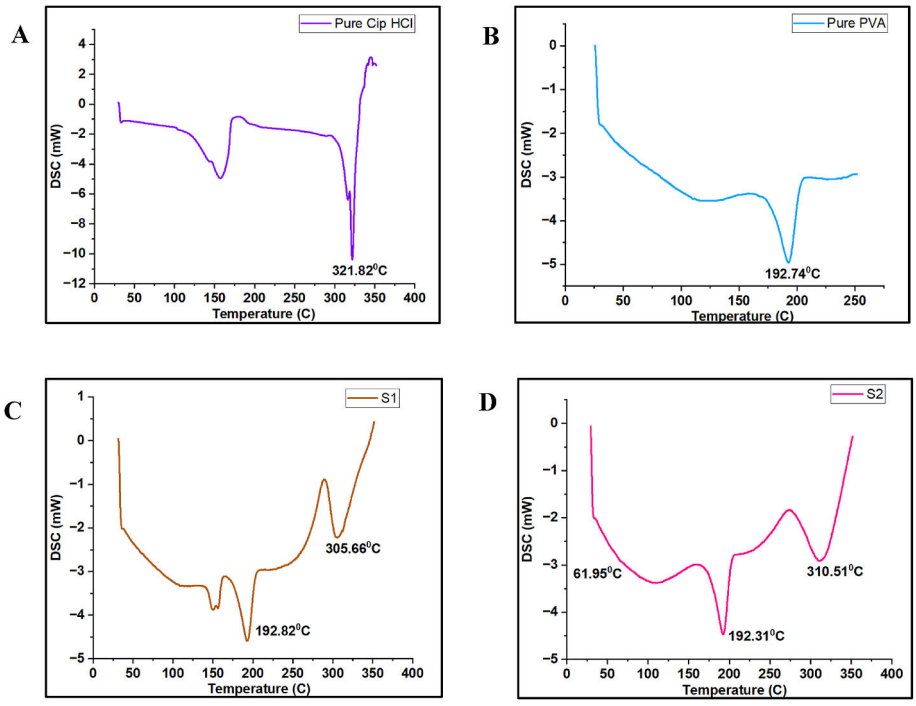

Fig. 4. DSC thermogram of (A) Pure Cip HCl, (B) Pure PVA, (C) Scaffold 1 and (D) Scaffold 2.

peak and the melting point was found to be more similar with pure PVA thermogram. Thus, these results portray that there was no significant interaction between the drug and polymer. Whereas, in another formulation S2, a very small new peak was observed at 61.95 °C corresponding to the loss of the physically adsorbed and the interlayer water molecules of doped HNTs [26]. The appearance of a very weak peak in the sample signifies the complete homogeneity of doped HNTs within the polymeric matrix. Cip HCl exhibited a single broad endothermic peak at 310.51 °C and PVA revealed a sharp endothermic peak at 192.31 °C, corresponding to their melting point. Thus, the data confirms the compatibility between drug and excipients and no significant interaction was witnessed.

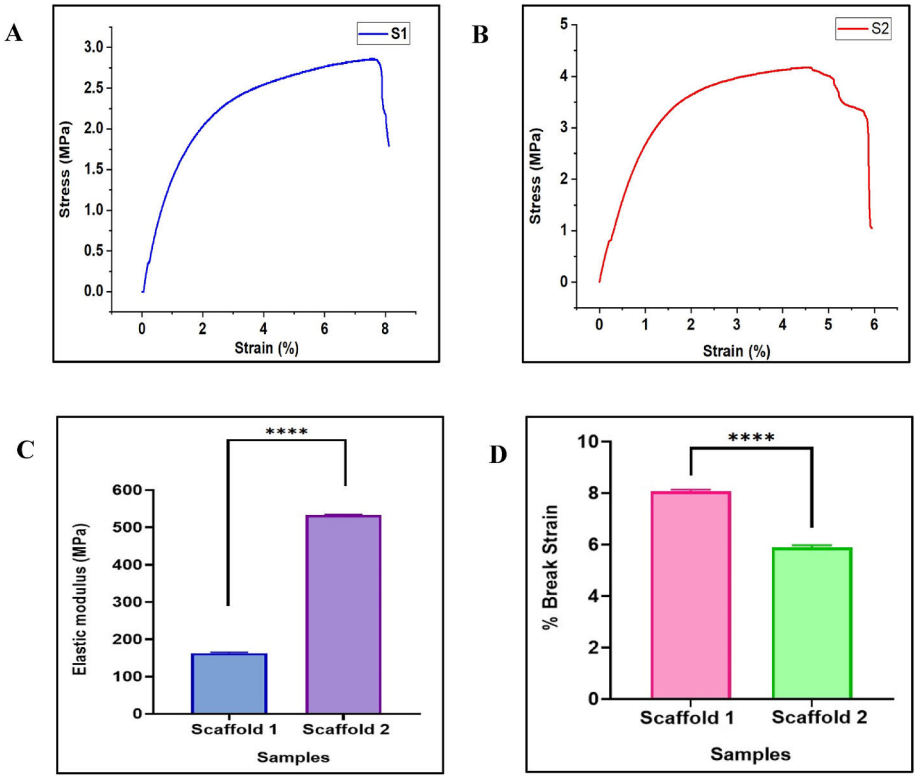

Fig. 5. Mechanical properties: (A) Tensile strength of scaffold 1, (B) Tensile strength of scaffold 2
(C) Elastic modulus of S1 and S2 (****$p \leq 0.05$ using unpaired *t*-test n = 3) and (D) % Break strain of S1 and S2 (****$p \leq 0.05$ using unpaired *t*-test n = 3).

3.4. Tensile properties of the scaffold

The tensile strength of S1 was found to be 2.86 ± 0.01 MPa and for S2, the elastic modulus was 4.17 ± 0.02 MPa. It was observed that the tensile strength of S2 was significantly increased ($p \leq 0.05$) as compared to S1. The reduction in tensile strength in S1 is mainly due to the disruption of the homogeneity of the lattice structure by the presence of antibiotic molecules. The addition of an antibiotic (Cip HCl) reduced the tensile strength value by two folds as compared to S2 [27]. The increase in tensile strength of the S2 sample is mainly associated with the presence of silica groups on the surface of HNTs. These silica groups form a stiff layer to promote a high level of interactions and interfacial adhesion on the polymeric matrix by restricting the free displacement of polymeric chains [28].

The elastic modulus of S1 was found to be 160 ± 0.05 MPa and for S2, the elastic modulus was 533 ± 0.01 MPa. It was observed that the elastic modulus of S2 was significantly increased ($p \leq 0.05$) as compared to S1. The results of the elastic modulus of S1 and S2 are shown in (Fig. 5C). The plot of S2 evidenced a sharp increase in elastic modulus with the incorporation of doped HNTs as nanofillers. As a result, the presence of doped HNTs accelerates the rate of stress propagation and enlarges the clay network, which is desirable for the enhancement of the elastic modulus of the scaffold. Similarly, it was observed that the elastic modulus of S1 was decreased by three folds as compared to S2 and this could be attributed to the curtailment in the reticulated network, thereby facilitating the formation of a floppy core network in the composite scaffold [29].

The % break strain of S1 was found to be 8.09 ± 0.2%, while the % break strain for S2 was 5.95 ± 0.14%. It was observed that the elastic modulus of S2 was significantly decreased ($p \leq 0.05$) as compared to S1. The results of % break strain of S1 and S2 are illustrated in (Fig. 5D). In general, the relationship between elastic modulus and % break strain is inversely proportional to each other. Unlike the tensile strength and elastic modulus, the % break strain increased in S1; the increase in % break strain leads to softness and stiffness of the scaffold. Whereas, the % break strain decreased in S2 with an increase in tensile strength and elastic modulus. This in turn intensifies the structural rigidity of the scaffolds and makes them slightly brittle in nature [30].

3.5. Morphological characterization of filaments and scaffold

The morphology of prepared filaments and 3D printed scaffolds was analyzed by Scanning electron microscopy (SEM) analysis. The surface of the filament (F1) was slightly rough in nature; this roughness of the surface suggests the existence of Cip HCl coated PVA material around the filament. The deposition of Cip HCl on the surface of the filament was identified by the appearance of slight projections, which are highlighted by a pink arrow mark. Subsequently, it was observed that the surface of filament (F2) was highly rough with a dense and uniform deposition of Cip HCl loaded γ-MPS doped HNTs coated PVA material.

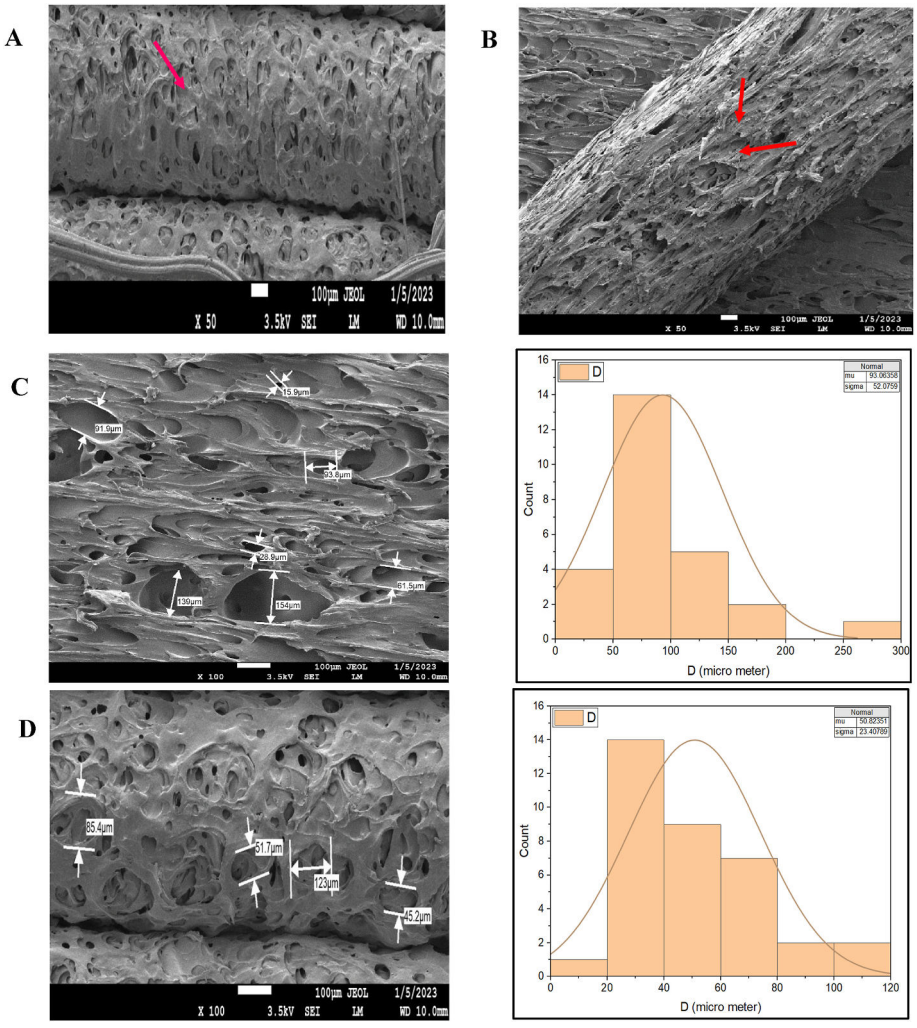

Fig. 6. SEM images with pore diameter distribution curve obtained by Image J software: (A) Cip HCl coated PVA filament, (B) Cip HCl loaded doped HNTs coated PVA filament, (C) Scaffold 1 and (D) Scaffold 2.

The superficial portion of the filament was highly projected with a lamination of doped HNT (indicated by a red arrow mark) and the edge walls of the filament appeared with a wrinkled and fuzzy pattern. This type of appearance signifies the perfect wrapping of Cip HCl loaded doped HNTs coated PVA material on the filament. At last, both the filaments F1 and F2 appeared to be cylindrical shaped, with some hollow openings present in (Fig. 6A and B) indicating the coating of the material on the filaments.

Cip HCl coated PVA scaffolds (S1) exhibited an excellent porous architecture with irregular interconnected pore shapes and sizes. These scaffolds revealed an oval shaped thin walled porous microstructure with a modest increase in porosity. The pore diameter of the designed scaffold ranged from 28 to 198 μm, but the average pore diameter of the scaffold was found to be 93.06 ± 52 μm with a porosity of 82%. The increased porosity is mainly responsible for the uniform dispersion of Cip HCl within the composite scaffold, thereby facilitating the formation of strong molecular bonding between Cip HCl and the PVA network [24]. Similarly, the Cip HCl loaded doped HNTs coated PVA scaffold (S2) presented a round shaped granular porous structure with a marked increase in the pore wall thickness. It was also notably observed that the surface and pore walls of the scaffolds were rough in nature and the appearance of the roughness is associated with the integration of doped HNTs [14]. Additionally, surface roughness favors cell growth and adhesion as compared to the smooth surface of the scaffolds. These scaffolds revealed an average pore diameter of 50.82 ± 23 μm with a porosity of 60%. As a result, a decrease in porosity strengthens the material and results in increased tensile strength and elastic modulus. Thus, the pore diameter of the scaffold in the range of 50 – 250 μm proves to be ideal for tissue regeneration (Fig. 6C and D). depict the SEM images of Cip HCl coated PVA scaffolds and Cip HCl loaded doped HNTs coated PVA scaffolds, along with the pore diameter distribution curve obtained by Image J Software.

3.6. Drug content analysis

Drug content analysis was carried out for both the scaffolds and the drug content ranged from 81.13% ± 0.022 – 88.24% ± 0.053, indicating that both scaffolds were acceptable with respect to Cip HCl content with minimum variability.

3.6.1. In-vitro drug release profile of Cip HCl loaded 3D printed scaffolds

The drug release patterns of Cip HCl coated PVA scaffolds (S1) and Cip HCl loaded doped HNTs coated PVA scaffolds (S2) are shown in (Fig. 7). Scaffold 1 presented a complete release pattern of Cip HCl 73.35% ± 0.02 within 2 h of the time profile. This pattern of release is mainly associated with the porous nature of the scaffold as well as the orientation of the networks within the scaffolds. The porous nature of the scaffolds results in the formation of a loose network, thereby facilitating the easy penetration of release media within the scaffolds, followed by complete diffusion of the drug from the matrix [31]. Interestingly, when Cip HCl loaded doped HNTs coated PVA scaffolds were analyzed, a burst followed by prolonged drug release activity was observed. A burst effect of Cip HCl was observed with a release of 42.84% ± 0.05 by the second hour of the analysis. An early burst of antibiotic administration appears to be more promising in preventing bacterial growth before proliferation at the site of action [32]. An early burst release is accomplished as a number of active molecules are fastened to the external surface of doped HNTs. Similarly, after the second hour of testing, the drug release rate was extensively sustained with almost 80.92% ± 0.10 by the sixth hour and furthermore, the release profile remained constant with 85.54% ± 0.17 at the end of the twelfth hour. This type of release profile was achieved by the strong electrostatic interaction and hydrogen bonding between drug and doped HNTs within the lumen of nanotubes. Another key factor that favors the sustained release of the drug is the coating thickness of drug loaded doped HNTs on the PVA filaments; increased coating thickness leads to an extended drug diffusion path and promotes sustained release of the drug from the scaffolds [33].

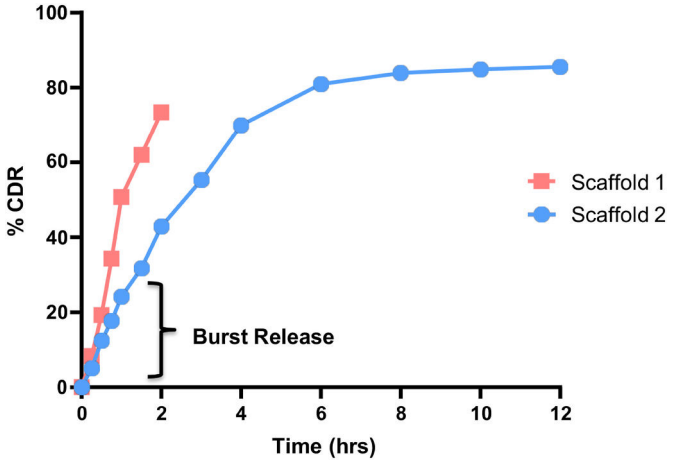

Fig. 7. *In -vitro* drug release pattern of Scaffold 1 and Scaffold 2.

3.7. Wound healing migration assay of A549 cells

Ideally, in an *in-vitro* wound healing assay, an artificial incision like gap is created by giving a slight scratch to a confluent cell monolayer and the migration of the cells in order to close the gap is assessed via microscopy or other image capturing tools at different time intervals. The inclusion of selective nanomaterials and biomaterials modulates wound healing activity either by promoting or inhibiting the rate of cell migration. In the proposed research work, A549 cells were selected to perform a cell migration assay. The results of the cell migration assay indicated that the cells treated with Cip HCl loaded DHNTs coated PVA scaffolds (test sample) at 1 mg/ml closed the gap with 63.30% at 24 h and 80.16% of wound closure was observed at 48 h of the time profile ($R^2 = 0.9985$) illustrated in (Fig. 8D). Similarly, the intensity of wound closure was slightly reduced for the cells treated with pure Cip HCl (control) as compared to the test sample. The % wound closure at 24 h was found to be 32% and at 48 h 56.18% of wound closure was witnessed ($R^2 = 0.9936$). The above findings manifest that the cells treated with the test sample exhibited the highest cell migration, as evidenced by improved wound healing activity. The increased mobilization of the cells is mainly associated with the porosity of the scaffolds. The porous structure facilitates the easy penetration and proliferation of the cells within the 3D network of scaffolds and exhibits a similar microenvironment that mimics the native extracellular matrix. Moreover, the exposure of A549 cells to a test sample resulted in a considerable reduction in the wound scratch area shown in (Fig. 8C) after 12 h as compared with the cells treated with a control sample. Similarly, it was observed that the scratch width of the cells treated with the test sample was significantly decreased at the end of 48 h of the study (Fig. 8E). The reduction in scratch width indicates that the intensity of the cell population near the edges of the wound was significantly higher than in the control sample. The increase in cell population is mainly attributed to the incorporation of DHNTs in the scaffolds, which inturn act as cell growth stimulators and favor the complete closure and healthy healing of the wound. Lastly, we could observe that the cells treated with the test sample presented a higher rate of cell migration, with an average value of 7.04 μm/h at 24 h and 10.93 μm/h at the end of 48 h of the study, this data correlates with the findings of % wound closure of test sample. In contrast, the rate of cell migration was slightly decreased in the control sample and remained constant with an average value of 3.88 μm/h at 24 h and 4.24 μm/h at 48 h as illustrated in (Fig. 8F). Thus, the inclusion of doped halloysite nanotubes into the scaffolds facilitated an increase in gap closure, thereby enabling faster wound healing activity.

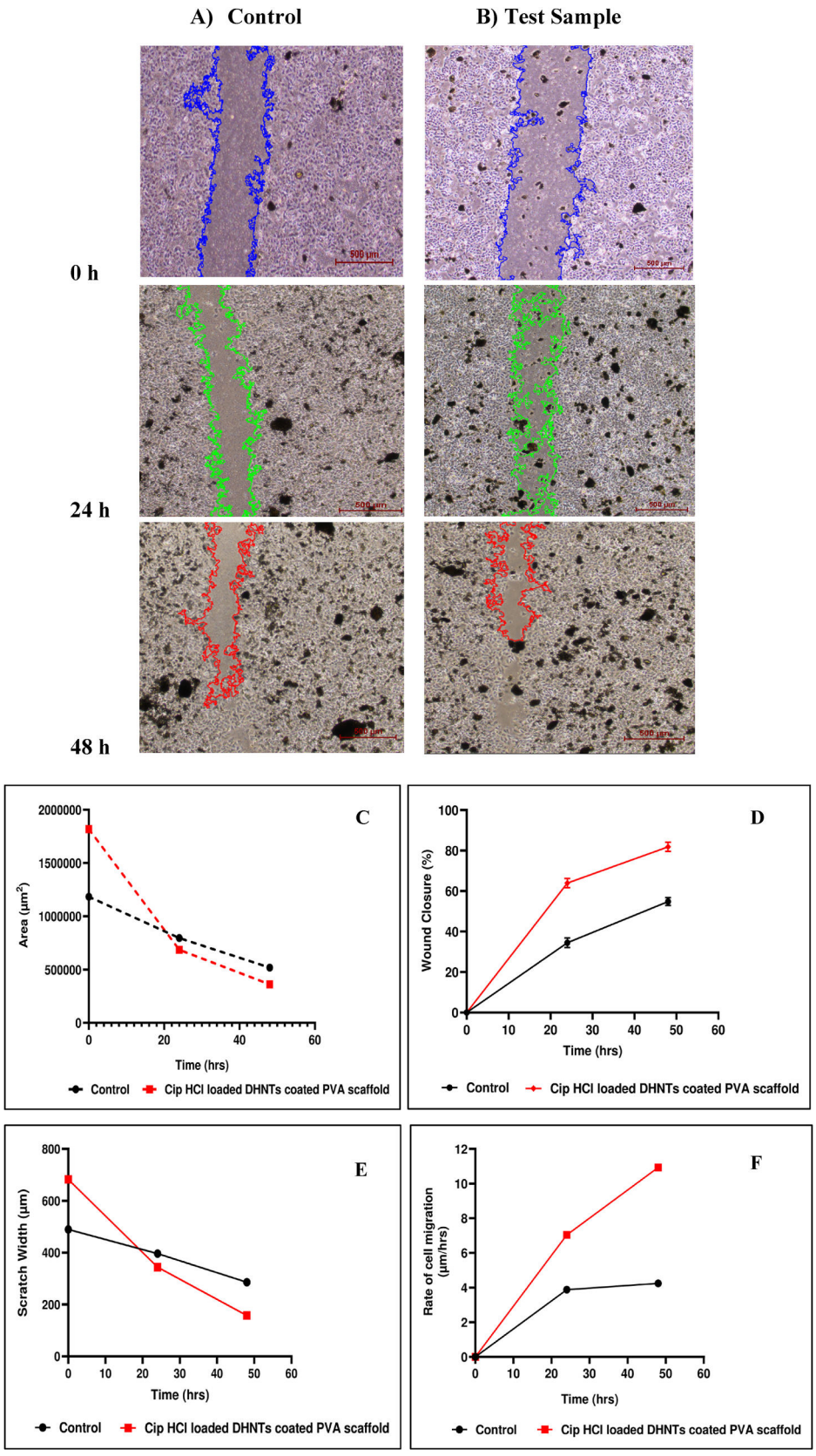

Fig. 8. Microscopic and graphical illustration of monolayer wound healing migration assay of A549 cells treated with (A) Control, (B) Cip HCl loaded DHNTs coated PVA scaffolds and for both the samples images were captured at 0 h, 24 h and 48 h, (C) Wound area in μm^2, (D) Percentage of wound closure area, (E) Wound width in μm and (F) Rate of cell migration in μm/h.

3.8. Stability studies

The stability studies of the scaffolds were determined at room temperature. No change in color was observed, surface texture of both the scaffolds were smooth with a polished finish at the base and on the lateral side of the scaffolds. There was no variation in % drug content and % *in-vitro* drug release of both the scaffolds. The drug content of S1 in 7.4 pH phosphate buffer was found to be 82.42% ± 0.015 and that of S2 was 90.16% ± 0.012. Similarly, the *in-vitro* release of S1 was 75.27% ± 0.032 at the end of 2 h of time profile, while S2 exhibited a burst release by the second hour of the analysis, followed by the sustained release of 83.84% ± 0.024 at the end of twelfth hour. Thus, from the data obtained it is clear that no much difference was observed and the designed scaffolds were found to be stable at the given storage condition.

4. Conclusion

In conclusion, the present study demonstrated a systematic approach to develop a continuous flow process of personalized dosage form for burn injuries using FDM 3D printing technology. The Cip HCl coated PVA pellets and Cip HCl loaded doped HNTs coated PVA pellets were successfully extruded by hot melt extrusion process for the preparation of filaments with tunable printing qualities. The filaments were further designed and printed into three dimensional scaffolds using FDM 3D printing technique. The mechanical properties and drug release profiles of the scaffolds were found to be ideal for wound healing applications. The scaffold 2 presented a sustained release profile with an early burst release, which can effectively control the bacterial load and promote faster wound healing. The stability studies confirmed the stability of designed scaffolds under given storage conditions. Therefore, the proposed study highlights the potentials of 3D printing technology for the development of personalized dosage forms for burn injuries.

Author statement

All the authors have equal contribution and participation in the proposed research work., **Revati Dharampal Sagare:** Conceptualization, Data curation, Investigation, Writing – Original draft preparation. **Fatima Sanjeri Dasankoppa:** Conceptualization, Methodology, Writing- Reviewing and Editing, Supervision. **Hasanpasha N Sholapur:** Software, Methodology and Visualization. **N R Banapurmath and M An Umarfarooq:** Methodology and Data analysis.

Funding

The research work was supported by funding agency AICTE - RPS Scheme, Government of India. Scheme sanctioned vide file no: 8–89/FDC/RPS (POLICY-1)/2019–2020.

Declaration of competing interest

The authors state no declaration of interest statement.

Data availability

Data will be made available on request.

Acknowledgement

The authors express their deep gratitude to Aarti Drugs Ltd Mumbai, India for providing a gift sample of Cip HCl API. We also thank our Principal Dr. AHM Viswanatha Swamy for permitting us to utilize the lab facilities to carry out this research work. We would like to offer a special thanks to Deshpande Startups Hubballi, India for extending us the facility to design and print 3D scaffolds.

References

[1] C.K. Sen, Human wound and its burden: updated 2020 compendium of estimates, Adv. Wound Care 10 (2021) 281–292, https://doi.org/10.1089/wound.2021.0026.
[2] R. Norton, O. Kobusingye, Injuries. N Engl J Med. 368 (2013) 1723–1730, https://doi.org/10.1056/NEJMra1109343.
[3] Gumber A. Burden of Injury in India: Utilization and Expenditure Pattern. I994.
[4] A. Shpichka, D. Butnaru, E.A. Bezrukov, R.B. Sukhanov, A. Atala, V. Burdukovskii, et al., Skin tissue regeneration for burn injury, Stem Cell Res Ther. 10 (2019) 94, https://doi.org/10.1186/s13287-019-1203-3.
[5] Y. Yao, A. Zhang, C. Yuan, X. Chen, Y. Liu, Recent trends on burn wound care: hydrogel dressings and scaffolds, Biomater. Sci. 9 (2021) 4523, https://doi.org/10.1039/D1BM00411E.
[6] V.M. Goldberg, S. Stevenson, Natural history of autografts and allografts, Clin. Orthop. Relat. Res. 225 (1987) 7–16. PMID: 3315383.
[7] S. Dhivya, V.V. Padma, E. Santhini, Wound dressings - a review, Biomedicine 4 (2015) 22, 10.7603%2Fs40681-015-0022-9.
[8] F. Tsegay, M. Elsherif, H. Butt, Smart 3D printed hydrogel skin wound bandages: a review, Polymers 14 (2022) 1012, https://doi.org/10.3390/polym14051012.
[9] A.O. Lukomskyj, N. Rao, L. Yan, J.S. Pye, H. Li, B. Wang, J.J. Li, Stem cell-based tissue engineering for the treatment of burn wounds: a systematic review of preclinical studies, Stem Cell Rev. Rep. 18 (2022) 1926–1955, https://doi.org/10.1007/s12015-022-10341-z.
[10] F.J. Martinez-Vázquez, M.V. Cabanas, J.L. Paris, D. Lozano, M. Vallet-Regi, Fabrication of novel Si-doped hydroxyapatite/gelatine scaffolds by rapid prototyping for drug delivery and bone regeneration, Acta Biomater. 15 (2015) 200–209, https://doi.org/10.1016/j.actbio.2014.12.021.
[11] A. Eltom, G. Zhong, A. Muhammad, Scaffold technique and designs in tissue engineering functions and purposes: a review, Adv. Mater. Sci. Eng. (2019) 1–13, https://doi.org/10.1155/2019/3429527.
[12] B. Basa, G. Jakab, N.K. Szabo, B. Barbos, V. Fulop, E. Balogh, et al., Evaluation of biodegradable PVA-based 3D printed carriers during dissolution, Materials 14 (2021) 1350, https://doi.org/10.3390/ma14061350.
[13] R.D. Sagare, F.S. Dasankoppa, H.N. Sholapur, K. Buruga, Halloysite nanotubes: design, characterization and applications. A review, FARMACIA 69 (2021) 208–214, https://doi.org/10.31925/farmacia.2021.2.3.
[14] R.D. Sagare, F.S. Dasankoppa, H.N. Sholapur, Design, optimization and characterization of γ-methacryloxypropyltrimethoxysilane-doped halloysite clay nanotubes using ultra-turrax homogenizer, J. Pharm. Innov. (2022), https://doi.org/10.1007/s12247-022-09680-8.
[15] N. Sabbagh, A. Akbari, N. Arsalani, B. Eftekhari-Sis, H. Hamishekar, Halloysite-based hybrid bionanocomposite hydrogels as a potential drug delivery systems, Appl. Clay Sci. 148 (2017) 48–55, https://doi.org/10.1016/j.clay.2017.08.009.
[16] P.K. Sehgal, R. Sripriya, M. Senthilkumar, Drug delivery dressings, Adv. Text. Wound Care (2019) 261–288, https://doi.org/10.1533/9781845696306.2.223.
[17] X. Farto-Vaamonde, G. Auriemma, R.P. Aquino, A. Concheiro, C. Alvarez-Lorenzo, Post-manufacture loading of filaments and 3D printed PLA scaffolds with prednisolone and dexamethasone for tissue regeneration applications, Eur. J. Pharm. Biopharm. 141 (2019) 100–110, https://doi.org/10.1016/j.ejpb.2019.05.018.
[18] J.A. Weisman, U. Jammalamadaka, K. Tappa, D.K. Mills, Doped halloysite nanotubes for use in the 3D printing of medical devices, Bioeng (Basel). 4 (2017) 96, https://doi.org/10.3390/bioengineering4040096.
[19] C. Korte, J. Quodbach, Formulation development and process analysis of drug-loaded filaments manufactured via hot-melt extrusion for 3D-printing of medicines, Pharmaceut. Dev. Technol. 23 (2018) 1117–1127, https://doi.org/10.1080/10837450.2018.1433208.
[20] G. Mora-Castano, M. Millan-Jimenez, V. Linares, I. Caraballo, Assessment of the extrusion process and printability of suspension-type drug-loaded Affinisol™ filaments for 3D printing, Pharmaceutics 4 (2022) 871–888, https://doi.org/10.3390/pharmaceutics14040871.
[21] B.D. Kevadiya, S. Rajkumar, H.C. Bajaj, S.S. Chettiar, K. Gosai, H. Brahmbhatt, et al., Biodegradable gelatin-ciprofloxacin-montmorillonite composite hydrogels for controlled drug release and wound dressing application, Colloids Surf. B Biointerfaces 122 (2014) 175–183, https://doi.org/10.1016/j.colsurfb.2014.06.051.
[22] A. Suarez-Arnedo, F. Torres Figueroa, C. Clavijo, P. Arbeláez, J.C. Cruz, C. Muñoz-Camargo, An image J plugin for the high throughput image analysis of in vitro scratch wound healing assays, PLoS One 15 (2020), e0232565, https://doi.org/10.1371/journal.pone.0232565.
[23] R. Taheri-Ledari, W. Zhang, M. Radmanesh, N. Cathcart, A. Maleki, V. Kitaev, Plasmonic photothermal release of docetaxel by gold nanoparticles incorporated onto halloysite nanotubes with conjugated 2D8-E3 antibodies for selective cancer therapy, J. Nanobiotechnol. 19 (2021) 239, https://doi.org/10.1186/s12951-021-00982-6.
[24] N. Abbas, N. Qamar, A. Hussain, S. Latif, M.S. Arshad, Q.A. Ijaz, et al., Fabrication of modified release custom-designed ciprofloxacin tablets via fused deposit modelling 3D printing, J. 3D Print Med. 4 (2020) 17–27, https://doi.org/10.2217/3dp-2019-0024.
[25] S. Sahoo, C.K. Chakraborti, S.C. Mishra, Qualitative analysis of controlled release ciprofloxacin/carbopol 934 mucoadhesive suspension, "J. Adv. Pharm. Technol. Research"" (JAPTR)" 2 (2011) 195–204, https://doi.org/10.4303/2231-4040.85541.

[26] A. Zhang, Y. Zhang, Z. Zhu, Thermal properties of halloysite nanotubes (HNTs) intercalation complexes-A review, in: E3S Web of Conferences, EDP Sciences, 2019, 01055, https://doi.org/10.1051/e3sconf/201913101055, 131.
[27] S.E. Al-Mofty, A.H. Karaly, W.A. Sarhan, H.M.E. Azzazy, Multifunctional hemostatic PVA/chitosan sponges loaded with hydroxyapatite and ciprofloxacin, ASC Omega 7 (2022) 13210–13220, https://doi.org/10.1021/acsomega.2c00654.
[28] W. Ahmed, S. Siraj, A.H. Al-Marzouqui, Comprehensive characterization of polymeric composites reinforced with silica micro-particles using leftover materials of fused filament fabrication 3D printing, Polymers 13 (2021) 2423, https://doi.org/10.3390/polym13152423.
[29] S. Barbon, M. Contran, E. Stocco, S. Todros, V. Macchi, R.D. Caro, et al., Enhanced biochemical properties of poly vinyl alcohol-based hybrid scaffolds for cartilage tissue engineering, Processes 9 (2021) 730–764, https://doi.org/10.3390/pr9050730.
[30] K. Govindasamy, N.A. Dahlan, P. Janarthanan, K.L. Goh, S.P. Chai, P. Pasbakhsh, Electrospun chitosan/polyethylene-oxide (PEO)/halloysites (HAL) membranes for bone regeneration applications, Appl. Clay Sci. 190 (2020), 105601, https://doi.org/10.1016/j.clay.2020.105601.
[31] A. Kumar, V. Bali, M. Kumar, K. Pathak, Comparative evaluation of porous versus nonporous mucoadhesive films as buccal delivery system of glibenclamide, AAPS PharmSciTech 14 (2013) 1321–1332, https://doi.org/10.1208/s12249-013-0014-6.
[32] J. Teno, M. Pardo-Figuerez, K.J. Figueroa-Lopez, C. Prieto, J.M. Lagaron, Development of multilayer ciprofloxacin hydrochloride electrospun patches for buccal drug delivery, J. Funct. Biomater. 13 (2022) 170–189, https://doi.org/10.3390/jfb13040170.
[33] E.G. Bediako, E. Nayankson, D. Dodoo-Arhin, B. Agyei-Tuffour, D. Lukowiec, B. Tomiczek, et al., Modified halloysite nanoclay as a vehicle for sustained drug delivery, Heliyon 4 (2018), e00689, https://doi.org/10.1016/j.heliyon.2018.e00689.

Journal of Pharmaceutical Innovation
https://doi.org/10.1007/s12247-022-09680-8

ORIGINAL ARTICLE

Design, Optimization and Characterization of γ-Methacryloxypropyltrimethoxysilane-doped Halloysite Clay Nanotubes Using Ultra-turrax Homogenizer

Revati Dharampal Sagare[1] · Fatima Sanjeri Dasankoppa[1] · Hasanpasha N. Sholapur[2]

Accepted: 18 August 2022

Abstract

Objectives Doping of halloysite nanotubes (HNTs) with γ-methacryloxypropyltrimethoxysilane (γ-MPS) as a silane coupling agent has sparked the interest of researchers. The objective of the study was to design, characterize and critically optimize γ-MPS–doped HNTs by homogenization technique to achieve uniform dispersion and homogenous mixture of clay minerals.

Methods Optimization of doped HNTs was performed by applying custom design using JMP software 16.1, by considering 2 levels and 3 factors, to determine the impact of independent variables such as concentration of γ-MPS (X_1), HNTs (X_2) and ethanol (X_3) on the response variables diffraction angle (Y_1) and zeta potential (Y_2).

Results The results showed that γ-MPS was successfully doped on the surface of HNTs. Existence of characteristic peaks in Fourier-transform infrared analysis affirms the doping of pristine HNTs. From the x-ray diffraction patterns, it was observed that upon doping there was slight shift in the interlayer distance signifying the intercalation of γ-MPS onto the layers of HNTs. Scanning electron microscopic analysis revealed that the doped HNTs showed reduced aggregation as compared to pristine HNT. DHNT F3 and DHNT F7 exhibited higher zeta potential values indicating the excellent stability and dispersibility of the formulation. The predicted R^2 values for diffraction angle (2θ) (0.94) and zeta potential (mv) (0.95) were close to 1. The optimal values of the independent variables were obtained to measure the desirability of independent variables (X_1, X_2 and X_3) at the concentration of 9 ml, 37.5 g and 87.5 ml, respectively. The overall desirability D = 0.998, indicates the efficiency of custom design for the studied responses.

Conclusion The present study concluded that HNTs were successfully doped with γ-MPS using ultra-turrax homogenizer and the results of statistical analysis indicate that the application of custom design proves to be an ideal tool for optimizing the doping of HNTs.

Keywords Custom design · Halloysite nanotubes · γ-Methacryloxypropyltrimethoxysilane · Optimization · Statistical analysis

Abbreviations

PHNTs	Pristine Halloysite nanotubes
γ-MPS	γ-methacryloxypropyltrimethoxysilane
DHNT F1	Doped HNT Formulation 1
DHNT F2	Doped HNT Formulation 2
DHNTs F3	Doped HNT Formulation 3
DHNTs F4	Doped HNT Formulation 4
DHNTs F5	Doped HNT Formulation 5
DHNTs F6	Doped HNT Formulation 6
DHNTs F7	Doped HNT Formulation 7
DHNTs F8	Doped HNT Formulation 8

✉ Fatima Sanjeri Dasankoppa
fsdasankop@gmail.com

[1] Department of Pharmaceutics, KLE College of Pharmacy, Vidyanagar, Hubballi 580031 Karnataka, India

[2] Department of Pharmacognosy, KLE College of Pharmacy, Vidyanagar, Hubballi 580031 Karnataka, India

Introduction

The inclusion of organic moieties on the surface of HNTs has peaked attention, as it allows fabricating multifaceted compounds which results in significant increase for drug loading capacity, mechanical strength and also for the enhancement of dispersion of HNTs into polymer matrix [1]. HNTs are natural in origin, biocompatible, biodegradable, have remarkable thermal stability and high aspect ratio. An

alternative to these advantages, HNTs have some shortfalls such as insufficient mechanical strength, less drug polymer dispersion ability and lack of drug loading capacity. Naturally sourced HNTs are typically composed of several layers of alumino-silicate minerals with hollow nano-tubular structures, having a molecular formula $Al_2Si_2O_5$ (OH_4). $2H_2O$ with their lengths ranging from 400 to 1000 nm, outer diameter varies from 40 to 80 nm while the inner diameter ranges from 10 to 40 nm. The outer surface of HNTs are mainly constituted of siloxane (Si-O-Si) groups and the inner lumen is composed of aluminol (Al-OH) groups which makes them highly hydrophilic exhibiting gibbsite like order and the edges of HNTs consists of Al-OH and Si-OH groups [2]. The presence of large surface area, fine particle size, porous structure, enhanced surface to volume ratio [3], existence of positively charged inner surface (Al-OH) and negatively charged outer surface (Si-O-Si) enables HNTs to bind with many biological and synthetic macromolecules and aid in loading a wide range of drug molecules on the surface or within the lumen of HNTs [4]. Due to its unique and versatile properties, HNTs possess plentiful range of applications in biomedical sciences such as gene delivery, tissue engineering, cancer and stem cell isolation, fabrication of pharmaceutical novel drug delivery system, drug loading and bio-imaging [2]. Till date, there have been many studies and reports where, HNTs have been used as drug release vehicles or nano-containers for the design and development of targeted drug delivery system [5]. The most effective site for drug entrapment is the nano-pores of HNTs and due to their nanoporous structures, HNTs are widely considered as a host molecule for the loading of various guest molecules [6]. Similarly, the applications of HNTs can also be extended in the development of sustained drug delivery system; better delayed drug release rates can be achieved by coating a layer of various polymers on the surface of drug loaded HNTs [7]. There are various strategies to load drugs on the surface or into the lumen of HNTs, such as adsorption, intercalation and tubular entrapment (vacuum method). HNTs are generally used as nano-carrier, but they have a tendency to exhibit a weak bonding with drugs/active moieties and thereby, hindering the sustained release rates of drug substances.

To overcome the shortfalls of HNTs, the assemblage between the nanotubes and polymer must be engineered by doping process [2]. The surface of HNTs consists of siloxane, silanol and aluminol groups, which optimize the likelihood of complexation with different molecules through van der Waals forces, h-bonding, electrostatic and covalent interactions. The rationale for surface doping depends upon the quantum of hydroxyl groups and their accessibility for bonding with other components [8]. There are alternative ways to dope the surface of HNTs like surfactant modification, organosilane coupling agents, intercalation modification and acid etching method. Among these methods, organosilane modification has proven to be the most efficient and gifted technique to dope the surface of HNTs [9].

γ-Methacryloxypropyltrimethoxysilane is the most commonly used organosilane to dope the surface of HNTs. The hydrolysis of trimethoxy 3(OCH_3) groups present in γ-MPS activates to form tri-silanols 3(Si-OH) and the association of silanol groups with superficial hydroxyl groups results in the formation of siloxane bonds (Si-O-Si) and hence, the reduction in silanol groups intensifies the hydrophobicity of clay minerals thereby assisting homogenous mixture of HNTs, dispersibility and reinforcement into polymeric matrix [10].

HNTs have a tendency to agglomerate due to the impact of van der Waals forces. In-homogeneity and agglomeration characteristics of HNTs result in deterioration of eventual properties of homogenous mixtures of HNTs. The ideal strategy to achieve uniform dispersion and homogenous mixtures of clay into the polymeric network is the application of severe shear stress by homogenization technique [11]. Ultra-turrax is a high-performance dispersing machine used to execute homogenous mixtures and uniform dispersions of clay into polymer matrix, the working strategy of ultra-turrax homogenizer is based on the principle of "Rotor–Stator" mechanism or shear force mechanism, which is generated when a tangential force is applied. In addition to homogenization, surface doping using organosilanes empowers the enlargement of basal spacing by facilitating the intercalation of organic and inorganic moieties within the interface of HNTs and thereby opening a window to exfoliate distinctive layers [12].

Thus, in relation to this research, the objectives were entrenched to design, characterize and critically optimize γ-MPS–doped HNTs by homogenization technique to achieve uniform dispersion and homogenous mixture of clay minerals.

Experimental Methods

Materials

Halloysite nanotubes (HNTs) and γ-methacryloxypropyltrim ethoxysilane (γ-MPS) were purchased from Sigma Aldrich. Ethanol was procured from Fisher Scientific (Mumbai). All of the other chemicals and reagents used in this investigation were of commercial grade and were utilized exactly as they were received, with no further purification.

Experimental Design

To design the experiment, statistical tool JMP software® (Version 16, SAS Institute, Singapore) was imposed. Since the parameters were numeric with continuous values, custom design was chosen to analyze the impact of parameters on the responses. The selected independent variables were

concentration of γ-MPS (X_1), HNT (X_2) and Ethanol (X_3) at two different coded levels low (−1) and high (+1) levels. Diffraction Angle 2θ from XRD analysis (Y_1) and Zeta Potential mV (Y_2) were preferred as dependent variables, the independent and dependent variables are presented in Table 1 and the experimental design including the composition of γ-MPS–doped HNTs is shown in Table 2. Statistical parameters such as coefficient of determination (R^2), actual/predicted R^2, probability value (p-value) were calculated and the resulting data were fitted into JMP Software (Version 16, SAS Institute, Singapore), analysis of variance (ANOVA) was used to investigate the data and the data were also subjected to 3D response surface methodology to examine the impact of the selected formulation factors on the response variables [13].

Doping of HNTs with γ-MPS Using Homogenization Technique

Accurately weighed quantities of γ-MPS were mixed in a beaker containing ethanol and homogenized for 5 min at 24,000 rpm using ultra-turrax homogenizer T-25 basic (manufactured by IKA- WERKE Pvt. Ltd, Mumbai, India) as shown in Table 2. HNT was added to γ-MPS/ethanolic solution and the suspension was stirred for 30 min, followed by homogenization for 7 min, the resulting suspension was centrifuged at 10,000 rpm for 20 min and the doped HNTs (DHNTs) were dried in an oven at 40 °C for 24 h [14].

Characterization of γ-MPS–doped HNTs

Fourier Transform infrared (FTIR) spectroscopy analysis was performed using Nicolet 5700 FT-IR spectrometer (USA) coupled with a DTGS detector. A total of 1 mg of pristine HNT (PHNTs) and doped HNTs (DHNTs) were pressed with 100 mg of crystalline KBr to make pellets. The pellets were scanned in the range of 4000 to 400 cm^{-1} at a resolution of 2.5 cm^{-1}. The glass transition temperature (Tg) of pristine and doped HNTs were determined by using Shimadzu DSC – 60A (Japan). All samples were subjected to thermogravimetry analysis using Shimadzu Corp. DTG 50 apparatus, samples were heated to 1000 °C at a rate of 10 °C/min under nitrogen (N_2) atmosphere. The samples were dried prior to the analysis at 100 °C for 15 min to eliminate the moisture. To identify the precise structure and shifts in basal spacing of doped HNTs, X-Ray diffraction (XRD) analysis was performed by using Malvern Panalytical Empyrean 3rd Gen Diffractometer (UK). Cu-Kα radiation (λ = 1.504) was applied at a voltage of 45 kV and 40 mA rating and the samples were interpreted by scanning from 2 to 80° with step size of 0.02°. Scanning electron microscopy (SEM) was carried out using Gemini SEM 300 (Carl Zeiss, Germany) to investigate the surface morphology of pristine and doped HNTs. Surface topography was determined by using JOEL, JEM-1400HC transmission electron microscope analysis (TEM). Stability and surface charge of doped HNTs was measured by using Zeta-Meter system 3.0+ ZM3-U-G (Somatco, USA).

Table 1 Levels and factors for custom design

Factors (independent variables)	Levels used	
	Low (−1)	High (+1)
X_1: Concentration of γ-MPS	6	12
X_2: Concentration of HNT	25	50
X_3: Concentration of Ethanol	75	100
Responses (dependent variables)		
Y_1: Diffraction Angle (2θ)		
Y_2: Zeta Potential (mV)		

Table 2 Composition of two-level three factors for custom design

Runs	Factor levels		
	(X_1) Concentration of γ-MPS	(X_2) Concentration of HNT	(X_3) Concentration of ethanol
F1	6	25	75
F2	12	25	75
F3	12	25	100
F4	6	25	100
F5	6	50	75
F6	12	50	75
F7	12	50	100
F8	6	50	100

Results and Discussion

Chemical Analysis of γ-MPS doped HNTs

Fourier Transform Infrared Spectroscopy (FT-IR)

Doping of HNTs (DHNTs) with γ-MPS was confirmed by the presence of functional groups characterized by FT-IR analysis and the FTIR spectra of PHNT and DHNTs are shown in Fig. 1. Spectrum of PHNT revealed the absorption peaks at 910 cm^{-1} and 1031 cm^{-1} signifying the presence of Al-OH vibrations and Si-O groups. Some peaks were also observed at 437 cm^{-1} and 542 cm^{-1} as a result of deformation of Si-O, Si-O-Si and Al-O-Si groups [15]. Another peak was found at 3565 cm^{-1} representing the interlayer water molecule. Two new peaks were observed at 1496.96

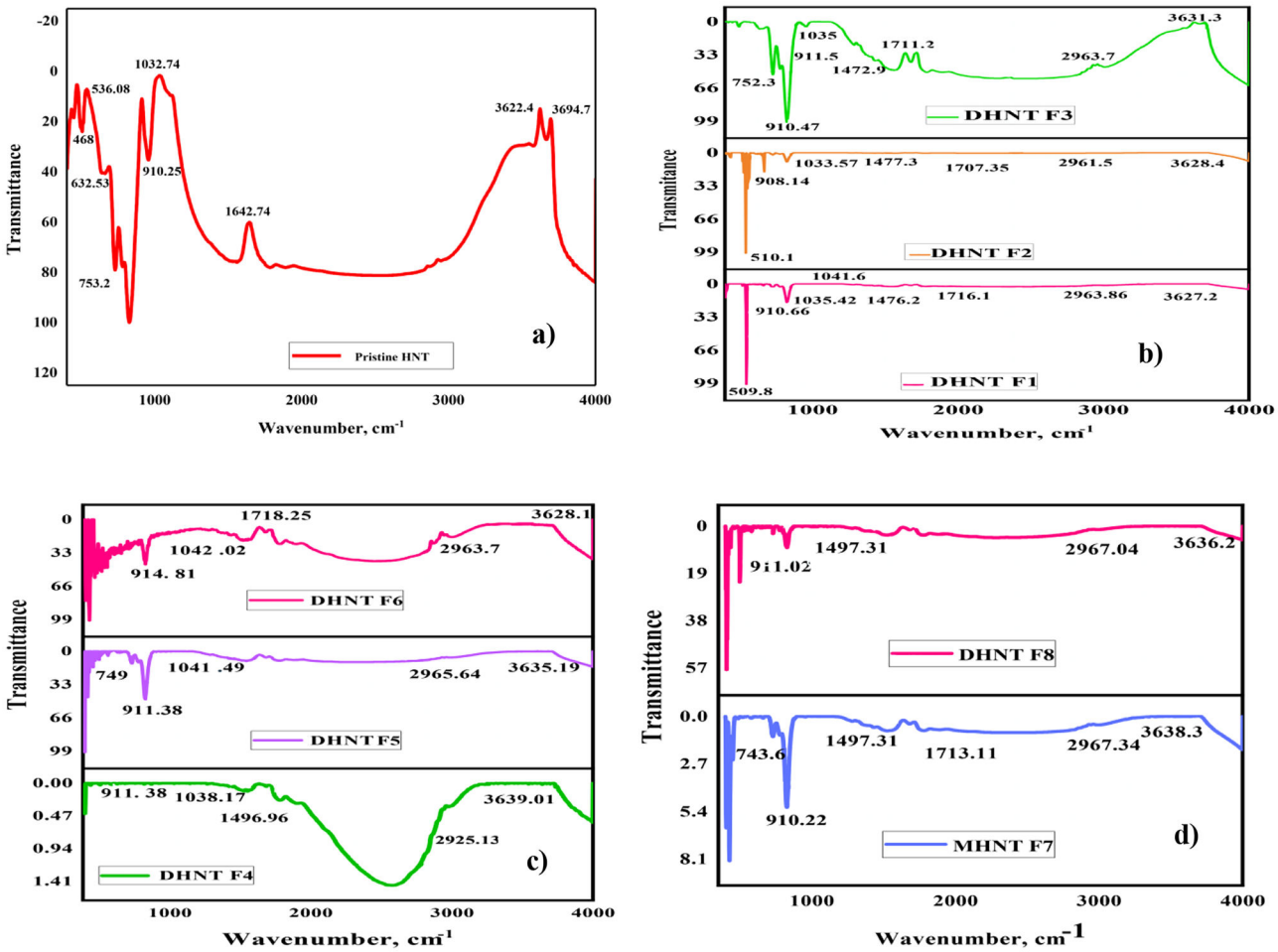

Fig. 1 FTIR spectra of **a** Pristine HNT, **b** DHNT F1-F3, **c** DHNT F4-F6, **d** MHNT F7 and DHNT F8

cm^{-1} and 2925 cm^{-1} attributed to deformation (scissoring) of CH_2 and symmetric stretching of C-H_2 [16]. As compared to PHNT, all doped HNTs exhibited these two peaks. Absence of a peak at 1700 cm^{-1} and the emergence of peaks at 911.38 cm^{-1}, 3621.42 cm^{-1} and 3694.25 cm^{-1} implies the scarcity of freely available hydroxyl groups of HNTs and unable the formation of hydrogen bond between HNTs and γ-MPS. Hence, the efficiency of HNTs modification was slightly decreased in DHNT Formulation 1 (DHNT F1), DHNT F2, DHNT F4 and DHNT F8 as shown in Fig. 1b and c. The appearance of peak at 1726.1 cm^{-1} is associated with stretching vibration of C=O bond of γ-MPS. DHNT F3 exhibited a narrow weak absorption band with a shoulder peak at 3631.3 cm^{-1}, signifying the presence of inner hydroxyl groups, existing between the sheets of one octahedral layer linked to tetrahedral one [17]. The appearance of absorption bands at 914.81 cm^{-1} and 1042.02 cm^{-1} in the spectra of DHNT F5 and DHNT F6 is attributed to Al-OH vibrations and Si-O stretching vibrations on the surface of HNTs. Another peak was observed at the frequency of 1031 cm^{-1} in the spectra of DHNTs emphasizing the formation of Si-O-Si bonds as Si groups of γ-MPS were linked to the surface of HNTs. In comparison with the spectrum of PHNT, a sharp intensified peak was observed at 910.22 cm^{-1} in modified HNT (MHNT F7) colloquially termed as doped HNTs, emphasizing the potentiality of RSi-O-Si and RSi-O-Al bonds between RSi-OCH_3 and RSi-OH groups of γ-MPS with Al-OH groups present at the edges of HNTs and Si-OH groups present on the surface resulting in HNT modification [18]. These findings authenticate the successful doping of γ-MPS on the surface of HNTs.

Thermogravimetric Analysis

Thermal stability of pristine and γ-MPS–doped HNTs were determined by thermo-gravimetric analysis (TGA) by monitoring the weight change that occurs as sample is heated at constant temperature. The primary weight loss for PHNT is in the temperature range from 50 to 100 °C due to dissipation of water molecule adsorbed on the surface and within

the lumen of HNT, PHNT showed a good thermal stability upto 350 °C without any significant weight loss. The secondary weight loss ranged from 360 to 550 °C, associated with de-hydroxylation of Al-OH groups and Si-O-Si groups of inner and outer surface of HNTs and the observed primary and secondary weight losses were 2.47% and 3.55% as shown in Fig. 2a. DHNT F1 sample resulted to an increased mass loss upto 2–5% as compared to PHNT in the temperature range of 45–90 °C, due to thermal decomposition of γ-MPS moieties, covalently bonded on the surface of HNTs [19]. Second curve was observed in the range of 400–590 °C corresponding to structural de-hydroxylation of Al-OH and Si-OH group as shown in Fig. 2b and this confirms the slight doping of HNTs using γ-MPS [20]. Whereas, in DHNT F2 and DHNT F3 sample mass loss was reduced in the range of 50–210 °C due to the presence of organosilanes, which in turn reduced the content of adsorbed water molecules from the surface and thereby enhanced the organophilicity of HNTs. The second peak was observed at the temperature of 210–380 °C with respective mass loss of 0.12% and 0.55%, as result of fragmentation of hydrogen bonds present in HNTs. The third peak is in the temperature of 365–595 °C associated with structural de-hydroxylation of Si-OH groups (Fig. 2b and c). DHNT F4 sample presented first peak in the temperature range of 80–110 °C due to evaporation of adsorbed water molecules, while in second peak, weight loss ranged from 390 to 570 °C. Similarly, DHNT F5 sample and DHNT F8 sample exhibited two mass loss peaks (Fig. 2c and d). The first peak was observed at 251–380 °C corresponding to thermal decomposition of silane moieties doped on the surface of HNTs. The second peak ranged from 380 to 595 °C due to structural de-hydroxylation of Al-OH and Si-O-Si groups. The main observation arising from these samples, include a sharp increase in weight loss, which can

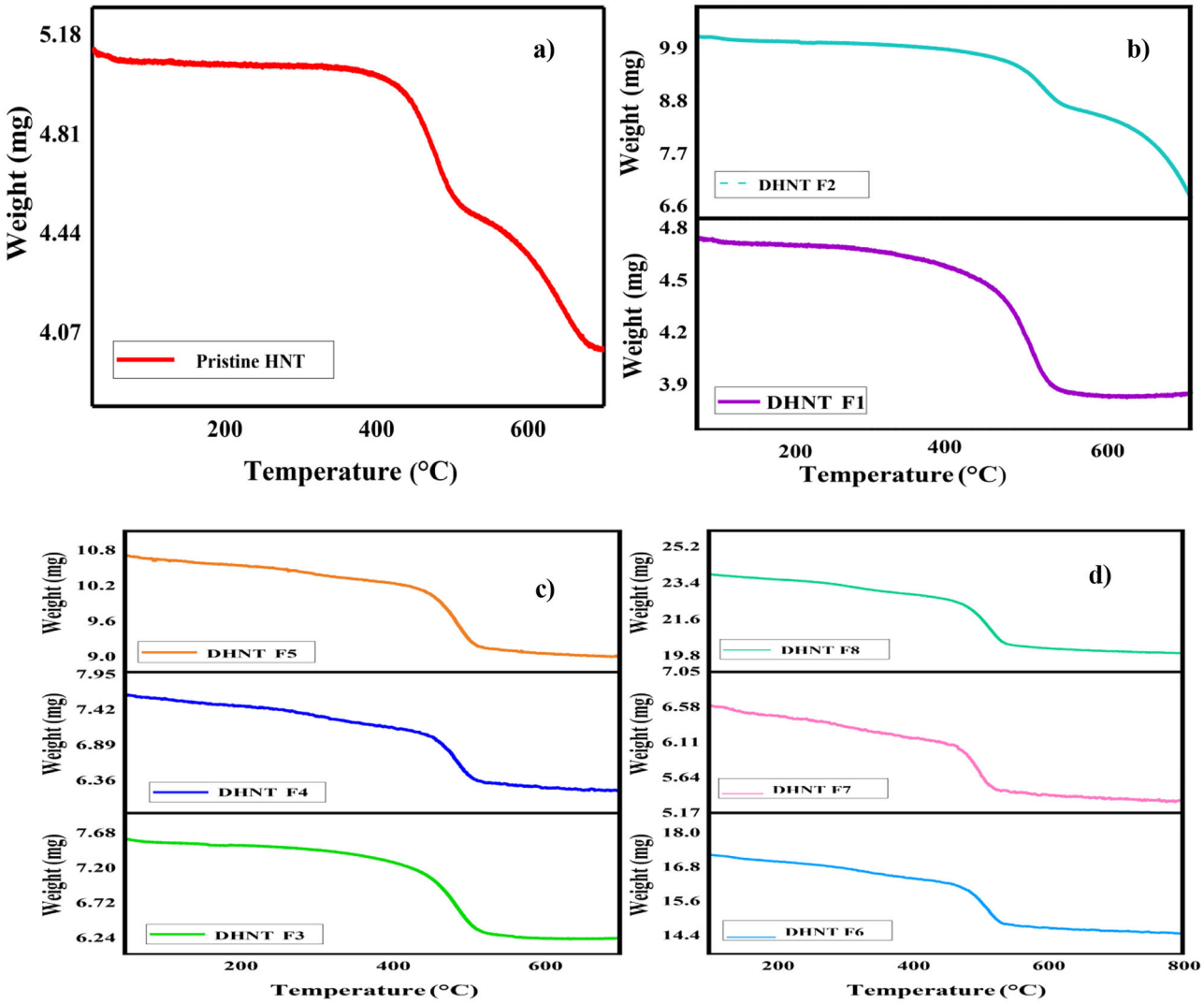

Fig. 2 TGA curves of **a** Pristine HNT, **b** DHNT F1-F2, **c** DHNT F3-F5, **d** DHNT F6-F8

be attributed to the interaction of methoxy groups of γ-MPS with the hydroxyl groups of HNTs. From this data, one may conclude that the effect of interaction reduces the efficiency of doping of HNTs using γ-MPS. As compared to other samples, TGA curves for DHNT F6 and DHNT F7 samples showed reduced mass loss at the temperature of 467–550 °C depicted in Fig. 2d. The reason for reduced mass loss is due to condensation of silanol groups, which resulted in the formation of siloxane groups. Therefore, formation of siloxane groups on the surface of HNTs contributed to successful doping of silanes on the surface of HNTs [21].

X-ray Diffraction Analysis

The X-ray diffraction patterns of pristine and doped HNTs are depicted in Fig. 3. PHNT revealed a sharp narrow peak at 2θ of 11.36° representing a basal spacing of 7.47 Å (determined by using Bragg's law), indicating that halloysite clay nanotubes belong to the state of hydration (7 Å hydration). Upon doping, the diffraction peak of DHNT F1 sample Fig. 3a showed a slight shift in the interlayer distance of 7.52 Å at 11.39°, indicating slight intercalation of γ-MPS into the layers of HNTs. Increase in basal spacing of DHNT F2 and DHNT F3 samples to 7.71 and 7.75 Å at the 2θ of 11.87° and 12.04° shown in Fig. 3b and c suggests better doping of HNTs [22]. It is observed from Fig. 3d and e that the intensity and sharpness of diffraction peaks in both DHNT F4 and DHNT F5 samples were drastically decreased to 2θ values of 11.67° and 11.41°, equal to d-spacing of 7.62 Å and 7.58 Å. This could be possible as a result of existence of strong hydrogen bonds between the layers and thereby assisting the inhibition of Al-OH groups present in the lumen and making them unavailable for doping of HNTs [23]. The diffraction pattern of DHNT F6 sample, Fig. 3f showed a slight broad peak at 2θ = 11.94° with a basal spacing of 7.73 Å indicating the amorphous state of doped HNTs [24]. Furthermore, the XRD pattern of DHNT F7 sample depicted in Fig. 3g, presented a sharp peak and the basal reflection of this sample shifted to higher 2θ value of 12.07°, indicating the successful doping of HNTs using γ-MPS as silane. This is achievable by the influence of high speed and temperature generated during homogenization and thereby culturing the framework to materialize the intercalation within the layers of clay nanotubes [25]. The basal reflection of DHNT F8 sample was decreased to 7.65 Å at 11.68° as shown in Fig. 3h suggesting slight doping of HNTs.

Morphological Characterization of Doped HNTs

Transmission electron microscopy is a widely used analytical tool for exploring the surface morphology and topography of clay nanotubes. Fig. 4a presents the structural and topographical characteristics of PHNTs. PHNTs are identically characterized by hollow tubular multilayered structure with an open-ended lumen, having an outer diameter of 40–70 nm, inner diameter of 10–30 nm and the length of HNT nanotube ranged from 400 to 800 nm [26]. After silylation of γ-MPS on the surface of HNTs, the outer diameter of DHNT F1 sample was slightly increased to 36.83 nm (Fig. 4b) and the surface texture was observed to be rough in nature, indicating the deposition of thin layer of silane moieties on the surface of HNTs. Micrograph of DHNT F2 sample presented in Fig. 4c revealed that the formation of covalent bond with γ-MPS on the surface of HNT resulted in disentanglement of HNTs. Thus, doping of HNTs with γ-MPS leads to an improvisation of entanglement of HNTs and thereby facilitating the dispersibility of HNTs [27]. Similarly, DHNT F3 sample (Fig. 4d) showed that the outer diameter was enlarged to 60.0 nm and the inner diameter was slightly reduced to about 20.0 nm, which represents that the surface of HNT was extensively doped. From TEM image of DHNT F4 sample depicted in Fig. 4e, it is clearly observed that the nanotubes were thin walled and exhibited smooth morphology with irregular diameter, indicating that the nanotubes were of low tubular quality. Morphology of DHNT F5 sample is observed to be in the form of aggregation as seen in Fig. 4f, such aggregation morphologies were formed under the influence of van der Waals forces [28]. The TEM image of DHNT F6 sample showed that the outer diameter in Fig. 4g was enlarged to 54.49 nm, while the inner diameter was reduced to 23.04 nm, signifying that a layer of γ-MPS was coated on the outer surface of HNT and also a part of lumen was stuffed with γ-MPS moieties. The surface morphology of DHNT F7 sample was found to be extensively uniform with an increased diameter and high tubular integrity as depicted in Fig. 4h. This is achievable because of increased concentration of γ-MPS, resulting in formation of siloxane groups on the surface and thereby enhancing the hydrophobicity of HNTs and maintaining the integrity of nanotube [29]. From Fig. 4i, it is clearly evident that the outer diameter of DHNT F8 sample was decreased to 42.47 nm with an increased inner diameter of 35.87 nm signifying slight doping of HNTs.

Zeta Potential

The zeta potential of pristine and γ-MPS–doped HNTs are shown in Fig. 5. PHNT exhibited a negative zeta potential value of −33.64 mV at pH of 7.0. This negative charge is mainly attributed to the silica groups present on the surface of halloysite nanotubes. After doping, the surface potential of doped HNTs was notably increased. The zeta potential value of DHNT F1 sample was −58.15 mV, indicating the moderate stability of formulation. In comparison to DHNT F1 sample, the zeta potential values for both DHNT F2 and DHNT F6 sample were found to be −79.23 mV and −87.15

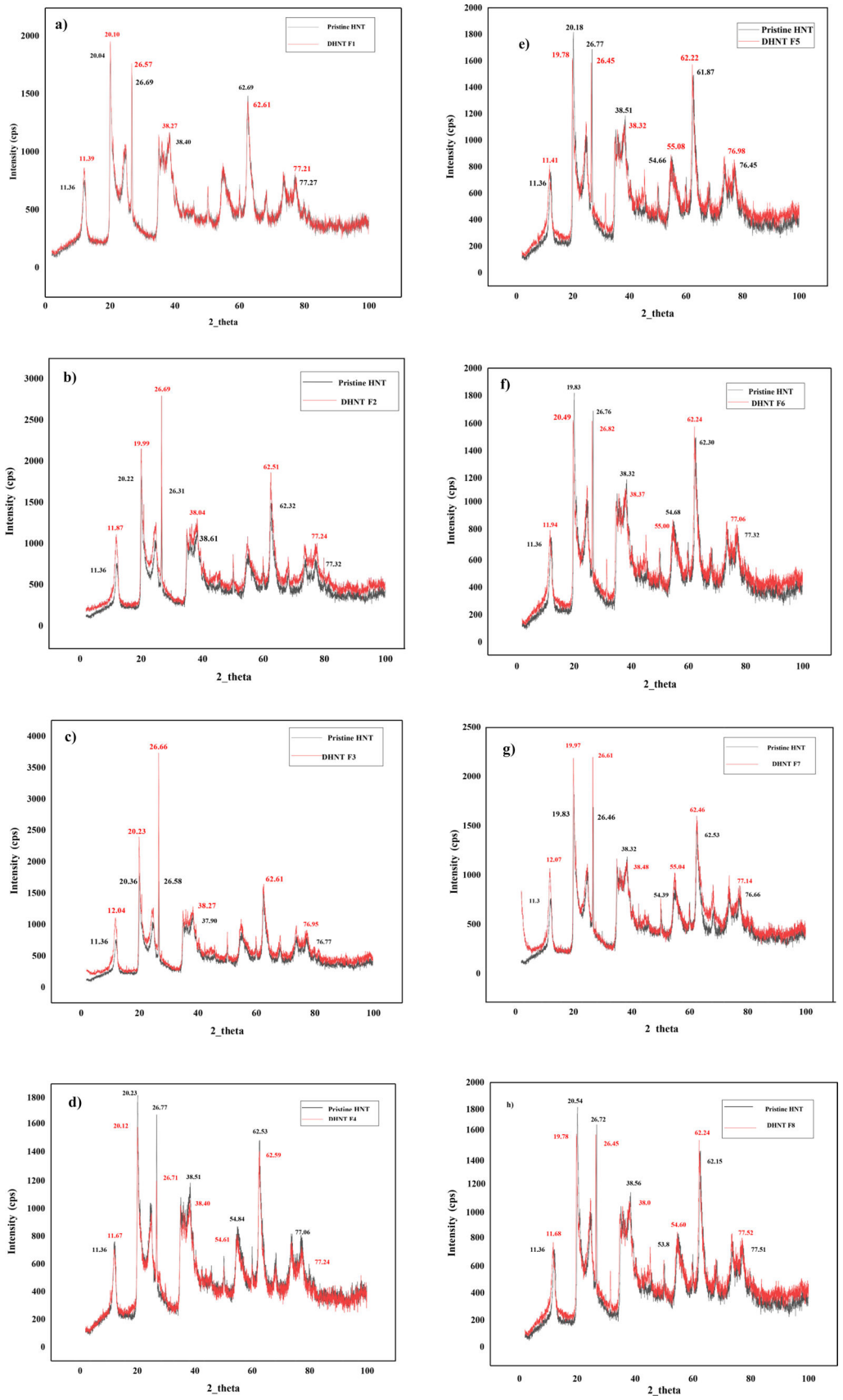

Fig. 3 X-ray diffraction patterns of **a** DHNT F1, **b** DHNT F2, **c** DHNT F3, **d** DHNT F4, **e** DHNT F5, **f** DHNT F6, **g** DHNT F1, **h** DHNT F1

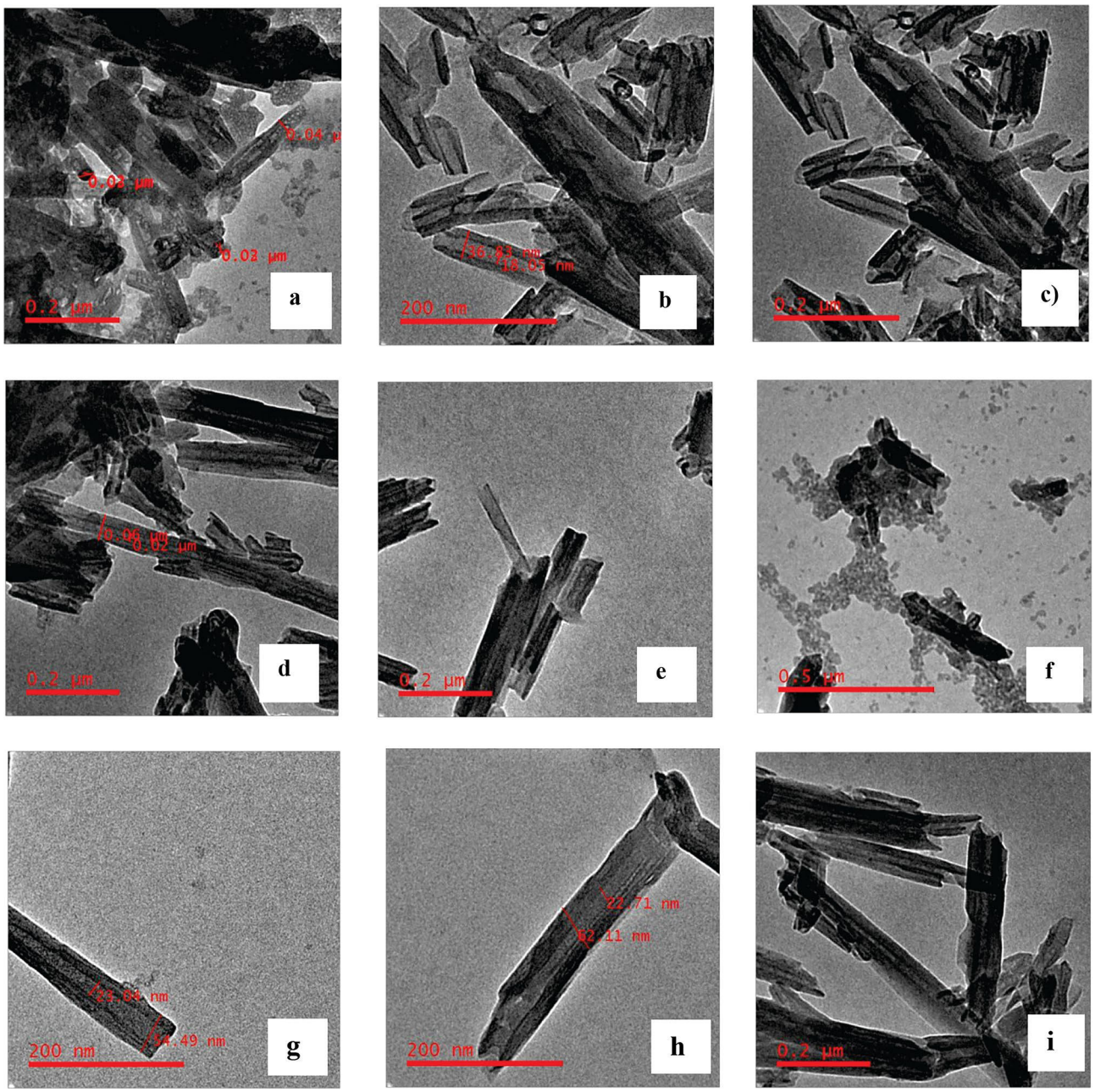

Fig. 4 TEM images of **a** Pristine HNT, **b** DHNT F1, **c** DHNT F2, **d** DHNT F3, **e** DHNT F4, **f** DHNT F5, **g** DHNT F6, **h** DHNT F7, **i** DHNT F8

mV suggesting the good stability and homogeneity of the formulation. Whereas, DHNT F4, DHNT F5 and DHNT F8 samples exhibited the surface potential values of −66.2 mV, −60.45 mV and −73.61 mV. This reduction in zeta potential is mainly attributed to the scarcity of –OH groups on the surface of HNTs. Similarly, DHNT F3 and DHNT F7 sample showed an increased zeta potential value of −90.38 mV and 95.7 mV. The exhibition of higher zeta potential value corresponds to excellent stability and dispersibility of the formulation [30].

Experimental Design Analysis

One of the most noticeable trends in the arena of pharmaceutical sciences is to maintain the standards and to fabricate high quality products, by fostering the proper balance between variables (input) and (output) responses of the experimental design. The selection of a specific design intensifies the generation of an optimal collection of experimental designs to examine the influence of independent factors on the selected responses. In the present study, custom

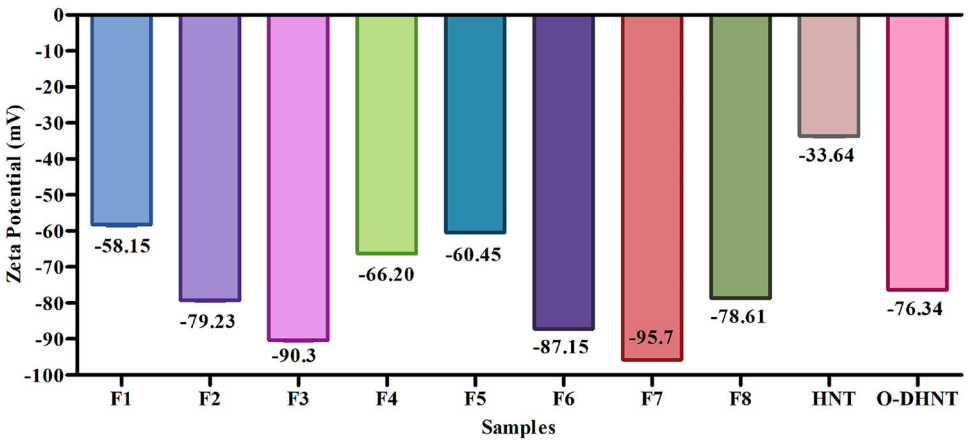

Fig. 5 Zeta potential of Pristine HNT, DHNT F1-F8 and Optimized DHNT

design was used to develop conceptual framework for process optimization and thereby enabling to explore the design space using graphical and mathematical design [31]. In accordance to the custom design, several statistical indicators were used to optimize the responses. Table 3 presents the complete pattern of experimental design along with the actual responses of the trial in the study.

Statistical Analysis for Diffraction Angle (2θ)

The model *F*-value of 114.65 implies that the model is significant for diffraction angle (Y_1) and there are 0.87% chances that a model *F*-value seems to be higher due to the noise for each case. Table 4 outlines the summary of statistical analysis for Y_1 response. From the data obtained, it is crystal clear that the variables X_1 (concentration of γ-MPS) and X_3 (concentration of Ethanol) were statistically significant for the response Y_1, as the ($p < 0.05$). Similarly, another variable X_2 (concentration of HNT) was found to be statistically non-significant for response Y_1, as ($p > 0.05$).

Effect of Formulation Variables on 2θ Value of Doped HNTs

The ability of γ-MPS to intercalate within the layers of HNTs is considered as critical parameter for optimizing the doping of HNTs. The 2θ value of all the doped HNTs ranged from 11.392 to 12.07° as shown in Table 3. 3D response plots for the effect of concentration of γ-MPS (X_1), concentration of HNT (X_2) and concentration of ethanol (X_3) on diffraction angle (2θ) of doped HNTs are depicted in Figure 6. The results of ANOVA tests presented a statistical significant effect on the response variable diffraction angle (2θ) (Y_1). The quadratic polynomial equation in terms of coded factors is as follows:

$$Diffraction\ Angle(20) = +9.525 + 0.156X_1 + 0.003X_2 + 0.0173X_3 - 0.0009X_1X_3 - 0.0004X_1X_2 \quad (1)$$

According to the polynomial equation, the positive sign of regression coefficient (X_1) signifies the synergistic effect

Table 3 The pattern of experimental design and actual responses of γ-MPS doped HNTs

Variables				Actual responses	
Run	Concentration of (X_1)	Concentration of (X_2)	Concentration of (X_3)	Diffraction angle (2θ) (Y_1)	Zeta potential (mV) (Y_2)
F1	6	25	75	11.392	−58.15
F2	12	25	75	11.873	−79.23
F3	12	25	100	12.004	−90.3
F4	6	25	100	11.677	−66.2
F5	6	50	75	11.416	−60.45
F6	12	50	75	11.944	−87.15
F7	12	50	100	12.075	−95.7
F8	6	50	100	11.682	−73.61

The X_1, X_2 and X_3 are the concentration of ɣ-MPS, HNT and ethanol

Table 4 Summary of statistical analysis for diffraction angle

Source	Sum of squares	DF	Mean square	*F*-value	*p*-value	Remarks
Model	0.4704	5	0.0941	114.65	0.0087	Significant
X_1	0.3737	1	0.3737	455.36	0.0022	Significant
X_2	0.0037	1	0.0037	4.45	0.1693	Non-significant
X_3	0.0826	1	0.00826	100.68	0.0098	Significant
C. Total	0.4721	7				
R^2	R^2 (pred)	R^2 (adj)				
99.65%	94.44%	98.78%				

The X_1,X_2 and X_3 are the concentration of ϒ-MPS, HNT and ethanol

on the response variable (Y_1). In other words, as the concentration of γ-MPS increases, the 2θ value of doped HNT also increased and this could be attributed to the intercalation of γ-MPS into the layers of HNTs, resulting in increased basal spacing and the peaks were observed to be slightly broad and shifted to a higher 2θ value. The existence of slight broad peaks represents amorphous nature of doped HNTs. The equation also signifies that by increasing the concentration of HNT, (X_2) exhibited a synergistic effect on diffraction angle (2θ) of doped HNTs. In contrast to the polynomial equation, the results of ANOVA test suggest that the impact of X_2 variable on the response variable (Y_1) was non-significant as the $p > 0.05$ and this could be due to reduced basal spacing, which resists the free movement of silane moieties into the layers of HNTs. The positive coefficient of concentration of ethanol (X_3) signifies that the 2θ value increased significantly by increasing the concentration of ethanol, this is achievable due to solubilization of silane

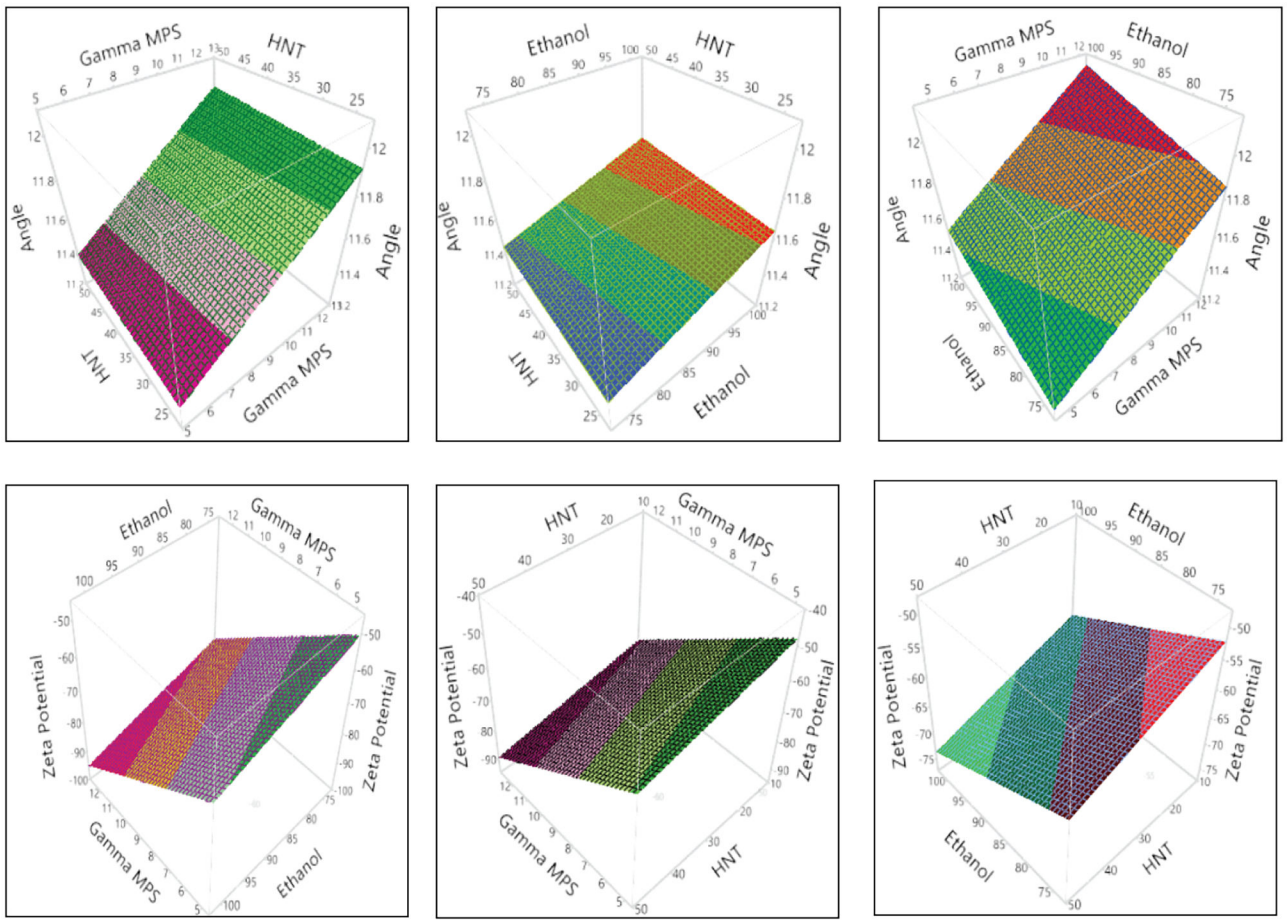

Fig. 6 3D surface plots highlighting the effect of independent variables on response variables (diffraction angle and zeta potential)

moiety in ethanol, resulting in increased basal spacing and shifted to higher 2θ value by enhancing the intercalation within the layers of HNTs. The statistical analysis indicates that X_3 variable has significant effect on Y_1 as ($p < 0.05$). The two factors' interactions were found in the quadratic Equation (1), where these factors (X_1, X_2 and X_3) exhibited negative effect on the response variable. The co-efficient of all the three factors did not exhibit that prominent effect on the response variable as the coefficient values were least for all the three factors.

Statistical Analysis for Zeta Potential (mV)

The model *F*-value of 61.96 implies that the model is significant for Zeta Potential (Y_2) and there are 0.10% chances that a model *F*-value seems to be higher due to the noise for each case. Table 5 outlines the summary of statistical analysis for Y_2 response. From the data obtained, it is crystal clear that the variable X_1 (concentration of γ-MPS), X_2 (concentration of HNT) and X_3 (concentration of ethanol) were statistically significant for the response Y_2, as the ($p < 0.05$).

Effect of Sample Variables on the Zeta Potential of Doped HNTs

Zeta Potential is a measure of the effective electric charge on the surface of nanoparticles. It is an indicator for the stability and homogeneity of HNTs. The structural configuration and dispersion behavior are the key parameters that influence the electrical potential of HNTs. The zeta potential value of all the doped HNTs ranged from −58.15 mV to −78.61 mV presented in Table 3. 3D response plots for the effect of concentration of γ-MPS (X_1), concentration of HNT (X_2) and concentration of ethanol (X_3) on zeta potential (mV) of doped HNTs are depicted in Fig. 6. The results of ANOVA analysis presented significant effect on all the three coded factors. The quadratic polynomial expression for different variables on response (Y_2) is as follows:

The ANOVA results of the experimental design showed that the zeta potential of doped HNTs was statistically significant with the coded factors as ($p < 0.05$) and this achievable, due to the wrapping of silanol groups on the surface of HNT resulting in the formation of Si-O-Si linkage. The highlights of 3D surface plots for the effects of independent variables on both diffraction angle and zeta potential response variables are shown in Fig. 6. The two factors interactions were observed in quadratic Equation (2) and the interaction factors X_1X_3 showed positive effect on the response variable, but the other interaction factors X_1, X2 and X_2, X3 exhibited negative effect on the selected response variable. The co-efficient of all the three factors presented slight prominent effect on the response variable as the coefficient values were slightly higher for all the three factors.

Optimization of Doped HNTs

Optimization is defined as "choosing the best element from some set of available alternatives". It is the process of applying a set of systemic strategies in order to achieve the best combination of product and/or process attributes under a given set of variables [32]. In order to analyze the effect of independent variables on the selected responses, selection of proper optimization tool and the application of desirability function is necessitated.

Desirability values were calculated using JMP software for achieving optimal doped HNTs (DHNTs) by using Custom design. The overall desirability of the optimal DHNTs was suggested to be prepared using 9 ml of γ-MPS (X_1), 37.5 g of HNT (X_2) and 87.5 ml of Ethanol (X_3). To confirm the model efficacy, the suggested optimal DHNTs were prepared, evaluated and compared with the predicted responses obtained from the software.

$$Zeta\ Potential(mV) = +0.6275 - 4.379X_1 - 0.0490X_2 - 0.3783X_3 + 0.0053X_1X_3 - 0.0020X_2X_3 - 0.0032X_2X_3 - 0.0032X_2X_3 \quad (2)$$

Table 5 Summary of statistical analysis for zeta potential

Source	Sum of squares	DF	Mean square	*F*-value	*p*-value	Remarks
Model	1379.63	5	275.93	61.96	0.001	Significant
X_1	1103.80	1	1103.80	274.87	0.0001	Significant
X_2	66.30	1	66.30	14.89	0.0068	Significant
X_3	208.39	1	208.39	46.80	0.0207	Significant
C. Total	1388.54	7				
R^2 99.36%	R^2 (pred) 95.74%	R^2 (adj) 97.76%				

The X_1, X_2 and X_3 are the concentration of γ-MPS, HNT and ethanol

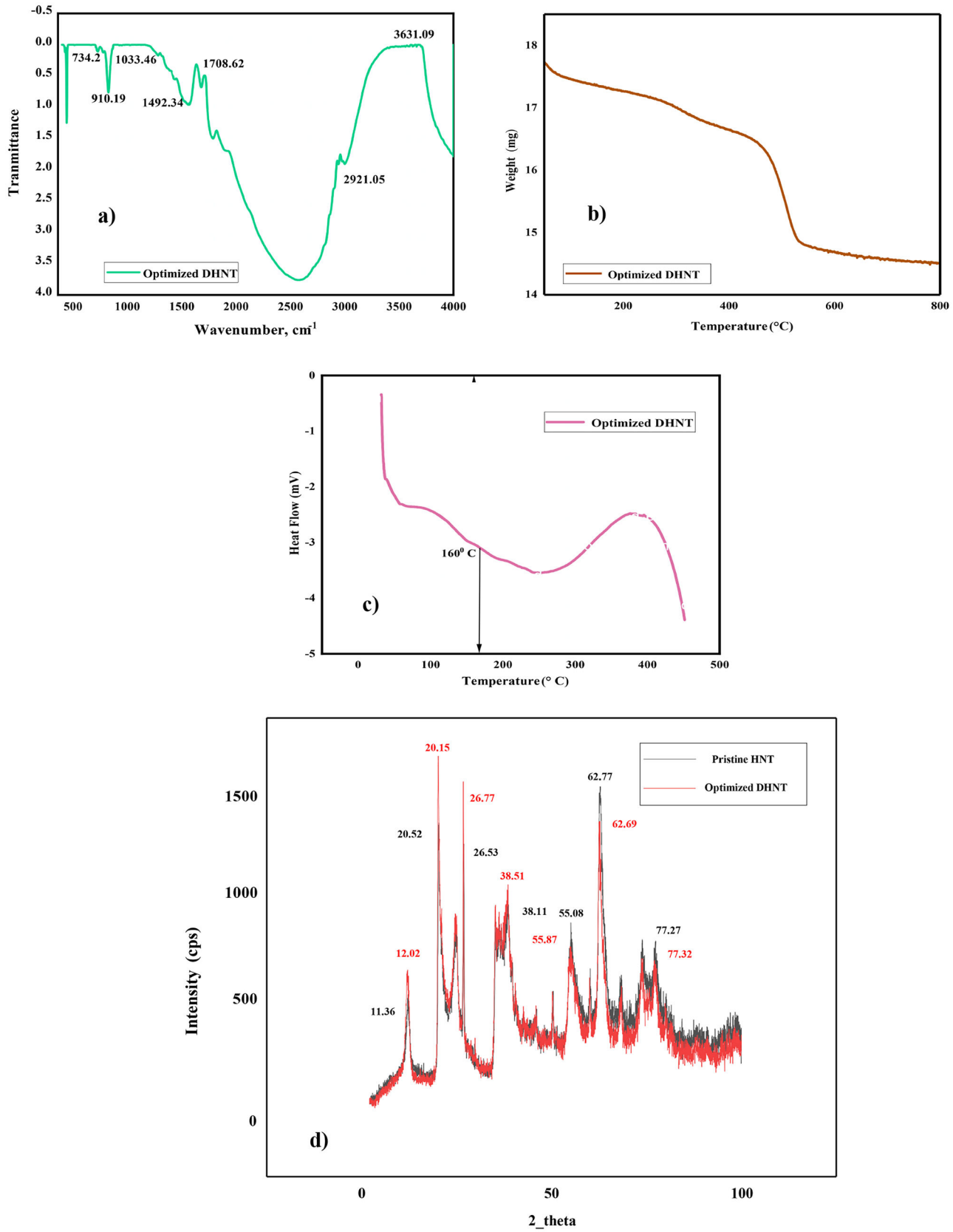

Fig. 7 **a** FTIR spectra of O-DHNT, **b** TGA curve of O-DHNT, **c** DSC thermogram of O-DHNT, **d** XRD pattern of O-DHNT

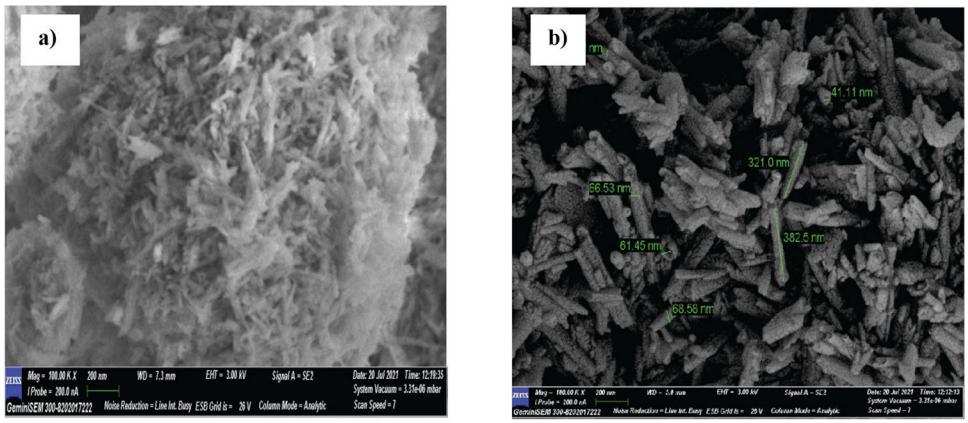

Fig. 8 SEM micrographs of **(a)** PHNT, **(b)** Optimized DHNTs

Characterization of Optimized DHNTs

FTIR spectrum of optimized DHNTs is shown in Fig. 7a. The absorption bands at 734.2 cm^{-1} and 910.19 cm^{-1} can be attributed to symmetric stretching of Si-O groups and O-H deformation of inner hydroxyl groups. The appearance of peak at 1033.46 cm^{-1} represents the formation of Si-O-Si bonds. The presence of two new peaks at 1492.34 cm^{-1} and 2921.05 cm^{-1} confirms the scissoring of C-H_2 groups and symmetric stretching of C-H_2 groups. A sharp peak was observed at the frequency of 1708.62 cm^{-1}assigned to the stretching of C=O group. The signals at the frequency of 3631.09 cm^{-1} are attributed to O-H stretching of inner hydroxyl groups. The presence of these functional groups confirms the optimization of doped HNTs. In doped-optimized sample, four mass loses were observed as seen in Fig. 7b. The first mass loss is in the range of 50–150 °C, and this mass loss is due to the evaporation of physically adsorbed water molecule. The second mass loss in the range of 150–300 °C is associated with thermal degradation of silane molecules present on the surface of HNTs. Another peak corresponding to third mass loss ranged from 300 to 475 °C due to the fragmentation of hydrogen bonds present in the lumen of HNTs. The fourth mass loss occurs in the temperature range of 475–550 °C, which is mainly associated with structural dehydroxylation of Si-OH and Al-OH groups. The overall weight loss of optimized sample was reduced to about 0.10% as compared to the other samples, signifying the successful optimization of doped HNTs. DSC thermogram of optimized DHNTs exhibited a small endothermic peak at the higher glass transition temperature of 160 °C (see Fig. 7c). The higher glass transition temperature is due to the interaction of surface silanols with carbonyl groups through hydrogen bonding [33]. The diffraction peak of optimized DHNTs showed an increase in basal spacing of 7.73Å at the 2θ value of 12.02°, indicating that a layer of γ-MPS was uniformly intercalated within the layers of HNTs as depicted in Fig. 7d. Optimized DHNTs presented a negative zeta potential value of −79.25 mV, indicating that the sample has exhibited good stability and homogeneity.

Morphological Characterization of Optimized DHNTs by Scanning Electron Microscopy

The SEM micrograph of PHNT is shown in Fig. 8a. The lengths of the nanotubes were small with uneven morphologies and these nanotubes were highly aggregated appearing as a cotton cloud of nanotubes. Such aggregation morphologies were due to the formation of van der Waals forces within the layers of HNTs. After doping, the intensity of aggregation was drastically reduced as seen in Fig. 8b, the tubes were clearly observable with significant dimensions of the nanotubes. This is possible due to the effect of silanization, by making the surface of HNTs highly hydrophobic in nature [34].

Optimization and Validation

Validation test was performed to confirm the reliability of predicted responses obtained from the optimal combinations of independent variables (X_1 = 9 ml, X_2 =37.5 g and X_3 = 87.5 ml). The doped samples were characterized for the response variables (Y_1 = Diffraction angle and Y_2=Zeta potential) and the obtained experimental data were compared with the predicted responses in Table 6. To validate the experimental design, the percent error was calculated for each response variable. The percent error was determined by the following equation [35],

Table 6 Data of actual, predicted values and percentage error

Responses	Predicted values	Actual values	% Error
Diffraction angle (2θ)	11.75°	12.02°	2.24%
Zeta potential (mV)	−76.34	−79.25	3.67%

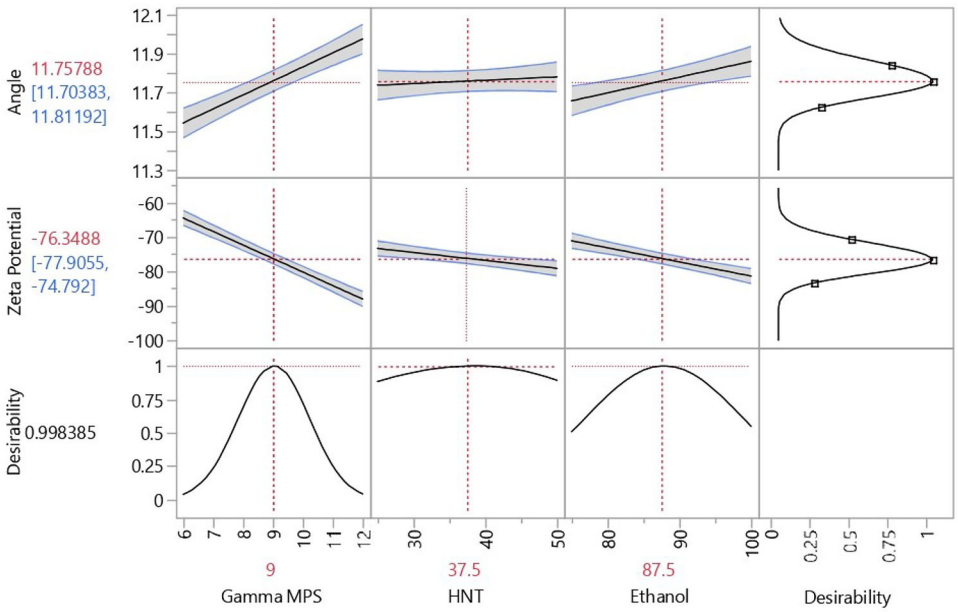

Fig. 9 Desirability plot for the optimization of process parameters

$$\%\ Error = \frac{(\text{Actual value} - \text{Predicted value}) * 100}{\text{Actual Value}} \quad (3)$$

From the above data as seen in Table 6, it is clear that the values of % error for all the response variables were found to be less than 5%, indicating that optimization by custom design proves to be a reliable method to optimize the process variables. The overall desirability was found to be D = 0.998 from the desirability plot depicted in Fig. 9, signifying the efficiency of custom design for the studied responses.

Conclusion

HNTs were successfully doped with γ-MPS as a silane coupling agent by using ultra-turrax homogenizer. The doped HNTs were subjected to thermal analysis, morphological characterization, FTIR analysis, XRD and Zeta potential analysis. On evaluating all the doped HNTs, it is observed that the presence of negative charge confirms the inclusion of γ-MPS on the surface of HNTs. The concept of custom design was applied to optimize the concentration of formulation variables with respect to response variables such as (Y_1 = Diffraction angle and Y_2 = Zeta potential). The optimal values were obtained to measure the desirability at the concentration of 9 ml (γ-MPS), 37.5 g (HNT) and 87.5 ml (ethanol). The overall desirability was found to be D = 0.998, signifying the efficiency of the design for the selected responses. Therefore, the results of statistical analysis indicate that the application of custom design proves to be a promising method for the optimization of doped HNTs.

Future Directions

The unique and versatile properties of doped HNTs such as natural in origin, non-toxic, biodegradable and bio-compatible in nature have given an edge to doped HNTs as a nano-carrier in delivering drugs effectively to the brain. The nano-scale structure, fine particle size and large surface area of doped HNTs enhance the degrees of dispersion and facilitate in loading Biopharmaceutical Classification of drugs (BCS Class II) and promote in enhancing the solubility and bioavailability of the drugs.

Supplementary Information The online version contains supplementary material available at https://doi.org/10.1007/s12247-022-09680-8.

Acknowledgements The authors are thankful to KLE College of Pharmacy, Belgaum for providing the facility to carry out zeta potential analysis. We also express special thanks to National Institute of Technology, Surathkal, Karnataka for XRD and SEM analysis, Jiwaji University, Gwalior for TGA, DSC and TEM analysis, Furthermore, we are also thankful to JMP support team to carry out optimization studies by using JMP software.

Author Contribution All the authors have equal contribution and participation in this research work. RS and FD have structured the study design and carried out the optimization, experimentation, collection and interpretation of data. RS and FD contributed in drafting and revision of the manuscript. HS has contributed in interpretation of statistical data analysis. RS, FD and HS have read and approved the manuscript.

Funding The research work was supported by funding agency AICTE - RPS Scheme, Government of India. Scheme sanctioned with file no: 8-89/FDC/RPS (POLICY-1) /2019-2020.

Declarations

Ethics Approval and Consent to Participate Not applicable.

Competing Interests The authors declare no competing interests.

References

1. Eveline B, Tales D, Douglas AS, Henri SS, Susana AL, Raquel SM. Organosilane-functionalized halloysite for high performance halloysite/heterophasic ethylene–propylene co-polymer nanocomposites. Appl Clay Sci. 2015;112:68–74. https://doi.org/10.1016/j.clay.2015.04.020.
2. Sagare RD, Dasankoppa FS, Sholapur HN, Buruga K. Halloysite nanotubes: design, characterization and applications. A review. Farmacia. 2021;69(2):218–14. https://doi.org/10.31925/farmacia.2021.2.3.
3. Bediako E, Nyankson E, Arhin D, Tuffour B, Lukowiec D, Tomiczek B, et al. Modified halloysite nanoclay as a vehicle for sustained drug delivery. Heliyon. 2018;4(7):1–22. https://doi.org/10.1016/j.heliyon.2018.e00689.
4. Satish S, Tharmavaram M, Rawtani D. Halloysite nanotubes as a nature's boon for biomedical applications. Nanobiomedicine. 2019;6:1–16.
5. Saif MJ, Asif HM. Escalating applications of halloysite nanotubes. J Chil Chem Soc. 2015;60(2):2949–53. https://doi.org/10.4067/S0717-97072015000200019.
6. Yuan P, Tan D, Bergaya F. Properties and applications of halloysite nanotubes: recent research advances and future prospects. Appl Clay Sci. 2015;112:75–93. https://doi.org/10.1016/j.clay.2015.05.001.
7. Santos AC, Ferreira C, Veiga F, Ribeiro AJ, Panchal A, Lvov Y, Agarwal A. Halloysite clay nanotubes for life sciences applications: from drug encapsulation to bioscaffold. Adv Colloid Interface Sci. 2018;257:58–70. https://doi.org/10.1016/j.cis.2018.05.007.
8. Barry A. Hydrophobicity, hydrophilicity and silanes. Paint and Coatings Industry. 2006;22(10):114.
9. Yang Y, Chen Y, Leng F, Huang L, Wang Z, Tian W. Recent advances on surface modification of Halloysite nanotubes for multifunctional applications. Appl Sci. 2017;7:1215. https://doi.org/10.3390/app7121215.
10. Riza Erdogan A, Ilker A, Cevdet K. Influences of aminosilanization of halloysite nanotubes on the mechanical properties of polyamide-6 nanocomposites. Polym Compos. 2014;35(7):1350–61. https://doi.org/10.1002/pc.22787.
11. Ravichandran G, Rathnakar G, Santosh N. Effect of heat treated HNT on physico-mechanical properties of epoxy nanocomposites. Compos Commun. 2019;13:42–6. https://doi.org/10.1016/j.coco.2019.02.005.
12. Dhankar P. Homogenization fundamentals. IOSR J Eng. 2014;4(5):1–8.
13. Aziz DE, Abdelbary AA, Elassasy AI. Implementing central composite design for developing transdermal diacerein loaded niosomes: *ex vivo* permeation and *in vivo* deposition. Curr Drug Deliv. 2018;15(9):1330–42. https://doi.org/10.2174/1567201815666180619105419.
14. Buruga K, Kalathi J. Fabrication of γ-MPS modified HNT-PMMA nanocomposites by ultrasound assisted mini-emulsion polymerization. JOM. 2018;70(7):1307–12. https://doi.org/10.1007/s11837-018-2829-9.
15. Padhi S, Acharya PGR, Nayak NC. Mechanical and morphological properties of modified halloysite nanotubes filled ethylene-vinyl acetate copolymer nanocomposites. J Polym Eng. 2017;184(24):271–9. https://doi.org/10.1515/polyeng-2017-0075.
16. Yuan P, Southon P, Liu Z, Green MR, Hook J, Antill S, Kepert C. Functionalization of halloysite clay nanotubes by grafting with γ-aminopropyltriethoxysilane. J Phys Chem C. 2008;112(40):15742–51. https://doi.org/10.1021/jp805657t.
17. Jozanikohan G, Abarghooei M. The Fourier transform infrared spectroscopy (FTIR) analysis for the clay mineralogy studies in a clastic reservoir. J Petrol Explor Prod Technol. 2022;12:2093–106. https://doi.org/10.1007/s13202-021-01449-y.
18. Pasbakhsk P, Ismail H, Fauzi Ahmed MN, Bakar AA. EPDM/modified halloysite nanocomposites. Appl Clay Sci. 2010;48(3):405–13. https://doi.org/10.1016/j.clay.2010.01.015.
19. Zargarian SS, Haddadi-Asl, Hematpour H. Carboxylic acid functionalization of halloysite nanotubes for sustained release of diphenhydramine hydrochloride. J Nanopart Res. 2015;218(17):1–13. https://doi.org/10.1007/s11051-015-3032-3.
20. Yiu H, Botting CH, Botting NP, Wright P. Size selective protein adsorption on thiol-functionalized SBA-15 mesoporous molecular sieve. Phys Chem Chem Phys. 2001;3(15):2983–5. https://doi.org/10.1039/B104729A.
21. Sederidou I, Karabela M. Effect of the amount of 3-methacycloxypropyltrimethoxy silane coupling agent on physical properties of dental resin nanocomposites. Dent Mater. 2009; 25(11):1315–24. https://doi.org/10.1016/j.dental.2009.03.016.
22. Fouad H. Experimental and numerical studies of notch strengthening behavior of semi-crystalline ultra-high molecular weight polyethylene. Materials & Design. 2010;31(3):1117–29. https://doi.org/10.1016/j.matdes.2009.09.042.
23. Frost R, Mako E, Kristof J, Horvath E, Kloprogge JT. Modification of kaolonite surfaces by mechanochemical treatment. Langmuir. 2001;17(16):4731–8. https://doi.org/10.1021/la001453k.
24. Schaak R, Holder C. Tutorial on powder X-ray diffraction for characterizing nanoscale materials. ACS Nano. 2019;13:7359–65.
25. Albdiry MT, Yousif BF, Ku H, Lau KT. A critical review on the manufacturing processes in relation to the properties of nanoclay/polymer composites. J Compos Mater. 2013;47(9):1093–1115. https://doi.org/10.1177/2F0021998312445592.
26. Terzopoulou Z, Papageorgiou D, Papageorgiou G, Bikiaris D. Effect of surface functionalization of halloysite nanotubes on synthesis and thermal properties of poly (ε-caprolactone). J Mater Sci. 2018;53(9):6519–41. https://doi.org/10.1007/s10853-018-1993-1.
27. Zhou Z, Wang S, Lu L, Zhang Y, Zhang Y. Functionalization of multi-wall carbon nanotubes with silane and its reinforcement on polypropylene composites. Compos Sci Technol. 2008;68(7):1727–33. https://doi.org/10.1016/j.compscitech.2008.02.003.
28. Mu B, Zhao M, Liu P. Halloysite nanotubes grafted hyperbranched (co) polymers via surface -initiated self –condensing vinyl (co) polymerization. J Nanopart Res. 2008;10(5):831–8. https://doi.org/10.1007/s11051-007-9319-2.
29. Zhan W, Yi H, Song S, Zhao W, Rao F. Hydrophobic agglomeration behaviors of clay minerals as affected by siloxane structure. Colloids Surf A. 2019;568:36–42. https://doi.org/10.1016/j.colsurfa.2019.01.061.
30. Nguyen TC, Nguyen TD, Vu DT, Dinh DP, Nguyen AH, Li TN, Dao PH, Nguyen TL, Bach LG, Thai H. Modification of titanium dioxide nanoparticles with 3-(Trimethoxysilyl) propyl methacrylate silane coupling agent. J Chem. 2020;1–10. https://doi.org/10.1155/2020/1381407.
31. Akram W, Garud N. Design expert as a statistical tool for optimization of 5-ASA-loaded biopolymer-based nanoparticles using Box Beknken factorial design. Futur J Pharm Sci. 2021;146(7):1–17. https://doi.org/10.1186/s43094-021-00299-z.
32. Garg RK, Singhavi I. Optimization techniques: an overview for formulation development. Asian J Pharm Res. 2015;5(3):217–21.

33. Blum F, Young E, Smith G, Sitton O. Thermal analysis of adsorbed poly (methyl methacrylate) on silica. Langmuir. 2006;22(10):4741–4. https://doi.org/10.1021/la053098.
34. Wang DH, Baek JB, Tan LS. Grafting of vapor-grown carbon nanofibers (VGCNF) with a hyperbranched poly (ether-ketone). Mater Sci Eng B. 2006;132(1–2):103–7. https://doi.org/10.1016/j.mseb.2006.02.039.
35. Tafere C, Yilma Z, Abrha S, Yehualaw A. Formulation, in vitro characterization and optimization of taste masked orally disintegrating co-trimoxazole tablet by direct compression. PLoS One. 2021;16(3):1–35. https://doi.org/10.1371/journal.pone.0246648.

https://doi.org/10.31925/farmacia.2021.2.3 **REVIEW**

HALLOYSITE NANOTUBES: DESIGN, CHARACTERIZATION AND APPLICATIONS. A REVIEW

REVATI DHARAMPAL SAGARE [1#], FATIMA SANJERI DASANKOPPA [2]*, H. N. SHOLAPUR [3#], KEZIA BURGA [4]

[1]*PhD. Student, Department of Pharmaceutics, Discipline of Pharmacy, KLE College of Pharmacy, Hubballi, India*
[2]*Department of Pharmaceutics, Faculty of Pharmacy, KLE College of Pharmacy, Hubballi, India*
[3]*Department of Pharmacognosy, Faculty of Pharmacy, KLE College of Pharmacy, Hubballi, India*
[4]*Scientific research assistant, Department of Chemistry, University of Warsaw, Warsaw, Poland*

**corresponding author: fsdasankop@gmail.com*
[#]*Authors with equal contribution.*

Manuscript received: May 2020

Abstract

Halloysite nanotubes (HNTs) have several exciting potential applications in polymer nanocomposites. These are naturally sourced nanomaterials obtained from the mines as a natural deposit. The hollow tubular nanostructure with biocompatibility, environmental friendly and low-cost possessing makes halloysite as trendsetter in green nanotechnology. These are composed of double-layered, aluminosilicate minerals with an ultra-tiny hollow tubular structure in submicron range. The specific characteristics of HNTs lead to plentiful range of applications in environmental sciences, dye removal, anticorrosive coatings, in cosmetics, flame retardants, forensic science, etc. HNTs display remarkable thermal stability, faster adsorption rates, tuneable release rates, excellent drug encapsulation, biocompatibility, mechanical properties and ease of availability, therefore with numerous pharmaceutical applications. Nanomedical applications are gene delivery, tissue engineering, cancer and stem cells isolation and bio-imaging. This review is focused on the detailing HNTs for its structure features, functionalization methods, drug loading and their versatile applications.

Rezumat

Nanotuburile din haloizit (NHT) prezintă o serie de aplicații interesante cu potențial în domeniul nanocompozitelor polimerice. Acestea sunt nanomateriale naturale obținute din depozitele naturale miniere. Structura nanotubulară goală pe interior ce prezintă proprietăți biocompatibile, benefice mediului înconjurător și costuri reduse sunt principalele avantaje ale halozitului ca și nano-tehnologie verde. Acestea sunt compuse din minerale aluminosilicate bistratificate, cu o structură tubulară submicronică, goală pe interior și cu diametru mic. Caracteristicile acestora determină o gamă variată de aplicații în domeniul științelor mediului, pentru îndepărtarea coloranților, a învelișurilor anticorozive, în industria cosmetică, în domeniul produselor ignifuge, în criminalistică etc. Nanotuburile de haloizit prezintă stabilitate termică pronunțată, viteză de absorbție ridicată și eliberare rapidă ce poate fi potențată, excelente proprietăți de încapsulare a substanțelor medicamentoase, biocompatibilitate, bune proprietăți mecanice și biodisponibilitate, găsindu-și numeroase aplicații în domeniul farmaceutic. Utilizările nanomedicale se regăsesc în terapia genică, în domeniul ingineriei tisulare, în izolarea celulelor stem și a celor canceroase și în bioimagistică. Articolul sintetizează cele mai noi informații referitor la nanotuburile de haloizit, respectiv a caracteristicilor structurale, a funcționalizării, a capacității de încărcare cu substanțe medicamentoase, precum și a utilizărilor versatile ale acestora.

Keywords: halloysite nanotubes (HNTs), biocompatible, cosmetics, gene drug delivery

Introduction

In the field of nanotechnology, various nanomaterials are used like carbon nanotubes, nanofluids, nano-emulsions, nanocapsules etc. Due to their harmful effects, these nano materials are not designed safe for individuals and for the environment as well [37]. Green nanotechnology is one of the promising technologies that aims in advancing environment safe and less harmful nanoproducts. HNTs, nanocomposites and nanopowders etc. are now emerging as trendsetter in green nanotechnology [14]. These are biocompatible and feasible carrier for the incorporation of biologically active molecules due to the hollow space inside the tubular structure [8]. HNTs are novel 1D naturally occurring clay minerals having the similar chemical composition as kaolinite [30].

They belong to the class of aluminosilicate clays, with molecular formula ($Al_2Si_2O_5(OH)_4 * 2\ H_2O$) exhibiting a hollow nanotubular structure [4] with their length ranging from 400 - 1000 nm, the inner and outer diameters of the nanotubes varying from 10 - 40 nm and 40 - 80 nm (Figure 1). The high aspect ratio (length/diameter) ranges from 10 - 50 nm [5]. HNTs are 1:1 phyllosilicates with six-membered rings, the atoms are arranged to form a structure of one octa-hedral and one tetrahedral sheet [45]. HNTs contain two types of hydroxyl groups, an inner one and an

outer one, which are placed between the layers, respectively on the surface of the nanotubes. The outer surface of HNTs is mainly formed by siloxane (Si-O-Si) groups, and the inner lumen surface is composed of aluminol groups (Al-OH) groups, making them Gibbsite-like highly hydrophilic (where Gibsite-like already relates to the monoclinic crystallography and the prismatic aspect of the crystals), the edges of the HNTs consists of Al-OH and Si-OH groups [32], (Figure 2). Hence, the inner surface of HNTs is chemically active, whereas the outer surface is considered as non-reactive [6]. Taking into consideration the state of hydration, HNTs are broadly classified into two groups: hydrated HNTs with a crystalline structure of 10 Å d_{001} spacing and the dehydrated HNTs with 7 Å d_{001} spacing. As it has been reported, that the existence or the age of interlayer water in HNTs is one of the most significant features differentiating HNTs from kaolinite [12].

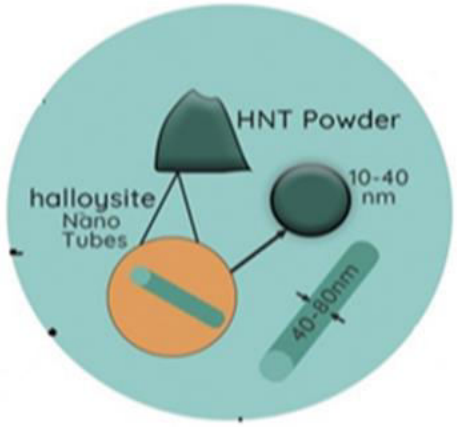

Figure 1.
Halloysite Nanotubular Structure
(inner diameter = 10 - 40 nm; outer diameter = 40 - 80 nm)

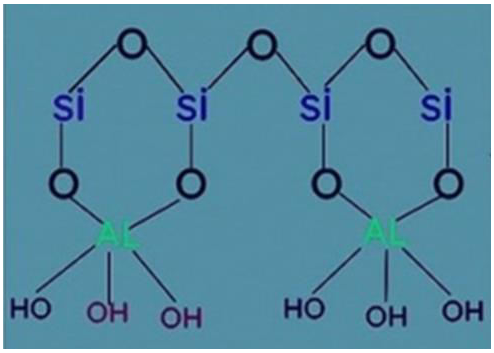

Figure 2.
Molecular Structure of HNT
HNTs consisting of Al-OH and Si-OH groups exhibiting the monolayer of water molecule

Physicochemical properties of HNTs

Physical properties of HNTs are presented in Table I [29].

Table I
Physical properties of HNTs [29]

Parameter	Values
Density	2.14 - 2.53 g/cm^3
Average Pore Size	80 - 100 Å
Typical Surface Area	22.1 - 81.6 m^2 * g
Pore volume	1.25 mL * g
Aspect Ratio (L/D)	9 - 50 nm
Specific gravity	2.53 g/cm^2
Cation exchange capability	0.1 - 0.7 mol * kg

Chemical Properties [34]

The outer surface of the HNTs has the similar properties to SiO_2 having a negative charge at pH 6 - 7 (zeta potential -18 mV), whereas the inner cylinder core is related to Al_2O_3 which is positively charged. The positive charge of the inner lumen urges the loading of HNTs with negative macromolecules within the void spaces. Negatively charged molecules are repelled by the negative charge present on the outer surface of HNTs.

Advantages of HNTs

HNTs are natural, non-toxic, biocompatible, eco-friendly and low-cost material, and it is recognized as nanomaterials (EPA 4) by the Environmental Protection Agency [40]. They have fine particle size and elegant dispersion property in matrix [15]. HNTs are capable of inhibiting the release, unless triggered and tunable release rates are achieved [38]. They possess immense cation exchange capacity [12]. A halloysite nanotube is able to load multiple active agents simultaneously [50]. It maintains constant, sustained release rates and not requiring an initial over-dosage [11, 14, 38]. HNTs have high aspect ratio, immense porosity and non-swelling nature [11]. During harsh material processing, halloysite protects active agent within its lumen [14]. It has remarkable loading rates compared to other carriers [11]. Halloysite has regeneration ability and enriches the bone healing efficacy [38]. HNTs have fast adsorption rate and high adsorption capacity [11] and HNTs can be used in many forms such as powders, creams, gels, lotions and sprays [21].

Solubility and Stability of HNTs

Solubilization and dispersion study of HNTs was performed by Mohtashim HS *et al*. without using organic solvents, to have a supramolecular product of HNTs and DNA [33]. A long-term stability study for natural HNTs was carried out at room temperature in three different solutions: strong acids (e.g., sulphuric acid, hydrochloric acid and acetic acid), strong base (e.g., sodium hydroxide) and distilled water. Both the acidic and basic environments reinforce the mechanism of nanotubes transformation to propose the dissolution of HNTs and precipitation of stable forms of amorphous Al $(OH)_3$ and SiO_2, respectively [46].

Functionalization of HNTs

Among the various phyllosilicate nanomaterials (silicate based layer structure) such as kaolin and montmorillonite, halloysite has some prominent advantages. HNTs are composed of small tubes that allow removal of nano-particles from a living organism. The active molecules can be incorporated into the lumen of an empty HNTs or even drug can be absorbed onto the outer surface of HNTs.

The chemical modification can be introduced into the external surface of the HNTs; whereas the lumen of the HNTs can simultaneously function by initiating supramolecular interactions of the drugs with the lumen of HNTs. The inner lumen is the most enticing feature of HNTs, with a diameter capable of entangling the chemical agents such as drugs, DNA, nanomolecules and nanodots and other chemically active agents e.g., anticorrosion for protective coating [31].

The optimized properties of nanocomposites are obtained by advancing the nano dispersion and stress transfer. The interfacial interaction between the nano-tubes and the polymer, should be carefully governed [41]. In other respects, impoverished load transfer among the nanotubes and circumferential polymer chain may induce interfacial spillage and reduces the mechanical properties of the composites. Thus, the functionalization of HNTs is highly essential for processing and increasing the properties of HNTs polymer nanocomposites, (Figure 3). The modified polymer nanocomposites nanotubes reveal enhanced mechanical and thermal properties, as the functionalization advances the dispersal and stress transfer [24].

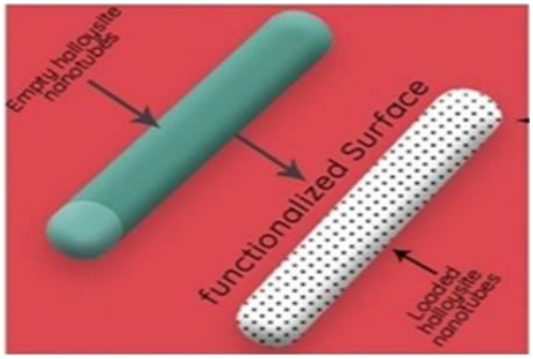

Figure 3.
Functionalization of HNTs

The functionalization of HNTs is achieved by two different processes, as follows.

Covalent functionalization

The inner surfaces and the edges of the sheets consist of hydroxyl group leading to the formation of multi-walled tubes that provide active sites for covalently adhering chemical substances.

The resulting outcomes are expected by adopting the relevant techniques.

Incorporation of hydrocarbons results in modification of chemical composition of HNTs surface, by minimizing the polarity of HNTs surface, safeguarding the surface hydroxyl group, and lastly, by generating the functional groups on the surface of HNTs. Poikelispaa *et al*. reported that the dispersion property of the HNTs can be enhanced in the solvents and polymers by booming their interfacial interactions [35].

Modification of HNTs with 2-hydroxybenzoic acid [23]. HNTs were modified by Li e*t al*. in 2008, by dissolving 2.8 g of 2-hydroxybenzoic acid (HBA) in 100 mL absolute ethanol and 4.5 g of HNT-3-aminopropyltriethoxysilane (APTES) was suspended in a mixture with continuous heating and stirring, adding 4 g of N, N′-Dicyclohexylcarbodiimide (DCC) to the suspension and then kept at reflux for 48 h at 86°C. The obtained product was filtered and washed with absolute ethanol and dried in an oven for 12 h at 60°C.

Silane Coupling. By condensation process, the most common covalent modification of HNTs is to graft silanes between the surface hydroxyl group of halloysite and hydrolyzed silane. Modification of the internal surface is significant for immobilization and controlled release process, whereas the modification on the external surface and edges benefits the nanocomposite applications. Yuan *et al*. in 2008 modified halloysite clay nanotubes by grafting with γ-aminopropyltri-ethoxysilane (APTES) [48].

Halloysite modification by Hexa-decyl-tri-methyl-ammonium bromide [18]. HNTs were modified by Khunova *et al*. in 2013. A 5% solution of Hexa-decyl-tri-methyl-ammonium bromide (HEDA) was used for the treatment of purified HNTs at 80°C for 24 h, followed by filtration and drying of HNTs in oven at 60°C for 24 h to obtain the modified HNTs.

The numerous types of silanes used for modifications of HNTs are listed in Table II [22].

Table II
Silanes used for modifications of HNTs [22]

Silanes	Composition
γ- Glycidoxypropyltrimethoxysilane (GPTS)	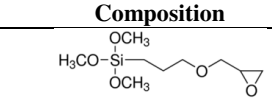
3- Aminopropyltrimethoxysilane (APS)	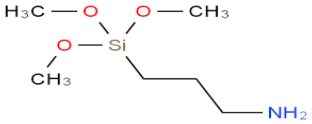

Silanes	Composition
3- Aminopropyltriethoxysilane (APTES)	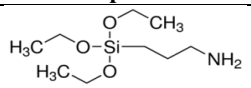
[3-(2-Aminoethylamino)propyl] trimethoxysilane (AEAPS)	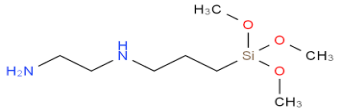
3-(Trimethoxysilyl)propyl methacrylate (MAPTS)	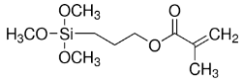
Vinyltrimethoxysilane (VTMS)	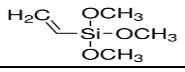

Non-covalent functionalization

Non-covalent functionalization is the most efficient approach to disperse the tubes in aqueous and non-aqueous solvents without damaging their unique structure and thus retaining their intrinsic properties [47].

Characterization of HNTs. HNTs are characterized by using scanning electron microscope (SEM), scanning force microscope (SFM) and transmission electron microscope (TEM). As reported, these techniques explains that most of the samples have cylindrical tubes with 40 - 50 nm diameter and 0.5 - 2 µm length. TEM images apparently illustrate the empty lumen of HNTs having a diameter of 15 - 20 nm [43].

Loading techniques in HNTs. There are few methods of loading drugs into HNTs and preferred methods are depicted in Figure 4.

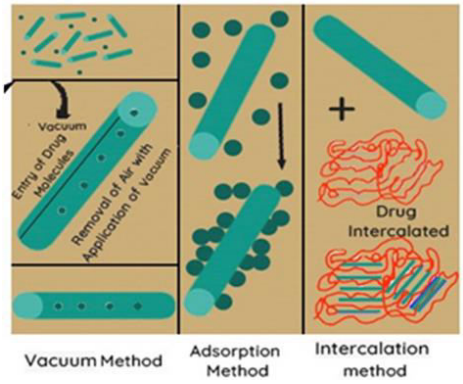

Figure 4.
Drug Loading Techniques of HNTs

Adsorption. The functional groups present on the surface of the HNTs such as Si-OH and Al-OH groups assist in determining the adsorption mechanism of HNTs. The surface charge of HNTs at pH 3 is positive, whereas above this pH it is negatively charged. An ionic pollutant does not possess high affinity for HNTs, as a result of negatively charged surfaces placed on the outer surfaces [19].

Intercalation. HNTs has the capacity to intercalate a wide number of organic and inorganic substances within the interlayer spaces. In this process, as the molecules penetrate the interlayer space, there is an origin of enlargement of these layers, due to the integration of water in the inter-lamellar spaces. The enlargement of these layers contributes to increase in d_{001} spacing between the layers [20]. The main criteria for developing the intercalation process are to entrap the water molecules between the walls of halloysite layers [13].

Tubular Entrapment. The most extensive and widely used method for loading of drug into HNTs is tubular entrapment method. It is also commonly known as *vacuum* method. This method was proposed by Kelly *et al*. in 2004 [16].

Applications of HNTs

Biomedical Applications of HNTs

Tissue Engineering Scaffolds. Tissue engineering scaffolds are components made of polymeric bio-materials to provide the structural support for cell attachment and subsequent tissue development [7]. HNTs are the rising materials in the field of tissue engineering, as they satisfy certain pre-requisites to be an ideal scaffold [26]. Zhou *et al*. in 2012 [25] fabricated halloysite-chitosan scaffolds by using freeze drying method. The halloysite-chitosan scaffold has revealed enhanced compressive strength, modulus, and thermal stability and has not induced any cyto-toxicity as compared to pure chitosan scaffold. Hence, HNTs polymer nanocomposite shows great potential for applications in tissue engineering.

HNTs as Wound Healing Sponges. Properties such as mechanical strength, good biocompatibility and haemostasis of tubular HNTs makes them ideal candidate for wound healing applications. HNTs-based nano-composite are tuned into dressings with wound healing properties. The porous and flexible chitosan composite sponges were fabricated by addition of HNTs which resulted in increased elastic modulus, compressive strength and toughness. Liu *et al*. have formulated chitosan-HNTs nanocomposite sponge by imposing freeze drying method. It was observed that the HNTs improved chitosan's blood clotting ability [27].

HNTs for Bone implant/Bone cement. Bone grafting is a surgical process which reinstates the missing bone in order to restore bone fractures. The most efficiently

available bone implants are dental implants and devices used in the improvement of damaged bones. The most extensively used bone cement is poly (methyl methacrylate) (PMMA) as it showed magnificent biocompatibility and mechanical properties for arthroplasty [39]. The bone cement is fabricated by incorporating the PMMA with gentamycin loaded HNTs. Thus, the PMMA/HNTs/gentamycin composite offered consistent sustained release up to 300 - 400 h and hence there by maintaining extended antibacterial protection [28].

HNTs for Cancer Cell Isolation. Curcumin is the most significant drug possessing the anti-inflammatory and anticancer properties and hence several methods have been adopted to load the curcumin into the lumen of HNTs. Massaro *et al*. in 2013 have reported that drug loading is carried out by functionalization of positively charged HNTs using tetrazolium salts. These HNTs-based carriers of curcumin were used as drug delivery for different cell line studies and were proved to be effective in many of cancer cells [36].

HNTs as potential Drug delivery vehicles. The most effective site for drug entrapment is the nanopore of HNTs [9]. The surface of drug loaded HNTs can be further coated with different polymers to achieve better delayed drug release rates [10]. Drugs, proteins and different substances can be loaded into the clay tube [2]. The chitosan and polyethyleneimine (PEI) coated HNTs reveal delayed release rates compared to uncoated HNTs [3], Figure 5.

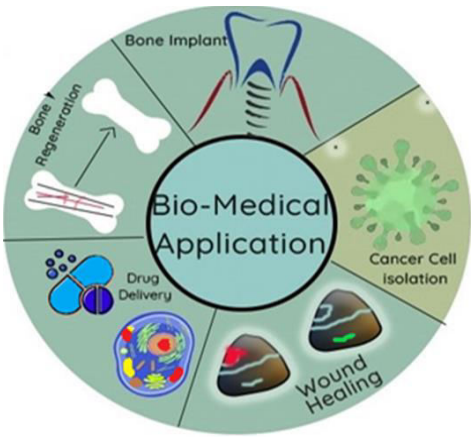

Figure 5.
Biomedical Applications of HNTs
Halloysite nanotubes possess wide range of biomedical applications such as in tissue engineering (bone regeneration), drug delivery, wound healing, bone implant and cancer cell isolation

HNTs for Non-Biomedical Applications

Use of HNTs as Nanoreactors and Nanocontainers

Nanoreactors

Nanoparticles and nanowires can be formulated by employing HNTs as nanoreactors. Synthesis of enzyme-catalysed inorganic reaction can be carried out by using HNTs bio-mineralization reactors, whereas HNTs lumen behaves as biomimetic nanoreactor [1].

Nanocontainers

Anti-Corrosion Coating with Benzotriazole. Corrosion of metals is a crucial technical problem. HNTs are used as tubular sacs for benzotriazole which is considered as corrosion inhibitor [48].

Use of HNTs in the synthesis of silver nanorods

Silver nanorods were fabricated by thermal decomposition of silver acetate from its aqueous solution and loaded into the lumen of the halloysite, by employing the *vacuum* cycling process. The polymer composite of silver nanorods revealed antimicrobial activity and increased tensile strength [42].

Gold Nanoparticles

Gold nanoparticles were prepared by reduction of chloroauric acid ($HAuCl_4$) using HNTs. Gold nanoparticles possess large surface area, which promotes high drug loading efficiency, biocompatible, and are freely accessible for the conjugation with biomolecules. These are non-cytotoxic to normal cells [17].

Application of HNTs for in situ chemical polymerization

The polyaniline (PANI) is laminated on the facet of the HNTs by adopting *in situ* soapless emulsion polymerization of anilinium chloride adsorbed on HNTs. Ammonium persulfate (APS), an oxidant, is used to roll out the HNTs in an aqueous solution of aniline with constant stirring and ultrasonic irradiation. The acidity of polymerizing media and adsorptivity of anilinium chloride on the surface of HNTs modify the structural characteristics of PANI/HNTs nanocomposites [51].

HNTs for Cosmetic Application

As a result of elongated hollow tubular structure and strong absorption capacity, HNTs can be availed as cleansing masks, which promote deep purification and clears the facial pores. The hollow HNTs can be loaded with a variety of active ingredients; particularly those used in cosmetics, household and personal care products [44], as shown in Figure 6.

Figure 6.
Non-Biomedical Applications of HNTs
Halloysite nanotubes have non-biomedical applications; therefore they can be used as anti-corrosive agent, cosmetics, in the fabrication of silver nanorods and gold nanoparticles

Conclusions

This review highlights the structural features, functionalization, biomedical and non-biomedical applications of HNTs. HNTs display remarkable thermal stability, faster adsorption rates, tuneable release rates, excellent drug encapsulation, biocompatibility, mechanical properties, and ease of availability therefore with numerous pharmaceutical applications. The functionalization of HNTs is a main necessity for processing and promoting the properties of HNTs polymer composites. HNTs have also established prominent character in various fields of biomedical sciences such as tissue engineering, bone implants, fillers in bone cement, and cancer cell isolation. Apart from biological features, HNTs have played roles in the synthesis of silver and gold nanoparticles, nano-reactors and nanocontainers, cosmetics, and drug delivery. Thus, it can be concluded that HNTs have acquired promising anticipation in the development of new structural and functional materials to emerge as trendsetters for green nanotechnology.

Conflict of interest

The authors declare no conflict of interest.

References

1. Abdullayev E, Price R, Shchukin D, Lvov Y, Halloysite tubes as nanocontainers for anticorrosion coating with benzotriazole. *ACS Appl Mater Interfaces*, 2009; 1(7): 1437-1443.
2. Abdullayev E, Joshi A, Wei W, Zhao Y, Lvov Y, Enlargement of halloysite clay nanotube lumen by selective etching of aluminum oxide. *ACS Nano*, 2012; 6(8): 7216-7226.
3. Abdullayev E, Abbasov V, Tursunbayeva A, Portnov V, Ibrahimov H, Mukhtarova G, Lvov Y, Self-healing coatings based on halloysite clay polymer composites for protection of copper alloys. *ACS Appl Mater Interfaces*, 2013; 5(10): 4464-4471.
4. Buruga K, Kalathi JT, Fabrication of γ-MPS-Modified HNT–PMMA Nanocomposites by Ultrasound-Assisted Miniemulsion Polymerization. *JOM.*, 2018; 70(7): 1307-1312.
5. Del Buffa S, Bonini M, Ridi F, Severi M, Losi P, Volpi S, Al Kayal T, Soldani G, Baglioni P, Design and characterization of a composite material based on Sr (II)-loaded clay nanotubes included within a biopolymer matrix. *J Colloid Interface Sci.*, 2015; 448: 501-507.
6. Deng S, Zhang J, Ye L, Halloysite–epoxy nanocomposites with improved particle dispersion through ball mill homogenization and chemical treatments. *Compo Sci Technol.*, 2009; 69(14): 2497-2505.
7. Fakhrullin RF, Lvov YM, Halloysite clay nanotubes for tissue engineering. *Nanomedicine (Lond.)*, 2016; 11(17): 2243-2246.
8. Ferrari PC, Araujo FF, Pianaro SA, Halloysite nanotubes-polymeric nanocomposites: characteristics, modifications and controlled drug delivery approaches. *Cerâmica*, 2017; 63(368): 423-431.
9. Fizir M, Dramou P, Dahiru NS, Ruya W, Huang T, He H, Halloysite nanotubes in analytical sciences and in drug delivery: A review. *Microchimica Acta*, 2018; 185(8): 389: 1-33.
10. Forsgren J, Jämstorp E, Bredenberg S, Engqvist H, Strømme M, A ceramic drug delivery vehicle for oral administration of highly potent opioids. *J Pharma Sci.*, 2010; 99(1): 219-226.
11. Fulekar MH, Pathak B, Environmental Nanotechnology. CRS Press Taylor and Francis Group, 2017; 93-94.
12. Gray N, Lumsdon DG, Hillier S, Effect of pH on the cation exchange capacity of some halloysite nanotubes. *Clay Miner*, 2016; 51(3): 373-383.
13. Hanif M, Jabbar F, Sharif S, Abbas G, Farooq A, Aziz M, Halloysite Nanotubes as a new drug-delivery system: A Review. *Clay Miner*, 2016; 51(3): 469-477.
14. Kamble R, Ghag M, Gaikawad S, Panda BK, Halloysite Nanotubes and Applications: A Review. *J Adv Sci Res.*, 2012; 3(2): 25-29.
15. Kausar A, Review on polymer/halloysite nanotubes nanocomposite. *Poly-Plast Tech Eng.*, 2018; 57(6): 548-564.
16. Kelly HM, Deasy PB, Ziaka E, Claffey N, Formulation and preliminary *in vivo* dog studies of a novel drug delivery system for the treatment of periodontitis. *Int J Pharma.*, 2004; 274(1-2): 167-183.
17. Khan AK, Rashid R, Murtaza G, Zahra A, Gold nanoparticles: synthesis and applications in drug delivery. *Trop J Pharma Res.*, 2014; 13(7): 1169-1177.
18. Khunova V, Kristóf J, Kelnar I, Dybal J, The effect of halloysite modification combined with *in situ* matrix modifications on the structure and properties of polypropylene/halloysite nanocomposites. *eXPRESS Poly Lett.*, 2013; 7(5): 471-479.
19. Kiani G, High removal capacity of silver ions from aqueous solution onto halloysite nanotubes. *Appl Clay Sci.*, 2014; 90: 159-164.
20. Krejčová K, Deasy PB, Rabišková M, Diclofenac sodium entrapment and release from halloysite nanotubules. *Ceska Slove Farma.*, 2013; 62(1): 28-34.
21. Kruif JK, Ledergerber G, Garofalo C, Fasler-Kan E, Kuentz M, On prilled nanotubes-in-microgel oral systems for protein delivery. *Eur J Pharma Biopharma.*, 2016; 101: 90-102.
22. Li C, Liu J, Qu X, Guo B, Yang Z, Polymer-modified halloysite composite nanotubes. *J Appl Poly Sci.*, 2008; 110(6): 3638-3646.
23. Li R, Hu Z, Zhang S, Li Z, Chang X, Functionalized halloysite nanotubes with 2-hydroxybenzoic acid for selective solid-phase extraction of trace iron (III). *Int J Environ An Chem.*, 2013; 93(7): 767-779.
24. Liu M, Guo B, Zou Q, Du M, Jia D, Interactions between halloysite nanotubes and 2, 5-bis (2-benzoxazolyl) thiophene and their effects on reinforcement of polypropylene/halloysite nanocomposites. *Nanotechnol.*, 2008; 19(20): 205709: 1-10.
25. Liu M, Zhang Y, Wu C, Xiong S, Zhou C, Chitosan/halloysite nanotubes bionanocomposites: structure, mechanical properties and biocompatibility. *Int J Biomed Macromol.*, 2012; 51(4): 566-575.
26. Liu M, Wu C, Jiao Y, Xiong S, Zhou C, Chitosan–halloysite nanotubes nanocomposite scaffolds for tissue engineering. *J Mater Chem B.*, 2013; 1(15): 2078-2089.

27. Liu M, Shen Y, Ao P, Dai L, Liu Z, Zhou C, The improvement of hemostatic and wound healing property of chitosan by halloysite nanotubes. *RSC Adv.*, 2014; 4(45): 23540-23553.
28. Luo BH, Hsu CE, Li JH, Zhao LF, Liu MX, Wang XY, Zhou CR, Nano-composite of poly (L-lactide) and halloysite nanotubes surface-grafted with L-lactide oligomer under microwave irradiation. *J Biomed Nanotechnol.*, 2013; 9(4): 649-658.
29. Lvov Y, Abdullayev E, Functional polymer–clay nanotube composites with sustained release of chemical agents. *Prog Poly Sci.*, 2013; 38(10-11): 1690-1719.
30. Lvov Y, Aerov A, Fakhrullin R, Clay nanotube encapsulation for functional biocomposites. *Adv Colloid Interface Sci.*, 2014; 207: 189-198.
31. Massaro M, Lazzara G, Milioto S, Noto R, Riela S, Covalently modified halloysite clay nanotubes: synthesis, properties, biological and medical applications. *J Mater Chem B.*, 2017; 5(16): 2867-2882.
32. Mingliang Du, Baochun G, Demin J, Newly emerging applications of halloysite nanotubes: a review. *Soci Chem Indus.*, 2010; 59(5): 574-582.
33. Mohtashim H Shamsi, Kurt E Geckeler, The first biopolymer-wrapped non-carbon nanotubes. *Nanotechnol.*, 2008; 19(7): 075604.
34. Nano by Nature, (Bernhardt Fudmya Design Group), www.bfdg.com, 2011.
35. Poikelispää M, Das A, Dierkes W, Vuorinen J, Synergistic effect of plasma-modified halloysite nanotubes and carbon black in natural rubber—butadiene rubber blend. *J Applied Poly Sci.*, 2013; 127(6): 4688-4696.
36. Riela S, Massaro M, Colletti CG, Bommarito A, Giordano C, Milioto S, Noto R, Poma P, Lazzara G, Development and characterization of co-loaded curcumin/triazole-halloysite systems and evaluation of their potential anticancer activity. *Int J Pharm.*, 2014; 475: 613-623.
37. Saif MJ, Asif HM, Escalating applications of halloysite nanotubes. *J Chil Chem Soc.*, 2015; 60(2): 2949-2953.
38. Saif MJ, Asif HM, Naveed M, Properties and modification methods of halloysite nanotubes: a state-of-the-art review. *J Chil Chemi Soc.*, 2018; 63(3): 4109-4125.
39. Santos AC, Ferreira C, Veiga F, Ribeiro AJ, Panchal A, Lvov Y, Agarwal A, Halloysite clay nanotubes for life sciences applications: From drug encapsulation to bioscaffold. *Adv Colloid Interface Sci.*, 2018; 257: 58-70.
40. Santos AC, Pereira I, Reis S, Veiga F, Saleh M, Lvov Y, Biomedical potential of clay nanotube formulations and their toxicity assessment. *Exp Opin Drug Deliv.*, 2019; 16(11): 1169-1182.
41. Shchukin DG, Sukhorukov GB, Price RR, Lvov YM, Halloysite nanotubes as biomimetic nanoreactors. *Small*, 2005; 1(5): 510-513.
42. Shchukin DG, Lamaka SV, Yasakau KA, Zheludkevich ML, Ferreira MG, Möhwald H, Active anticorrosion coatings with halloysite nanocontainers. *J Physi Chem C.*, 2008; 112(4): 958-964.
43. Singh B, Why does halloysite roll?—A new model. *Clays Clay Miner*, 1996; 44(2): 191-196.
44. Sun YJ, Kil DS, Chung KS, Abdullayev E, Lvov YM, Mongayt D, Natural nanocontainer for the controlled delivery of glycerol as a moisturizing agent. *J Nanosci Nanotechnol.*, 2011; 11(1): 661-665.
45. Suvendhu P, P Ganga Raju Achary, Nimai C Nayak, Mechanical and morphological properties of halloysite nanotubes filled ethylene-vinyl acetate copolymer nanocomposites. *Indian J Chem Technol.*, 2017; 24: 184-191.
46. White RD, Bavykin DV, Walsh FC, The stability of halloysite nanotubes in acidic and alkaline aqueous suspensions. *Nanotechnol.*, 2012; 23(6): 065705.
47. Wilson IR, Santos HD, Santos PD, Kaolin and halloysite deposits of Brazil. *Clay Miner*, 2006; 41(3): 697-716.
48. Yuan P, Southon PD, Liu Z, Green ME, Hook JM, Functionalization of halloysite clay nanotubes by grafting with γ-aminopropyltriethoxysilane. *J Phys Chem C.*, 2008; 112(40): 15742-15751.
49. Yuri M Lvov, Dmitry G Shchukin, Helmuth Möhwald, Ronald R Price, Halloysite Clay Nanotubes for Controlled Release of Protective Agents. *ACS Nano*, 2008; 2(5): 814-820.
50. Yuri L, Ronald P, Halloysite nanotubes applications in nanomaterials research. Merck. www.sigmaaldrich.com/.
51. Zhang L, Wang T, Liu P, Polyaniline-coated halloysite nanotubes *via in-situ* chemical polymerization. *Appl Surf Sci.*, 2008; 255(5): 2091-2097.

Indira Bahuuddeshiya Shikshan Sanstha, Buldana's

Dr. Rajendra Gode Institute of Pharmacy,

University-Mardi Road, Amravati (444602)

Certificate of Appreciation

This is to certified that **Revati D. Sagare** from **KLE College of Pharmacy, Hubballi, Karnataka** has been appreciated and recognized for her poster in online poster presentation competition during Two Days (Virtual) International Conference on, RECENT ADVANCES IN DRUG DISCOVERY held at Dr. Rajendra Gode Institute of Pharmacy, Amravati on 15th and 16th Dec. 2021.

Prof. Rahul D. Jawarkar
ORGANIZING SECRETARY

Dr. Snehal S. Manekar
CO-CONVENOR

Dr. Ravindra L. Bakal
CONVENOR

Indira Bahuuddeshiya Shikshan Sanstha, Buldana's

Dr. Rajendra Gode Institute of Pharmacy,

University-Mardi Road, Amravati (444602)

Certificate

This is to be certified that Ms. Revati D. Sagare From Kle College of Pharmacy Hubli, Karnataka. Presented a poster on topic "Halloysite Nanotubes: Design, Characterization and Applications: A Review" in Two Days (Virtual) International Conference on, RECENT ADVANCES IN DRUG DISCOVERY (QSAR Modeling, Molecular Docking, Molecular Simulation) held at Dr. Rajendra Gode Institute of Pharmacy, Amravati on 15th and 16th Dec. 2021.

Prof. Rahul D. Jawarkar
ORGANIZING SECRETARY

Dr. Snehal S. Manekar
CO-CONVENOR

Dr. Ravindra L. Bakal
CONVENOR

International Virtual Conference on Biomaterial-Based Therapeutics, Engineering and Medicine

BIOTEM-2021

Organized by

Departments of Biotechnology, Biomedical Engineering and Chemical Engineering, **Manipal Institute of Technology, MAHE**

Under the aegis of

Society for Biomaterials & Artificial Organs India (SBAOI) and **Society for Tissue Engineering and Regenerative Medicine India (STERMI)**

Co-organized by

The American Ceramic Society (ACerS)

CERTIFICATE

This is to certify that **Dr/Mr/Ms. Revati Dharampal Sagare** from **KLE College of Pharmacy, Hubballi**

has participated in **Oral presentation** and presented his/her research work entitled

"**Design, optimization and characterization of γ-methacryloxypropyltrimethoxysilane doped halloysite clay nanotubes using ultra turrax homogenizer**"

for the award of "**Dr. T.M.A. Pai "Researcher Award**" in the

"International Virtual Conference on Biomaterial-Based Therapeutics, Engineering and Medicine"

held from December 17 - 20, 2021.

Bikramjit Basu
President, SBAOI

Dr. Bharath Raja Guru
Convener, BIOTEM-2021

SHRI DHARMASTHALA MANJUNATHESHWARA UNIVERSITY

TRUTH LIBERATES

INTERNATIONAL CONFERENCE ON BIOMEDICAL AND CLINICAL RESEARCH

Organized by
Shri Dharmasthala Manjunatheshwara University
in association with
Association of Pharmaceutical Research

CERTIFICATE

This certificate is awarded to

Mr./Mrs./Ms./Dr. Revati Dharampal Sagare

for **Oral** Presentation entitled **"Optimization And Characterization Of Organo-Functionalized Natural Clay, Nanotubes With Selective Coupling Agent"** in the **International Conference on Biomedical and Clinical Research** held on 21st to 22nd of November 2022 at Shri Dharmasthala Manjunatheshwara University, Dharwad, Karnataka.

APR
Association of Pharmaceutical Research

Organising Secretary ICBMCR 2022	Founder & CEO APR	Chairperson ICBMCR 2022	Registrar SDM University	Vice Chancellor SDM University